# GUIDANCE CONTROL AND DYNAMICS OF A NEW GENERATION OF GEOSTATIONARY SATELLITES

# GUIDANCE CONTROL AND DYNAMICS OF A NEW GENERATION OF GEOSTATIONARY SATELLITES

## Proefschrift

ter verkrijging van de graad van doctor
aan de Technische Universiteit Delft,
op gezag van de Rector Magnificus prof. ir. K.C.A.M. Luyben,
voorzitter van het College voor Promoties,
in het openbaar te verdedigen op woensdag 3 mei 2017 om 12:30 uur

door

**Frederik Johannes (Ferdi) DE BRUIJN**

Master of Science in Aerospace Engineering,
Technische Universiteit Delft, Nederland,
geboren te Werkendam, Nederland.

Dit proefschrift is goedgekeurd door de

promotor: Prof. dr. E. Gill

Samenstelling promotiecommissie:

| | |
|---|---|
| Rector Magnificus | voorzitter |
| Prof. dr. E. Gill | Technische Universiteit Delft |
| Dr. D. Choukroun | Ben-Gurion University of the Negev |
| | |
| *Onafhankelijke leden:* | |
| Prof. dr. M. Guelman | Technion, Universität Würzburg |
| Prof. dr. M. Verhaegen | Technische Universiteit Delft |
| Prof. dr. P. Visser | Technische Universiteit Delft |
| Dr. M. Hooghe | SES Astra |
| Dr. S. Theil | German Aerospace Center (DLR) |

This research is supported by the German Aerospace Center DLR.

*Keywords:* Geostationary satellites, station-keeping, collocation, geometric constraints, modeling, dynamics, guidance, control

*Printed by:* Ipskamp Drukkers

*Front & Back:* Abstract impression of a sensor cone pointing towards Earth

ISBN 978-94-028-0606-9

An electronic version of this dissertation is available at
http://repository.tudelft.nl/.

*Doing a PhD is like riding a sine-wave superimposed on an affine function.*
*One should strive to maximize the slope of the affine function*
*and not be troubled by the unavoidable ups-and-downs of the wave.*

F.J. de Bruijn

# CONTENTS

# SUMMARY

Geostationary satellites have many advantages over other satellites, such as continuous coverage of a specific geographic region and 24/7 contact with a single ground station. These advantages have ensured that a large number of satellites are located in the geostationary orbit. To cope with the heavy population, the orbit has been divided into slots in geographic longitude and satellites are assigned to these geostationary slots. To maintain a satellite inside a slot, station-keeping maneuvers are needed, requiring accurate modeling of the orbital motion. In order to minimize the propellant required for these station-keeping maneuvers, clever guidance strategies need to be implemented, in order to maximize the lifetime of these highly valuable space assets. These topics, the guidance, control and dynamics of geostationary satellites are the subject of this work.

The scarcity of geostationary slots above prime locations has led operators to collocate several satellites in a single slot. This leads to a complication of the methods for modeling, guidance and control, as new constraints enter the problem such as maintaining a minimum separation distance between satellites in order to avoid collisions. Another potential constraint is the avoidance of interference between the satellites. Such interference can be caused by a satellite entering the field of view of a payload or another sensor on another satellite. Nowadays, the situation is further complicated by the fact that many newer satellites carry star sensors for more precise attitude measurements. Such star sensors can potentially be blinded by the sunlight reflecting off another satellite. These interferences can be avoided as part of the orbit control strategy, resulting in the addition of so-called sensor cone avoidance constraints to the guidance and control problem. The problem of maintaining minimum separation distances has been extensively treated in the literature whereas the problem of sensor cone avoidance constraints is still unsolved, motivating the need for new methods.

The motion of a geostationary satellite is governed by forces resulting from the gravity of the Earth, sun and moon, as well as solar radiation pressure and forces resulting from thrusters on-board the satellites. Since a geostationary satellite is actively controlled to stay inside its assigned slot, the perturbing accelerations and the impact of controlled accelerations can be approximated by those that a virtual satellite at the slot center would experience. This simplifying assumption is used to develop a novel linear, time-varying system of first order differential equations to describe motion of a geostationary satellite. The linear system is discretized and the resulting equations express an affine relation between state and controlled accelerations, suitable for use in convex optimization problems. A similar assumption is used to develop a method to transform between mean and osculating orbital elements.

The orbital state of a geostationary satellite is commonly represented using a set of synchronous orbital elements. These non-singular elements essentially describe the state of the satellite with respect to the center of the geostationary slot within which the satellite is controlled. The synchronous orbital elements are effectively relative or-

bital elements between a satellite and the slot center (which is the "zero state"). Relative orbital elements between two satellites are usually defined as the arithmetic difference between the synchronous orbital elements of two satellites in the same slot. An approximate linear transformation can be used to relate the relative orbital elements to Cartesian position and velocity in the radial, tangential and normal reference frame. Just like the absolute orbital elements define the size and orientation of a satellite's orbit, the relative orbital elements define the size and orientation of the relative orbit. A set of rational relative orbital elements is introduced by dividing the relative orbital elements by the magnitude of the relative eccentricity vector.

Three types of operational constraints have been identified: staying inside the geostationary slot, maintaining minimum separation distances and the sensor cone avoidance constraints. The first constraint is a convex constraint, whereas the latter two are non-convex constraints. These non-convex constraints are dealt with by relative orbit design. The combinations of relative orbital elements satisfying these constraints are identified and visualized using the newly introduced rational relative orbital element set. A key change, compared to the conventional collocation strategies, is that the relative mean longitude of the satellites needs active control in order to guarantee satisfaction of the sensor cone avoidance constraints. An analysis of a sensor cone avoidance constraint for an Earth-pointing sensor further reveals that the usual eccentricity/inclination vector separation strategy no longer leads to satisfactory results and a change in the strategy is required to satisfy minimum distance constraints and sensor cone avoidance constraints simultaneously. A design process is introduced and demonstrated to determine a set of (convex) tolerance windows on relative orbital elements that satisfy various constraints simultaneously for any satellite position inside all of the resulting relative orbits.

The single-satellite station-keeping problem is formulated as a convex optimization problem in terms of orbital elements. This is made possible by the novel formulation of the dynamics in the form of a linear time-varying system of first order differential equations. A sequence of increasingly complex problems is formulated. The final problem and its solution constitute a novel method to the problem of station-keeping. This new method results in a unique combination of the following beneficial characteristics:

- The problem is convex, well-scaled and guaranteed to have a solution satisfying the constraints.
- The problem solution provides directly a maneuver plan with the thrusts that are required for each thruster. Arbitrary thruster configurations can be defined and included in the problem formulation.
- The thruster firings can be constrained to account for a maximum thrust force and to avoid thruster firings during certain periods of time, e.g., to avoid firings during eclipses or to allow firings only at certain days of a maneuver cycle.
- The method is applicable both to high thrust-to-mass chemical propulsion systems as well as low-thrust-to-mass electric propulsion systems.
- Convex inequality and affine equality constraints on the satellite state can be added to the problem, allowing to formulate constraints at any (or every) discrete node.

The final problem formulation is defined using both a single-shooting and a multiple-shooting approach. The first approach is conceptually simpler and results in a smaller

optimization problem. The latter approach increases the problem size, but also the sparsity of the problem and is especially suitable for solving problems with large horizons and many variables.

A validation of the new method for calculating station-keeping maneuvers consists of comparing the results with a conventional scheme with two east/west maneuvers per week and one north/south maneuver per fortnight. A simulation was performed in which the new method was configured to reproduce similar results as the conventional method. The results are compared side-by-side and a one year simulation reveals exactly the same number of maneuvers in both cases, with maneuver size, location, cumulative $\Delta V$ and state trajectories being near-identical.

A further analysis of the method is performed by solving the station-keeping problem with a one-year horizon using a problem formulation with the multiple shooting approach. A variety of problems were defined and solved and the solutions reveal classic guidance strategies such as the sun-pointing perigee strategy and the strategy to make north/south maneuvers such that these maneuvers oppose the inclination vector's secular drift. Further investigations reveal relations between the size of the sun-pointing perigee circle and the east/west propellant consumption, as well as the size of the eccentricity and inclination vector windows, propellant consumption and number of thruster firings required. A further demonstration shows that the sun-pointing perigee strategy is only beneficial for typical chemical propulsion thruster configurations with thrusters pointing in north and south directions. Electric propulsion configurations with thrusters pointing away from the purely north and south directions no longer require a sun-pointing perigee strategy to save propellant.

Further simulation results demonstrate that the method works well in a variety of scenarios, both for satellites with high thrust-to-mass ratios as well as satellites with low-thrust-to-mass ratios. The simulations include realistic errors in thrust force magnitude, direction and orbit determination, as well as errors resulting from mismodeling of the dynamics. The results show that the magnitude of the errors in orbit prediction depend on the thrust force, as well as on the thruster configuration. The simulation results of a scenario in which the method was used as a receding horizon controller show that highly accurate control of the state trajectory is possible using the novel method.

The method is extended from single-satellite station-keeping to collocation of multiple satellites in a single slot. A leader/follower hierarchy is used, where the leader satellite is controlled using the method developed for single-satellite station-keeping, whereas the follower satellites are controlled with respect to the leader satellite. The problem is formulated in terms of relative orbital elements and both the minimum distance constraint as well as the sensor cone avoidance constraints can be included in the problem formulation by defining convex control windows on relative orbital elements that guarantee a satisfaction of the constraints. The method is robustified by including the various error sources affecting the orbit prediction accuracy explicitly. The impact of orbit determination errors, modeling errors and thruster errors on the state trajectory in terms of relative orbital elements is investigated and $3\sigma$ bounds on these errors are included in the robustified problem formulation as well.

The results of the collocation control simulations show that the method is suitable for controlling an inhomogeneous fleet of four satellites with different characteristics in terms of propellant type, configuration and area-to-mass ratio. The method can also be applied to much larger fleets, as demonstrated in another simulation, where sixteen identical satellites are controlled within a small ±0.05° slot, albeit with a maneuver cycle duration of only one day. Further simulations show how the method is able to deal with highly complex scenarios not solvable with previous methods. Such scenarios include dealing with several sensor cone avoidance constraints and minimum distance constraints simultaneously, while maintaining the fleet in its assigned geostationary slot. The results demonstrate that the method was able to satisfy all constraints without a degradation of performance in terms of propellant consumption. The robustified formulation and solution of the problem is used in the last set of simulations. The results show on one hand how the satellite state can be kept inside the predefined tolerance windows, while on the other hand demonstrating some potential pitfalls of the robustified method.

The key conclusions from the work are that the new method is well able to deal with complex problems of both single-satellite station-keeping as well as collocation control of a fleet of satellites. The various geometric constraints can be dealt with successfully without having (significant) negative impacts on the propellant consumption or number of thruster firings of the satellites.

# SAMENVATTING

Geostationaire satellieten hebben vele voordelen ten opzichte satellieten in een andere baan, zoals constante dekking van een bepaald geografisch gebied en slechts één enkel grondstation is nodig om 24/7 contact te hebben met de satelliet. Deze voordelen hebben ervoor gezorgd dat de geostationaire baan druk bezet is. Om met deze grote hoeveelheid satellieten om te gaan is de geostationaire baan verdeeld in “slots” in geografische lengtegraden. Om een satelliet in een dergelijke slot te behouden zijn baanmanoeuvres noodzakelijk, hetgeen nauwkeurige modellering van satellietenbanen benodigd. Om de brandstofconsumptie te beperken zijn slimme sturingsstrategiën gewenst, om de levensduur van de satelliet te maximaliseren. Deze onderwerpen, het modelleren, sturen en regelen van geostationaire satellieten worden in deze dissertatie onderzocht.

De schaarste van geostationaire slots boven belangrijke gebieden heeft ervoor gezorgd dat operateuren meerdere satellieten in één slot plaatsen: co-lokatie. Dit compliceert de methoden voor het modelleren, sturen en regelen van de satellietbanen, omdat nieuwe randvoorwaarden aan het probleem worden toegevoegd. Een voorbeeld is het behouden van een minimale afstand tussen de satellieten, om botsingen te voorkomen. Een andere mogelijke randvoorwaarde is het vermijden van interferentie tussen satellieten. Interferentie kan worden veroorzaakt doordat een satelliet door het zichtveld vliegt van een sensor op een andere satelliet. Tegenwoordig kan deze situatie vaker voorkomen omdat de meeste nieuwe satellieten worden uitgerust met sterrensensoren om hun oriëntatie met hoge nauwkeurigheid te bepalen. Zulke sterrensensoren kunnen geblindeerd worden door zonlicht dat vanaf een andere satelliet gereflecteerd wordt. Deze vormen van interferentie kunnen worden vermeden door geschikte satellietbanen te kiezen en de satellietbanen nauwkeurig te regelen. De randvoorwaarde voor het ontwerp van zulke (relatieve) banen is het vermijden van het zichtveld van sensoren op nabije satellieten. De eerste randvoorwaarde, het behouden van een minimale afstand, is reeds in detail onderzocht in de literatuur, terwijl daarentegen de zichtveldvermijding een onopgelost probleem is. Dit onopgeloste probleem is een belangrijke motivatie voor dit onderzoek.

De beweging van geostationaire satellieten wordt bepaald door gravitatie van aarde, zon en maan, alsook door stralingsdruk van zonlicht en de krachten die worden uitgeoefend op de satelliet als gevolg van het uitvoeren van een baanmanoeuvre. Omdat een geostationaire satelliet actief geregeld wordt om in zijn aangewezen slot te blijven is het mogelijk om de krachten die op de satelliet werken te benaderen door de krachten die een virtuele satelliet zou ervaren die zich in het centrum van de slot bevindt. Deze aanname wordt gebruikt om een nieuw lineair tijdsafhankelijk model op te stellen om de beweging van de satelliet te modelleren. Dit lineaire system wordt gediscretiseerd en de resulterende vergelijkingen beschrijven een affiene relatie tussen de staat van de satelliet en de krachten die worden uitgeoefend door het maken van baanmanoeuvres. Dit systeem is geschik voor het gebruik in convexe optimalisatieproblemen. Een soortgelijke

aanname wordt gebruikt om een methode te ontwikkelen om transformaties tussen gemiddelde en osculerende baanelementen te maken.

De staat van een geostationaire satelliet wordt doorgaans weergegeven met behulp van synchrone baanelementen. Dit zijn baanelementen zonder singulariteiten, welke de staat van de satelliet beschrijven ten opzichte van het centrum van de slot waarin de satelliet zich bevind. De synchrone baanelementen zijn effectief relatieve baanelementen tussen een satelliet en het centrum van de slot (welke ook wel de nulstaat wordt genoemd). Relatieve baanelementen tussen twee satellieten zijn doorgaans gedefiniëerd als het arithmetische verschil van de synchrone baanelementen van twee satellieten die zich in dezelfde slot bevinden. Een lineaire transformatie kan worden gebruikt om een benadering te maken van de Cartesische positie en snelheid in een radiaal, tangentiaal, normaal referentie system, op basis van de relatieve baanelementen. Evenals absolute baanelementen beschrijven de relatieve baanelementen de grootte en oriëntatie van de relatieve satellietbanen. Een set van rationele relatieve baanelementen wordt geïntroduceerd als de ratio van de relatieve baanelementen en de grootte van de relatieve eccentriciteitsvektor.

Drie verschillende operationele randvoorwaarden worden gedefiniëerd: de satellieten moeten in hun slot blijven, een minimale afstand moet worden gerespecteerd en het zichtveld van sensoren op andere satellieten moet worden vermeden. De eerste randvoorwaarde is convex, terwijl de andere twee niet-convex zijn. Om aan deze niet-convexe randvoorwaarden te voldoen worden relatieve satellietbanen ontworpen. De combinaties van relatieve baanelementen die aan de verschillende randvoorwaarden voldoen worden geïdentificeerd en gevisualiseerd door gebruik te maken van de geïntroduceerde rationele relatieve baanelementen. Dit resulteert in de noodzakelijkheid van een belangrijke verandering ten opzichte van conventionele baanregelingsstrategiën: de relatieve lengtegraad van de satellieten moet actief worden geregeld. Ook de conventionele eccentriciteit/inclinatie-vector separatie strategie, welke voornamelijk ontwikkeld is om een minimale afstand tussen satellieten te garanderen, leidt niet langer tot het gewenste resultaat. Door de randvoorwaarde van zichtveldvermijding van sensoren moet ook deze strategie veranderd worden. Een ontwerpproces wordt geïntroduceerd om tot een strategie te komen die gelijktijdig aan alle randvoorwaarden voldoet. Het resultaat van dit ontwerpproces is een set van convexe tolerantievensters waarin de relative baanelementen gehouden moeten worden.

Een methode is ontwikkeld om een satelliet in zijn slot te behouden: station-keeping. Dit station-keeping probleem wordt geformuleerd als een convex optimalisatieprobleem in termen van synchrone baanelementen. Deze convexe formulering is mogelijk gemaakt door het eerder geïntroduceerde lineaire tijdsafhankelijke dynamische model. Een reeks optimalisatieproblemen wordt gedefinïeerd met toenemende complexiteit. Deze formulering van het probleem, samen met de oplossing, vormen een nieuwe station-keeping methode. Deze nieuwe method resulteert in een unieke combinatie van voordelige eigenschappen:

- Het probleem is convex, goed geschaald, en dusdanig geformuleerd dat er altijd een oplossing bestaat die aan de randvoorwaarden voldoet.
- De oplossing van het probleem is een plan met manoeuvres die uitgevoerd moeten worden door het propulsiesysteem aan boord van de satelliet. Elke willekeurige

configuratie van het propulsiesysteem kan worden ondersteund.
- Er kan rekening gehouden worden met de maximale stuwkracht van de motoren, en met periodes waarin geen manoeuvres mogelijk zijn, bijvoorbeeld tijdens eclipsen.
- De methode is zowel toepasbaar op satellieten uitgerust met chemische motoren met sterke stuwkracht als ook op satellieten met elektrische motoren die slechts een zwakke stuwkracht leveren.
- Convexe ongelijkheden of affiene vergelijkingen in staat of regel variabelen kunnen aan het probleem worden toegevoegd, waardoor het mogelijk is om randvoorwaarden te definïeren op elk discreet knooppunt.

De resulterende formulering van het probleem is zowel als zogenaamd “single-shooting” probleem, als ook als “multiple-shooting” probleem gedefinïeerd. De eerste formulering resulteert in een kleiner optimalisatieprobleem, terwijl de tweede formulering het probleem ijler maakt, waardoor grotere problemen met meer discrete stappen opgelost kunnen worden.

De methode wordt gevalideerd door de resultaten te vergelijken met conventionele methoden voor station-keeping van geostationaire satellieten. De conventionele methode gebruikt twee oost-west manoeuvres per week en één noord-zuid manoeuvre per twee weken. De nieuwe methode wordt zo geconfigureerd dat een oplossing ontstaat met dezelfde eigenschappen als de conventionele oplossingsmethode. De oplossingen worden vergeleken over een simulatieperiode van één jaar. De benodigde brandstof is nagenoeg identiek, terwijl het aantal benodigde manoeuvres exact gelijk is. Deze overeenkomsten vormen een belangrijke validatie van de methode.

De methode wordt verder onderzocht door het probleem te formuleren over de duur van één jaar. De oplossing van dit probleem levert direct alle manoeuvres die tijdens dit jaar moeten worden uitgevoerd om de positie van de satelliet te regelen. Een verscheidenheid aan problemen wordt gedefinïeerd en opgelost en de oplossingen reproduceren bekende sturingsstrategïen zoals de strategie om de eccentriciteitsvektor (en dus het perigeum van de baan) richting de zon te laten wijzen, als ook de strategie om noord-zuid manoeuvres altijd in de richting te maken van de seculaire drift van de inclinatievektor. Verder onderzoek onhult zowel relaties tussen de grootte van de cirkel die de eccentriciteitsvektor beschrijft en de brandstofconsumptie voor oost/west manoeuvres, als ook tussen de grootte van de tolerantievensters voor eccentriciteitsvektor en inclinatievektor, de brandstofconsumptie en het aantal benodigde manoeuvres. Tevens wordt aangetoont dat de strategie om het perigeum richting de zon te laten wijzen slechts voordelig is voor typische propulsiesysteem configuraties met chemische motoren. Omdat propulsiesystemen met elektrische motoren doorgaans niet richting het noorden of het zuiden zijn uitgericht, levert deze conventionele strategie geen besparing van brandstof meer op.

Verdere simulatieresultaten laten zien dat de nieuwe methode goede prestaties levert in tal van scenariën, zowel voor satellieten met chemische als elektrische motoren. Realistische fouten in grootte en richting van de stuwkracht, de baanbepaling en de modelering zijn toegevoegd aan de simulaties. De resultaten laten zien dat de grootte van fouten in de baanvoorspelling afhankelijk zijn van zowel de grootte van de stuwkracht als ook van de configuratie van het propulsiesysteem. De methode is tevens geïmplementeerd als een regelmechanisme met een voortlopende horizon. Deze implementatie laat zien dat ook hoognauwkeurige regeling mogelijk is met de nieuwe methode.

Vervolgens wordt de methode uitgebreid om ook co-lokatie van meerdere satellieten in een enkele slot te ondersteunen. Hiervoor wordt een leider/volger hiërarchie gebruikt: de leider wordt geregeld met behulp van de hier boven beschreven methode voor één satelliet terwijl de volgers worden geregeld met betrekking tot de leider. Het probleem wordt geformuleerd in termen van relatieve baanelementen en zowel de randvoorwaarde om een minimale afstand aan te houden, als ook om het zichtveld van sensoren te vermijden kunnen worden toegevoegd aan het probleem. Deze laatste twee randvoorwaarden worden voldaan door de relatieve baanelementen in convexe tolerantievensters te houden die voldoening van deze randvoorwaarden garanderen. Een robustere variant van het probleem wordt geformuleerd door expliciet rekening te houden met de verschillende bronnen van fouten die een invloed hebben op de nauwkeurigheid van de baanvoorspelling. De invloed van fouten in baanbepaling, manoeuvres en modelering op de baanvoorspelling wordt onderzocht in termen van relatieve baanelementen en de $3\sigma$-grenzen van deze fouten worden toegevoegd aan de robustere formulering van het probleem.

De resultaten van de co-lokatie simulaties laten zien dat de nieuwe method geschikt is om een inhomogene vloot van vier satellieten te regelen, waarin de satellieten verschillende karakteristieken hebben, zoals type en configuratie van het propulsiesysteem, massa en oppervlakte van de satelliet. De methode kan ook worden toegepast op grotere vloten, dit wordt gedemonstreerd in een andere simulatie, waarin zestien satellieten in een kleine slot van 0.05° gehouden worden. De duur van de manoeuvre-cyclus wordt hierbij gereduceerd tot één dag. De simulaties laten ook zien hoe de methode omgaat met zeer complexe scenariën, die niet uitgevoerd kunnen worden met conventionele methoden. In deze scenariën wordt tegelijkertijd voldaan aan de randvoorwaarden van zichtveldvermijding van sensoren, het behouden van minimale afstanden tussen satellieten en het behouden van de satelliet in de toegewezen slot. De resultaten laten zien dat de methode ook in zulke complexe scenariën succesvol is, zonder dat hierbij de brandstofconsumptie omhoog gaat. De robustere variant wordt in de laatste set van simulaties onderzocht. De resultaten laten zien dat enerzijds de satelliet in de tolerantievensters gehouden kan worden, anderzijds laten de resultaten ook een mogelijke negatieve bijwerking van de robuste variant zien: een significante toename van het aantal benodigde manoeuvres.

De belangrijkste conclusies van dit onderzoek zijn dat de ontwikkelde methode om kan gaan met de complexe problemen van station-keeping en co-lokatie van geostationaire satellieten. Zowel nieuwe als conventionele geometrische randvoorwaarden kunnen worden vervuld zonder significante negatieve invloeden op de brandstofconsumptie en het aantal benodigde manoeuvres.

# NOMENCLATURE

## Symbols

| | |
|---|---|
| $A$ | Surface area exposed to solar radiation pressure [$\mathrm{m}^2$] |
| AU | Astronomical Unit (149597870700 m) |
| $\tilde{\mathbf{A}}$ | System matrix of the discretized system |
| $\mathscr{B}$ | Scaling matrix for equality constraints |
| $\tilde{\mathbf{B}}$ | Input matrix of the discretized system |
| $\mathbf{C}$ | Covariance matrix |
| $\mathscr{C}$ | Scaling matrix for inequality constraints |
| $C_R$ | Solar radiation pressure coefficient of a satellite [-] |
| $\bar{C}_{nm}$ | Normalized geopotential coefficients of order $m$ and degree $n$ |
| $E$ | Eccentric anomaly [rad] |
| $\mathbf{F}$ | System matrix of the concatenated system |
| $\mathbf{H}$ | Input matrix for $\mathbf{u}_{\mathrm{tot}}$ of the concatenated system |
| $J_2$ | Gravitational perturbation of degree 2 and order 0 |
| $J_{22}$ | Gravitational perturbation of degree 2 and order 2 |
| $\mathbf{J}$ | Input matrix for $\mathbf{d}_{\mathrm{tot}}$ of the concatenated system |
| $L$ | Argument of mean longitude $L = \omega + \Omega + M$ [rad] |
| $\Delta L$ | Relative mean longitude or mean longitude difference [rad] |
| $\delta L$ | Relative mean longitude difference (= relative mean longitude) [rad] |
| $M$ | Mean anomaly [rad] |
| $\delta M$ | Angle between satellite position vector and relative eccentricity vector [rad] |
| $P$ | Radiation pressure [$\mathrm{N/m}^2$] |
| $\bar{P}_{nm}$ | Normalized associated Legendre function of order $m$ and degree $n$ |
| $R$ | Radius of a body [m] |

| | |
|---|---|
| $\Delta R$ | Relative radius [m] |
| $\bar{S}_{nm}$ | Normalized geopotential coefficients of order $m$ and degree $n$ |
| $T$ | Thrust force [N] |
| $\mathrm{T}$ | Orbital period [s] |
| $\mathbf{T}$ | Scaling matrix for the thrust force vector $[N^{-1}]$ |
| $\mathscr{T}$ | Scaling matrix for the thrust force vector for all discrete nodes $[N^{-1}]$ |
| $\mathbf{W}_a$ | Weighting matrix for the affine equality constraints |
| $\mathbf{W}_\tau$ | Weighting matrix for thrust vector $\boldsymbol{\tau}_{\mathrm{tot}}$ |

| | |
|---|---|
| $a$ | Semi-major axis [m] |
| $\delta a$ | Non-dimensional semi-major axis difference ($\Delta a/a$) [-] |
| $\mathbf{a}$ | Acceleration vector [m/s$^2$] |
| $\mathbf{a}(\cdot)$ | Vector of affine equality constraints |
| $\hat{\mathbf{b}}_s$ | Sensor bore-sight unit vector |
| $\mathbf{c}(\cdot)$ | Vector of inequality constraints |
| $\tilde{\mathbf{d}}$ | Disturbing accelerations on the discretized system [m/s$^2$] |
| $e$ | Eccentricity [-] |
| $\delta e$ | Magnitude of relative eccentricity vector [-] |
| $\mathbf{e}$ | Eccentricity vector $\mathbf{e} = \left(e_x,\ e_y\right)^T$ [-] |
| $\Delta\mathbf{e}$ | Relative eccentricity vector $\Delta\mathbf{e} = \left(\Delta e_x,\ \Delta e_y\right)^T$ [-] |
| $\hat{\mathbf{e}}_j$ | Unit vector in direction specified by subscript $j$ |
| $h$ | Discretization or integration timestep [s] |
| $\delta\mathbf{h}_\varphi$ | Rational relative-orbit normal vector [-] |
| $\delta\mathbf{h}$ | Relative angular momentum vector [m$^2$/s] |
| $i$ | Inclination [rad] |
| $\delta i$ | Magnitude of relative inclination vector [rad] |
| $\mathbf{i}$ | Inclination vector $\mathbf{i} = \left(i_x,\ i_y\right)^T$ [rad] |

| | |
|---|---|
| $\Delta\mathbf{i}$ | Relative inclination vector $\Delta\mathbf{i} = \left(\Delta i_x,\ \Delta i_y\right)^T$ [rad] |
| $\ell$ | Argument of true longitude $\ell = \omega + \Omega + \nu$ [rad] |
| $m$ | Satellite mass [kg] |
| $n$ | Mean orbital motion [rad/s] |
| $\Delta n$ | Relative mean orbital motion or mean orbital motion difference [rad/s] |
| $\mathbf{oe}$ | Set of (synchronous) orbit elements |
| $p$ | Semi-latus rectum [m] |
| $r_e$ | Radius of eccentricity circle |
| $r$ | Magnitude of position vector [m] |
| $\mathbf{r}$ | Position vector [m] |
| $\mathbf{s}_a$ | Vector of affine equality constraint slack variables |
| $\mathbf{s}_c$ | Vector of inequality constraint slack variables |
| $t$ | Time [sec] |
| $u_j$ | Component of perturbing acceleration in the direction specified by $j$ [m/s$^2$] |
| $\mathbf{u}$ | Control input vector, here: accelerations in radial, tangential and normal directions [m/s$^2$] |
| $v$ | Magnitude of velocity [m/s] |
| $\mathbf{v}$ | Velocity vector [m/s] |
| $w_{cj}$ | Weighting factor for the $j^{\text{th}}$ inequality constraint |
| $x, y, z$ | Components of relative position vector in radial, tangential and normal direction [m] |
| $\mathbf{x}$ | State vector, here: $\mathbf{x} = \left(\Delta n,\ e_x,\ e_y,\ i_x,\ i_y,\ \Delta L\right)^T$ |
| | |
| $\Gamma$ | Thruster configuration matrix [kg$^{-1}$] |
| $\boldsymbol{\Gamma}$ | Thruster configuration matrix for the concatenated system [kg$^{-1}$] |
| $\Delta_\alpha$ | Normally distributed random variable capturing thrust attitude uncertainty |
| $\Delta_\tau$ | Normally distributed random variable capturing thrust magnitude uncertainty |
| $\boldsymbol{\Phi}(t, t_0)$ | State transition matrix between $t_0$ and $t$ |
| $\Omega$ | Right ascension of ascending node [rad] |

| | |
|---|---|
| $\delta\Omega$ | Phase angle of relative inclination vector [rad] |
| $\alpha$ | Right ascension of geostationary position [rad] |
| $\beta$ | Off-radial pointing angle thruster [rad] |
| $\beta_s$ | Sensor half-cone angle [rad] |
| $\gamma$ | Off-north pointing angle thruster [rad] |
| $\theta$ | Azimuth angle [rad] |
| $\lambda$ | Longitude [rad] |
| $\Delta\lambda$ | Relative longitude [rad] |
| $\mu$ | Gravitational parameter [$\mathrm{m}^3/\mathrm{s}^2$] |
| $\nu$ | True anomaly [rad] |
| $\rho$ | Magnitude of relative position vector [m] |
| $\boldsymbol{\rho}$ | Relative position vector [m] |
| $\dot{\boldsymbol{\rho}}$ | Relative velocity vector [m/s] |
| $\boldsymbol{\tau}$ | Vector of thrusts of individual thrusters [N] |
| $\phi$ | Latitude [rad] |
| $\Delta\phi$ | Relative latitude [rad] |
| $\phi_p$ | Polar angle [rad] |
| $\varphi_L$ | Rational relative mean longitude difference [-] |
| $\varphi_a$ | Rational relative semi-major axis difference [-] |
| $\varphi_i$ | Rational relative inclination difference [-] |
| $\omega$ | Argument of perigee [rad] |
| $\tilde{\omega}$ | $\tilde{\omega} = \omega + \Omega$ [rad] |
| $\delta\omega$ | Angle between relative eccentricity and inclination vectors [rad] |
| $\delta\tilde{\omega}$ | Phase angle of relative eccentricity vector [rad] |

### Indices

| | |
|---|---|
| $\{\cdot\}_0$ | At epoch $t_0$ |
| $\{\cdot\}_{3\mathrm{b}}$ | Third body |

| | |
|---|---|
| $\{\cdot\}_E$ | Earth |
| $\{\cdot\}^{\text{EW}}$ | East-West |
| $\{\cdot\}^{FB}$ | Finite burn |
| $\{\cdot\}^{I}$ | Impulsive |
| $\{\cdot\}_K$ | Kamel |
| $\{\cdot\}^{L}$ | Linear addition |
| $\{\cdot\}_{\text{MC}}$ | Maneuver Cycle |
| $\{\cdot\}^{MO}$ | Due to modeling |
| $\{\cdot\}_{\text{N}}$ | Refers to the last ($N^{\text{th}}$) discrete node |
| $\{\cdot\}^{\text{NS}}$ | North-South |
| $\{\cdot\}^{OD}$ | Due to orbit Determination |
| $\{\cdot\}^{Q}$ | Quadratic addition |
| $\{\cdot\}^{TD}$ | Due to thrust direction errors |
| $\{\cdot\}^{TM}$ | Due to thrust magnitude errors |
| $\{\cdot\}_c$ | Controlled |
| $\{\cdot\}_d$ | Disturbing |
| $\{\cdot\}_{\text{des}}$ | Desired |
| $\{\cdot\}_{\text{geo}}$ | Geostationary, referring to the slot center of an ideal geostationary orbit |
| $\{\cdot\}_{\text{gpot}}$ | Geopotential |
| $\{\cdot\}_k$ | Referring to the $k^{\text{th}}$ discrete node |
| $\{\cdot\}^{m}$ | Mean elements |
| $\{\cdot\}_m$ | Maneuver |
| $\{\cdot\}_{\text{max}}$ | Maximum |
| $\{\cdot\}_{\text{min}}$ | Minimum |
| $\{\cdot\}_{\text{msi}}$ | The $i^{\text{th}}$ multiple-shooting segment |
| $\{\cdot\}_{\text{nom}}$ | Nominal |
| $\{\cdot\}_n$ | In normal direction |
| $\{\cdot\}^{\text{o2m}}$ | The difference between osculating and mean elements |

| | |
|---|---|
| $\{\cdot\}^{\text{osc}}$ | Osculating elements |
| $\{\cdot\}^{\perp}$ | Perpendicular |
| $\{\cdot\}_p$ | Perturbed |
| $\{\cdot\}_r$ | In radial direction |
| $\{\cdot\}_{\text{rn}}$ | In the radial-normal plane |
| $\{\cdot\}_s$ | Sun |
| $\{\cdot\}_{\text{tot}}$ | Referring to all concatenated discrete nodes simultaneously |
| $\{\cdot\}_t$ | In tangential direction |
| $\{\cdot\}_{\text{tol}}$ | Tolerance |
| $\{\cdot\}^{\text{unc}}$ | Uncertainty |

# ACRONYMS

| | |
|---|---|
| **AOCS** | Attitude and Orbit Control System |
| **AT** | Automated Task |
| **BSS** | Boeing Satellite Systems |
| **CER** | Constraint Enforcement Ratio |
| **ECEF** | Earth Centered Earth Fixed |
| **ECI** | Earth Centered Inertial |
| **EW** | East-West |
| **FDIR** | Fault Detection, Isolation and Recovery |
| **GEO** | Geostationary Orbit |
| **GNSS** | Global Navigation Satellite System |
| **GPS** | Global Positioning System |
| **GSO** | Geosynchronous Orbit |
| **ITU** | International Telecommunications Union |
| **JPL** | Jet Propulsion Laboratory |
| **LEO** | Low Earth Orbit |
| **LTV** | Linear Time-Varying |
| **MC** | Maneuver Cycle |
| **NLP** | Nonlinear Programming Problem |
| **NS** | North-South |
| **OD** | Orbit Determination |
| **OT** | Operator Task |
| **RHC** | Receding Horizon Controller |
| **RMS** | Root Mean Square |
| **RTN** | Radial Tangential Normal |

| | |
|---|---|
| **SPP** | Sun-Pointing Perigee |
| **SRP** | Solar Radiation Pressure |
| **WARC** | World Administrative Radio Conferences |

# 1

# INTRODUCTION

*There is no such thing as an unsolvable problem.*

Sergei Korolov

*It is difficult to say what is impossible,*
*for the dream of yesterday*
*is the hope of today*
*and the reality of tomorrow.*

Robbert H. Goddard

***Abstract***
*A geostationary orbit has the prime advantage that a satellite in this orbit is at a fixed location in the sky for an observer on Earth. This unique characteristic has lead to a strong population of this particular orbit with satellites, or fleets of satellites, collocated together within assigned slots. Safe collocation requires to constrain the relative motion of collocated satellites, in order to avoid collisions and interferences caused when a satellite enters the field of view of a sensor on another satellite. The avoidance of such interferences motivates the development of new methods for modeling, guidance and control of geostationary satellites. The recent advancements of applying convex optimization techniques to distributed space systems enable novel methods that can handle such problems.*

A geostationary orbit is an ideal orbit around the Earth with the special characteristic that any satellite in this orbit remains stationary above a point on the Earth's equator. We say ideal because in reality no satellite will remain stationary, since perturbing forces move the satellite away from its stationary position. In that sense, the geostationary orbit is an unstable orbit, and we can only achieve (an approximate) stationary position by actively controlling the satellite's orbit. In order to do so, we need to accurately model the satellite and the environment, we need to develop a strategy to make efficient use of the scarce resources (e.g. propellant) while adhering to certain constraints, and we need to determine the necessary control action to execute the strategy. These topics, the guidance, control and dynamics of satellites in a geostationary orbit, are treated in this dissertation.

## 1.1. THE GEOSTATIONARY ORBIT

A satellite in a geostationary orbit has an orbital period of one sidereal day, i.e. the time it takes for the Earth to make a full revolution about its own axis relative to the stars. The satellite is thus in "sync" with the Earth, hence the geostationary orbit is a subset of the more general type of orbit, namely the Geosynchronous Orbit (GSO). All geosynchronous orbits share the same orbital period, and hence have identical semi-major axes. Ideal geostationary orbits have two further characteristics, namely, zero eccentricity and zero inclination. The latter causes the orbit to lie in the equatorial plane, while the former defines a circular orbit with a constant angular orbital motion of a satellite in this orbit. The three characteristics together, an orbital period of one sidereal day, zero eccentricity and zero inclination define the ideal geostationary orbit, and cause it to have its unique properties.

The idea of a synchronous orbit appeared already in the thought experiments of Konstantin Tsiolkovsky in the late 19th century. In his "Dreams of Earth and Sky" he imagined asteroids with mountains so high that they reach the critical or synchronous orbital altitude [1]. A more technical description of geosynchronous and geostationary orbits is found in Hermann Noordung's (or Potočnik) book "Das Problem der Befahrung des Weltraums - der Raketen-Motor" [2], published already in 1929. Figure 1.1 shows the geostationary orbit as presented in [2]. The most well-known historic references of geostationary orbits are those in Wireless World, by Arthur C. Clarke, the first being his letter to the editor, published in the 1945 February issue. Later that year a full article titled "Extra-terrestrial relays" appeared in the November issue of Wireless World in which Clarke expands on his ideas of geostationary space-stations for radio communication [3].

Reality followed shortly afterwards. Syncom 2 was launched in 1963 and was the first satellite to arrive in a geosynchronous orbit. The next Syncom satellite, Syncom 3, arrived in a geostationary orbit in 1964 [4]. From that moment onwards, many satellites followed, and the geostationary orbit has become increasingly populated. Since satellites in a geostationary orbit are stationary with respect to the Earth, they can have 24/7 ground contact using only a single stationary ground station. The satellites can be observed from Earth for latitudes between approximately -81° and 81° and only three satellites are needed to cover the complete 360° longitude range. These properties make geostationary satellites ideal candidates to host a multitude of different payloads.

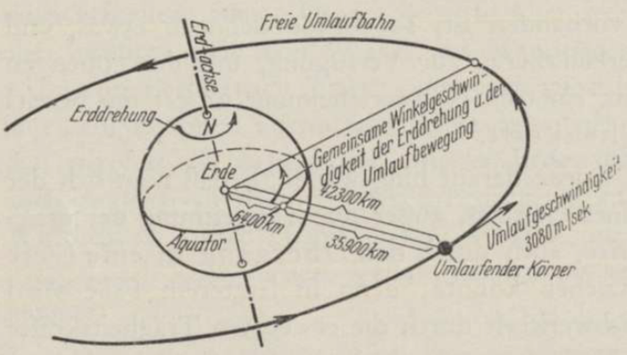

Figure 1.1: The geostationary orbit from [2].

The most dominant usage of geostationary satellites is for communication purposes. Examples range from military communication satellites to satellites broadcasting television channels as well as data relay satellites. Geostationary satellites are also used to broadcast navigation signals, making meteorological observations and perform Earth observation.

A key downside of the geostationary orbit is its altitude at approximately 35800 km. A satellite requires a large amount of energy to arrive at the geostationary orbit, the altitude causes a communication latency of approximately a quarter of a second and it limits the achievable spatial resolution of Earth imaging sensors, especially compared to their counterparts in Low Earth Orbit (LEO). The geostationary orbit lies in the outer radiation belt (van Allen belt), which has significant impacts on the satellite design. Despite of these disadvantages the geostationary orbit remains the single most populated Earth orbit.

The popularity of the orbit required regulation of the orbital positions of satellites, as well as their communication frequencies. The International Telecommunications Union (ITU) is responsible for frequency allocation for radio communication and since 1959 this includes communication with satellites. Decisions on allocations are taken at the World Administrative Radio Conferences (WARC) and during the 1971 WARC the geostationary orbit was recognized as a “limited natural resource”. As of 1973, decisions on the division of slots are also taken at the WARC [5]. Thus since that time, satellite operators are required to maintain their satellites inside assigned orbital slots. These slots usually have a size of 0.2° in longitude and latitude (or approximately 150 km) although nowadays slots that are only 0.1° in longitude are common as well. At the moment of writing, up to four satellites are collocated in a single slot. The most densely populated slots are currently at 19.2°E, 26°E, 74°E and 83.1°E, all of which contain four satellites [6]. However, in the recent past, satellite operator SES has managed to collocate up to eight satellites simultaneously in the slot at 19.2°E [7].

Since geostationary satellites generally serve a specific location on Earth, and even more so because geostationary satellites are assigned to small slots, the orbits of geostationary satellites need to be actively controlled. Station-keeping strategies are required to counteract the many orbital perturbations acting on the satellites. This task becomes even more challenging when multiple satellites are assigned to the same slot, requiring not only to maintain their position inside the slot, but also to control the relative position of the satellites in order to avoid collisions or other types of interferences. These are the topics treated in this work.

## 1.2. PREVIOUS WORK

In this section we discuss the previous work that is of relevance to our research. This includes key works describing current operational practice in guidance and control of geostationary satellites as well as theoretic approaches that have been proposed in the literature over the years. We also discuss some particular works in the more general field of distributed space systems (including formation flying) that were inspirational to this work. Lastly, we discuss a number of ongoing technological developments that enable new approaches to guidance and control of geostationary satellites. In the discussions that follow we make several comparisons of methods from the literature to methods developed in this work. These comparisons are most useful if the reader is aware of the methods developed in this work and it is advised to read at least the summary of this work before continuing this section.

### 1.2.1. MODELING OF ABSOLUTE AND RELATIVE DYNAMICS

Orbital dynamics of artificial satellites has been a topic of research for many years. Reading and understanding the vast body of work on this topic might take a lifetime and thus we focused only on a small subset of available material. We used [8], [9] and [10] as key sources of information on the topic of orbital dynamics. The works [5], [11] and [12] provide fundamental information specifically focused on satellites in geostationary orbits. We used these works to develop the numeric propagator underlying the various simulations that were executed as part of this research.

#### ABSOLUTE DYNAMICS

Since the launch of the Syncom satellites, a great increase in research on orbital dynamics of geosynchronous satellites occurred. The work by Shrivastava [13] contains over 200 references and provides a good overview and summary of relevant work up to 1978. In the same year, Kamel presented a method to determine the solution of the equations of motion of a geostationary satellite by three decoupled sets of pendulum type equations with forced oscillations [14]. Kamel's solution includes Earth gravity perturbations up to third order and degree, as well as Sun and Moon gravity perturbations. Kamel's solutions still have merit today, thus we have implemented Kamel's method and use it to transform between mean and osculating orbital elements.

Losa developed a Linear Time-Varying (LTV) model of the dynamics of a satellite in a geostationary orbit, including Earth gravity perturbations up to third order and degree, Sun and Moon gravity perturbations and Solar Radiation Pressure (SRP) [15]. This model was of particular interest as it relates closely to the model developed later in this work. Losa gives approximate analytic expressions for the various perturbations affecting a geostationary satellite by expanding the dynamics (including perturbations) in a first order Taylor series about the center of the slot. We make a simplification and use only the perturbations as experienced by the geostationary slot center while ignoring the partial derivatives of these perturbations with respect to the satellite state in our linearized model. The advantage is that we can more easily incorporate also higher order perturbations (i.e. we do not need to calculate the partial derivatives of these perturbations with respect to the state) or use models of perturbing accelerations that are not analytic in nature. Furthermore, we can evaluate all perturbing accelerations ahead of time. The disadvantage is that our model has a reduced accuracy when the same perturbing forces as in Losa's model are included. The consequence of this reduced modeling accuracy for an operational implementation is very limited since the orbit prediction errors are dominated by orbit determination and actuation errors and not by the simplified linear, time-varying dynamics.

#### RELATIVE DYNAMICS

The most famous linearized model of the relative motion of two satellites in a near-circular orbit was developed by Clohessy and Wiltshire in their 1960 paper on a terminal guidance system for satellite rendezvous [16]. A relative motion model for collocated geostationary satellites was presented by Blumer in [17]. Blumer's model describes the motion of a slave satellite in the reference frame attached to a master satellite as a function of non-singular relative orbital elements. The model relies on the orbit of the master satellite to be near-circular with near-zero inclination and as such applies well to geostationary satellites. The same equations can also be used as a linear transformation between relative orbital elements and Cartesian position and velocity in a Radial Tangential Normal (RTN) reference frame attached to a leader (or master satellite) and this application is extensively used in this work.

### 1.2.2. GUIDANCE AND CONTROL METHODS

Since both station-keeping and collocation of geostationary satellites are activities that have been performed for decades, a lot of relevant information has appeared in books treating the subject in detail. The book by Soop (1994) [5] is an excellent reference treating orbital dynamics, station-keeping, collocation and also orbit determination of geostationary satellites. A much newer work by Li (2014) [12] also extensively treats geostationary dynamics, station-keeping and collocation.

#### STATION-KEEPING

The scientific literature on geostationary station-keeping has three focal points of particular interest: (optimal) station-keeping methods under the assumption that maneuvers can be approximated as impulsive delta-V corrections, methods for satellites with low-thrust propulsion systems and methods focusing on "autonomous" strategies. The paper by Shrivastava [13] introduced earlier also provides an overview of the literature on station-keeping up to 1978. Many ideas have been investigated up to that point, including optimal strategies for impulsive maneuvers, continuous maneuvers using optimization techniques such as dynamic programming, separating high frequency terms from osculating elements to obtain mean elements and control those mean elements, as well as studies of autonomous systems for orbit control. Several newer works are discussed in more detail in the following paragraphs.

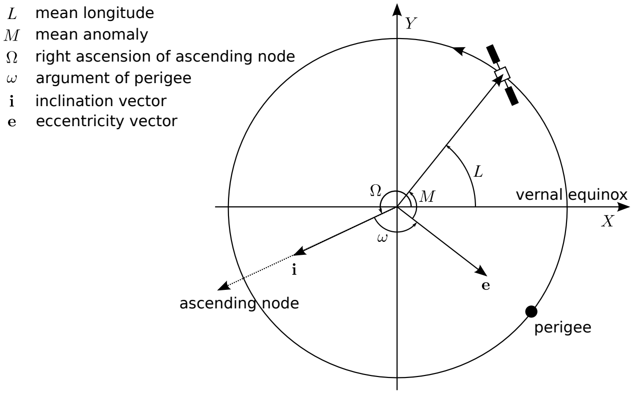

Figure 1.2: Visualization of a geostationary orbit defining the eccentricity vector **e** and inclination vector **i**.

### STATION-KEEPING: IMPULSIVE MANEUVERS

In terms of station-keeping for satellites with a high thrust-to-mass ratio, a fundamental work is the paper by Eckstein, [18], in which several strategies are discussed for calculating impulsive maneuvers, both for an ideal propulsion system as well as in the presence of deterministic thruster cross-couplings. Eckstein's work still forms the basis for the control strategy of many satellites that are nowadays in orbit and we have implemented one of his strategies and use it as a reference to validate the method developed in this work.

Slavinskas et al. introduced an efficient strategy for inclination control of geostationary satellites [19]. Corrections to the inclination vector are usually made at a frequency of one to several weeks. The concepts of eccentricity vector and inclination vector are explained in Figure 1.2. Typical orbit control software cannot separate larger periodic variations of the inclination vector from the (observed) osculating inclination vector and hence, to save propellant, Slavinskas et al. propose to make inclination vector corrections always in the direction opposite of the direction of secular inclination vector variations (instead of controlling the inclination vector towards a fixed point) and as such save up to 4 percent of propellant required for inclination control. In this work we use the observations made by Slavinskas et al., however, we include the periodic variations due to luni-solar perturbations with a period of one year and shorter in our mean-to-osculating conversion and control the mean inclination vector. As such we obtain the same benefits as Slavinskas et al., but we can still control the mean inclination vector as desired.

In [20], Kelly et al. formulate a combined eccentricity and longitude control strategy for geostationary satellites. They improve on the legacy Sun-Pointing Perigee (SPP) strategy (which aims to keep the eccentricity vector pointing towards the sun, thus following the natural eccentricity circle but with a smaller radius) by accounting for the long period luni-solar perturbations in their strategy. Their method allows a slight increase of the eccentricity control circle radius, thereby saving some propellant for East-West (EW) control. The algorithm simultaneously maintains the eccentricity vector within its allowed circle as well as the longitude within a tolerated band. The algorithm chooses the number of required maneuvers based on the particular slot, a chosen maneuver cycle duration and some additional parameters. The algorithm is demonstrated to work close to one of the two unstable points in the geostationary orbit (the geostationary orbit has four points where the perturbations due to tesseral harmonics vanish, two of which are stable, whereas the other two are unstable). Although our method works vastly different, we can achieve similar performance because we can choose to actively constrain the osculating orbital elements not just at the initial and final times of a maneuver cycle, but also at intermediate points in time and thus enforce the same constraints.

Another work, [21], aims to maximize the time between regular EW maneuvers, such that a minimum number of maneuvers is required for EW control. The work assumes that a normal SPP strategy is used and that EW corrections are executed using two impulses separated by half an orbit. A nonlinear programming problem is formulated for a one year horizon and solved for different maneuvers cycle durations. Results are shown for maneuver cycles of one, seven and fourteen days. Unfortunately, the paper provides insufficient data to make a proper comparisons with the method developed in this work.

### STATION-KEEPING: LOW THRUST

Performing station-keeping maneuvers using electric propulsion has both advantages and disadvantages. The key idea is to benefit from the much higher specific impulse that an electric propulsion system can deliver and hence, less propellant mass is required for station-keeping. This propellant mass reduction can outweigh mass penalties of the propulsion system and the power system together, especially for missions with a long lifetime. As such it is possible to increase the payload mass fraction of the satellite and improve the satellite's capability for providing terrestrial services compared to a satellite with a chemical propulsion system. From an orbit control point of view, a disadvantage is that, because of their wide exhaust plume, the electric thrusters have to point away from the North-South direction to avoid contamination of the solar panels, which extend in these directions. This off-pointing reduces the efficiency of these maneuvers (which usually account for more than 90% of the propellant consumption). Another disadvantage is that maneuvers last much longer due to the extremely low thrust force, thus it is no longer possible to make maneuvers only at the most efficient locations in orbit. The long duration of the maneuvers further invalidates the assumption that a maneuver is impulsive, thereby requiring new methods to calculate maneuvers. Many works propose methods to solve the station-keeping problem using electric propulsion. Most of these works use optimization techniques in the calculation of station-keeping maneuvers. We discuss a number of works in more detail.

In [22], Eckstein introduces an optimization-based method to find the optimal thrust arcs for a satellite with a low thrust electric propulsion system. Eckstein's problem finds the optimal thrust arcs given a set of initial and final orbital elements and the number of thruster firings. He first poses the problem without constraints on the allowed firing times and later including constraints on the thrust arcs, where the unconstrained problem solution is used as an input to the constraint problem. Eckstein proposes a cost function which minimizes a weighted combination of final state errors and propellant consumption, thus leading to a problem that is always feasible. However, his problem solution will not achieve the desired final states (although, the solution can get arbitrarily close by changing the weight functions appropriately). Our method is more general than Eckstein's as we can include state constraints anywhere along the trajectory, do not necessarily require fixed target values to be achieved at the end of the maneuver, do not need to specify the number of maneuvers a-priori and can deal with arbitrary thruster configurations.

Losa formulates an optimization-based method to calculate station-keeping maneuvers for electric propulsion geostationary satellites using a differential inclusion approach [23]. The equations of motion are formulated as a linear time-varying model, which is discretized assuming constant thrusts over each discretization interval. The differential inclusion method is used to reduce the dimensionality of the problem. The resulting problem (in the transformed variables) is formulated as a quadratic programming problem with affine state and control constraints. The resulting problem is solved and Losa shows that the resulting control inputs maintain a satellite inside a geostationary slot. A disadvantage of the solution is that an almost continuous thrust profile results which is not readily implementable. A follow-on paper [24] deals with this issue by solving a second optimization problem using the solution of the first problem. The second problem requires some assumptions, such as each thruster is only fired once and the problem horizon for both problems is limited to one day. The resulting thrust profiles, after solving the second problem, are readily implemented by a realistic propulsion system. Our method has many similarities with Losa's method (Losa's work was inspirational to ours); we rely also on a LTV model for the dynamics and we can include constraints on state and control along the trajectory. However, we do not use a differential inclusion approach in formulating the problem, neither do we require two subsequent optimization problems to be solved to arrive at a solution. A key difference is that we include the $\ell_1$ norm of control input in the cost function and naturally obtain a sparse solution that is easily processed so it can be executed by a realistic propulsion system. Furthermore, the results in terms of propellant consumption obtained by the method developed in this work are superior to the results from [24] and [25].

A recent study performed simultaneously by Airbus and GMV under an ESA contract also investigated the optimization of geostationary satellite station-keeping strategies using electric propulsion [26], [27]. Two tools resulted from these studies STAKE and OPASKEP, respectively from Airbus and GMV. Both tools formulate the station-keeping problem as a Nonlinear Programming Problem (NLP) and rely on ASTOS Aerospace Trajectory Optimization Software by Astos Solutions for transcription and solution of the optimization problems. Both tools can deal with a variety of different cost functions and constraints. They are able to combine orbit control with angular momentum management and some preliminary investigations into optimal thruster configurations are presented. The tools developed in these studies seem to be very capable and provide a lot of flexibility in specifying the problem. The method developed in this work differs through the formulation of the station-keeping problem as a convex optimization problem. The results presented in [26] and [27] unfortunately do not allow a direct comparison, as propellant consumption is given in kilograms of propellant, while the specific impulse of the thrusters is omitted.

### STATION-KEEPING: AUTONOMY

Another line of work focuses on concepts or algorithms for station-keeping that can function autonomously (possibly on-board the satellite). The key advantage of increasing automation is a reduction in operational costs. A key enabler to allow on-board autonomy is the availability of reliable orbit determination information. Since geostationary satellites have the advantage that 24/7 contact with a single ground station is possible, automation does not necessarily need to be implemented on-board, instead, the processes can be fully automated on-ground as well. The tasks of planning or checking planned station-keeping maneuvers, approving these plans and commanding the satellite are usually performed by operators. Automating these repetitive tasks can relief the workload of operators and reduce costs for ground operations.

A paper by Leibold and Eckstein [28] introduces a potential autonomous station-keeping system. The paper discusses both the required hardware as well as algorithms for orbit determination and correction. A sensor suite consisting of Earth sensors, Sun sensors and a Polaris sensor is used for orbit determination, while four electric propulsion thruster are used as actuators. Leibold and Eckstein's method for calculating station-keeping maneuvers splits the problem of North-South (NS) and EW control and calculates the corrective maneuvers separately. An analytic solution for NS maneuvers is found by executing two NS maneuvers per orbit and maximizing the number of these maneuvers over the period allocated for NS maneuvers. For EW maneuvers an optimal solution is found only under the assumption of impulsive maneuvers (since EW maneuvers are small, this assumption introduces an acceptably small error) and a strategy with three EW maneuvers per cycle is implemented. The simulation results show that the system is able to maintain a satellite in a geostationary slot, with occasional small violations in case random thrust errors are introduced. The propellant consumption for NS control is very much in line with the expected consumption for an optimal strategy, whereas the propellant consumption for EW control is rather large (but the expectation is that this is due mainly due to the relatively poor orbit determination accuracy of the system). The method introduced in this work does not (need to) split NS and EW control, which provides a strong benefit for a thruster configuration as introduced by Leibold and Eckstein, namely almost all EW control can be obtained as a by-product of NS control, thus saving a significant portion of propellant. The disadvantage of our method, if it would be implemented in an on-board autonomous fashion, is increased computational load. This is not seen as critical due to the infrequent plan updates (daily to weekly) that are required in a normal operational scenario.

In [29] several autonomous station-keeping strategies are presented for on-board orbit determination using a Global Positioning System (GPS) receiver. The performance of two different receiver clock types was investigated and the paper reports 1-$\sigma$ accuracies of 10, 100, 48 m and 8, 25, 12 m in radial, tangential and normal directions for crystal and atomic receiver clocks, respectively. The station-keeping strategies rely on the availability of predetermined ephemerides, where the on-board controller keeps the satellite close to these predetermined ephemerides. Several strategies are presented, including an innovative strategy that treats the problem as a formation flying problem with the predetermined ephemerides representing a virtual satellite with respect to which the actual satellite is controlled. This strategy relies on maneuvers being executed at a fixed frequency, every 6h or 8h. The reported additional propellant to keep a satellite close to the predetermined ephemerides ranges between 2.5 and 5.5 m/s/year for a receiver with an atomic clock and between 7.3 and 13.9 m/s/year for a satellite with a crystal clock. The additional propellant is directly driven by the measurement errors. The advantage of this method is that the satellite position is known (within the accuracy of control) ahead of time. The disadvantage compared to our method is the additional propellant consumption that is required to keep the satellite close to the reference ephemerides.

Park et al. [30] propose another approach to autonomous station-keeping which builds on the work from Chao ([29]). Instead of relying on GPS signals, they use two ground stations that send out GPS-like signals and use these signals for orbit determination. Similar to Chao they rely on the availability of a predetermined reference trajectory, however, they focus on improved reliability and low computational burden in the development of the algorithm. The controller relies on the Clohessy-Wiltshire equations. A linear quadratic feedback controller is presented for EW maneuvers making three maneuvers per orbit (as in [29]) at equidistant points in time, based on a cost function that penalizes propellant consumption and the error with respect to the reference trajectory in tangential direction only (to save propellant at the cost of control accuracy). The NS control strategy executes maneuvers at the location that is defined by the reference data, while applying a correction to the predefined magnitude based on the error with respect to the reference velocity in normal direction. The orbit determination algorithm is based on a linear Kalman filter. The system is simulated and shown to be able to maintain position errors of less than 5 km with respect to the reference trajectory. The simulations also show the robustness of the system to a 20-day failure in one of the two ground stations. The resulting velocity increment ($\Delta V$) for a one year period was equal to 57.1 m/s. With the method developed in this research a better performance is obtained, but at a much higher computational burden.

Emma and Pernicka [31] derive equations for autonomous control of longitude and eccentricity of a geostationary satellite both for a single as well as for two-part in-plane corrections. The resulting equations are very similar to those presented by Eckstein [18], with the exception that they assume that a thruster system may not be able to deliver a pure tangential drift, and hence Emma and Pernicka account for a radial component as well. The algorithm is developed for an autonomous on-board implementation, however, neither the autonomy concept nor their approach to autonomous orbit determination are discussed.

The work by Guelman [32] introduces another autonomous closed-loop station keeping method. In contrast to other works, Guelman formulates the equations of motion in an Earth-fixed reference frame and derives a closed-loop controller, first without, then with active longitude control. Using the proposed controller, Guelman achieves control of the satellite longitude deviation and latitude within respectively 0.004° and 0.001° under the assumption that the acceleration profiles are implemented exactly as resulting from the controller. When assuming thrusters with fixed acceleration levels, by using a threshold function that applies a constant acceleration if the desired acceleration is above a certain threshold, accurate control is still achieved, albeit with reduced performance (0.03° in longitude and 0.005° in latitude). Guelman reports that 70 m/s was required for one year of station-keeping under the assumption that the propulsion system can deliver accelerations in radial, tangential and normal directions. Since our method does not directly control latitude and longitude the results cannot be compared one-to-one with Guelman's in terms of control accuracy. However, we can state that our implementation as receding horizon controller achieves a similar order of magnitude accuracy in terms of mean orbital elements at a more favorable propellant consumption.

### COLLOCATION

Collocating several satellites in a single geostationary slot introduces risks of interference between these satellites. The most destructive of such interferences would be a collision between two collocated satellites. Other possibilities are radio frequency interference or interfering with sensors on other satellites by passing through their field of view [33]. Several coordination strategies for the station-keeping of collocated satellites have been developed to avoid collisions, whereas other interferences have not been dealt with to date.

In a fundamental work, [34], Hubert and Swale developed collocation strategies for six satellites sharing a 0.6° longitude band. The strategies included a division of the longitude band in six small boxes and assigning one satellite to each box, as well as dividing the longitude band in respectively two and three boxes, with three and two satellites per box. The proposed strategy for multiple satellites per box is the (now legacy) combined eccentricity and inclination vector separation strategy. The eccentricity inclination vector separation strategy relies on parallel eccentricity and inclination vectors to ensure that radial separation is maximal when normal separation vanishes and vice versa.

In [35], Eckstein et al. developed collocation strategies for a four-satellite cluster located at 19° West. Three different strategies were introduced; a separation in longitude, a separation strategy using the eccentricity vector only and also the combined $e/i$-vector separation strategy. The latter is still the prime strategy used today to safely collocate geostationary satellites. The strategy was implemented also in the geostationary satellite control system (geo-control) for station-keeping and collocation [36] which has been used to operate many satellites. We present application cases relying on this strategy, but also propose adaptions to this strategy to account for another geometric constraint, namely, to avoid the field of view of a sensor on another satellite in the fleet.

The work by Blumer introduced earlier ([17]) introduces a concept for coordinated control of a fleet of collocated geostationary satellites. One satellite is designated the master satellite, the orbit of which is determined and controlled from ground. The other satellites are so-called slave satellites, and the master satellite determines the relative orbits of the slaves as well as the required orbit maneuvers for controlling the relative orbits. The control method relies on the $e/i$-vector separation strategy. Although mention is made of the problem of sensor interferences and link occultations, no analysis of the problem or solutions thereof were included in the subsequent developments. The paper introduces a concept for on-board relative orbit determination using inter-satellite links and a tracking unit placed on the master satellite. The maneuvers are calculated using a nonlinear programming method. We adopt a similar formation control hierarchy as Blumer with one leader satellite and several follower satellites. The method of calculating the maneuvers are vastly different between Blumer's method and this work.

In a series of two papers, [37] and [38], Wauthier et al. introduce the strategy and operational experience of collocating three to six satellites in a single slot, using the $e/i$-vector separation strategy. The problem of sensor interference is mentioned, including the fact that the $e/i$-vector separation strategy is not ideal to avoid interference with Earth-pointing sensors. The problem has not been dealt with in the strategy development but an analysis of the occurrences of such interference events is included. The analysis showed that frequency interference can be expected to occur between once per month to once per week per satellite for three to six collocated satellites. The papers further showed the success of the strategy, safe separation was achieved at all times, as well as the successful increase of the cluster from three to six satellites.

Beigelman and Gurfil [39] present a method for collocation of geostationary satellites using relative orbital element corrections. The collocation problem is essentially formulated as a formation keeping problem and optimal collocation maneuvers under the influence of the $J_2$ perturbation are investigated, while omitting other important perturbations. We also use relative orbital elements in the analysis and solution of the collocation problems presented in this work, albeit with a much more accurate dynamics model (actually the synchronous elements can already be interpreted as relative orbital elements between a geostationary satellite and the geostationary slot center, which allows one to interpret the general problem of station-keeping as a formation keeping problem between a satellite and the slot center).

Another work that builds on the idea of using relative orbital elements for controlling collocated geostationary satellites is by Rausch and Howell ([40], [41]). The work by Eckstein [18] is extended to a fleet of collocated satellites and the equations for calculating impulsive corrections for a propulsion system including deterministic thruster cross-couplings are given. The paper uses a leader follower control architecture for controlling the relative motion of a set of follower satellites with respect to a leader satellite that is controlled using conventional station-keeping techniques. The simulations in the paper show that only a minor increase in propellant is required for the follower satellites compared to the leader satellite. We use a similar architecture and rely also on relative orbital elements. The key difference is that we use a completely different method for calculating the corrective maneuvers relying on the solution of a convex optimization problem instead of an analytic solution as proposed in the reference. Our method is more versatile as it can cope with both high thrust and low thrust satellites and can include a variety of constraints that cannot be dealt with explicitly using the method from Rausch and Howell.

### 1.2.3. DISTRIBUTED SPACE SYSTEMS

The problem of collocation is closely related to the field of orbit control of distributed space systems (including formation and cluster flying). Some of the theories developed for collocation of geostationary satellites have been inspirational to the field of distributed space systems. A good example is the adaptation of the $e/i$-vector separation strategy by d'Amico and Montenbruck to formations in LEO [42]. This strategy is used, for example, on the TerraSAR-X / TanDEM-X formation [43]. In turn, some works in the field of formation flying have been inspirational to the developments in this research.

In [44] Wang and Nakasuka develop a method for cluster flight (relative) orbit design. The paper formulates requirements in terms of minimum distance in the radial-normal plane, a maximum distance and a condition of identical inclinations in order to minimize propellant consumption, by eliminating the $J_2$ induced out-of-plane drift. The analysis and design problems are formulated in terms of relative orbital elements and solved using both heuristic approaches as well as nonlinear programming techniques. We treat a similar problem (stay inside the geostationary slot while maintaining minimum separation distances), albeit in a different way. We investigate (and visualize) those areas of the $(e, i)$-vector space that satisfy the constraints and use the resulting graphs to design a configuration complying to our requirements, taking into account also that the relative orbits can vary in mean longitude and semi-major axis (e.g. due to maneuvers).

To ensure safe separation between satellites one usually relies only on radial and normal directions, because the orbit prediction accuracy in tangential direction is typically much larger than in the other directions. This observation was key to the development of the $e/i$-vector separation strategy. Under one simplifying assumption, namely zero semi-major axis difference, the minimum distance can be defined as a function of the relative eccentricity and inclination vector only [5]. The derivation of the minimum distance in the radial-normal plane for nonzero semi-major axis differences was first worked out in detail in a recent work by Gaias and Ardeans [45]. Their work describes a safety concept for a formation flying experiment (AVANTI) with two (noncooperative) spacecraft. We build on the work from Gaias and Ardeans and formulate similar equations in terms of non-dimensional (rational) orbit elements, which forms the basis for dealing with the minimum distance constraint in our collocation design approach.

One method of particular interest that appears often in the formation flying literature is model predictive control (or receding horizon control). A model predictive controller determines the optimal (according to some cost function) control inputs, taking into account future dynamics of the system while at the same time being able to account for constraints on state and control at current and future (discrete) times. Essentially an optimization problem is solved to determine the optimal control input over a finite horizon. Only a small portion of the plan of optimal control inputs is executed, after which the process is repeated and a new set of optimal controls are determined. Manikonda et al. [46] were among the firsts to apply this method to formation keeping of satellites (both attitude and position) using feedback linearization of the nonlinear dynamics.

The works by Tillerson et al. [47] and Breger and How [48] were especially inspirational as they present methods for station-keeping (and reconfiguration) of a formation using model predictive control techniques based on convex optimization. The first paper develops the method using a formulation of the relative dynamics in terms of Cartesian coordinates, while the second paper uses relative orbital elements. Both works end up with a LTV formulation of the dynamics (albeit with only a subset of perturbing forces included) and derive a model predictive controller for formation keeping and reconfigurations under various state and control constraints. The key idea that we adopted from these papers was the formulation of the problem using an $\ell_1$ norm of propellant consumption in the cost function, leading naturally to a sparse solution of the problem and hence only a small number of orbit control maneuvers required. This type of cost function makes the solution of the optimization problem readily implementable by a realistic propulsion system that has only a single qualified operational point (essentially an on/off thruster), while at the same time having beneficial effects on the lifetime of a thruster (which is usually qualified only for a limited number of duty cycles).

Convex optimization techniques have seen an increase in applications in path planning and control of spacecraft in the last decade. The main theory on convex optimization is well captured in [49]. Acikmese et al. ([50]) developed a convex guidance algorithm for formation reconfigurations in deep space (double integrator dynamics) and in orbit based on the Clohessy-Wiltshire equations. The only non-convex constraint in the problem formulation was the minimum distance constraint which was convexified by approximating the constraint by a series of half-spaces generated using a heuristic approach based on the unconstrained problem solution. Lu and Liu [51] take this several steps further (building on further work by Acikmese, Blackmore et al., [52], [53], [54], [55]). An optimal control problem for rendezvous and proximity operations is defined, including nonlinear dynamics and a non-convex constraint on the thrust vector. A more relaxed version of the problem is defined which includes a convexification of the thrust vector constraint and a proof of equivalence with the original problem is given. The nonlinear dynamics are dealt with by a clever change of variables and by solving successive convex optimization problems with linearized approximations of the dynamics, leading to the solution of the original nonlinear problem. Morgan and Jung [56] develop a path planning and control approach for (reconfigurations) of swarms of satellites using successive convex optimization. The minimum distance constraint is treated using a series of half-spaces as in [50], but successive approximations are used to find the optimal solution, not relying on a heuristic to determine the half-spaces. These works all formulate the control problem in Cartesian coordinates and treat the minimum distance constraint (or other non-convex constraints) as part of the problem formulation, requiring either a convexification of the constraint or a successive approximation algorithm converging towards the original problem solution. We focus on the formulation of the station-keeping problem in terms of relative orbital elements using a LTV model and identify convex regions in orbital element space satisfying the various nonconvex constraints by analysis, thereby avoiding to deal with these constraints in the optimization problem.

### 1.2.4. RECENT TECHNOLOGICAL DEVELOPMENTS

The classic attitude determination suite on a geostationary satellite consists of Sun sensors, Earth sensors and gyroscopes. Nowadays, star sensors are the standard type of sensor if more accurate attitude determination is required and most newer geostationary satellites have replaced the less accurate Earth sensors with star sensors [57], [58], [59]. When considering a fleet of collocated satellites, a star sensor provides another possible constraint for the fleet. A satellite should stay out of the field of view of a star sensor on another satellite in the fleet to avoid blinding the sensor [60]. This constraint has appeared in the literature for Earth sensors or radio interferences, but not yet for star sensors.

Orbit determination of geostationary satellites is normally performed by using one or more ground stations to make angle measurements and range and/or range-rate measurements. The use of Global Navigation Satellite System (GNSS) receivers for orbit determination is commonly done on low Earth orbiting satellites and this technology is currently being applied to higher orbits, including the geostationary orbit [61], [62], [63]. The key benefits of having a GNSS receiver on a geostationary satellite are a significant performance increase as well as continuous availability of an orbit determination solution. Chapel et al. [63] report position errors of 54.2, 4.4 and 8.2 m ($3\sigma$) in respectively radial, tangential and normal directions in a worst-case scenario including NS, EW and momentum dumping maneuvers. This performance is expected to improve even further with the availability of the full constellation of Galileo satellites and improved hardware in the form of AGGA-4 chipsets [64].

In order to increase the payload mass fraction, satellite manufacturers look for ways to decrease the mass of the satellite bus and a key candidate is the propulsion system. By using solar electric propulsion thrusters, much higher efficiencies can be achieved (more than an order of magnitude difference) compared to chemical propulsion systems. This led several manufacturers to develop all-electric platforms (e.g. [65] and [66]) which can significantly increase the payload mass in a geostationary orbit for a given launch mass. Although these are not the first missions that use electric propulsion systems for station-keeping of geostationary satellites, extending the use of the electric propulsion system to the transfer from the launch orbit to a geostationary orbit leads to much more significant mass savings. Therefore, the availability of these types of satellites is certainly a threat to the conventional chemically propelled satellites and will lead to an increased use of electric propulsion.

## 1.3. MOTIVATION AND CONTRIBUTIONS

This section presents the motivations for the research in this dissertation. The research questions are formulated and an overview of the contributions of this research to the body of knowledge are given.

### 1.3.1. MOTIVATION

Station-keeping and collocation of geostationary satellites is a mature technology and many methods exist today that not only show successful results in simulations, but have been applied successfully in practice on a day-to-day basis for many years. However, reviewing the literature, we discovered one definitive open point: the ability to avoid mutual interferences such as sensor interference or radio-frequency interference. This problem has been recognized for many years but no solutions appeared to date. The problem used to revolve around interference with the broadcasting of a signal towards Earth or a satellite passing through the field of view of an Earth sensor on another satellite. Nowadays most new satellites are equipped with star sensors to provide accurate inertial attitude measurements. The presence of a star sensor introduces yet another case for sensor interference. If a satellite is passing through the field of view of a star sensor on another satellite while reflecting sunlight towards the star sensor, this satellite can appear as an object much brighter than other stars or even much brighter than the moon. The brightness depends on the relative geometry, mounting location, pointing direction of the star sensor and attitude of the reflecting satellite. Depending on the brightness level, type of star sensor and relative geometry such interferences can cause outages of a star sensor that could last up to two hours [60]. Such interferences, both from Earth-pointing payloads and star sensors, can be dealt with through the design and control of relative motion orbits, thus impacting the guidance and control methods for station-keeping and collocation. The need for a method that can deal with these geometric constraints is the primary motivation of this work.

Secondary motivations arise from two technological developments; the first being the increased use of solar electric propulsion systems on geostationary satellites. The very low thrust that these propulsion systems produce invalidate typical station-keeping strategies relying on the assumption that the thrust arcs can be approximated as impulsive velocity corrections, thus requiring different (but not necessarily new) station-keeping strategies. The second technological development is the use of GNSS technology for orbit determination in geostationary orbit. The current generation of GPS receivers ([62], [63]) are already prepared for use in Geostationary Orbit (GEO). One disadvantage in GEO is that a much smaller number of GPS satellites is visible, with possibly large data gaps in the reception of signals. This problem is being alleviated with the rapid build-up of the Galileo constellation, as well as through the development of other technologies such as the ability to track signals with extremely low signal-to-noise ratios (which will enable tracking also side lobes of the GNSS signals). The availability of a continuous orbit determination solution paves the way for different type of maneuver planning schedules, relying more on autonomy (whether on-board or on-ground), with shorter duration station-keeping cycles than currently used. The acceptance of such technologies allows for a decrease of the minimum distance between satellites, which in turn allows to collocate more satellites in a single slot.

Considering these developments, we see a need for the development of a method that can address both the current situation with ground-based maneuver planning, according to fixed schedules, for satellites with chemical or electrical propulsion systems, as well as addressing the new paradigm in which frequent orbit determination solutions are readily available and maneuver planning and execution are fully automated. The analysis of the geometric constraints of sensor cone avoidance and minimum distance, the formulation of a guidance method that can deal with these constraints and the development of a maneuver planning method that has the versatility to deal with the different operational implementations are the prime goals of this dissertation.

### 1.3.2. RESEARCH QUESTIONS

Considering the motivations we set out to answer the following research questions in this research:

1. How to do safe and economic guidance and control of geostationary satellites based on convex optimization?
    (a) Can the perturbed equations of motion be described using convex functions only?
    (b) Can station-keeping maneuver plans be determined using numerical optimization methods for convex problems?
    (c) How are station-keeping strategies resulting from numeric optimization methods related to the current state-of-art?
    (d) What are benefits and disadvantages compared to conventional methods in terms of propellant consumption, maneuver frequency, control accuracy, flexibility and robustness?
2. How to extend the proposed optimization methods to collocate several satellites under geometric constraints?

   (a) Can the geometric constraints be formulated as a convex constraint?
   (b) What is the impact of the geometric constraints on the conventional coordination and station-keeping strategies?
   (c) How to incorporate the geometric constraints and to solve the resulting constrained optimization problem?
   (d) Can the conventional $e/i$-vector separation strategy be adapted to account for geometric constraints?

3. Can station-keeping and collocation guidance and control of satellites in GEO be improved with on-board orbit determination and electric propulsion capabilities?
   (a) What are suitable sensors and actuators and what are their performance?
   (b) Is it realistic to perform autonomous on-board station-keeping using numeric optimization based methods?
   (c) What are potential concepts for collocation with increased onboard autonomy?
   (d) How to transition towards on-board autonomous control within realistic operational constraints and requirements?

The first question focuses on the development of a convex-optimization based method for station-keeping of geostationary satellites. This development is a stepping stone towards developing a method for collocating a fleet of satellites subject to various geometric constraints. The analysis of the constraints and the extension of the methodology towards multiple satellites is the subject of the second question. The third question addresses opportunities that arise through the availability of an on-board orbit determination capability and the presence of an electric propulsion system. The research focused mainly on the first two research questions and each of the research questions will be addressed in this dissertation, however, some open points remain, leading to a number of recommendations for future work.

### 1.3.3. RESEARCH METHODOLOGY AND CONTRIBUTIONS

The first key focal point is the modeling of absolute and relative dynamics of geostationary satellites. A review of the equations of perturbed motion of a satellite in a geostationary orbit is performed. Two simplifying assumptions are posed that lead to the formulation of the dynamic equations in the form of a linear, time-varying model. This model includes the dominant perturbations of Earth gravity, sun gravity, moon gravity and solar radiation pressure. A validation of the LTV model is performed, both analytically and numerically, and bounds on the modeling accuracy are presented. An auxiliary method is developed for converting between mean and osculating orbital elements, such that constraints on the motion of a geostationary satellite can be expressed in terms of mean and osculating orbital elements. Equations relating the relative motion in Cartesian coordinates to orbital element differences are given, as well as a relative motion model defined in rational relative orbital elements. These rational relative orbital elements are obtained by dividing the relative orbital elements by the product of semi-major axis and relative eccentricity vector magnitude. We developed a simulation environment in which we can develop and test algorithms for guidance and control of geostationary satellites. A simple satellite model is included with different types of propulsion systems. We introduce errors into the simulation environment to represent realistic modeling errors, orbit determination errors and maneuver errors. The key contributions to the body of knowledge are:

- the definition and validation of a novel LTV model of dynamics of a geostationary satellite,
- the introduction of relative rational orbital elements.

The second focal point is the analysis of the different geometric constraints in terms of (relative) orbital elements. We analyze the geostationary slot boundaries in terms of orbital elements and define bounds on inclination magnitude and combined eccentricity magnitude and mean longitude difference that guarantee a satellite to remain inside the geostationary slot. We then define the minimum distance constraint (in the radial-normal plane) in terms of relative orbital elements and, in more general form, in terms of rational relative orbital elements. The introduction of the rational relative orbital elements reduces the number of elements in the design space of the minimum distance constraint to only two variables, allowing us to visualize clearly how combinations of these elements affect minimum distances. We then investigate the sensor cone avoidance constraint, also in terms of relative orbital elements. One key finding is that the presence of the sensor cone avoidance constraint requires active control of the relative mean longitude of satellites in the fleet. We define a metric to evaluate combinations of rational relative orbital elements with respect to a particular sensor cone avoidance constraint. This metric essentially represents the size of a tolerance window of the relative mean longitude that is allowed without violating the sensor cone avoidance constraint. We can then visualize the space of relative eccentricity and inclination vectors and their performance regarding the newly defined metric. The maps thus created (both for the minimum distance constraint as well as for the sensor cone avoidance constraint) support the design of a guidance method satisfying the various constraints simultaneously. A number of steps leading to the design of a successful guidance are defined. This process is applied to an extensive example case leading to the design of a guidance that satisfies the various constraints simultaneously. The key contributions to the body of knowledge here are:

- the analysis of the minimum distance constraint in terms of rational relative orbital elements,
- the analysis of the sensor cone avoidance constraint in terms of rational relative orbital elements,
- the clear visualization of the constraints in rational relative orbital elements and
- an applied design process leading to a successful guidance method dealing with sensor cone avoidance constrains and minimum distance constraints simultaneously.

The last focal point is the development and application of a convex-optimization based method for station-keeping and collocation. We focused on convex optimization methods because convexity of the problem has several advantages: the optimum found by solving the convex problem solution corresponds to a global optimum, crude bounds on the required computation time can be derived and very stable algorithms exist to solve the problem.

We present several formulations of the problem with increasing complexity. One key characteristic of our approach is the minimization of the $\ell_1$-norm of control action, leading naturally to a sparse solution of the optimization problem. In the case of geostationary satellite station-keeping (or collocation) this translates into the need for only a small number of thruster firings, readily implementable by a realistic propulsion system that can only provide a fixed constant thrust level when switched on. A simple post-processing of the optimization problem is introduced that results in a simple plan stating which thruster to fire when over a station-keeping cycle. We actively constrain the thrust force to be at or below this constant thrust level in the formulation of the optimization problem. The dynamics are formulated using the discretized linear, time-varying formulation introduced earlier, with the possibility to define convex constraints on the state variables at any discrete node. These constraints allow to maintain (relative) orbital elements in convex windows that, corresponding to the analysis, guarantee that the minimum distance constraints and sensor cone avoidance constraints are satisfied. The problem is scaled to improve the numerical behavior of the problem and slack variables are introduced to guarantee feasibility. We present both single-shooting and multiple shooting formulations of the problem, where the former is conceptually simpler with a smaller number of optimization variables, while the latter results in a more sparse problem solution which decreases computation time and required memory. The multiple-shooting formulation is especially useful for solving long horizon optimization problems with many variables.

We validate our method by comparing the results under specific settings to results obtained using a conventional tried-and-true station-keeping strategy. We investigate long-term optimal strategies by formulating and solving several optimization problems with a one-year problem horizon. We demonstrate the method in the presence of modeling, orbit determination and actuation errors and introduce a receding horizon implementation that could benefit from the presence of frequent orbit determination solutions.

In terms of collocation we formulate the relative dynamics simply by subtracting the absolute state of the leader satellite from the absolute state of the follower satellite. We introduce a more robust formulation that accounts for errors in modeling, orbit determination and actuation in the problem formulation and solution. Several cases are studied including an inhomogeneous fleet of four satellites, a homogeneous fleet of 16 satellites in a small slot, fleets of respectively two and four satellites subject to sensor cone avoidance constraints and a fleet of two satellites controlled using the robustified formulation of the problem. We demonstrate the advantages of the method and point out where it falls short. The key contributions to the body of knowledge are:

- The formulation of the station-keeping and collocation problems as convex optimization problems that result in sparse solutions
- The analysis of the station-keeping strategies using an optimization problem with a one year horizon
- The robustified formulation of the collocation problem
- The analysis of several station-keeping and collocation strategies relying on the

convex optimization-based method for calculating the maneuvers.

Taken together, the various contributions listed in this section provide a powerful method to treat the complex problem of collocation of geostationary satellites under geometric constraints. The geostationary slot boundaries, minimum distance and sensor cone avoidance constraints are dealt with simultaneously. This method is the main contribution of this research to the current state of art.

## 1.4. THESIS ROADMAP

This dissertation is structured into four main parts. Chapter 2 covers the modeling aspects of geostationary satellite dynamics. This includes the nonlinear equations of motion, a simplified linear, time-varying model of the satellite motion in non-singular synchronous orbital elements and the equations for relative motion. The method to convert between osculating and mean orbital elements is discussed and rational orbital elements are introduced. A reference mission and satellite are defined and overview is given of the elements of the simulation environment as well as an introduction of the various modeling errors that are introduced into the simulations for testing the methods developed in later chapters.

In Chapter 3 we discuss the analysis and design of the guidance method in terms of relative orbital elements. We analyze the geostationary slot boundaries, the minimum separation distance and the sensor cone avoidance constraints in terms of relative orbital elements and in rational relative orbital elements. We look at some typical convex sets of relative eccentricity and inclination vectors and the realization in rational space, and vice versa. We then introduce a basic design process and work out this process in an elaborate example case in which we design the guidance for a fleet of satellites subject to minimum distance constraints and sensor cone avoidance constraints.

The development of the convex optimization-based method is discussed in Chapter 4. We introduce a concept of operations and validate the convex optimization-based method by comparison to an existing method. We investigate long-term optimal strategies using an the optimization-based method with a one year horizon. We investigate two station-keeping strategies relying on the new method at their core. These simulations include realistic errors in orbit determination, actuation and modeling.

The collocation problem is introduced in Chapter 5 and the convex optimization-based method is adapted to collocate a fleet of satellite using a leader-follower architecture. A more robust formulation of the problem is introduced to actively deal with the dominant forms of uncertainty. Several simulations are analyzed including an inhomogeneous fleet of four satellites, a large homogeneous fleet of sixteen satellites, fleets of two and four satellites subject to sensor cone avoidance constraints and a demonstration of the robustified implementation of the method.

Chapter 6 provides concluding remarks and outlook and includes an identification of topics of further research.

## REFERENCES

[1] J. Pearson, *Konstantin tsiolkovsky and the origin of the space elevator, 48$^{st}$ International Astronautical Congress,* (1997), Turin, 6-10 October, IAF-97-IAA-2.1.09.

[2] H. Noordung, *Das Problem der Befahrung des Weltraums - der Raketen-Motor* (Richard Carl Schmidt and Co., 1961).

[3] A. Clarke, *Extra-terrestrial relays,* Wireless World **51**, 305 (1945).

[4] D. Martin, P. Anderson, and L. Bartamian, *Satellite history - episode 5 - syncom 1 to 3,* SatMagazine (2008).

[5] E. M. Soop, *Handbook of Geostationary Orbits* (Microcosm and Kluwer, Dordrecht, 1994).

[6] E. Johnston, *List of satellites in geostationary orbit,* `http://www.satsig.net/sslist.htm`.

[7] P. Wauthier, *Fleet at 19.2° e,* personal communication.

[8] O. Montenbruck and E. Gill, *Satellite Orbits* (Springer, 2000).

[9] H. Schaub and J. L. Junkins, *Analytical Mechanics Of Space Systems* (American Institute of Aeronautics and Astronautics (AIAA), 2003).

[10] D. A. Vallado, *Fundamentals of Astrodynamics and Applications*, Vol. 12 (Springer Science & Business Media, 2001).

[11] C.-C. G. Chao, *Applied Orbit Perturbation and Maintenance* (American Institute of Aeronautics and Astronautics (AIAA), 2005).

[12] H. Li, *Geostationary Satellites Collocation* (Springer, 2014).

[13] S. K. SHRIVASTAVA, *Orbital perturbations and stationkeeping of communication satellites,* Journal of Spacecraft and Rockets **15**, 67 (1978).

[14] A. Kamel, *Geosynchronous satellite perturbations due to earth's triaxiality and luni-solar effects,* in *Astrodynamics conference, Palo Alto, CA, USA* (American Institute of Aeronautics and Astronautics, 1978).

[15] D. Losa, *High vs low thrust station keeping maneuver planning for geostationary satellites,* Ph.D. thesis, École Nationale Supérieure des Mines de Paris (2007).

[16] Clohessy and Wiltshire, *Terminal guidance system for satellite rendezvous,* Journal of the Aerospace Sciences **27**, 653 (1960).

[17] P. Blumer, *A future concept of coordinated orbit control of colocated geostationary satellites,* in *Astrodynamics Conference* (American Institute of Aeronautics and Astronautics (AIAA), 1992).

[18] M. Eckstein, *Geostationary orbit control considering deterministic cross coupling effects,* in *41st congress of the International Astronautical Federation* (1990) Dresden, IAF Paper 90-326.

[19] D. SLAVINSKAS, H. DABBAGHI, W. J. BENDEN, and G. K. JOHNSON, *Efficient inclination control for geostationary satellites,* Journal of Guidance, Control, and Dynamics **11**, 584 (1988).

[20] T. J. Kelly, L. K. White, and D. W. Gamble, *Stationkeeping of geostationary satellites with simultaneous eccentricity and longitude control,* Journal of Guidance, Control, and Dynamics **17**, 769 (1994).

[21] P. Romero and J. M. Gambi, *Optimal control in the east/west station-keeping manoeuvres for geostationary satellites,* Aerospace Science and Technology **8**, 729 (2004).

[22] M. C. Eckstein, *Optimal station keeping by electric propulsion with thrust operation constraints,* Celestial Mechanics **21**, 129 (1980).

[23] D. Losa, M. Lovera, R. Drai, T. Dargent, and J. Amalric, *Electric station keeping of geostationary satellites: a differential inclusion approach,* in *Proceedings of the 44th IEEE Conference on Decision and Control* (Institute of Electrical & Electronics Engineers (IEEE), 2005).

[24] D. Losa, M. Lovera, J. paul Marmorat, T. Dargent, and J. Amalric, *Station keeping of geostationary satellites with on-off electric thrusters,* in *2006 IEEE International Conference on Control Applications* (CrossRef Test Account, 2006).

[25] D. Losa, *High vs Low Thrust Station Keeping Maneuver Planning for Geostationary Satellites*, Ph.D. thesis, École Nationale Supérieure des Mines de Paris (2007).

[26] M. le Berre and A. Gicquel, *Optimization of SK for GEO Satellites using EP*, Tech. Rep. (Airbus under ESA contract, 2010) aRTES 5.1.

[27] J. L. Gonzalez, C. Praile, S. Erb, J. del Cura, G. Rodriguez, and S. Weikert, *Optimization of NS, EW Station-Keeping Manoeuvres for GEO Satellites using Electric Propulsion (OPASKEP)*, Tech. Rep. (GMV under ESA contract, 2010) aRTES 5.1.

[28] A. LEIBOLD and M. ECKSTEIN, *RESULTS OF a STUDY OF ON-BOARD AUTONOMOUS STATION KEEPING OF GEOSTATIONARY SATELLITES AND ITS IMPACT TO GROUND SYSTEMS,* in *Space tracking and data systems: Proceedings of the Symposium* (American Institute of Aeronautics and Astronautics (AIAA), 1981).

[29] C. Chao and H. Bernstein, *Onboard stationkeeping of geosynchronous satellite using a global positioning system receiver,* Journal of Guidance, Control, and Dynamics **17**, 778 (1994).

[30] B.-K. Park, M.-J. Tahk, H.-C. Bang, C.-S. Park, and J.-H. Jin, *A new approach to onboard stationkeeping of GEO-satellites,* Aerospace Science and Technology **9**, 722 (2005).

[31] B. P. Emma and H. J. Pernicka, *Algorithm for autonomous longitude and eccentricity control for geostationary spacecraft,* Journal of Guidance, Control, and Dynamics **26**, 483 (2003).

[32] M. M. Guelman, *Geostationary satellites autonomous closed loop station keeping,* Acta Astronautica **97**, 9 (2014).

[33] A. Harting, *Approach to the evaluation of interferences between co-located geostationary satellites,* in *Proceedings of the 3rd international symposium on spacecraft flight dynamics* (1991).

[34] S. Hubert and J. Swale, *Stationkeeping of a constellation of geostationary communications satellites,* in *Astrodynamics Conference* (American Institute of Aeronautics and Astronautics (AIAA), 1984).

[35] M. Eckstein, C. Rajasingh, and P. Blumer, *Colocation strategy and collision avoidance for the geostationary satellites at 19 degrees west,* in *International Symposium on Space Flight Dynamics* (1989).

[36] O. Montenbruck and M. C. E. J. Gonner, *The geo-control system for station keeping and colocation of geostationary satellites,* Tech. Rep. (German Aerosspace Center DLR, 1992).

[37] P. Wauthier and P. Francken, *The ASTRA co-location strategy for three to six satellites,* Revista Brasileira de Ciencias Mecanicas (ISSN 0100-7386), vol. 16, p. 163-171 **16**, 163 (1994).

[38] P. Wauthier, P. Francken, and H. Laroche, *Co-location of six astra satellites: Assessment after one year of operations,* in *Proceedings of the 12th International Symposium on Space Flight Dynamics* (1997).

[39] I. Beigelman and P. Gurfil, *Optimal geostationary satellite collocation using relative orbital element corrections,* Journal of Spacecraft and Rockets **46**, 141 (2009).

[40] R. R. Rausch and K. C. Howell, *Semi-autonomous stationkeeping of collocated geostationary satellites using relative orbit control,* in *International Workshop on Satellite Constellation and Formation Flying* (2010).

[41] R. R. Rausch, *RELATIVE ORBIT CONTROL OF COLLOCATED GEOSTATIONARY,* Ph.D. thesis, Purdue University West Lafayette (2012).

[42] S. D'Amico and O. Montenbruck, *Proximity operations of formation-flying spacecraft using an eccentricity/inclination vector separation,* Journal of Guidance, Control, and Dynamics **29**, 554 (2006).

[43] J.-S. Ardaens and D. Fischer, *TanDEM-x autonomous formation flying system: Flight results,* IFAC Proceedings Volumes **44**, 709 (2011).

[44] J. Wang and S. Nakasuka, *Cluster flight orbit design method for fractionated spacecraft,* Aircraft Eng & Aerospace Tech **84**, 330 (2012).

[45] G. Gaias and J.-S. Ardaens, *Design challenges and safety concept for the AVANTI experiment,* Acta Astronautica **123**, 409 (2016).

[46] V. Manikonda, P. Arambel, M. Gopinathan, R. Mehra, and F. Hadaegh, *A model predictive control-based approach for spacecraft formation keeping and attitude control,* in *Proceedings of the 1999 American Control Conference (Cat. No. 99CH36251)* (Institute of Electrical & Electronics Engineers (IEEE), 1999).

[47] M. Tillerson, G. Inalhan, and J. P. How, *Co-ordination and control of distributed spacecraft systems using convex optimization techniques,* International Journal of Robust and Nonlinear Control **12**, 207 (2002).

[48] L. Breger and J. P. How, *Gauss's variational equation-based dynamics and control for formation flying spacecraft,* Journal of guidance, control, and dynamics **30**, 437 (2007).

[49] S. Boyd and L. Vandenberghe, *Convex Optimization* (Cambridge University Press, 2004).

[50] B. Acikmese, D. Scharf, F. Hadaegh, and E. Murray, *A convex guidance algorithm for formation reconfiguration,* in *AIAA Guidance, Navigation, and Control Conference and Exhibit* (American Institute of Aeronautics and Astronautics (AIAA), 2006).

[51] P. Lu and X. Liu, *Autonomous trajectory planning for rendezvous and proximity operations by conic optimization,* Journal of Guidance, Control, and Dynamics **36**, 375 (2013).

[52] B. Acikmese and S. R. Ploen, *Convex programming approach to powered descent guidance for mars landing,* Journal of Guidance, Control, and Dynamics **30**, 1353 (2007).

[53] L. Blackmore, B. Acikmese, and D. P. Scharf, *Minimum-landing-error powered-descent guidance for mars landing using convex optimization,* Journal of Guidance, Control, and Dynamics **33**, 1161 (2010).

[54] L. Blackmore, B. Acikmese, and J. M. Carson, *Lossless convexification of control constraints for a class of nonlinear optimal control problems,* in *2012 American Control Conference (ACC)* (Institute of Electrical & Electronics Engineers (IEEE), 2012).

[55] B. Acikmese, J. M. Carson, and L. Blackmore, *Lossless convexification of nonconvex control bound and pointing constraints of the soft landing optimal control problem,* IEEE Transactions on Control Systems Technology **21**, 2104 (2013).

[56] D. Morgan, S.-J. Chung, and F. Y. Hadaegh, *Model predictive control of swarms of spacecraft using sequential convex programming,* Journal of Guidance, Control, and Dynamics **37**, 1725 (2014).

[57] H. Kramer, *Goes (geostationary operational environmental satellite) 2nd generation series,* `https://directory.eoportal.org/web/eoportal/satellite-missions/content/-/article/goes2`.

[58] L. Gaudic, E. Brouillard, J. Pasquet, and H. Renault, *In-flight geostationnary aocs based on star tracker,* in *Proceedings of the 6th International ESA conference on Guidance, Navigation and Control Systems* (2006).

[59] C. Chasset, P. Bodin, N. Neumann, R. Larsson, and A. Edfors, *Evolution of the AOCS design for EDRS and the satellites of the Small GEO family,* in *Proceedings of the 9$^{th}$ International ESA Conference on Guidance, Navigation and Control* (ESA, 2014).

[60] M. Hooghe, *Coning constraint for collocated geostationary satellites in eccentricity and longitude separation,* personal communication.

[61] T. Ebinuma and M. Unwin, *GPS receiver demonstration on a galileo test bed satellite,* Journal of Navigation **60**, 349 (2007).

[62] N. Neumann, F. de Bruijn, B. Lubke-Ossenbeck, R. Larsson, S. Zehetmayer, S. Sassen, and P. Krauss, *Use of gnss receivers within the smallgeo product line,* in *proceedings of the 65th International Astronautical Congress* (2014).

[63] J. Chapel, D. Stancliffe, T. Bevacqua, S. Winkler, B. Clapp, T. Rood, D. Gaylor, D. Freesland, and A. Krimchansky, *Guidance, navigation, and control performance for the GOES-r spacecraft,* CEAS Space J (2015), 10.1007/s12567-015-0077-1.

[64] J. Rosello, P. Silvestrin, G. L. Risueno, R. Weigand, J. V. Perello, J. Heim, and I. Tejerina, *AGGA-4: Core device for GNSS space receivers of this decade,* in *2010 5th ESA Workshop on Satellite Navigation Technologies and European Workshop on GNSS Signals and Signal Processing (NAVITEC)* (Institute of Electrical & Electronics Engineers (IEEE), 2010).

[65] S. A. Feuerborn, D. Neary, and J. Perkins, *Finding a way: Boeings all electric propulsion satellite,* in *49th Joint Propulsion Conference, AIAA-2013-4126* (2013).

[66] M. De Tata, P.-E. Frigot, S. Beekmans, H. Lübberstedt, D. Birreck, A. Demairé, P. Rathsman, E. Rezugina, and N. Kutufà, *Sgeo electric propulsion subsystem development status and future opportunities,* in *Proc. 33rd Int. Electr. Propuls. Conf* (2013) pp. 1–15.

# 2

# MODELING GEOSTATIONARY SATELLITE AND ORBIT DYNAMICS

> *Research is what I am doing when I do not know what I am doing.*
>
> Wernher von Braun

> *The two most powerful warriors are patience and time.*
>
> Leo Tolstoy

***Abstract***
*The development of methods for guidance and control of geostationary satellites requires a model of the orbital dynamics at its core. To this end, the full nonlinear equations of motion are used to develop a linear, time-varying model. The accuracy of the model is analyzed using analytical and numerical methods. A method for the conversion between mean and osculating orbital elements is presented, as well as a model of relative motion in terms of relative and rational orbital elements. The simulation environment that is used to evaluate guidance and control methods is presented together with a reference mission and the key satellite parameters.*

In this chapter we explore the equations of motion for satellites in a geostationary orbit. We use both Cartesian representations, as well as synchronous orbital element representations, both for the absolute and relative states of the satellites. The dynamics are expressed as a linear time-varying system by making a set of simplifying assumptions. We investigate the validity and merits of the linear time-varying system and conclude its suitability for guidance and control of the orbits of geostationary satellites. We then define a set of rational orbital elements that we use in the design of a guidance method in the next chapter. We also introduce the key satellite and mission characteristics, as well as the simulation environment used for the analysis performed in later chapters.

## 2.1. DEFINITION OF REFERENCE FRAMES

This work relies on three different reference frames, namely an Earth Centered Inertial (ECI)-frame, an Earth Centered Earth Fixed (ECEF)-frame and a RTN-frame. Each reference frame is an orthogonal right-handed reference frame. We provide a short description of these reference frames. Additional information can be obtained from [1] and [2].

As ECI-frame we use the EME2000 reference frame, where EME stands for Earth Mean Equator. The fundamental (x,y)-plane is the Earth Mean Equator at the J2000 epoch. The x-axis is in the direction of the mean vernal equinox at J2000. The coordinate system has its origin at the center of mass of the Earth.

The ECEF-frame is an Earth-fixed rotating reference frame that is obtained from a time-dependent rotation of ECI by a transformation matrix capturing sidereal time angle, precession and nutation [3], [4]. Polar motion is neglected in this work, which makes the ECEF-frame a crust-fixed frame. Although this simplification can lead to small (meter-level errors after a week) propagation errors, it has virtually no impact on the results, since these errors are much smaller than other error sources considered in this work (introduced in Section 2.8). The ECEF reference frame is thus a true-of-date rotating reference frame, and coordinates in ECEF are related to the international terrestrial reference system by a rotation using a polar motion transformation matrix [2]. The (x,y)-plane of the ECEF frame is the Earth's true-of-date equator with the x-axis pointing towards the zero meridian. We use both Cartesian and spherical coordinates to describe a position in the ECEF reference frame.

Finally, the RTN-frame is centered on a satellite with axes obtained from the satellite state in ECI: the x-axis points radially outward, the z-axis in the direction of the orbit angular momentum and the y-axis completes the right handed system.

## 2.2. REVIEW OF EQUATIONS OF MOTION

This section presents the equations of motion of a satellite in Cartesian coordinates (in ECI). These equations were implemented in the propagator that is used in the simulations presented in this work. Besides the equations introduced in this section, a model for transforming between ECI and ECEF was included, as introduced in the previous section. Analytic models for the position of the Sun and Moon were used, as presented in [1].

### 2.2.1. CARTESIAN REPRESENTATION OF PERTURBED EQUATIONS OF MOTION

The motion of a satellite around the Earth can be described by the following differential equation:

$$\ddot{\mathbf{r}} = -\mu_E \frac{\mathbf{r}}{r^3} + \mathbf{a}_d, \tag{2.1}$$

where $\mathbf{r}$ is the position vector of the satellite in ECI, with $r$ its magnitude, $\mu_E$ the gravitational parameter of the Earth and $\mathbf{a}_d$ comprises the disturbing accelerations. The term $-\mu_E\mathbf{r}/r^3$ describes the gravitational acceleration in a two-body problem, where the mass of the satellite is neglected over that of the Earth. All other accelerations, gravitational and non-gravitational, including controlled accelerations, are comprised in the vector $\mathbf{a}_d$. In the sequel we provide a brief summary of the key perturbing accelerations.

### 2.2.2. DOMINANT PERTURBATIONS IN GEOSTATIONARY ORBIT

The dominant perturbations for a satellite in a geostationary orbit are caused by the difference between the true geopotential and a spherical approximation of Earth with uniform density, by Sun and Moon gravity and by SRP. We shortly discuss these perturbations in the following.

#### GEOPOTENTIAL

The geopotential perturbations are given by [1]:

$$\mathbf{a}_{d,\text{gpot}} = \nabla \frac{\mu_E}{r} \sum_{n=2}^{\infty} \sum_{m=0}^{n} \frac{R_E^n}{r^n} \bar{P}_{nm}\left(\sin\phi\right)\left(\bar{C}_{nm}\cos\left(m\lambda\right) + \bar{S}_{nm}\sin\left(m\lambda\right)\right), \tag{2.2}$$

where $m$ and $n$ are the order and degree of the spherical harmonics included in the equation, $R_E$ is the radius of Earth, $\bar{P}_{nm}$ is the normalized associated Legendre function, $\lambda$ and $\phi$ are respectively longitude and latitude and $\bar{C}_{nm}$ and $\bar{S}_{nm}$ are the normalized geopotential coefficients. The dominant terms for a geostationary satellite in the above equation are caused by the equatorial bulge, represented by the zonal term of degree 2 and order 0 (commonly referred to as $J_2$), and the tesseral term of order and degree 2, representing the Earth's triaxiality (commonly referred to as $J_{22}$). The $J_2$ perturbation causes a gravitational acceleration in radial direction, towards the Earth, thus slightly changing the ideal (Keplerian) GEO semi-major axis. The $J_{22}$ perturbation causes a tangential acceleration on a GEO satellite, resulting in a longitudinal drift of the satellite, which will move the satellite away from its assigned location if not compensated for. The size of this acceleration is longitude dependent. The geopotential can be modeled up to very high order and degree, and with very high accuracy.

#### THIRD BODY GRAVITY PERTURBATION

The perturbing accelerations due to third bodies can be expressed as [1]:

$$\mathbf{a}_{d,3\text{b}} = \mu_{3\text{b}}\left(\frac{\mathbf{r}_{3\text{b}} - \mathbf{r}}{\left|\mathbf{r}_{3\text{b}} - \mathbf{r}^3\right|} - \frac{\mathbf{r}_{3\text{b}}}{\left|\mathbf{r}_{3\text{b}}\right|^3}\right), \tag{2.3}$$

where $\mu_{3\text{b}}$ and $\mathbf{r}_{3\text{b}}$ are respectively the gravitational parameter and position vector of the third body. For a geostationary satellite the third bodies of prime interest are the Sun and

Moon. In order to evaluate the above equation, an accurate model of the positions of the Sun and Moon in ECI is required. Low-precision Solar and Lunar coordinates can be modeled analytically. Alternatively, high precision planetary ephemerides are provided by the Jet Propulsion Laboratory (JPL) [5]. The secular effect of Sun and Moon gravity perturbations is dominant in normal direction, causing oscillations of the satellite in North-South direction. These perturbations are well-known and well-understood and can be modeled with a very high accuracy.

### SOLAR RADIATION PRESSURE

An approximate relation for the SRP perturbation, assuming that the surface normal is oriented towards the Sun, is given by [1]:

$$\mathbf{a}_{d,\mathrm{srp}} = -P_{\mathrm{sun}} C_R \frac{A}{m} \frac{\mathbf{r}_{\mathrm{sun}}}{r_{\mathrm{sun}}^3} \mathrm{AU}^2, \tag{2.4}$$

where $P_{\mathrm{sun}}$ is the solar radiation pressure, $C_R$ is the radiation pressure coefficient, $A$ the surface area exposed to solar radiation, $m$ the satellite mass and AU is the astronomical unit (the mean distance between the Earth and the Sun). Whereas the perturbing accelerations due to gravity can be determined with very high accuracy, those due to SRP can only be approximated with low accuracy, as they depend on the satellites' characteristics and orientation. Uncertainty in satellites mass, surface area and orientation of the surface areas with respect to the Sun direction, and absorption and reflectivity characteristics cause errors in the modeling of SRP.

## 2.2.3. EQUATIONS OF MOTION IN SYNCHRONOUS ORBITAL ELEMENTS

Instead of Cartesian coordinates, the motion of a satellite can also be described using a set of orbital elements. We start with a presentation of the variational equations in classic orbital elements as given in [6], originally from [7]:

$$\begin{aligned}
\frac{\mathrm{d}a}{\mathrm{d}t} &= \frac{2}{n\eta}\left(e u_r \sin\nu + \frac{p}{r} u_t\right) \\
\frac{\mathrm{d}e}{\mathrm{d}t} &= \frac{\eta}{na}\left(u_r \sin\nu + u_t \left(\cos E + \cos\nu\right)\right) \\
\frac{\mathrm{d}i}{\mathrm{d}t} &= \frac{1}{na\eta}\frac{r}{a} u_n \cos\left(\omega + \nu\right) \\
\sin i \frac{\mathrm{d}\Omega}{\mathrm{d}t} &= \frac{1}{na\eta}\frac{r}{a} u_n \sin\left(\omega + \nu\right) \\
e \frac{\mathrm{d}\tilde{\omega}}{\mathrm{d}t} &= \frac{\eta}{na}\left(-u_r \cos\nu + u_t\left(1 + \frac{r}{p}\right)\sin\nu\right) + 2\sin^2\frac{i}{2}\frac{\mathrm{d}\Omega}{\mathrm{d}t} \\
\frac{\mathrm{d}L_0}{\mathrm{d}t} &= -\frac{2r}{na^2} u_r + \frac{e^2}{1+\eta}\frac{\mathrm{d}\tilde{\omega}}{\mathrm{d}t} + 2\eta \sin^2\frac{i}{2}\frac{\mathrm{d}\Omega}{\mathrm{d}t},
\end{aligned} \tag{2.5}$$

where $n = \sqrt{\mu / a^3}$ is the mean orbital motion, $\tilde{\omega} = \omega + \Omega$, $L_0 = \Omega + \omega + M_0$ is the mean longitude at epoch $t_0$, $r$ is the orbital radius, $\eta = \sqrt{1 - e^2}$, $E$ is the eccentric anomaly, $p = a\left(1 - e^2\right)$ the semi-latus rectum, $\nu$ is the true anomaly, $u_r$, $u_t$, $u_n$ are the perturbing accelerations in radial, tangential and normal directions and $a$, $e$, $i$, $\Omega$, $\omega$, $M$ are classical orbital elements.

Since an ideal geostationary orbit is characterized by zero eccentricity and zero inclination it is customary to use a set of non-singular synchronous orbital elements describing the state of the satellite with respect to a reference position in the geostationary orbit. This approach avoids singularities associated to the use of classic orbital elements. The following representation is used in this dissertation:

$$\mathbf{oe}\left(t\right)=\begin{pmatrix}\Delta n\\ e_x\\ e_y\\ i_x\\ i_y\\ \Delta L\end{pmatrix}=\begin{pmatrix}n-n_{\mathrm{geo}}\\ e\cos\left(\tilde{\omega}\right)\\ e\sin\left(\tilde{\omega}\right)\\ i\cos\left(\Omega\right)\\ i\sin\left(\Omega\right)\\ L_0+\int_{t_0}^{t}n\mathrm{d}t-\alpha\left(t\right)\end{pmatrix}, \tag{2.6}$$

where $n_{\mathrm{geo}}$ is the mean orbital motion of an ideal geostationary orbit (equal to the Earth's rotation rate), $L=L_0+\int_{t_0}^{t}n\mathrm{d}t$ is the mean longitude, $\alpha$ is the right ascension of the reference geostationary position. The center of the geostationary slot in which a satellite is maintained is normally used as the reference position. Note that the reference position is given by the zero state vector and thus this particular non-singular synchronous orbital element set can be interpreted as a set of relative orbital elements between the satellite and the geostationary slot center. The elements can be interpreted as follows: $\Delta n$ is the angular rate difference between the satellite and the geostationary slot, $\left(e_x,e_y\right)$ is the (relative) eccentricity vector, $\left(i_x,i_y\right)$ is the (relative) inclination vector and $\Delta L$ is the difference in mean longitude between the satellite and the geostationary slot center. Using Eqs. (2.5) the time-rate-of-change of the synchronous orbital elements was derived:

$$\begin{aligned}
\frac{\mathrm{d}\Delta n}{\mathrm{d}t}=&-\frac{3e\sin\nu}{\eta a}u_r-\frac{3p}{r\eta a}u_t\\
\frac{\mathrm{d}e_x}{\mathrm{d}t}=&\frac{\eta\sin\ell}{na}u_r+\frac{\eta\left(\cos\ell+\cos\tilde{\omega}\cos E-r/p\sin\tilde{\omega}\sin\nu\right)}{na}u_t\\
&-\frac{r\sin\tilde{\omega}\tan\left(i/2\right)\sin\left(\omega+\nu\right)}{na^2\eta}u_n\\
\frac{\mathrm{d}e_y}{\mathrm{d}t}=&-\frac{\eta\cos\ell}{na}u_r+\frac{\eta\left(\sin\ell+\sin\tilde{\omega}\cos E+r/p\cos\tilde{\omega}\sin\nu\right)}{na}u_t\\
&+\frac{r\cos\tilde{\omega}\tan\left(i/2\right)\sin\left(\omega+\nu\right)}{na^2\eta}u_n\\
\frac{\mathrm{d}i_x}{\mathrm{d}t}=&\frac{r}{na^2\eta}\left(\cos\Omega\cos\left(\omega+\nu\right)-\frac{i}{\sin i}\sin\Omega\sin\left(\omega+\nu\right)\right)u_n\\
\frac{\mathrm{d}i_y}{\mathrm{d}t}=&\frac{r}{na^2\eta}\left(\sin\Omega\cos\left(\omega+\nu\right)+\frac{i}{\sin i}\cos\Omega\sin\left(\omega+\nu\right)\right)u_n\\
\frac{\mathrm{d}\Delta L}{\mathrm{d}t}=&\Delta n-\left(\frac{e\eta\cos\nu}{\left(1+\eta\right)na}+\frac{2r}{na^2}\right)u_r+\frac{e\eta\left(1+r/p\right)\sin\nu}{\left(1+\eta\right)na}u_t\\
&+\frac{r\tan\left(i/2\right)\sin\left(\omega+\nu\right)}{na^2}\left(1+\frac{e}{\left(1+\eta\right)\eta}\right)u_n.
\end{aligned} \tag{2.7}$$

In these equations $\ell = \omega + \Omega + \nu$ is the true longitude. The singularity at $i = 0$ in the equations for $i_x$ and $i_y$ can be avoided by expanding $i/\sin i$ in a Taylor series as:

$$\frac{i}{\sin i} = \frac{1}{\sum_{n=0}^{\infty} \frac{(-1)^n}{(2n+1)} i^{2n}}, \tag{2.8}$$

and truncating at an order in line with the accuracy requirements of the application. Truncating after the zeroth order term results in the approximation $i/\sin i \approx 1$. For an inclination $i < 0.1°$ this approximation leads to an error $|i/\sin i - 1|$ that is smaller than $5.1 \cdot 10^{-7}$. Thus, if we allow the following assumption:

**Assumption 2.1.** The approximation $i/\sin i \approx 1$ introduces a negligible error in the dynamics when used to model a satellite inside a geostationary slot with $i < 0.1°$,

then, the equations for the time rate of change of $i_x$ and $i_y$ can be simplified as follows:

$$\begin{aligned} \frac{\mathrm{d}i_x}{\mathrm{d}t} &= \frac{r\cos\ell}{na^2\eta} u_n \\ \frac{\mathrm{d}i_y}{\mathrm{d}t} &= \frac{r\sin\ell}{na^2\eta} u_n. \end{aligned} \tag{2.9}$$

Equations (2.7) and (2.9) constitute a system of equations that is nonlinear in state and affine in control:

$$\dot{\mathbf{x}}(t) = \mathbf{A}\mathbf{x}(t) + \mathbf{B}(\mathbf{x}(t))\,\mathbf{u}_c(t) + \mathbf{B}(\mathbf{x}(t))\,\mathbf{u}_d(\mathbf{x}(t)). \tag{2.10}$$

The definition of $\mathbf{A}$ (a time-invariant matrix with all zero entries, except $A_{61} = 1$) follows directly from Eqs. (2.7). The vector $\mathbf{u} = (u_r, u_t, u_n)^T$ was split into $\mathbf{u}_c$ and $\mathbf{u}_d$, representing respectively controlled and disturbing accelerations and is expressed in the RTN frame, in contrast to $\mathbf{a}_d$ in Eq. (2.1), which is expressed in an inertial frame. The input matrix $\mathbf{B}(\mathbf{x}(t))$ and disturbing input $\mathbf{u}_d(\mathbf{x}(t))$ are state-dependent as evident from Eqs. (2.7).

## 2.3. LINEAR TIME-VARYING FORMULATION

Since geostationary satellites are typically controlled to stay inside a geostationary slot with a size of up to ±0.1° in longitude and latitude, a coarse approximation of the position of a geostationary satellite is obtained by assuming that the satellite is nominally at the center of its assigned slot. The maximum “error” thus made is half of the geostationary slot size in radial, tangential and normal direction. For this coarse approximation of the satellite position (i.e. the geostationary slot center), we can determine the perturbing accelerations for any point in (future) time using accurate models of the perturbations. Now, if the perturbing accelerations at the geostationary slot center are a good approximation of the perturbing accelerations at an arbitrary location inside the geostationary slot, we can integrate Eqs. (2.7) using the approximated perturbing accelerations. This hypothesis is central to the developments in this section and its validity is investigated. The center of the geostationary slot is given by the zero state (i.e. $\mathbf{x}_{\text{geo}} = [0,0,0,0,0,0]^T$).

### 2.3.1. ASSUMPTIONS AND EQUATIONS

The hypothesis introduced before can be captured by two key assumptions. The first assumption is formulated loosely in the following.

**Assumption 2.2.** The input matrix at the ideal geostationary slot center provides an accurate enough approximation of the input matrix at an arbitrary position inside the geostationary slot.

The meaning of "accurate enough" is application dependent and the key application investigated in this work is the calculation of station-keeping maneuvers with a propagation horizon between one and seven days. This assumption simplifies Eqs. (2.7) greatly by allowing the **B** matrix to be approximated at the geostationary slot center, defined by $a = a_{\text{geo}}$, $e = 0$, $i = 0$ and $\ell = \alpha$, and hence $p = r = a_{\text{geo}}$, $\eta = 1$, $E = \nu$ and $n = n_{\text{geo}}$. These simplifications result in the following approximation to **B**, valid in the neighborhood of the slot center:

$$\mathbf{B}(\alpha(t)) \approx \frac{1}{n_{\text{geo}} a_{\text{geo}}} \begin{pmatrix} 0 & -3n_{\text{geo}} & 0 \\ \sin\alpha & 2\cos\alpha & 0 \\ -\cos\alpha & 2\sin\alpha & 0 \\ 0 & 0 & \cos\alpha \\ 0 & 0 & \sin\alpha \\ -2 & 0 & 0 \end{pmatrix}. \tag{2.11}$$

This assumption is commonly used in determining station-keeping maneuvers for geostationary satellites and is the basis for analytically calculating maneuver size (as impulsive $\Delta V$) and maneuver location (in terms of $\alpha$) resulting in desired changes to the orbital elements. The analytic calculation of maneuvers under this assumption has been applied in operations for more than 30 years and is still the state-of-art for calculating station-keeping maneuvers for geostationary satellites. Key maneuver strategies relying on these assumptions are outlined in [6] and [8].

Under Assumption 2.2, the **B** matrix is no longer state-dependent. It remains time-dependent through its dependency on the right ascension of the geostationary slot center, which is calculated as:

$$\alpha(t) = \alpha(t_0) + n_{\text{geo}}(t - t_0). \tag{2.12}$$

Thus the **B**-matrix can be determined for a particular geostationary slot at any point in time. A similar hypothesis can be applied to the perturbing accelerations:

**Assumption 2.3.** The differential perturbing accelerations between a satellite at an arbitrary position inside a geostationary slot and a virtual satellite located at the ideal geostationary slot center are so small that the perturbing accelerations for a satellite at an arbitrary position inside the slot can be approximated by the perturbing accelerations of a virtual satellite at the geostationary slot center.

This assumption removes the dependency of the perturbing accelerations on the satellite state. The perturbing accelerations remain nonlinear functions of time, but the state-dependency is no longer present. As discussed before, the key perturbations in the geostationary orbit are 1) gravity perturbations due to non-homogeneous, non-spherical Earth, 2) perturbations due to Sun and Moon gravity, and 3) solar radiation pressure. The magnitude and direction of these perturbations can be modeled with high accuracy and determined ahead of time for any point in time for any particular geostationary slot center. This allows us to describe the dynamics of a satellite in GEO by a linear time-varying state-space system, driven by a time-dependent but known perturbing function. Using Eqs. (2.10)-(2.11) we can write the linear time-varying system as:

$$\dot{\mathbf{x}}(t) \approx \mathbf{A}\mathbf{x}(t) + \mathbf{B}(\alpha(t))\mathbf{u}_c(t) + \mathbf{B}(\alpha(t))\mathbf{u}_d\left(\mathbf{x}_{\text{geo}}(t)\right), \tag{2.13}$$

with **A** as before, **B** and $\mathbf{u}_d$ are still time-dependent, however, the state-dependency is removed through the two simplifying assumptions. Hence, Eq. (2.13) can be used to obtain a linear approximation (linear in terms of initial state and controlled accelerations) to any future state, while accounting for all dominant perturbations.

The same conclusion can be reached by linearizing Eq. (2.10) using a first order Taylor series expansion around $\mathbf{x}_0(t)$:

$$\begin{aligned}\dot{\mathbf{x}}(t) \approx & \left(\mathbf{A}\mathbf{x}(t) + \mathbf{B}\mathbf{u}_c + \mathbf{B}\mathbf{u}_d\right)\Big|_{\mathbf{x}(t)=\mathbf{x}_0(t)} \\ & + \left(\mathbf{A} + \frac{\partial \mathbf{B}}{\partial \mathbf{x}}\mathbf{u}_c + \frac{\partial \mathbf{B}}{\partial \mathbf{x}}\mathbf{u}_d + \mathbf{B}\frac{\partial \mathbf{u}_d}{\partial \mathbf{x}}\right)\Big|_{\mathbf{x}(t)=\mathbf{x}_0(t)} (\mathbf{x} - \mathbf{x}_0).\end{aligned} \tag{2.14}$$

Assumptions 2.2 and 2.3 imply that both $\partial\mathbf{B}/\partial\mathbf{x}$ and $\partial\mathbf{u}_d/\partial\mathbf{x}$ are very small. By neglecting these terms and substituting $\mathbf{x}_0 = \mathbf{x}_{\text{geo}} = \mathbf{0}$ we retrieve Eq. (2.13).

Losa, [9], also arrives at a LTV system for the dynamics, albeit using a first order Taylor series expansion. The model by Losa is therefore more accurate if the same perturbing accelerations are considered. The LTV formulation proposed here also has an important advantage: there is no need for explicit partial derivatives of both the input matrix and the perturbing accelerations in terms of the synchronous orbital element set used. The perturbing accelerations (with respect to the geostationary slot center) can be obtained by any method deemed suitable by the user, as long as they are finally provided in the radial, tangential, normal reference frame. This makes it easier to include high order gravity perturbations or rely on models of perturbations that are not analytic in nature.

The worst-case errors that are introduced through the simplifying assumptions are investigated analytically in the next section in order to validate and establish fidelity in the modeling approach.

### 2.3.2. VALIDITY OF ASSUMPTIONS

Assumption 2.2 is commonly used both in the literature and in practice and is generally assumed to hold for satellites inside the geostationary slot. We are interested to obtain insight in the error introduced through this simplification. In order to quantify the error we define the difference in **B**-matrix between an arbitrary position inside the geostationary slot and the **B**-matrix corresponding to the geostationary slot center:

$$\Delta\mathbf{B} = \mathbf{B} - \mathbf{B}_{\text{geo}}, \tag{2.15}$$

where **B** corresponds to the matrix obtained from Eq. (2.7) and $\mathbf{B}_{\text{geo}}$ as per Eq. (2.11). As in [10], the induced two-norm (or maximum singular value) is used as a measure of the relative error:

$$e_1 = \frac{\|\Delta\mathbf{B}\|_2}{\|\mathbf{B}_{\text{geo}}\|_2}. \tag{2.16}$$

The largest possible error is then investigated by randomly generating $\mathbf{B}_{\text{geo}}$ and $\mathbf{B}$ under the following (uniform randomly generated) variations:

$$\begin{array}{lllllll} a & = & a_{\text{geo}}+\Delta a, & \Delta a & \in & [-5,5] & \text{km} \\ e & = & \Delta e, & \Delta e & \in & [0,8.8\cdot 10^{-4}] & \\ i & = & \Delta i, & \Delta i & \in & [0,17.6\cdot 10^{-4}] & \text{rad} \\ \Omega & = & \Omega, & \Omega & \in & [0,2\pi] & \text{rad} \\ \omega & = & \omega, & \omega & \in & [0,2\pi] & \text{rad} \\ L & = & \alpha+\Delta L & \Delta L & \in & [-17.6\cdot 10^{-4},17.6\cdot 10^{-4}] & \text{rad} \\ & & & \alpha & \in & [0,2\pi] & \text{rad.} \end{array} \tag{2.17}$$

The bounds on these orbital elements were chosen to contain the complete region in which a GEO satellite in a large (±0.1°) slot normally moves and a worst-case error of 0.00246, or 0.246%, was found over 10 million randomly generated samples.

Assumption 2.3 states that the errors made by evaluating the perturbations at the geostationary slot center instead of at the actual position of the satellite are acceptably small. To validate this assumption, an analytical treatment is presented in the following sections, resulting in bounds on the maximum relative error due to the three largest perturbations, namely the gravitational perturbation due to the equatorial bulge of the Earth $J_2$, Sun and Moon gravity. The worst-case relative errors are investigated for any position within the geostationary slot defined in Cartesian coordinates in the Hill frame, so that the maximum deviation from the slot center is 37.5 km in radial, and 75 km in tangential and normal direction, corresponding again to a large (±0.1°) geostationary slot.

### THE $J_2$ PERTURBATION

The dominant Earth gravity perturbation is due to its oblateness and is characterized largely by the term $J_2$ and can be expressed in ECI coordinates as [11, p. 408]:

$$\mathbf{a}_{J_2} = -\frac{3}{2}J_2\mu_E\frac{R_E^2}{r^5}\begin{pmatrix}\left(1-5\left(\frac{z}{r}\right)^2\right)x \\ \left(1-5\left(\frac{z}{r}\right)^2\right)y \\ \left(3-5\left(\frac{z}{r}\right)^2\right)z\end{pmatrix}. \tag{2.18}$$

Since $J_2$ is a so-called "zonal" perturbation it is independent of longitude, hence we can choose a nominal position vector on the geostationary orbit around which to expand the perturbing acceleration. Let us choose $\mathbf{r} = (r,0,0)^T$ as the nominal position vector so that

$$\mathbf{a}_{J_2} = -\frac{3}{2}J_2\mu_E\frac{R_E^2}{r^5}\begin{pmatrix} r \\ 0 \\ 0\end{pmatrix}. \tag{2.19}$$

The perturbed vector is $\mathbf{r}_p = \left(r+\Delta x,\Delta y,\Delta z\right)^T$ and for the specific choice of $\mathbf{r}$, $\Delta x$, $\Delta y$ and $\Delta z$ correspond to radial, tangential and normal directions. Approximating $r_p$ using a first order Taylor series expansion with $\Delta x$, $\Delta y$, $\Delta z \ll r$, results in:

$$r_p = \sqrt{(r+\Delta x)^2 + \left(\Delta y\right)^2 + (\Delta z)^2} \approx r + \Delta x \tag{2.20}$$

and equivalently

$$\frac{1}{r_p^5} \approx \frac{1}{r^5} - \frac{5\Delta x}{r^6}. \tag{2.21}$$

Substituting $\mathbf{r}_p$ in Eq. (2.18), using Eq. (2.20-2.21) and keeping only first order terms in $\Delta x$, $\Delta y$ and $\Delta z$ allows to approximate the differential perturbation as:

$$\Delta \mathbf{a}_{J_2} = \mathbf{a}_{J_2}\left(\mathbf{r}_p\right) - \mathbf{a}_{J_2}\left(\mathbf{r}\right) \approx -\frac{3}{2} J_2 \mu_E \frac{R_E^2}{r^5} \begin{pmatrix} -4\Delta x \\ \Delta y \\ \Delta z \end{pmatrix}. \tag{2.22}$$

For evaluation of the relative error, the $\ell_2$-norm is used:

$$\frac{\|\Delta \mathbf{a}_{J_2}\|_2}{\|\mathbf{a}_{J_2}\|_2} \leq \frac{\sqrt{(4\Delta x_{\max})^2 + \left(\Delta y_{\max}\right)^2 + (\Delta z_{\max})^2}}{r} = 0.0044, \tag{2.23}$$

where $\Delta x_{\max} = 37.5$ km and $\Delta y_{\max} = \Delta z_{\max} = 75$ km. Thus the relative error is at all times smaller than 0.44%.

### SUN AND MOON GRAVITY PERTURBATIONS

The approximate relation for a third body gravity perturbation is taken from [1, p. 69] as

$$\mathbf{a}_{3\mathrm{b}} \approx \frac{\mu_{3\mathrm{b}} r}{s^3} \left(-\hat{\mathbf{e}}_r + 3\hat{\mathbf{e}}_s \left(\hat{\mathbf{e}}_s \cdot \hat{\mathbf{e}}_r\right)\right), \tag{2.24}$$

where $\mathbf{s}$ represents the position of the third body in ECI and $\hat{\mathbf{e}}_r$ and $\hat{\mathbf{e}}_s$ are unit vectors pointing towards the satellite and the third body respectively. In the radial, tangential, normal reference frame a perturbed radius vector can be represented by $r_p = r + \delta r$ in radial direction, and $\hat{\mathbf{e}}_{r_p} = \hat{\mathbf{e}}_r + \delta\hat{\mathbf{e}}_r$ in tangential and normal direction. Expanding Eq. (2.24) and using $\delta r \ll r$ results in the differential acceleration

$$\Delta \mathbf{a}_{3\mathrm{b}} \approx \frac{\mu_{3\mathrm{b}} r}{s^3} \left(-\delta\hat{\mathbf{e}}_r + 3\hat{\mathbf{e}}_s \left(\hat{\mathbf{e}}_s \cdot \delta\hat{\mathbf{e}}_r\right)\right) + \frac{\mu_{3\mathrm{b}} \delta r}{s^3} \left(-\hat{\mathbf{e}}_r + 3\hat{\mathbf{e}}_s \left(\hat{\mathbf{e}}_s \cdot \hat{\mathbf{e}}_r\right)\right). \tag{2.25}$$

Evaluating the norm of the differential acceleration results in:

$$\|\Delta \mathbf{a}_{3\mathrm{b}}\|_2 \leq \frac{\mu_{3\mathrm{b}} r}{s^3} \|2\delta\hat{\mathbf{e}}_r\|_2 + 2\frac{\mu_{3\mathrm{b}} \delta r}{s^3}, \tag{2.26}$$

where it was used that:

$$\|\hat{\mathbf{e}}_s\|_2 = 1,$$

$$\| -\delta\hat{\mathbf{e}}_r + 3\hat{\mathbf{e}}_s \left(\hat{\mathbf{e}}_s \cdot \delta\hat{\mathbf{e}}_r\right) \|_2 \leq \|2\hat{\mathbf{e}}_r\|_2 \quad \text{and}$$

$$\| -\hat{\mathbf{e}}_r + 3\hat{\mathbf{e}}_s \left(\hat{\mathbf{e}}_s \cdot \hat{\mathbf{e}}_r\right) \|_2 \leq \|2\hat{\mathbf{e}}_r\|_2 = 2.$$

Substituting $\delta r = \Delta R$ and $\|\delta \hat{\mathbf{e}}_r\|_2 \approx (1/r)\sqrt{(\Delta T)^2 + (\Delta N)^2}$ for the deviations in radial $\Delta R$, tangential $\Delta T$ and normal $\Delta N$ directions allows to evaluate the maximum relative error due to third body gravity:

$$\frac{\|\Delta \mathbf{a}_{3\mathrm{b}}\|_2}{\|\mathbf{a}_{3\mathrm{b}}\|_2} \leq \frac{2\sqrt{(\Delta T_{\mathrm{max}})^2 + (\Delta N_{\mathrm{max}})^2} + 2\Delta R_{\mathrm{max}}}{r} = 0.0068, \tag{2.27}$$

where we used

$$\| -\hat{\mathbf{e}}_r + 3\hat{\mathbf{e}}_s\,(\hat{\mathbf{e}}_s \cdot \hat{\mathbf{e}}_r)\,\|_2 \geq \|\hat{\mathbf{e}}_r\|_2 = 1$$

for the smallest absolute perturbation due to third body gravity. A worst-case error of 0.68% is observed.

### OTHER SIGNIFICANT PERTURBATIONS

Solar radiation pressure and the perturbation due to $J_{22}$ also play a major role in the dynamics of a GEO satellite. The approximate relation for the disturbing acceleration due to SRP is given by [1, p.79]:

$$\mathbf{a}_{\mathrm{srp}} = -P_{\mathrm{sun}} C_R \frac{A}{m} \frac{\mathbf{r}_{\mathrm{sun}}}{r_{\mathrm{sun}}^3} \mathrm{AU}^2. \tag{2.28}$$

This equation does not depend on the position of the satellite and thus no (significant) differential perturbations are expected.

The perturbing acceleration due to $J_{22}$ varies slowly with longitude, see e.g. [12], and the differential acceleration between arbitrary points within the same geostationary slot is small (we found a worst-case difference in acceleration of $4 \cdot 10^{-8}$ m/s$^2$ for a ±0.1° slot). Note that in contrast to the other perturbations, a bound on the relative acceleration $\|\Delta \mathbf{a}_{J_{22}}\|_2 / \|\mathbf{a}_{J_{22}}\|_2$ is not very informative, since the absolute perturbing acceleration due to $J_{22}$ vanishes at the stable points 75.1°E and 105.3°W, and unstable points 11.5°W and 161.9°E, respectively [8, p.72]. In [8, p.73] it is further stated that accelerations due to tesseral gravity terms, including $J_{22}$, within a 1° longitude band can be assumed constant, whereas we use a band of only ±0.1°.

### FURTHER CONSIDERATIONS

The previous sections presented a worst case analysis of the errors resulting from a negligence of differential perturbations in a geostationary slot with respect to its center. Even under worst-case assumptions the relative error made by evaluating the perturbations at the geostationary slot center is smaller than 0.68%. In reality, the expected time-averaged error is even smaller. The key reason is that small eccentricities and inclinations will cause a periodic motion around the geostationary slot center. Integrating the effect over an orbital period will cancel out most of the differential accelerations. In addition, the satellite is controlled to stay close to the reference position and is not expected to come close to the edge of the slot and certainly will not stay there for a long time.

### 2.3.3. DISCRETIZATION OF DYNAMICS

The optimization-based method that is developed in Chapter 4 requires a discretized form of the dynamics, which is introduced here. This discretization is achieved here by applying the Runge-Kutta fourth order (RK4) scheme [13] to the system in Eq. (2.13), while using a zero-order hold on the control input $\mathbf{u}_c(t)$, matching well to a thruster pulse with constant thrust, i.e. the controls are constant over a discrete interval. The RK4 scheme is applied because it is sufficiently accurate for integrating the dynamics studied in this work and results in a clean discrete system as is shown next. Recall

$$\mathbf{x}_{k+1} = \mathbf{x}_k + \tfrac{1}{6}h\left(k_1 + k_2 + k_3 + k_4\right), \tag{2.29}$$

$$t_{k+1} = t_k + h, \tag{2.30}$$

where $h$ is the stepsize and $_k$ indicates the discrete node. With a zero-order hold on the control input $\mathbf{u}_c$ we obtain:

$$\begin{aligned}
k_1 &= \mathbf{A}\mathbf{x}_k && +\mathbf{B}_{k1}\mathbf{u}_{c,k} + \mathbf{B}_{k1}\mathbf{u}_{d1,k}\\
k_2 &= \mathbf{A}\left(\mathbf{x}_k + \tfrac{h}{2}k_1\right) && +\mathbf{B}_{k2}\mathbf{u}_{c,k} + \mathbf{B}_{k2}\mathbf{u}_{d2,k}\\
k_3 &= \mathbf{A}\left(\mathbf{x}_k + \tfrac{h}{2}k_2\right) && +\mathbf{B}_{k2}\mathbf{u}_{c,k} + \mathbf{B}_{k2}\mathbf{u}_{d2,k}\\
k_4 &= \mathbf{A}\left(\mathbf{x}_k + hk_3\right) && +\mathbf{B}_{k3}\mathbf{u}_{c,k} + \mathbf{B}_{k3}\mathbf{u}_{d3,k},
\end{aligned} \tag{2.31}$$

where

$$\begin{aligned}
\mathbf{B}_{k1} &= \mathbf{B}\left(t_k\right), & \mathbf{u}_{d1,k} &= \mathbf{u}_d\left(t_k\right),\\
\mathbf{B}_{k2} &= \mathbf{B}\left(t_k + \tfrac{h}{2}\right), & \mathbf{u}_{d2,k} &= \mathbf{u}_d\left(t_k + \tfrac{h}{2}\right),\\
\mathbf{B}_{k3} &= \mathbf{B}\left(t_k + h\right), & \mathbf{u}_{d3,k} &= \mathbf{u}_d\left(t_k + h\right).
\end{aligned}$$

Combining these steps results in the discrete update

$$\mathbf{x}_{k+1} = \tilde{\mathbf{A}}\mathbf{x}_k + \tilde{\mathbf{B}}_k\mathbf{u}_k + \tilde{\mathbf{d}}_k, \tag{2.32}$$

which is an affine function in state and control. Explicit definition of $\tilde{\mathbf{A}}$, $\tilde{\mathbf{B}}_k$ and $\tilde{\mathbf{d}}_k$ are given below:

$$\tilde{\mathbf{A}} = \frac{1}{24}\mathbf{A}^4h^4 + \frac{1}{6}\mathbf{A}^3h^3 + \frac{1}{2}\mathbf{A}^2h^2 + \mathbf{A}h + \mathbf{I} \tag{2.33}$$

$$\begin{aligned}
\tilde{\mathbf{B}}_k = &\left(\frac{1}{24}\mathbf{A}^3h^4 + \frac{1}{12}\mathbf{A}^2h^3 + \frac{1}{6}\mathbf{A}h^2 + \frac{1}{6}h\mathbf{I}\right)\mathbf{B}_{k1}\\
&+\left(\frac{1}{12}\mathbf{A}^2h^3 + \frac{1}{3}\mathbf{A}h^2 + \frac{2}{3}h\mathbf{I}\right)\mathbf{B}_{k2} + \frac{1}{6}h\mathbf{B}_{k3}
\end{aligned} \tag{2.34}$$

$$\begin{aligned}
\tilde{\mathbf{d}}_k = &\left(\frac{1}{24}\mathbf{A}^3h^4 + \frac{1}{12}\mathbf{A}^2h^3 + \frac{1}{6}\mathbf{A}h^2 + \frac{1}{6}h\mathbf{I}\right)\mathbf{B}_{k1}\mathbf{u}_{d1,k}\\
&+\left(\frac{1}{12}\mathbf{A}^2h^3 + \frac{1}{3}\mathbf{A}h^2 + \frac{2}{3}h\mathbf{I}\right)\mathbf{B}_{k2}\mathbf{u}_{d2,k} + \frac{1}{6}h\mathbf{B}_{k3}\mathbf{u}_{d3,k}.
\end{aligned} \tag{2.35}$$

Matrix **I** is the identity matrix with a size equal to **A**. Repeatedly applying Eq. (2.32) from $k = 1$ to $k = N$ allows to write the $N$ future states as a function of the current state and future control inputs:

$$\mathbf{x}_{\text{tot}} = \mathbf{F}\mathbf{x}_0 + \mathbf{H}\mathbf{u}_{\text{tot}} + \mathbf{J}\mathbf{d}_{\text{tot}}, \tag{2.36}$$

where

$$\mathbf{x}_{\text{tot}} = \begin{pmatrix} \mathbf{x}_1 \\ \mathbf{x}_2 \\ \vdots \\ \mathbf{x}_N \end{pmatrix}, \quad \mathbf{u}_{\text{tot}} = \begin{pmatrix} \mathbf{u}_0 \\ \mathbf{u}_1 \\ \vdots \\ \mathbf{u}_{N-1} \end{pmatrix},$$

$$\mathbf{d}_{\text{tot}} = \begin{pmatrix} \tilde{\mathbf{d}}_0 \\ \tilde{\mathbf{d}}_1 \\ \vdots \\ \tilde{\mathbf{d}}_{N-1} \end{pmatrix}, \quad \mathbf{F} = \begin{pmatrix} \tilde{\mathbf{A}} \\ \tilde{\mathbf{A}}^2 \\ \tilde{\mathbf{A}}^3 \\ \vdots \end{pmatrix},$$

$$\mathbf{H} = \begin{pmatrix} \tilde{\mathbf{B}}_0 & & & \\ \tilde{\mathbf{A}}\tilde{\mathbf{B}}_0 & \tilde{\mathbf{B}}_1 & & \\ \tilde{\mathbf{A}}^2\tilde{\mathbf{B}}_0 & \tilde{\mathbf{A}}\tilde{\mathbf{B}}_1 & \tilde{\mathbf{B}}_2 & \\ \vdots & & & \ddots \end{pmatrix},$$

$$\mathbf{J} = \begin{pmatrix} \mathbf{I} & & & \\ \tilde{\mathbf{A}} & \mathbf{I} & & \\ \tilde{\mathbf{A}}^2 & \tilde{\mathbf{A}} & \mathbf{I} & \\ \vdots & & & \ddots \end{pmatrix}.$$

Hence, all future states $\mathbf{x}_{\text{tot}}$ are written as an affine combination of the current state $\mathbf{x}_0$ (known), the control inputs $\mathbf{u}_{\text{tot}}$ (the controlled accelerations, to be determined by a maneuver planning algorithm) and a term representing the perturbing accelerations $\mathbf{J}\mathbf{d}_{\text{tot}}$ (known).

### 2.3.4. ACCURACY OF DISCRETIZED MODEL

This section investigates the accuracy that is achieved using the discretized dynamics formulation in the absence of controlled accelerations. Since both the input matrix and the disturbing accelerations are approximated at the geostationary slot center, the accuracy depends on the actual trajectory that is flown and to gain quantitative insight, a Monte-Carlo analysis was done. Trajectories inside the geostationary slot with random initial conditions are compared between the discretized linear dynamics approach introduced in this work and a validated propagator (see Section 2.7) including all major perturbations.

In order to use Eq. (2.32) both the **B** matrix and the disturbing accelerations at the geostationary slot center are required at every discrete node. To obtain the disturbing accelerations, the aforementioned propagator was used to obtain the accelerations at all discrete points in time in the interval of interest.

The initial state was determined using random variations of the orbital elements in the same interval as presented in Eq. (2.17), except for $\Delta a$, since a large $\Delta a$ would drift the satellite quickly outside of the geostationary slot and hence $\Delta a \in [-500, 500]$ m. In addition to the aforementioned random initial conditions, the day of the year was also randomly chosen to account for any part of the solar year. The analysis has been done for the particular geostationary slot at 19.2°E corresponding to the reference mission defined in Section 2.6.

The results are presented in terms of Cartesian distances in Figures 2.1 and 2.2 and in terms of orbital elements in Figures 2.3 and 2.4. The discretization timesteps range from several hundred seconds to half a day. The figures show the Root-Mean-Square (RMS) and Worst-Case (WC) errors after respectively 1 and 7 days of propagation, for several timesteps. The values are obtained using 2000 Monte-Carlo runs with random initial conditions as specified before.

Several conclusions can be drawn from the figures. The first is that reducing the discretization timestep further than approximately 3000 s will not increase the accuracy of propagation using the discretized linear dynamics formulation. Secondly, the errors that are introduced through the simplifying assumptions discussed in Section 2.3 are clearly visible, but acceptably small for station-keeping purposes, even if used in an open-loop control setting. Realistic uncertainties after one week of propagation as a result of orbit determination errors only are in the order of 400 m, 4000 m and 1800 m in respectively radial, tangential and normal directions [14]. Including also maneuver errors will significantly increase these values and hence, even the worst-case modeling errors observed only have a small impact on the total error budget. Thirdly, for discretization timesteps below 3000 s, the error grows roughly linear over time, i.e. the error after 7 days of propagation is roughly 7 times the error after one day (this was confirmed for a range of errors between 0 and 7 days).

## 2.4. MEAN AND OSCULATING ORBITAL ELEMENTS

The synchronous elements, with the exception of $\Delta L$, are integration constants in the Keplerian two-body problem [15]. In the absence of controlled and disturbing accelerations, the orbital elements $\left(\Delta n,\ e_x,\ e_y,\ i_x,\ i_y\right)^T$ are thus constants, while $\Delta L$ is changing at a constant rate of $\Delta n$. In the presence of disturbing accelerations the orbital elements vary in time. By integrating Eqs. (2.7) with perturbing accelerations as inputs we obtain the orbital element variations. The orbital element variations can be separated into short-term periodic variations, long-term periodic variations and secular variations. Station-keeping of a geostationary satellite generally requires "maintaining the satellite inside the geostationary slot" for a single satellite, or "maintaining the satellites inside the geostationary slot while maintaining a minimum separation distance with respect to other satellites" in case of collocation. A minimization of propellant consumption is always (one of) the major objectives of the guidance and control strategy. Therefore, it is generally desirable to compensate only for the effects of secular variations (unless the periodic effects are so large that other constraints are violated, e.g. the geostationary slot boundaries). Since an accurate orbit determination gives us the satellites' osculating

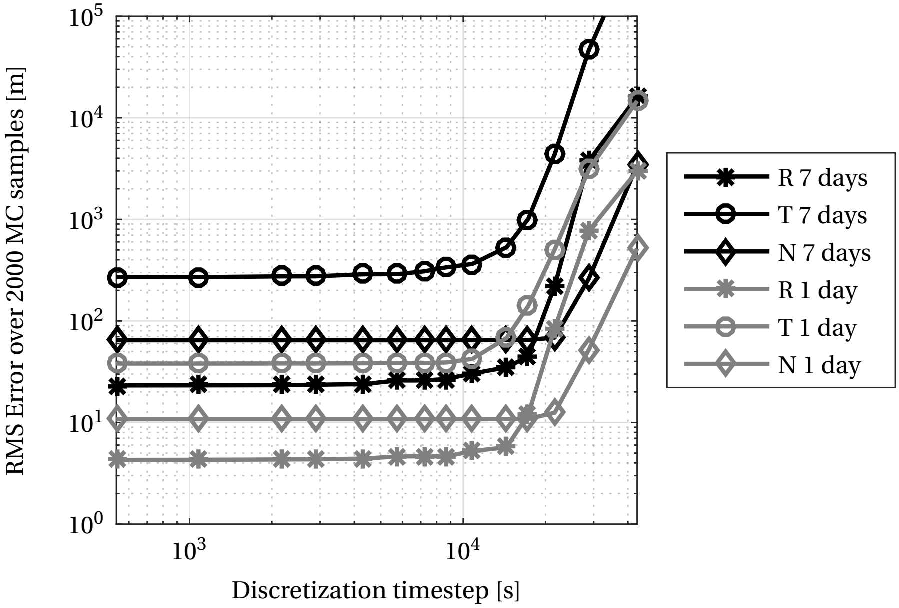

Figure 2.1: RMS error in RTN frame after 1 and 7 days of propagation as a function of discretization timestep

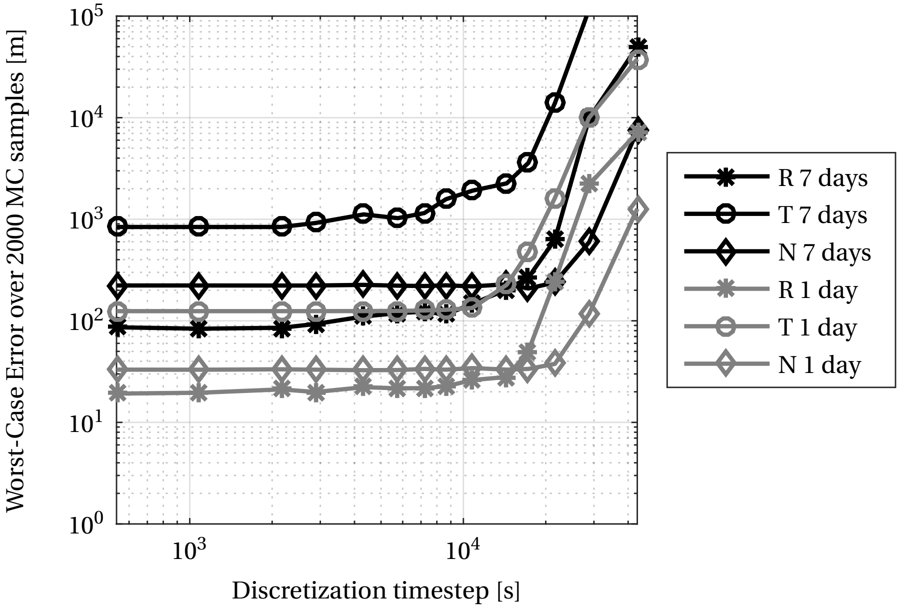

Figure 2.2: Worst-Case error in RTN frame after 1 and 7 days of propagation as a function of discretization timestep

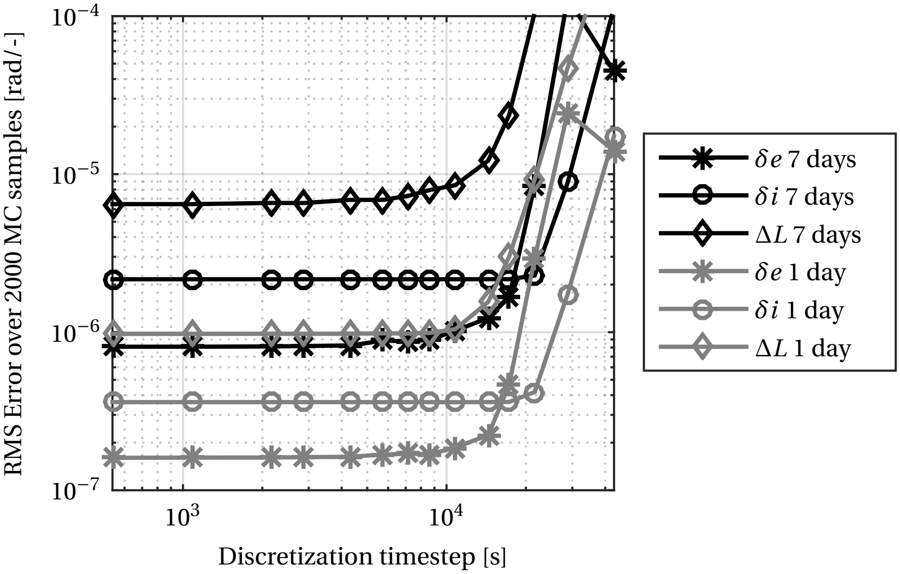

Figure 2.3: RMS error after 1 and 7 days of propagation as a function of discretization timestep

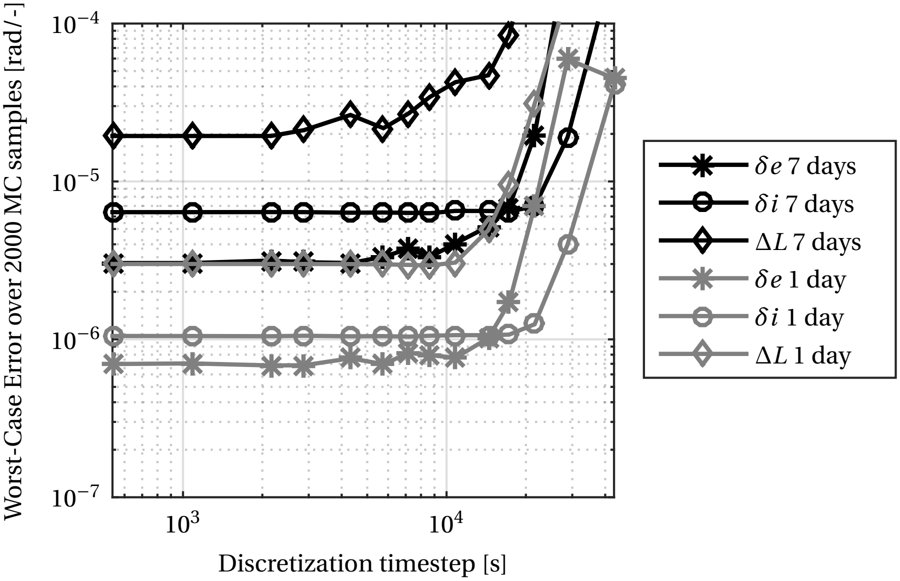

Figure 2.4: Worst-Case error after 1 and 7 days of propagation as a function of discretization timestep

state (i.e. equivalent to the instantaneous (osculating) orbital elements, including also the periodic variations), and since guidance strategies for geostationary satellite station-keeping might be more efficiently defined in terms of mean orbital elements (i.e. the orbital elements with (some) periodic variations removed), a method is required to convert between mean and osculating orbital elements.

The usual approach is to define the mean orbital elements as orbital elements that are averaged over some period. The most common averaging period is one orbital period $T$, resulting in the following definition of mean orbital elements:

$$\mathbf{oe}^{\mathrm{m}}(t) = \frac{1}{T}\int_{t-T/2}^{t+T/2} \mathbf{oe}(\tau)\,\mathrm{d}\tau. \tag{2.37}$$

Using this equation for averaging removes only periodic variations with one orbital period. By choosing a longer averaging time, periodic variations with longer periods can be removed as well.

We identify the periodic variations that we wish to remove and motivate this with a qualitative argument regarding the orbital element variations due to perturbing accelerations in the RTN reference frame. The impact of a perturbing acceleration on the orbital elements can be seen from Eq. (2.7). Since an ideal geostationary satellite is stationary with respect to a certain position on the Earth, the perturbing accelerations due to the geopotential are approximately constant (as long as the satellite is controlled to stay within a predefined geostationary slot). Looking at the terms in **B** in Eq. (2.11) such constant accelerations cause only periodic effects with orbital period on the eccentricity and inclination vectors, while the effect on the mean orbital motion and mean longitude difference are of secular nature and hence can be excluded from the transformation between mean and osculating elements. The perturbation due to solar radiation pressure has its main effect on the eccentricity vector; the eccentricity vector traces out an approximate circle over the course of one year with the satellite's relative perigee pointing in the direction of the Sun (relative perigee here refers to the perigee relative to the center of the circle that is traced out). This natural eccentricity circle is usually so large that it would result in violations of the geostationary slot boundaries, hence the effects of this perturbation need to be compensated by the control strategy. Thus, we should exclude this perturbation from the conversion between mean and osculating orbital elements. The two remaining dominant perturbations are due to Sun and Moon gravity. These perturbations have both short term periodic effects with orbital period as well as effects with much longer periods. We found that the periodic variations of mean orbital motion difference, eccentricity vector and inclination vector due to luni-solar gravity with periods up to one year are small enough to leave uncontrolled. In terms of mean longitude difference the periodic variations with (half-)yearly period have too large of an effect on the mean longitude difference and these variations need to be controlled, whereas the periodic effect with smaller period can be left uncontrolled.

Table 2.1 provides an overview of the periodic variations that we wish to include in the transformation between mean and osculating orbital elements. We note that in a setup in which mean orbital elements are constrained we should account for the (maximum) magnitude of the mean-to-osculating variation to avoid crossing the geostationary slot boundaries. What remains is to develop a method that approximates these variations as a function of time for a particular geostationary slot.

Table 2.1: Overview of the periodic variations that should be included in the transformation between mean and osculating orbital elements.

|  | **Geopotential** | **SRP** | **Sun/Moon gravity** |
|---|---|---|---|
| **Element** | Periods to include in transformation |  |  |
| $\Delta n$ | None | None | $\leq 1$ year |
| $e_x$ | $T$ | None | $\leq 1$ year |
| $e_y$ | $T$ | None | $\leq 1$ year |
| $i_x$ | $T$ | None | $\leq 1$ year |
| $i_y$ | $T$ | None | $\leq 1$ year |
| $\Delta L$ | None | None | $\leq 1$ month |

In order to do so we implemented Kamel's synchronous satellite ephemeris ([16]), which essentially provides a solution to the equations of motion of a satellite in a geostationary orbit, assuming that the satellite is kept close to some desired location, e.g. a geostationary slot center. Kamel's solution considers the Earth's geopotential, up to 3rd order and degree and luni-solar perturbations. Kamel uses a slightly deviating set of non-singular synchronous elements,

$$\mathbf{oe}_K(t) = \begin{pmatrix} h_1 \\ h_2 \\ e_1 \\ e_2 \\ g_1 \\ g_2 \end{pmatrix} = \begin{pmatrix} \sin i \cos(\Omega) \\ \sin i \sin(\Omega) \\ e \cos(\tilde{\omega}) \\ e \sin(\tilde{\omega}) \\ L_0 + \int_{t_0}^{t} n \mathrm{d}t - \alpha(t) \\ 0.5\left(a/a_{\text{geo}} - 1\right) \end{pmatrix}, \tag{2.38}$$

which we can easily convert to the set of orbital elements used in this work, Eq. (2.6). To analyze the orbital element variations we use the method outlined in [16], while setting the terms in the solution of $g_1$ and $g_2$ arising from Earth gravity perturbations to zero. The resulting variations in the orbital elements are the required variations due to the geopotential with orbital period (eccentricity and inclination vectors only) and the perturbations due to the luni-solar gravity (including also variations with longer periods than the desired ones from Table 2.1), under the assumption that the satellite stays close to the geostationary slot center.

To determine the mean elements from the osculating elements we average the elements over the longest period of the variations that we wish to capture in the transformation according to Table 2.1. Thus for a particular orbital element the integral

$$\mathbf{oe}^{\text{m}}(t) = \frac{1}{P_{\text{av}}} \int_{t-P_{\text{av}}/2}^{t+P_{\text{av}}/2} \mathbf{oe}(\tau)\,\mathrm{d}\tau, \tag{2.39}$$

where $P_{\text{av}}$ is the averaging period (one year for the first five elements and one month for $\Delta L$), can be evaluated to obtain the mean element at Epoch $t$. To obtain the difference between mean and osculating elements we evaluate

$$\mathbf{oe}^{\text{o2m}}(t) = \mathbf{oe}^{\text{osc}}(t) - \mathbf{oe}^{\text{m}}(t) \tag{2.40}$$

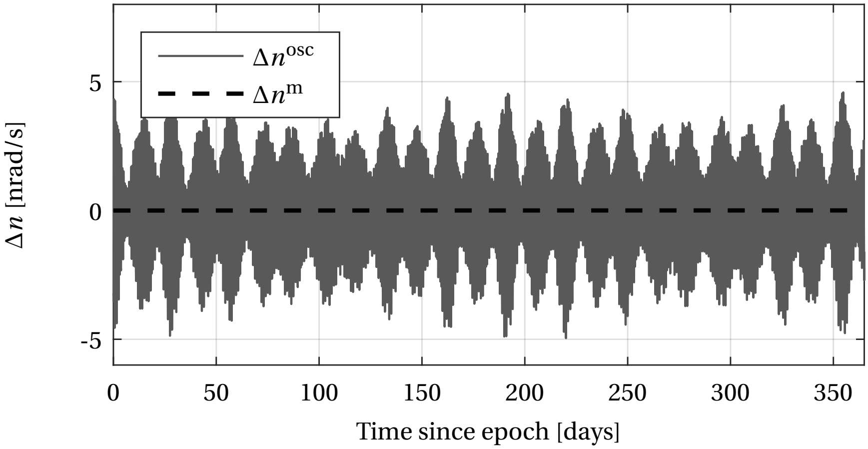

Figure 2.5: Osculating and mean variations of the mean orbital motion based on Kamel's synchronous satellite ephemeris

at epoch $t$. Under Assumptions 2.2 and 2.3 the accelerations (and hence also the variations) at any point in the slot can be approximated by those experienced by a virtual satellite in the center of the slot and hence the difference between mean and osculating elements $\mathbf{oe}^{\mathrm{o2m}}(t)$ can be evaluated ahead of time for any time in the foreseeable future.

Instead of evaluating the integral in Eq. (2.39) we can approach this problem in a simpler manner. We assume that we can approximate the mean variations $oe^{\mathrm{m}}(t)$ using an affine function (at least for the first five elements). To get this approximated mean variation an affine function is fitted though the orbital element variations from Kamel's solution. The difference between the "real" variations and the affine fit is our mean-to-osculating conversion (i.e. a nonlinear function of time for each element, which is, as before, time-dependent but not state dependent). This approach is used for $\Delta n$ and the elements of the eccentricity- and inclination vector. We have performed and compared both approaches, Eq. (2.39) and an affine fit, and although the difference is small we choose to use the affine fit as it leads to a small improvement in propellant consumption (approximately 0.07% for the investigated period of March 2010 to March 2011) at the cost of slightly larger absolute values of $\mathbf{oe}^{\mathrm{o2m}}(t)$.

Figures 2.5, 2.6 and 2.9 show the nonlinear orbital element variation over the course of a year (starting from the zero state), together with a linear fit. Figures 2.7 (and a zoom in Figure 2.8) and 2.10 show the osculating to mean function (for $\Delta n$ this plot was omitted, since it indistinguishable from the $\Delta n^{\mathrm{osc}}$ plot, because for $\Delta n$ the mean is zero (i.e. the mean orbital energy does not change (significantly) over time). The figures were all derived starting on 1 March 2010, 10:00:00 UTC, for 365 days, at a longitude of 19.2°.

For the mean longitude we do not fit a linear function, but an 8th order polynomial function. The key reason for doing this is that we wish to capture the yearly periodic behavior inside the mean variation. If we would not do this, the difference between the natural variations of $\Delta L$ due to Sun and Moon gravity and a mean approximated by an

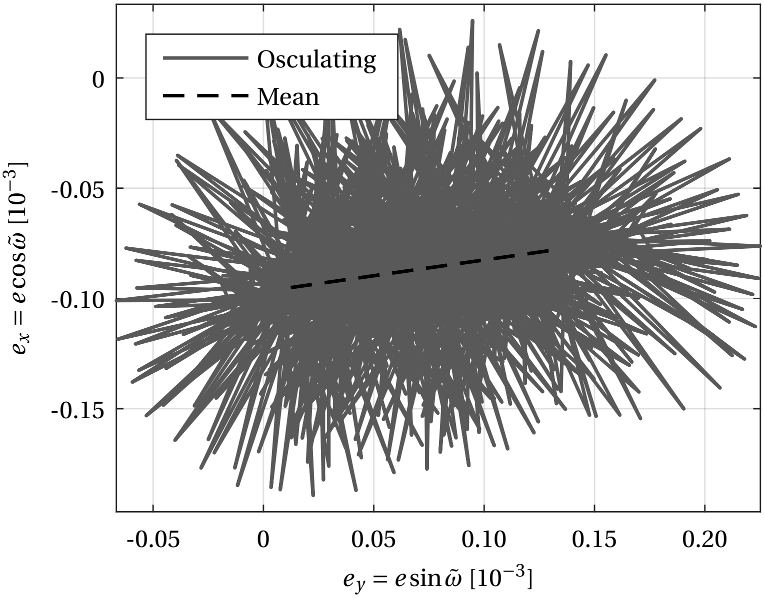

Figure 2.6: Osculating and mean variations of the eccentricity vector based on Kamel's synchronous satellite ephemeris

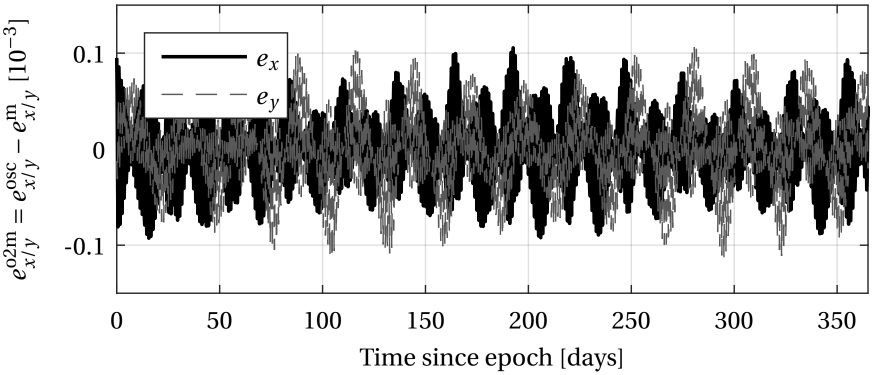

Figure 2.7: Osculating-to-mean variations of the eccentricity vector based on Kamel's synchronous satellite ephemeris

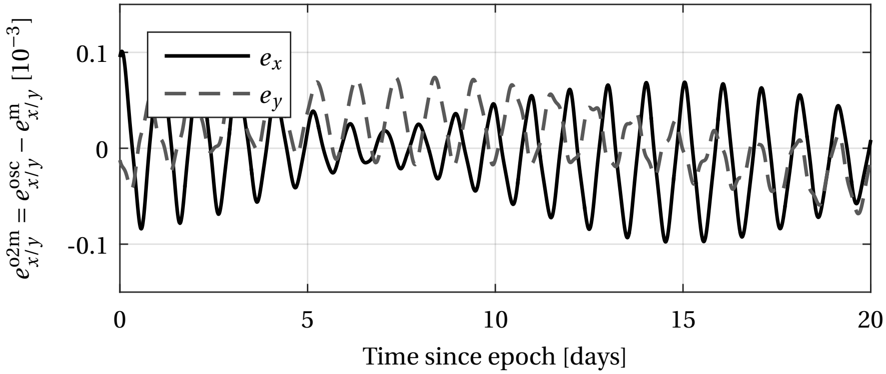

Figure 2.8: Zoom of osculating-to-mean variations of the eccentricity vector based on Kamel's synchronous satellite ephemeris

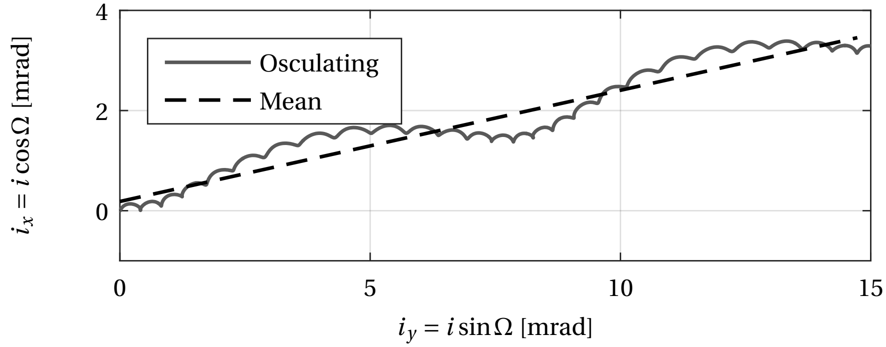

Figure 2.9: Osculating and mean variations of the inclination vector based on Kamel's synchronous satellite ephemeris

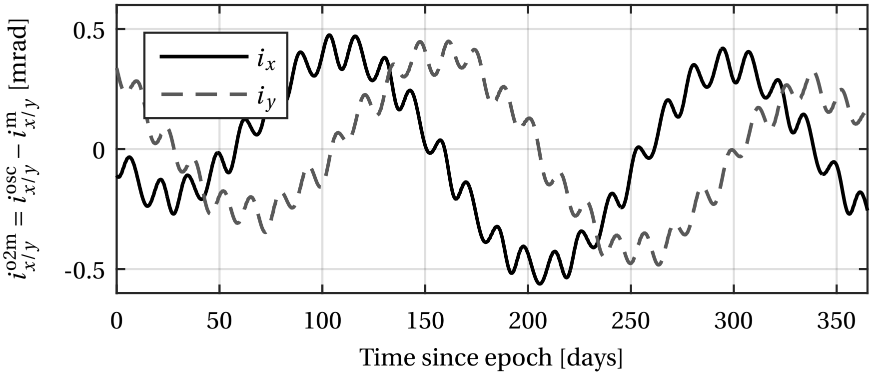

Figure 2.10: Osculating-to-mean variations of the inclination vector based on Kamel's synchronous satellite ephemeris

affine fit would take up most of the longitude window. This approach is equivalent to averaging $\Delta L$ over a period of one month (as indicated in Table 2.1). Furthermore, the longitude corrections are usually obtained as a by-product of eccentricity control and no (significant) increase in propellant consumption is expected because of controlling these yearly variations. The approach for $\Delta L$ is visualized in Figure 2.11 and it is clear from the figure that an affine fit would leave large variations in the transformation between mean to osculating elements.

In an operational scenario the osculating orbital elements at some epoch $t$ are obtained from an orbit determination. The difference between osculating and mean elements $\mathbf{oe}^{\mathrm{o2m}}(t)$ is obtained using the outlined approach. In practice we determine $\mathbf{oe}^{\mathrm{o2m}}(t)$ once over a time period of interest (e.g. one year, or the duration of the mission) and store this function for transforming between mean and osculating elements as a set of piecewise polynomials in a database, which can be queried at any time of interest.

The transformation between mean and osculating elements is reduced to a time-dependent addition (or subtraction) which is identical for all satellites in a geostationary slot because it is determined for the geostationary slot center. This has an advantage for collocation; the relative orbital elements between two satellites formed using mean orbital elements are identical to those formed using osculating orbital elements and we can use either one to evaluate the relative geometry using Eq. (2.43). Table 2.2 provides the maximum mean-to-osculating variations over the course of one year for an exemplary satellite located at 19.2°E.

We used Kamel's solution to the equations of motion to obtain the transformation between mean and osculating elements. Alternatively, we could have integrated Eq. (2.13) with the perturbing accelerations (Earth, Sun and Moon gravity) as experienced by the geostationary slot center (with the terms arising from the Earth gravity perturbations set to zero for respectively $\Delta n$ and $\Delta L$). This method would increase the accuracy of the transformation because the model used to obtain the transformation would be consis-

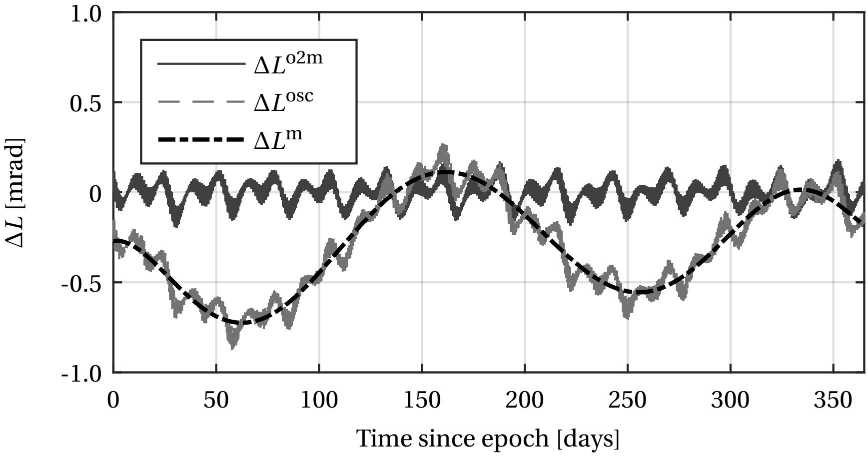

Figure 2.11: Osculating, mean and osculating-to-mean variations of the mean longitude difference based on Kamel's synchronous satellite ephemeris

Table 2.2: Maximum mean to osculation variations of the synchronous orbital elements over one year for a satellite at 19.2°, over the period 1 March 2010 to 1 March 2011.

| **Max. mean to osculating variation** | | |
|---|---|---|
| $\Delta n$ | 4.8 | nrad/s |
| $e_x$ | 0.12 | $10^{-3}$ |
| $e_y$ | 0.12 | $10^{-3}$ |
| $i_x$ | 0.53 | mrad |
| $i_y$ | 0.49 | mrad |
| $\Delta L$ | 0.23 | mrad |

tent with the model underlying our simulations. We choose not to do so and as such introduce a slight error between our simulated "reality" and the variations as expected from Kamel's model in much the same way that a model used in operations would differ from the actual perturbations as experienced by the satellite. We performed a comparison to verify that the variations obtained from Kamel's model match well with our propagator providing an indirect validation that both Kamel's model as well as the propagator were implemented correctly.

## 2.5. RELATIVE DYNAMICS

After having analyzed the single satellite dynamics, we extend the analysis to the relative motion of multiple geostationary satellites. The relative dynamics of geostationary satellites find their application when multiple satellites are collocated in a single slot. The equations we provide describe the position of a follower satellite relative to a leader satellite.

### 2.5.1. RELATIVE ORBITAL ELEMENTS

Blumer, [17], introduces the following relative motion model in spherical coordinates valid for near circular, near equatorial orbits:

$$\begin{array}{lcl} \Delta R & \approx & -\frac{2}{3}\frac{a}{n}\Delta n - a\Delta e_x \cos L - a\Delta e_y \sin L \\ \Delta\lambda & \approx & \Delta L + 2\Delta e_x \sin L - 2\Delta e_y \cos L + \Delta n\,(t - t_0) \\ \Delta\phi & \approx & \Delta i_x \sin L - \Delta i_y \cos L. \\ \Delta\dot{R} & \approx & na\Delta e_x \sin L - na\Delta e_y \cos L \\ \Delta\dot{\lambda} & \approx & \Delta n + 2n\Delta e_x \cos L + 2n\Delta e_y \sin L \\ \Delta\dot{\phi} & \approx & n\Delta i_x \cos L + n\Delta i_y \sin L, \end{array} \tag{2.41}$$

where the relative orbital elements on the right side of the equation, indicated by Δ, are the arithmetic differences between a follower and a leader satellite. The absolute orbital elements refer to the leader's orbital elements (i.e. $a$, $n$ and $L$). These relative spherical coordinates can be mapped into Cartesian relative position and velocity in the RTN-frame attached to the leader satellite as follows:

$$\begin{pmatrix} x \\ y \\ z \\ \dot{x} \\ \dot{y} \\ \dot{z} \end{pmatrix} \approx \begin{pmatrix} \Delta R \\ a\Delta\lambda \\ a\Delta\phi \\ \Delta\dot{R} \\ a\Delta\dot{\lambda} \\ a\Delta\dot{\phi} \end{pmatrix}, \tag{2.42}$$

where $x$, $y$ and $z$ are the relative Cartesian coordinates in the RTN reference frame attached to the leader satellite. Substituting the expressions on the right side of Eq. (2.42) by those on the right side of Eq. (2.41) and setting $t = t_0$, we obtain a linear mapping between relative orbital elements and the relative Cartesian position and velocity in the

RTN reference frame:

$$\begin{pmatrix} x \\ y \\ z \\ \dot{x} \\ \dot{y} \\ \dot{z} \end{pmatrix} \approx a \begin{pmatrix} -\frac{2}{3n} & -cL & -sL & 0 & 0 & 0 \\ 0 & 2sL & -2cL & 0 & 0 & 1 \\ 0 & 0 & 0 & sL & -cL & 0 \\ 0 & nsL & -ncL & 0 & 0 & 0 \\ 1 & 2ncL & 2nsL & 0 & 0 & 0 \\ 0 & 0 & 0 & ncL & nsL & 0 \end{pmatrix} \begin{pmatrix} \Delta n \\ \Delta e_x \\ \Delta e_y \\ \Delta i_x \\ \Delta i_y \\ \Delta L \end{pmatrix}. \tag{2.43}$$

Here $cL$ and $sL$ refer to respectively $\cos L$ and $\sin L$. This mapping is not only valid for relative orbital elements of a leader and a follower satellite, it is also valid for the synchronous orbital elements of a satellite and the center of the geostationary slot. The geostationary slot center is the zero state, thus any absolute synchronous state is also a relative state between a satellite and its slot center.

The mapping is still depending on the leader's state. If required, this dependency can be removed by replacing $a$ by $a_{\text{geo}}$, $n$ by $n_{\text{geo}}$ and $L$ by $\alpha_{\text{geo}}$ for satellites inside a geostationary slot (i.e. the mapping is linear).

We further analyze this mapping to understand how relative orbital elements can be used to ensure safe separation distances between satellites. As in [15] we write relative eccentricity and inclination vectors in polar notation:

$$\Delta\mathbf{e} = \begin{pmatrix} \Delta e_x \\ \Delta e_y \end{pmatrix} = \delta e \begin{pmatrix} \cos\delta\tilde{\omega} \\ \sin\delta\tilde{\omega} \end{pmatrix}, \tag{2.44}$$

$$\Delta\mathbf{i} = \begin{pmatrix} \Delta i_x \\ \Delta i_y \end{pmatrix} = \delta i \begin{pmatrix} \cos\delta\Omega \\ \sin\delta\Omega \end{pmatrix}. \tag{2.45}$$

Note that we intentionally used $\delta e \neq \Delta e$ and $\delta i \neq \Delta i$ to indicate the magnitude and $\delta\tilde{\omega} \neq \Delta\tilde{\omega}$ and $\delta\Omega \neq \Delta\Omega$ to indicate the phase of relative eccentricity and inclination vectors. We further define $\delta M = L - \delta\tilde{\omega}$ as the angle between the (approximate) satellite position vector and the relative eccentricity vector and $\delta\omega = \delta\tilde{\omega} - \delta\Omega$ as the angle between relative eccentricity and inclination vectors. We also define $\delta L = \Delta L_i - \Delta L_j \left(= L_i - L_j = \Delta L\right)$ as the difference in mean longitude between satellite $i$ and $j$. Lastly we can define $\delta a = \Delta a / a$ (non-dimensional) and rewrite $-2/3a/n\Delta n$ as $a\delta a$ allows to write the relative position in RTN coordinates from Eq. (2.43) as:

$$\begin{aligned} x &\approx a\delta a - a\delta e \cos\delta M \\ y &\approx a\delta L + 2a\delta e \sin\delta M \\ z &\approx a\delta i \sin(\delta M + \delta\omega). \end{aligned} \tag{2.46}$$

From these equations we obtain a set of equations in non-dimensional coordinates by scaling each equation by $a\delta e$:

$$\begin{aligned} x/(a\delta e) &\approx \varphi_a - \cos\delta M \\ y/(a\delta e) &\approx \varphi_L + 2\sin\delta M \\ z/(a\delta e) &\approx \varphi_i \sin(\delta M + \delta\omega). \end{aligned} \tag{2.47}$$

where $\varphi_a = \delta a/\delta e$, $\varphi_L = \delta L/\delta e$ and $\varphi_i = \delta i/\delta e$ are defined as rational relative orbital elements. We introduce these elements to support the design of relative motion under geometric constraints in Chapter 3.

### 2.5.2. RELATIVE ORBITAL MOTION

In this section we analyze the instantaneous non-dimensional relative orbit as a function of the rational elements $\varphi_a$, $\varphi_e$, $\varphi_i$ and the phasing angle between relative eccentricity and inclination vectors $\delta\omega$. The instantaneous relative orbit is obtained by evaluating Eqs. (2.47) for fixed $\varphi_a$, $\varphi_e$, $\varphi_i$, $\delta\omega$ in the interval $\delta M \in [0, 2\pi]$.

The instantaneous relative orbit is restricted to lie on the surface of an elliptical cylinder of height $\varphi_i$. The projection of the relative orbit in the radial and tangential plane is a 1:2 ellipse, forming the base of the cylinder. The center of the ellipse is shifted by $\varphi_a$ in radial, and by $\varphi_L$ in tangential-direction. The relative mean anomaly $\delta M$ is the fast variable and determines the position of the satellite in the relative orbit. Under the condition of drift-free motion $\Delta n = 0$ (or energy matching, or semi-major axis matching), and assuming Keplerian motion, the relative orbit is closed. Due to the scaling by $a\delta e$, the non-dimensional relative orbit is fully specified by only four parameters in a Cartesian coordinate system. The center of the relative orbit is given by $\left(\varphi_a,\ \varphi_L,\ 0\right)^T$. The non-dimensional height is specified by $\varphi_i$ and to retrieve the dimensional height $a\delta e$ is required. The orientation of the relative orbital plane is a function of $\varphi_i$ and $\delta\omega$ and can be defined by the relative orbit-normal vector:

$$\delta\mathbf{h}_\varphi = \begin{pmatrix} -2\varphi_i \sin\delta\omega \\ \varphi_i \cos\delta\omega \\ -2 \end{pmatrix} \tag{2.48}$$

To verify that this vector is indeed perpendicular to the relative orbital plane we need to show that its perpendicular to $\delta\mathbf{p} = \left(-\cos\delta M,\ 2\sin\delta M,\ \varphi_i \sin\left(\delta M + \delta\omega\right)\right)^T$ for any choice of $\delta M$. We work out the inner product between these vectors and show that it is equal to zero:

$$\begin{aligned} \delta\mathbf{h}_\varphi \cdot \delta\mathbf{p} &= 2\varphi_i \cos\delta M \sin\delta\omega + 2\varphi_i \sin\delta M \cos\delta\omega - 2\varphi_i \sin\left(\delta M + \delta\omega\right) \\ &= 2\varphi_i \sin\left(\delta M + \delta\omega\right) - 2\varphi_i \sin\left(\delta M + \delta\omega\right) \\ &= 0. \end{aligned} \tag{2.49}$$

In the following, we present a set of figures that demonstrate the effect of variations in these rational elements on the relative orbital plane. The simplest variations are variations in $\varphi_a$ and $\varphi_L$. They simply shift the instantaneous relative orbit in respectively radial and tangential directions. Figures 2.12 and 2.13 demonstrate this in three dimensions, with the bar on the right of the figures indicating the magnitude of the variations in respectively $\varphi_a$ and $\varphi_L$. From Figure 2.13 we observe that by increasing (or decreasing) $\varphi_L$, the relative orbits trace out a tube. The same would be true for $\varphi_a$ if we had chosen a different value for $\delta\omega$ (i.e. $\delta\omega = 0$ is the degenerate case tracing out a line).

Next, we investigate the variation in $\varphi_i$. By increasing or decreasing this rational element, the relative orbit is respectively stretched or squeezed in normal direction. Figure 2.14 shows this stretching and squeezing and also shows the direction of the relative orbit-normal vector $\delta\mathbf{h}_\varphi$. For vanishing $\varphi_i$, this vector points in the direction of the negative normal axis, while for increasingly large $\varphi_i$, the pointing direction approaches the tangential axis.

Lastly, we investigate the effect of varying $\delta\omega$. By varying $\delta\omega$, only the orientation of the relative orbit changes. In terms of the elliptical cylinder introduced earlier, the

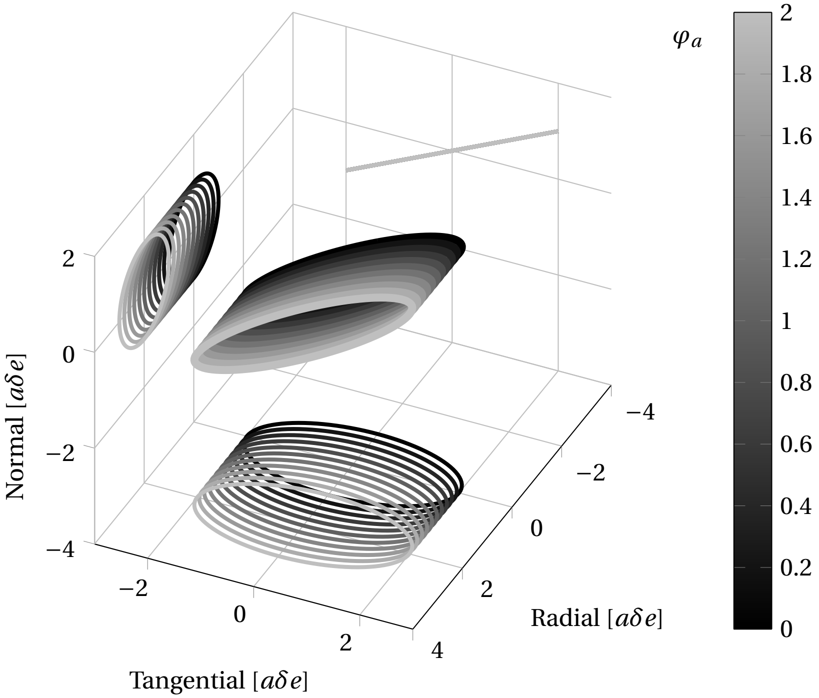

Figure 2.12: Visualization of the effect of varying $\varphi_a$ on the instantaneous relative orbit. The other elements are kept constant: $\delta\omega = 0$, $\varphi_i = 1$ and $\varphi_L = 0$

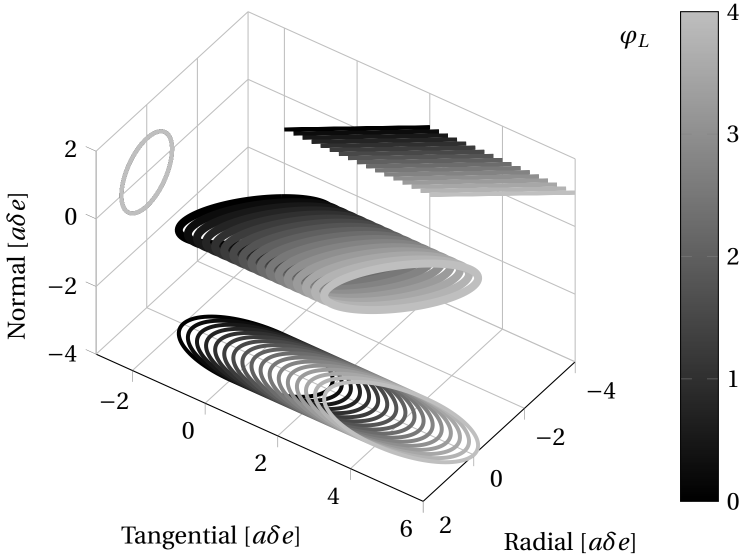

Figure 2.13: Visualization of the effect of varying $\varphi_L$ on the instantaneous relative orbit. The other elements are kept constant: $\delta\omega = 0$, $\varphi_i = 1$ and $\varphi_a = 0$

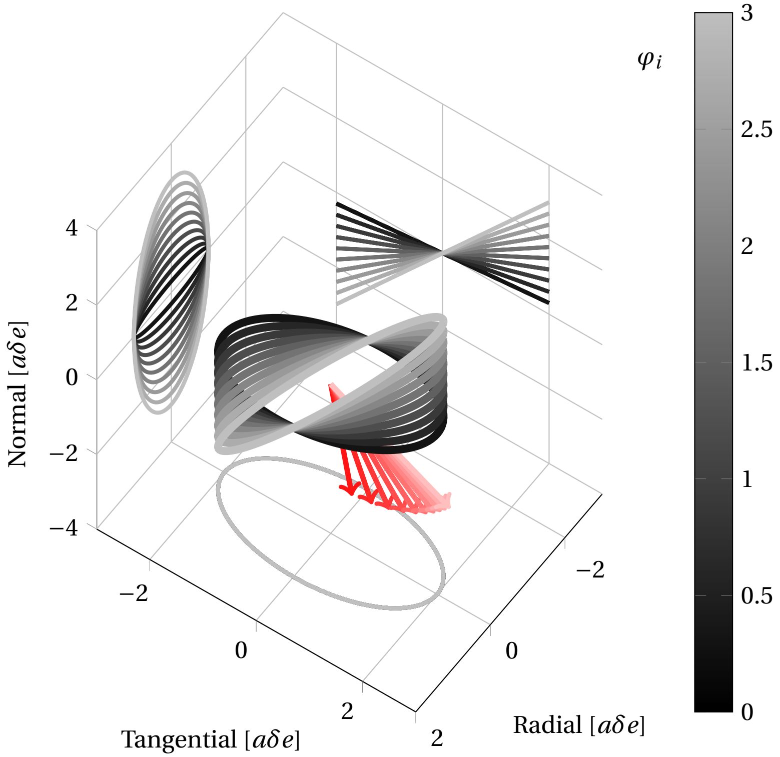

Figure 2.14: Visualization of the effect of varying $\varphi_i$ on the instantaneous relative orbit. The other elements are kept constant: $\delta\omega = 0$, $\varphi_a = 0$ and $\varphi_L = 0$

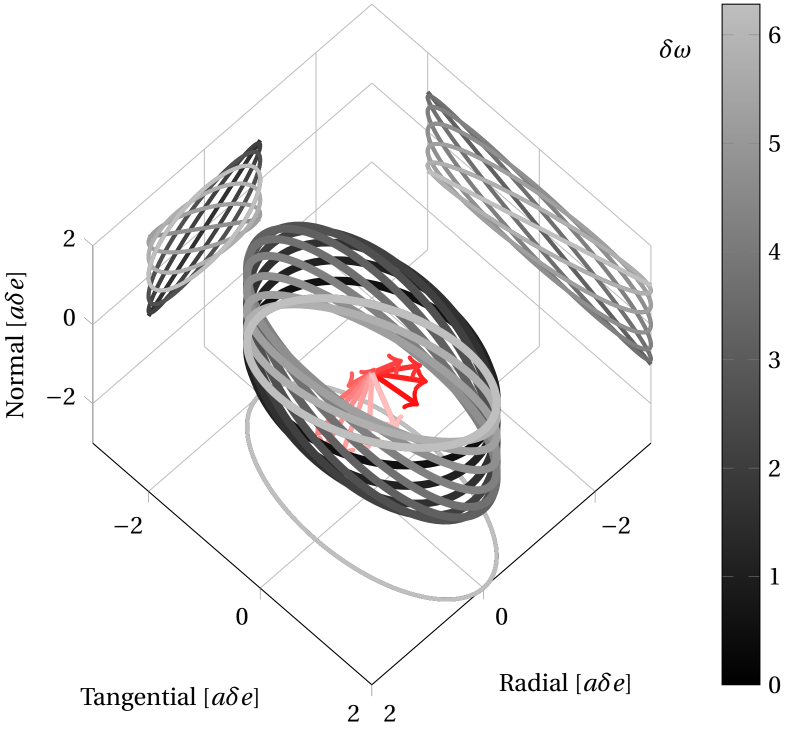

Figure 2.15: Visualization of the effect of varying $\delta\omega$ on the instantaneous relative orbit. The other elements are kept constant: $\varphi_a = 0$, $\varphi_L = 0$ and $\varphi_i = 1$

location where the relative orbit reaches the top of the cylinder makes a complete revolution of the cylinder top boundary for $\delta\omega \in [0,\ 2\pi]$, as visualized in Figure 2.15. The figure also clearly shows the elliptical cylinder itself, with height $\varphi_i$ and its center located at $\left(\varphi_a,\ \varphi_L\right)^T$. As $\delta\omega$ is varied from 0 to $2\pi$ the relative orbit-normal vector traces out the boundary of a 2:1 elliptical cone as expected from Eq. (2.48).

## 2.6. REFERENCE MISSION AND SATELLITE CHARACTERISTICS

In this section we present a number of key characteristics of the reference mission underlying the simulations presented in this work, together with a number of important characteristics of the simulated satellites.

### 2.6.1. MISSION CHARACTERISTICS

Although all methods developed in this work are independent of the particular longitude of the geostationary satellite, we choose to focus on one particular longitude, namely a geostationary slot centered on 19.2°E. This slot was chosen for several reasons;

- it is a slot in which the satellite operator SES currently collocates several satellites, i.e. the slot has a demonstrated relevance,

- the slot has a significant perturbing acceleration due to tesseral gravity perturbations (approximately $5 \cdot 10^{-6}$ m/s),
- the derivative of this perturbing acceleration with respect to longitude is also significant (approximately $-2.2 \cdot 10^{-7}$ m/s$^2$/deg).

As such it is a challenging slot for using the LTV dynamics. All simulations done in this work focus on a geostationary slot centered on this longitude. The simulations all start at the same epoch, namely 1 March 2010 at 10:00:00 (UTC). Focusing on the same slot and the same simulation epoch allows us to easily compare the simulation results.

### 2.6.2. SATELLITE CHARACTERISTICS

We consider a medium to large class geostationary satellite, with a considerable surface area. The satellite is assumed to have an in-orbit mass of 3000 kg, a surface area of 120 m$^2$ and a reflection coefficient $C_R$ of 1.2. This area-to-mass ratio is slightly above average [18] and therefore rather worst-case regarding the SRP perturbation. In one of the simulations we reduce the surface area of one of the satellites in the fleet to 90 m$^2$ so that the satellites in that particular simulation are influenced differently by SRP.

Most common geostationary satellites are three-axis stabilized platforms with an Earth-pointing payload and solar panels on drive mechanisms. This design allows to keep the satellite attitude constant in an Earth-fixed reference frame and thus for a geostationary satellite also in the RTN reference frame. We state the assumption explicitly:

**Assumption 2.4.** The satellite attitude is constant in the radial, tangential, normal reference frame.

This assumption allows us to ignore attitude control in the station-keeping algorithm and ensures a time-invariant sensor geometry in RTN reference frame.

The most relevant satellite characteristics for the maneuver planning are the thruster configuration and characteristics. We use two types of thrusters in the analysis, based on typical chemical and electric thrusters. Since we neglect the mass decrease due to expenditure of propellant, the only relevant characteristics of the thrusters are the thrust force and the minimum on-time. Chemical thrusters are able to produce much larger thrust forces, and the on-time of these thrusters can go down to millisecond level. We assume a 10 N thruster in our simulations and limit the minimum on-time to 0.1 s [19]. Electric propulsion systems typically have a much smaller thrust force. Their key advantage is that they are an order of magnitude more efficient, so that the propellant-to-mass ratio of the satellite can be decreased. When electric thrusters are switched on, it takes a much longer time before reaching a reliable and stable burn, i.e. the transient behavior is much longer. Therefore, the minimum on-time for an electric thruster is usually constrained to a much higher value than for a chemical propulsion system. The typical values used in this work are modeled after the Boeing XIPS 25 cm thruster (79 mN thrust) [20] and SPT-100 thruster (83 mN thrust) [21] and summarized in Table 2.3.

Chemical propulsion thrusters are generally aligned with North, East, South and West directions. We define a reference (REF) configuration for a satellite with a chemical propulsion system in Fig. 2.16. The arrows in the thruster configuration diagrams point in the direction of the force that is exerted on the spacecraft by each thruster (which is opposite to the exhaust plume). Such a thruster configuration ties in well with the dy-

Table 2.3: Thrusters and characteristics used in this work.

| | Chemical thruster | Electric thruster |
|---|---|---|
| Thrust force | 10 N | 80 mN |
| Minimum on-time | 0.1 s | 60 s |

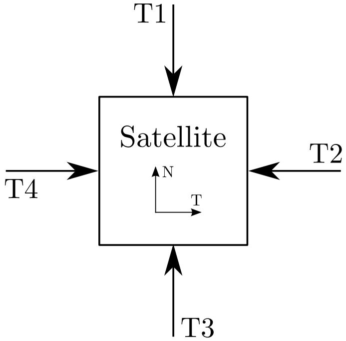

Figure 2.16: Schematic of thruster configuration REF. The arrow points in the direction of the force exerted on the satellite by the thruster. None of the thrust vectors have a radial component.

namics, since the controlled accelerations are defined in radial, tangential and normal direction of the orbital reference frame (n.b. tangential and normal directions correspond to respectively East/West and North/South directions) and the dynamics in the radial and tangential plane are decoupled from the normal dynamics, see Eq. (2.11). Note that on most satellites, the thrusters do not really point towards the center of mass as in these simplified pictures, but instead are offset, such that the orbit control maneuvers can be used to simultaneously manage the satellite's angular momentum. Such configurations are not further investigated in this work; we assume each thrust force vector to pass through the satellite's center of mass and attitude dynamics are ignored.

Satellites employing an electric propulsion system usually have a different layout. North and South sides are home to solar panels, and the plumes originating from an elec-

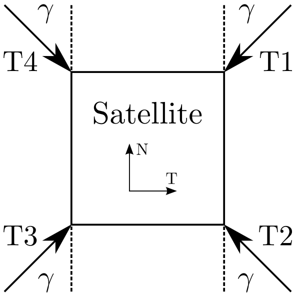

Figure 2.17: Schematic of thruster configuration A. The arrow points in the direction of the force exerted on the satellite by the thruster. None of the thrust vectors have a radial component.

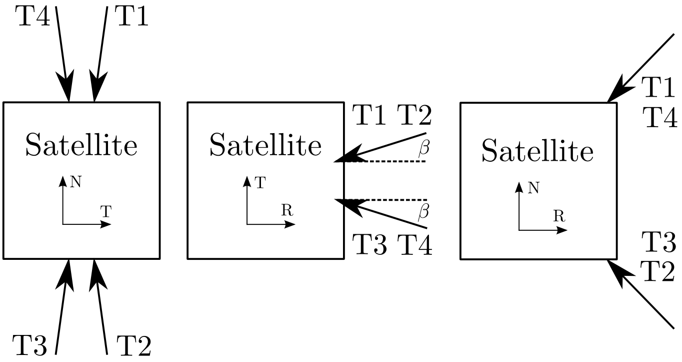

Figure 2.18: Schematic of thruster configuration B with thrust vector projections on TN, RT and RN planes. The arrow points in the direction of the force exerted on the satellite by the thruster.

tric thruster can cause significant degradation of the solar panel. Hence, the thrusters are generally tilted away from the North and South directions to avoid contamination. Furthermore, such configuration reduces the effect of plume impingement, which can cause parasitic thrusts in undesired directions. We define two exemplary electric propulsion thruster configuration with four thrusters. We seek symmetric configurations and describe the orientation of the thrusters by two rotations. For thrusters T1 and T4 we first rotate a vector pointing North over an angle $\gamma \in [0, 90°]$, while for T2 and T3 we rotate a vector pointing South over an angle $\gamma \in [0, 90°]$, both rotations are toward the radial direction. A second rotation is applied as follows; thrusters T1 and T2 are rotated by an angle $\beta \in [0, 90°]$ about the North-axis (towards the East) and T3 and T4 at an angle $\beta \in [0, 90°]$ about the South-axis (towards the West). One configuration (A) used in this work is obtained for $\gamma = 45°$ and $\beta = 90°$, shown in Fig. 2.17. With this choice for $\beta$ and $\gamma$ the thrust vector lies completely in the tangential-normal plane, which is a common choice for geostationary satellites. This configuration is similar as implemented on the Hispasat Advanced Generation 1 mission [22]. Another configuration (B), that is analyzed in this work, is obtained by choosing $\gamma = 45°$ and $\beta = 10°$. Fig. 2.18 shows the projected thrust force vectors in the TN, RT and RN planes. Note that for this configuration the thrusters are all pointing away from the solar panels as well as away from the Earth-facing panel. This configuration is similar to the configuration defined by Anzel in [23].

For thruster configuration A it is possible to calculate maneuvers in EW and NS directions and realize these maneuvers using the thrusters (e.g. a pure North maneuver would be executed by firing thrusters T2 and T3 simultaneously). Alternatively, the thruster configuration can be taken into account in the dynamics formulation by employing a matrix that maps the individual thrust directions to accelerations in the radial, tangential and normal directions. The second approach is used in this work because it enables thruster configurations that cannot realize for instance, pure North or South maneuvers, such as configuration B, and a slight reduction in propellant consumption is possible by directly optimizing the individual thruster firings. Thrust forces are mapped into radial, tangential and normal directions as follows;

$$\mathbf{u} = \Gamma\boldsymbol{\tau}, \tag{2.50}$$

where $\boldsymbol{\tau} = (T_1, T_2, T_3, T_4)^T$ is the vector of individual thrust forces and $\Gamma$ is the thruster configuration matrix. For our definition of $\beta$ and $\gamma$ we obtain:

$$\Gamma = \frac{1}{m}\begin{pmatrix} -\sin\gamma\cos\beta & -\sin\gamma\cos\beta & -\sin\gamma\cos\beta & -\sin\gamma\cos\beta \\ -\sin\gamma\sin\beta & -\sin\gamma\sin\beta & \sin\gamma\sin\beta & \sin\gamma\sin\beta \\ -\cos\gamma & \cos\gamma & \cos\gamma & -\cos\gamma \end{pmatrix} \tag{2.51}$$

This matrix can be used to reformulate Eq. (2.36) to:

$$\mathbf{x}_{\text{tot}} = \mathbf{F}\mathbf{x}_0 + \mathbf{H}\boldsymbol{\Gamma}\boldsymbol{\tau}_{\text{tot}} + \mathbf{J}\mathbf{d}_{\text{tot}}, \tag{2.52}$$

with

$$\boldsymbol{\Gamma} = \begin{pmatrix} \Gamma & & \\ & \Gamma & \\ & & \ddots \end{pmatrix}. \tag{2.53}$$

and $\boldsymbol{\tau}_{\text{tot}} = \left(\boldsymbol{\tau}_0^T, \boldsymbol{\tau}_1^T, \ldots, \boldsymbol{\tau}_{N-1}^T\right)^T$. This formulation relates the thrusts by each thruster to the satellite state, described in synchronous orbital elements.

Note that these thruster configuration matrices can simultaneously be used to capture (the deterministic part of) thruster cross couplings due to, e.g., plume impingement or misalignments.

## 2.7. SIMULATION ENVIRONMENT

Simulations are used to analyze the guidance and control strategies for station-keeping and collocation that are developed in the next chapters. This section provides a short overview of the simulation environment and the models that were implemented. The actual simulation results follow in later chapters, after introducing the guidance and control methods.

The simulations are carried out using Matlab. The simulation architecture resembles that of the control loop depicted in Figure 2.19. The core of the simulator is the plant model, which is essentially a propagator that was developed and validated in the frame of this research. The propagator numerically integrates the equations of motion, Eq. (2.1) with perturbing accelerations from Eqs. (2.2), (2.3) and (2.4). This is generally referred to as Cowell's method. We are using the classic 4th order Runge-Kutta method for the numerical integration with a 108 s timestep. An investigation revealed that this timestep resulted in relative errors of less than 1 m for a propagation horizon of 7 days. Note that 108 s has the convenience that exactly 800 timesteps fit inside a single day. The propagator includes Earth gravity perturbations up to 10th order and degree. The implemented model is the 2008 Earth Gravity Model [24]. Further perturbations are those due the Sun and Moon gravity with analytic models for the position of Sun and Moon according to [1], as well as solar radiation pressure, including the effect of eclipses. Hence

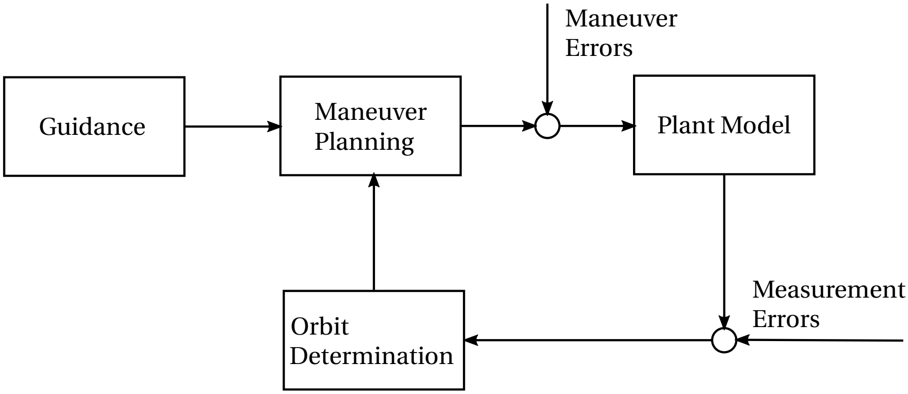

Figure 2.19: High level simulation architecture

the dominant perturbations in a geostationary orbit are included. To increase the computational speed we have auto-coded the propagator to C, compiled it into a mex function, which we then call from Matlab. The propagator properly deals with discontinuous events caused by thruster firings, by temporarily adjusting the integration step-size.

Following the control loop in Figure 2.19 in clockwise direction, the next building block is a module for orbit determination. In an operational scenario, this is where measurements are used to determine the satellite's orbit. These measurements are typically originating from one or two ground stations making angular measurements of the satellite's position (i.e. they determine the satellite's azimuth and elevation with respect to the station) and/or range and range-rate measurements. These measurements are then used to determine an orbit that fits the measurements. To achieve this fitting, the measurements are modeled and the orbit determination process attempts to determine an initial state and a set of parameters such that the difference between the modeled and actual measurements is minimized, usually in a (weighted) least-squares sense. An alternative source of measurements, or even an orbit determination solution, is a GNSS receiver. Such receivers are nowadays standard on LEO satellites, and are slowly being applied to geostationary satellites [25], [26]. The reason for this delayed application is that it is much more challenging to track GNSS signals and reliably determine the satellite state from GNSS measurements in GEO. The GNSS satellites are pointing their antennas (which are highly directional) towards the Earth, and since geostationary satel-

Table 2.4: Overview of perturbations included in the simulations. The models were implemented based on [1].

| **Perturbation** | **Implementation** |
|---|---|
| Geopotential | 10th order and degree |
| Sun gravity | Analytic model |
| Moon gravity | Analytic model |
| SRP | Analytic model |

lites are in a higher orbit than these GNSS satellites, they can only receive the signals that “just” miss the Earth (at least for the main lobes of the signals). This significantly reduces the number of satellites that are visible from GEO. Furthermore, since the signal strength decreases with the square of the distance, the signals are much weaker in GEO than in LEO. Lastly, the signals are all coming from within a small cone (as see from the GEO satellite), resulting in a significantly less beneficial observation geometry than in LEO (but typically better than using ground station tracking measurements). These factors make it much more difficult to perform an orbit determination from GNSS satellites in GEO and explain the reduced acceptance compared to LEO satellites. GNSS receivers for GEO satellites are nevertheless an important development that may pave the way for more automatic or autonomous station-keeping strategies. Since we focused our efforts on the guidance and control blocks, the orbit determination module is basically an empty module and we assume that state measurements (inertial position and velocity) are available in the maneuver planning module (albeit with an uncertainty characterized by a covariance matrix as discussed in Section 2.8).

Apart from the orbit determination module, the guidance module provides inputs to the maneuver planning. This guidance module is one of the key focal points in this work. We treat the problem of station-keeping of a geostationary satellite, or a fleet of satellites, using relative orbital elements. The guidance module is then the place where the “desired” relative orbital elements are determined (either in terms of mean or osculating orbital elements), together with their tolerance windows. It is also the place where the duration of the maneuver cycle is determined, and where constraints on the maneuvers are formulated. Examples are to exclude maneuvers on the $7^{\text{th}}$ day of the maneuver cycle, or to avoid maneuvers during eclipses or if maneuvers are executed according to a schedule, this is the place to formulate the schedule. In summary, it is the place where the state and control constraints are defined.

Both the guidance module and the orbit determination module provide inputs to the maneuver planning module. This module contains the algorithm(s) that are used to calculate the actual maneuvers, whether based on the solution of an optimization problem, or on a set of analytical equations. In the case of a maneuver plan resulting from an optimization problem, we usually obtain (as a by-product) also the predicted satellite trajectory. In case of collocation of a fleet of satellites, the predicted trajectory of one satellite (e.g. the leader satellite) can be used as in input to the maneuver planning module of another satellite (e.g. a follower satellite). The output of the maneuver planning module is a maneuver plan. Before arriving at a maneuver plan, there is usually a processing step that takes either the analytically calculated $\Delta V$’s in RTN directions, or a solution of an optimization problem and transforms this input into a maneuver plan. In our simulations such a maneuver plan basically states the start-time and end-time of each thruster firing, the thruster that executes the firing and the magnitude of the thrust. Before transferring the plan to the propagator, maneuver errors are included and a second processing takes place that transforms the maneuver plan into a set of accelerations, together with start- and end-times.

The maneuver plan (including errors) arrives at the plant and is used as an input to the propagator to simulate the motion of the satellite over the propagation horizon (usually the duration of a maneuver cycle), before the process starts again.

In Chapters 3 to 5 we will discuss the guidance and maneuver planning modules in more detail.

## 2.8. MODELING OF ERRORS

Comparing real-world data to simulated data will invariably result in differences. These differences can enter the system, e.g., through erroneous measurements, deviations from planned and actual actuation or from differences between the real world and the models used to describe the real world. Not considering the presence of sensor errors, actuator errors and modeling errors can invalidate results, or depict the performance of certain methods too optimistic. Hence, to validate the ideas and methods developed in this work, we introduce errors into the simulations to evaluate the performance and robustness of the methods. We identified the following dominant errors sources:

- Thrust force errors, both magnitude and direction,
- Orbit determination errors,
- Errors due to mismodeling of the SRP perturbation.

We discuss each of these errors briefly and present the set of simple models that were used to model these errors.

### THRUST FORCE ERRORS

An error in the magnitude of the thrust force is modeled as a constant error per thruster firing (i.e. the error has no dynamics of its own) and we implement a thrust force error as multiplicative error:

$$\tau = \tau_{\text{nom}} \left(1 + \Delta_\tau\right), \quad \text{with} \quad \Delta_\tau = \mathcal{N}\left(0, \sigma_\tau\right), \tag{2.54}$$

in which $\tau_{\text{nom}}$ is the nominal magnitude of the thrust force and $\Delta_\tau$ is a normally distributed random variable with zero mean and standard deviation $\sigma_\tau$. We assume that all thruster firings are independent events (both multiple firings of the same thruster and firings of different thrusters), since systematic errors can be minimized through a calibration as part of routine operations. Thrust magnitude errors are implemented by generating a random variable with the distribution of $\Delta_\tau$ for each thruster firing in a maneuver plan and adding it (in the multiplicative sense of Eq. (2.54)) to the nominal thrust force. The thrust magnitude errors are generated from a standard distribution with $\sigma_\tau = 0.0167$, such that we have $3\sigma$ errors of 5% in thrust force magnitude. This value is conservative, [27] and [28] report an impulse bit standard deviation well under 1% for thruster firings exceeding 0.1 s in duration and a common value for electric propulsion systems is 0.5% $1\sigma$ ([29]).

A thrust direction error is implemented by generating a random vector on the unit sphere, and rotating the nominal thrust vector by an angle about this unit vector. The random unit vector is defined by two angles, the azimuth $\theta$ and the polar angle $\phi_p$ in spherical coordinates. These angles are formed using two random variables with uniform random distribution in the interval $[0,\ 1]$, $u$ and $v$ [30] such that:

$$\theta = 2\pi u \tag{2.55}$$

and

$$\phi_p = \cos^{-1}\left(2v - 1\right) \tag{2.56}$$

The nominal thrust force vector is then rotated about the unit vector

$$\mathbf{w} = \left(\cos\theta\sin\phi_p,\ \sin\theta\sin\phi_p,\ \cos\phi_p\right)^T \tag{2.57}$$

over an angle $\alpha$ representing the magnitude of the attitude uncertainty with $\alpha = \mathcal{N}(0, \sigma_\alpha)$, which is achieved using the rotation matrix

$$\mathbf{C} = \mathbf{I} + \boldsymbol{\Omega}\sin\alpha + \boldsymbol{\Omega}^2(1-\cos\alpha), \tag{2.58}$$

where $\mathbf{I}$ is the identity matrix and $\boldsymbol{\Omega}$ is the skew-symmetric matrix associated to $\mathbf{w}$:

$$\boldsymbol{\Omega} = \begin{pmatrix} 0 & -\cos\phi_p & \sin\theta\sin\phi_p \\ \cos\phi_p & 0 & -\cos\theta\sin\phi_p \\ -\sin\theta\sin\phi_p & \cos\theta\sin\phi_p & 0 \end{pmatrix}. \tag{2.59}$$

The errors in thrust direction are also considered statistically independent between thruster firings and applied separately for each thruster firing in a maneuver plan. Systematic off-pointing or misalignments and deterministic cross-couplings are assumed to be identified as part of routine operations and included in the thruster configuration matrix. The remaining errors are due to satellite attitude errors and stochastic variations in the thrust direction between consecutive firings. These remaining uncertainties are dependent on the characteristics of the attitude and orbit control system and the propulsion system. In this work we generate the thrust direction errors using a $\sigma_\alpha$ of 0.5°.

### ORBIT DETERMINATION ERRORS

Whenever a maneuver plan is calculated we assume that the satellite state is available from an orbit determination process. Since no orbit determination process is perfect, we perturb that satellite state by generating a 6-dimensional state error from a distribution described by the covariance matrix in Table 2.5. The covariance matrix is based on real data from a single ground station, using Azimuth, Elevation and range measurements over a 24-hour data arc. A more accurate orbit determination could be achieved using two (or more) ground stations and hence the orbit determination accuracy assumed here is conservative. Note that the covariance matrix is defined in the RTN frame and thus we can interpret a 6-dimensional state error generated using this covariance matrix as a relative state in the RTN-frame and this erroneous relative state is transformed back to the inertial frame.

### SOLAR RADIATION PRESSURE MODELING ERRORS

As discussed earlier, uncertainty in the satellite's mass, surface area and orientation of the surface areas with respect to the Sun direction, as well as absorption and reflectivity characteristics cause errors in the modeling of SRP. A rough bound on the uncertainty in modeling SRP can be derived by assuming an uncertainty of 10% in area-to-mass ratio (capturing mass, surface area and orientation of the surface area) and 5% uncertainty in reflectivity characteristics. A worst-case (linear) addition results in a maximum 15% uncertainty in SRP acceleration. The perturbing accelerations due to SRP are dominant in the radial and tangential plane. The direction depends on the time-of-day.

Table 2.5: Covariance matrix of orbit determination error, Radial (R), Tangential (T) and Normal (N) position $[m^2]$ and velocity (V) $[m^2/s^2]$

| | R | T | N | VR | VT | VN |
|---|---|---|---|---|---|---|
| R | 8.83E+00 | -3.39E+01 | -1.57E−02 | 1.88E−06 | -1.18E−03 | -1.86E−05 |
| T | -3.39E+01 | 1.32E+05 | -1.78E+01 | 6.33E−04 | 3.65E−03 | -2.95E−03 |
| N | -1.57E−02 | -1.78E+01 | 4.24E+02 | -1.19E−05 | 3.65E−06 | -9.40E−05 |
| VR | 1.88E−06 | 6.33E−04 | -1.19E−05 | 3.22E−08 | -2.00E−10 | -1.30E−09 |
| VT | -1.18E−03 | 3.65E−03 | 3.65E−06 | -2.00E−10 | 1.61E−07 | 1.90E−09 |
| VN | -1.86E−05 | -2.95E−03 | -9.40E−05 | -1.30E−09 | 1.90E−09 | 2.25E−06 |

### DISCUSSION OF ERRORS

The size and implementation of the various errors that are affecting the performance of the station-keeping and collocation methods have an important impact on the results. Each of the implementations used in this work can be questioned. For example, are the thrust uncertainties really statistically independent? Although this would be the goal of a calibration campaign, it cannot be guaranteed. Is the covariance matrix for generating the state error not time-varying and dependent on the particular state and observation geometry? Yes, but it is questionable whether simulating an orbit determination would really render a more reliable representation of the error since the quality of an orbit determination solution depends on many factors such as:

- the tracking schedule,
- the ground-station equipment used for making the measurements,
- the particular observation geometry, i.e. the location of satellite with respect to ground station(s),
- measurement characteristics,
- and the accuracy of the models used for orbit determination.

Thus, even if we would be able to simulate an orbit determination in line with today's state-of-art, the results would still be valid only for the particular geometry, under chosen assumptions.

We conclude here the following concept; the errors that were implemented in this research are realistic and in most cases conservative. The key idea is that if we can come up with a method that can be used to control a (fleet of) satellite(s) under the errors assumed in these simulations, it has a real chance of succeeding under real-world conditions.

## 2.9. CONCLUDING REMARKS

In this chapter we presented an overview of the modeling approach that was used in this work. The dynamics of a satellite in a geostationary orbit were approximated using a discretized LTV model. The model was derived using two key assumptions, namely, the input matrix and the perturbing accelerations at the center of a geostationary slot provide a good enough approximation for a satellite anywhere else in the slot. The resulting model expressed all states at the discrete nodes as an affine function of the initial state and controlled accelerations (or thrusts) over the discrete intervals. The formulation is directly suitable for use in a convex parameter optimization problem. The accuracy of the model has been investigated both analytically and numerically and although the model is not accurate enough for high accuracy propagation purposes, it suffices for use in operational scenarios to determine station-keeping or collocation maneuvers. In such a scenario orbit determination errors and actuator errors are still an order of magnitude larger than the errors introduced through the LTV approximation of the dynamics.

The approach to transforming between mean and osculating orbital elements relied on the same assumption as the derivation of the LTV model. The periodic variations of the synchronous orbital elements were analyzed assuming that the satellite experienced perturbing accelerations as if it were at the slot center. The periodic variations that were small enough to leave uncontrolled in a station-keeping strategy were identified and only those variations were included in the transformation between mean and osculating orbital elements. Kamel's synchronous satellite ephemeris was used to analyze the variations and to obtain expressions for the transformation between mean and osculating orbital elements, either by averaging over a suitable period or by fitting an affine function through the orbital element variations.

To support the formulation of guidance and control strategies for a fleet of collocated satellites also the relative dynamics have been analyzed. A model was presented that enables a linear transformation between relative (synchronous) orbital elements and Cartesian position and velocity coordinates in the RTN frame. The linear model was further simplified through the introduction of rational relative orbital elements. These rational relative orbital elements are well-suited for the visualization of constraints on relative states treated in the next chapter.

The key mission and satellite characteristics were introduced. An important characteristic is the propulsion system configuration and three different configurations were provided; one classic configuration for use with chemical thrusters and two thruster configurations for an electric propulsion system. The formulation of the dynamics was extended to include the thruster configuration explicitly, relating directly the thrust forces over the discretization intervals to the state at the discrete nodes. Finally, an introduction was provided of the simulation environment and modeling errors that were included in the simulations.

## REFERENCES

[1] O. Montenbruck and E. Gill, *Satellite Orbits* (Springer, 2000).

[2] CCSDS Secretariat, *CCSDS report concerning navigation data-definitions and conventions, 500.0-G-3,* `http://public.ccsds.org/publications/archive/500x0g3.pdf`.

[3] J. H. Lieske, *Precession matrix based on iau/1976/system of astronomical constants,* Astronomy and astrophysics **73**, 282 (1979).

[4] P. K. Seidelmann, *1980 IAU theory of nutation: The final report of the IAU working group on nutation,* Celestial Mechanics **27**, 79 (1982).

[5] R. S. Park, *Solar system dynamics - jpl ephemerides*, `http://ssd.jpl.nasa.gov/?ephemerides`.

[6] M. Eckstein, *Geostationary orbit control considering deterministic cross coupling effects*, in *41$^{st}$ congress of the International Astronautical Federation* (1990) Dresden, IAF Paper 90-326.

[7] D. Brouwer and G. Clemence, *Methods of Celestial Mechanics* (Academic Press, New York, 1961).

[8] E. M. Soop, *Handbook of Geostationary Orbits* (Microcosm and Kluwer, Dordrecht, 1994).

[9] D. Losa, *High vs low thrust station keeping maneuver planning for geostationary satellites*, Ph.D. thesis, École Nationale Supérieure des Mines de Paris (2007).

[10] L. Breger and J. P. How, *Gauss's variational equation-based dynamics and control for formation flying spacecraft*, Journal of guidance, control, and dynamics **30**, 437 (2007).

[11] H. Schaub and J. L. Junkins, *Analytical Mechanics Of Space Systems* (American Institute of Aeronautics and Astronautics (AIAA), 2003).

[12] S. Hardacre, *Control of colocated geostationary satellites*, Ph.D. thesis, Cranfield University (1996).

[13] J. C. Butcher, *Coefficients for the study of runge-kutta integration processes*, Journal of the Australian Mathematical Society **3**, 185 (1963).

[14] P. Wauthier and P. Francken, *The ASTRA co-location strategy for three to six satellites*, Revista Brasileira de Ciencias Mecanicas (ISSN 0100-7386), vol. 16, p. 163-171 **16**, 163 (1994).

[15] D'Amico, S, *Autonomous Formation Flying in Low Earth Orbit*, Ph.D. thesis, Delft University of Technology (2010).

[16] A. Kamel, *Geosynchronous satellite perturbations due to earth's triaxiality and luni-solar effects*, Journal of Guidance, Control, and Dynamics **5**, 189 (1982).

[17] P. Blumer, *A future concept of coordinated orbit control of colocated geostationary satellites*, in *Astrodynamics Conference* (American Institute of Aeronautics and Astronautics (AIAA), 1992).

[18] M. Hooghe, *Typical satellite characteristics*, personal communication.

[19] Airbus, *10 n bipropellant thruster*, `http://www.space-propulsion.com/spacecraft-propulsion/bipropellant-thrusters/10n-thruster.html`.

[20] D. Goebel, M. Martinez-Lavin, T. Bond, and A. King, *Performance of XIPS electric propulsion in on-orbit station keeping of the boeing 702 spacecraft*, in *38th AIAA/ASME/SAE/ASEE Joint Propulsion Conference & Exhibit* (American Institute of Aeronautics and Astronautics (AIAA), 2002).

[21] M. Nakles, W. Hargus, J. Delgado, and R. Corey, *A performance and plume comparison of xenon and krypton propellant on the SPT-100,* in *48th AIAA/ASME/SAE/ASEE Joint Propulsion Conference and Exhibit* (American Institute of Aeronautics and Astronautics (AIAA), 2012).

[22] C. Chasset, P. Bodin, N. Neumann, R. Larsson, and A. Edfors, *Evolution of the AOCS design for EDRS and the satellites of the Small GEO family,* in *Proceedings of the 9th International ESA Conference on Guidance, Navigation and Control* (ESA, 2014).

[23] B. Anzel, *Method for satellite station keeping,* (1991), uS Patent 5,020,746.

[24] N. K. Pavlis, S. A. Holmes, S. C. Kenyon, and J. K. Factor, *The development and evaluation of the earth gravitational model 2008 (EGM2008),* Journal of Geophysical Research: Solid Earth **117**, n/a (2012).

[25] N. Neumann, F. de Bruijn, B. Lubke-Ossenbeck, R. Larsson, S. Zehetmayer, S. Sassen, and P. Krauss, *Use of gnss receivers within the smallgeo product line,* in *proceedings of the 65th International Astronautical Congress* (2014).

[26] J. Chapel, D. Stancliffe, T. Bevacqua, S. Winkler, B. Clapp, T. Rood, D. Gaylor, D. Freesland, and A. Krimchansky, *Guidance, navigation, and control performance for the GOES-r spacecraft,* CEAS Space J (2015), 10.1007/s12567-015-0077-1.

[27] U. Gotzig, G. Schulte, and A. Sowa, *New generation 10n bipropellant MMH/NTO thruster with double seat valve,* in *35th Joint Propulsion Conference and Exhibit* (American Institute of Aeronautics and Astronautics (AIAA), 1999).

[28] M. Fick, T. Dreer, U. Gotzig, G. Schulte, J. Bachmann, F. Lagier, and E. Benoit, *Eadsst's latest bipropellant 10n thruster and 400 n engine: The fully european solution,* in *4th International Spacecraft Propulsion Conference*, Vol. 555 (2004) p. 92.

[29] N. Neumann, *Uncertainty in electric propulsion thrusters,* personal communication.

[30] *Wolfram Mathworld - Sphere Point Picking,* `http://mathworld.wolfram.com/SpherePointPicking.html`, accessed: 2016-05-06.

# 3

# ANALYSIS AND DESIGN OF GUIDANCE UNDER GEOMETRIC CONSTRAINTS

*I have yet to see any problem,*
*however complicated, which,*
*when you looked at it the right way,*
*did not become still more complicated.*

Poul Alderson

*Mystery creates wonder and wonder is the basis of man's desire to understand.*

Neil Armstrong

***Abstract***
*We identify three types of geometric constraints for station-keeping and collocation of geostationary satellites: stay inside the geostationary slot, maintain minimum separation distances and avoid the field of view of sensors. These constraints are analyzed in terms of (relative) orbital elements. An approach for dealing with such constraints is presented and an elaborate example is introduced to further substantiate the methodology.*

The goal of this chapter is to present a control-free analysis and an approach to design a guidance method using relative orbital elements. Both guidance for single satellite station-keeping and collocation of a fleet of satellites are treated. Although several optimization problems are formulated and solved in this chapter, the goal is not to solve the guidance problem by optimization. Instead, a set of tools is provided that allows a mission analyst direct insight into fundamental relations between (rational relative) orbital elements and geometric constraints on the satellite state.

## 3.1. APPROACH AND SCOPE OF ANALYSIS

The focus in this work is on guidance and control of geostationary satellites using *relative orbital elements*. Note that for a single satellite, the synchronous orbital elements are identical to the relative orbital elements between a satellite and the geostationary slot center. For two satellites, the set of relative orbital elements are the arithmetic differences between the satellites' synchronous orbital elements. In the analysis in this chapter we also use the rational relative orbital elements introduced in Section 2.5.1.

The relative orbital elements are used to analyze the following three geometric constraints on geostationary satellites:

1. maintain the satellite(s) inside an assigned geostationary slot,
2. maintain a minimum separation distance between satellites collocated inside the same geostationary slot,
3. avoid the field of view of (conic) sensors on other satellites in the same geostationary slot.

An important observation from these constraints is that the first constraint is convex, while the latter two constraints are non-convex. The non-convex constraints are typically harder to deal with.

In the subsequent analysis and in the design of the guidance method(s) we focus on relative orbital elements. The key idea is to deal with the various constraints by designing a set of time-invariant convex constraints on relative orbital elements that satisfy the geometric constraints for all positions inside the relative orbit (i.e. satisfaction of the constraints for any value of the mean longitude $L$). The key benefit of this approach is that for Keplerian orbits these relative orbital elements (with the exception of $\Delta L$) are constants of motion. By maintaining the orbital elements inside certain (convex) control windows, the satellites will automatically exhibit a natural orbital motion (as opposed to some forced motion). Thus, what we are actually doing is designing a set of relative orbits satisfying the constraints.

In the developments that follow, we first analyze whether a constraint is satisfied by a particular relative state over the course of an orbit. We then extend this analysis to investigate whether a constraint is satisfied if the relative state is constrained within some specific convex tolerance window. The selection of such a tolerance window is then a relative orbit design task (i.e. the definition of these convex tolerance windows on relative orbital elements is essentially equivalent to the design of the guidance method). To support this design activity we use rational orbital elements to create maps showing the level of satisfaction or influence of certain constraints with respect to the rational elements. The key purpose of these maps is to present the design-space in a human understandable format, so that a designer can make an informed selection of convex tolerance windows on the relative orbital elements that ensure satisfaction of the constraints.

## 3.2. GEOSTATIONARY SLOT BOUNDARIES AND THE CONFIGURATION SPACE

Since geostationary satellites are allocated to specific slots, satellite operators are required to maintain their satellites inside the assigned geostationary slots ([1]). A geostationary slot is generally defined in an Earth-fixed reference frame by a longitude window centered at a specific longitude, together with a latitude window (centered at zero latitude). The radius is implicitly defined as the geostationary orbit radius and, although usually omitted, a radius window could be defined centered on this geostationary orbit radius. In Cartesian space a geostationary slot can easily be visualized as a “box” centered on a specific longitude above the equator at the geostationary altitude. The linear mapping in Eq. (2.43) allows us to analyze the space in which relative orbital elements between a satellite and the slot center are allowed to vary such that the geostationary slot boundaries are respected. We present the configuration space relating to a geostationary slot of ±0.1° in longitude and ±0.1° in latitude and approximately half the size in altitude. The size of the geostationary slot is defined by minimum and maximum deviations from the slot center in respectively longitudinal direction ($\Delta\lambda$), latitudinal direction ($\phi$) and radial direction ($\Delta R$), or equivalently, East, North, Up:

$$-\Delta\phi_{\text{min}} = \Delta\phi_{\text{max}} = -\lambda_{\text{min}} = \lambda_{\text{max}} = \frac{0.1^\circ \cdot \pi}{180^\circ} \approx -\frac{2\Delta R_{\text{min}}}{a_{\text{geo}}} = \frac{2\Delta R_{\text{max}}}{a_{\text{geo}}} \tag{3.1}$$

Let $\Delta R$, $\Delta T$ and $\Delta N$ be the deviations from the geostationary slot center in respectively radial, tangential and normal directions. In terms of these deviations, the geostationary slot can be defined in Cartesian space as:

$$-2\Delta R_{\text{min}} = 2\Delta R_{\text{max}} = -\Delta T_{\text{min}} = \Delta T_{\text{max}} = -\Delta N_{\text{min}} = \Delta N_{\text{max}} = 75\ \text{km}. \tag{3.2}$$

Results for a slot with a different size are trivially obtained from the presented results.

We analyze the deviations from the slot center using the synchronous orbital elements. As observed from Eqs. (2.41), in longitudinal direction, the deviations are a function of the mean longitude difference and the magnitude of the relative eccentricity vector:

$$\Delta L_{\text{min}} - 2\delta e_{\text{max}} \leq \Delta\lambda \leq \Delta L_{\text{max}} + 2\delta e_{\text{max}}. \tag{3.3}$$

In latitudinal direction the magnitude of the relative inclination vector is characteristic for the minimum and maximum deviation:

$$-\delta i_{\text{max}} \leq \phi \leq \delta i_{\text{max}}. \tag{3.4}$$

The deviation in radial direction is a function of the magnitude of the relative eccentricity vector and the mean orbital motion difference. The variations are given by:

$$-\delta e_{\max} - \frac{2}{3}\frac{\Delta n_{\max}}{n_{\text{geo}}} \leq \frac{\Delta R}{a_{\text{geo}}} \leq \delta e_{\max} - \frac{2}{3}\frac{\Delta n_{\min}}{n_{\text{geo}}}. \tag{3.5}$$

From Eqs. (3.3) and (3.5) we make two observations; 1. the bounds on $\Delta\lambda$ are much more restrictive than the bounds on $\Delta R$ (in practice, variations of $\left|\Delta n/n_{\text{geo}}\right|$ are one or two orders of magnitude smaller than variations of $|\Delta L|$) and 2. to maintain bounds on $\Delta\lambda$, the size of the configuration space for $\Delta\mathbf{e}$ and $\Delta L$ are traded with respect to each other. Thus we define the tolerable configuration space (i.e. a subset of the configuration space in (relative) orbital elements that satisfies the constraints) for $\Delta\mathbf{e}$ and $\Delta L$ such that bounds on $\Delta\lambda$ are maintained, whereas the tolerable configuration space for $\Delta\mathbf{i}$ is chosen so that bounds on $\phi$ are maintained. Bounds on $\Delta R$ are normally kept as a consequence of the chosen configuration space of $\Delta\mathbf{e}$. However, if necessary, bounds on $\Delta n$ can be defined explicitly such that bounds on $\Delta R$ are guaranteed.

To guarantee that a satellite stays within the geostationary slot it is required to maintain the *osculating* orbital elements within bounds. If osculating-to-mean variations are not actively controlled (i.e. it would cost a lot of propellant to do so, thus controlling these variations is usually omitted) the tolerable configuration space should be reduced by the expected maximum variation between mean and osculating orbital elements $\delta e^{\text{o2m}}_{\max}$. Including this value as margin guarantees that if mean orbital elements are kept inside the reduced configuration space, the geostationary slot boundaries are guaranteed to be respected. Orbit determination, actuation and modeling errors require a further margin, $\delta e^{\text{unc}}_{\max}$, on the configuration space. As discussed above, a trade-off is required between the configuration space for $\Delta\mathbf{e}$ and $\Delta L$. If the variations of $\Delta L$ are contained within a symmetric centered window $[-\Delta L_{\max}, \Delta L_{\max}]$ the eccentricity vector configuration space is bounded by:

$$\delta e_{\max} = \frac{\Delta\lambda_{\max} - \Delta L_{\max}}{2} - \delta e^{\text{o2m}}_{\max} - \delta e^{\text{unc}}_{\max}. \tag{3.6}$$

Similarly, the inclination vector configuration space is bounded by:

$$\delta i_{\max} = \Delta\phi_{\max} - \delta i^{\text{o2m}}_{\max} - \delta i^{\text{unc}}_{\max}. \tag{3.7}$$

Figure 3.1 visualizes these concepts. We normally set bounds on $|\Delta L|_{\max}$ in line with expected longitudinal drift and maneuver cycles duration and eccentricity and inclination are kept within the values calculated from Eqs. (3.6) and (3.7). These bounds will guarantee satisfaction of the constraint to remain within the geostationary slot boundaries.

## 3.3. MINIMUM SEPARATION DISTANCE

Collisions pose a major threat to the safety of space assets. This may be even more true for the satellites in a geostationary orbit; not only because it is the most populated orbit, but also because it is the only Earth orbit that allows satellites to be stationary in an Earth-fixed reference frame, not to mention the satellites themselves being extremely

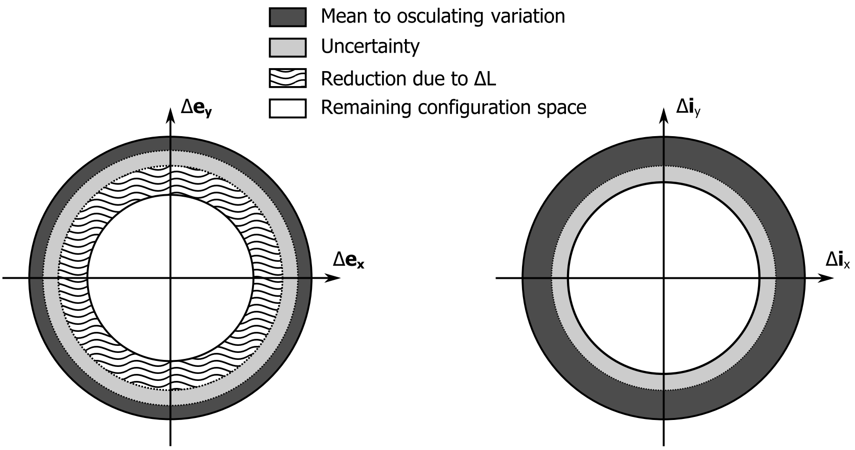

Figure 3.1: Configuration space of (absolute) inclination and eccentricity vectors (not to scale)

valuable assets. A collision could result in many debris particles in the geostationary orbit, which could render (parts of) the GEO-belt unusable, with consequent societal impact. To avoid collisions, satellites are tracked at regular intervals. Close approaches between satellites are analyzed in detail to establish risk parameters such as probability of collision. In the design of the relative motion of collocated satellites, such risks can be mitigated by maintaining a minimum separation distance between satellites occupying the same slot.

### 3.3.1. DEFINITION OF MINIMUM DISTANCE CONSTRAINT

The general definition of the separation distance is the Euclidean distance between two satellites. This separation distance can be defined in Cartesian coordinates or in relative orbital elements as follows (see Eq. (2.46)):

$$\begin{aligned} \rho &= \sqrt{x^2+y^2+z^2} \\ &= \sqrt{(a\delta a - a\delta e\cos\delta M)^2 + (a\delta L + 2a\delta e\sin\delta M)^2 + (a\delta i\sin(\delta M+\delta\omega))^2}. \end{aligned} \tag{3.8}$$

The minimum distance constraint would then be to maintain this separation distance above a certain threshold. In the design of *safe* relative motion between satellites it is however customary to use only the distance in the radial-normal plane and maintain this distance above a certain threshold [2], [3]. There are two factors motivating this; 1.) an orbit prediction is usually less accurate in tangential direction and 2.) in case of an anomaly (e.g. a thruster failure) drift in the tangential direction will be significantly higher than drift in radial or normal direction (n.b. in case of Keplerian motion only the tangential direction will be subject to significant drift). Thus, in order to maintain safe separation distances between satellites it is customary to maintain the separation distance in the radial-normal plane above a certain threshold:

$$\rho_{\mathrm{rn}} = \sqrt{(a\delta a - a\delta e \cos\delta M)^2 + (a\delta i \sin(\delta M + \delta\omega))^2} \geq d_{\min}. \tag{3.9}$$

This is the philosophy followed in this research and Eq. (3.9) is referred to as the "general" minimum distance constraint.

### 3.3.2. ANALYSIS OF MINIMUM DISTANCE

We investigate the minimum separation distance in the radial-normal plane as a function of relative orbital elements.

#### SIMPLIFIED MINIMUM DISTANCE

We begin the analysis under the following simplifying assumption:

**Assumption 3.1.** The satellites have identical semi-major axes: $\delta a = 0$, or alternatively, the relative mean orbital motion is equal to zero: $\Delta n = 0$.

This assumption implies energy matching of the satellites and the relative orbits are closed under the assumption of Keplerian motion. Under Assumption 3.1 the minimum distance is defined as:

$$\rho_{\mathrm{rn}} = \sqrt{(a\delta e \cos\delta M)^2 + (a\delta i \sin(\delta M + \delta\omega))^2} \quad \geq d_{\min}, \tag{3.10}$$

which we define as the "simplified" minimum distance constraint. This simplified minimum separation distance is found by minimizing:

$$\rho_{\mathrm{rn}}^2 = x^2 + z^2 = a^2\delta e^2 \cos^2\delta M + a^2\delta i^2 \sin^2(\delta M + \delta\omega) \tag{3.11}$$

over $\delta M \in [-\pi, \pi)$. Taking the derivative of $\rho_{\mathrm{rn}}^2$ with respect to $\delta M$ and applying some trigonometric identities we obtain:

$$\frac{\mathrm{d}}{\mathrm{d}\delta M}\left(\rho_{\mathrm{rn}}^2\right) = -a^2\delta e^2 \sin 2\delta M + a^2\delta i^2 \sin(2\delta M + 2\delta\omega), \tag{3.12}$$

which can be rewritten to

$$c_1 \sin(2\delta M + c_2), \tag{3.13}$$

where $c_1$ and $c_2$ are constants determined as follows:

$$c_1 = a^2\sqrt{\delta e^4 + \delta i^4 - 2\delta e^2\delta i^2 \cos 2\delta\omega}, \tag{3.14}$$

$$c_2 = \operatorname{atan2}\left(\delta i^2 \sin 2\delta\omega,\ -\delta e^2 + \delta i^2 \cos 2\delta\omega\right). \tag{3.15}$$

The minimum is found by solving:

$$\frac{\mathrm{d}}{\mathrm{d}\delta M}\left(\rho_{\mathrm{rn}}^2\right) = 0, \tag{3.16}$$

which occurs at $\delta M = -c_2/2 + k/2 \cdot \pi$, and hence there are four solutions in the domain of interest, two corresponding to the maximum separation distance, and two corresponding to the minimum separation distance. The symmetry of the relative motion requires us to only examine one of the solutions to find the minimum distance. If we choose $\delta M = -c_2/2$ we can verify ($c_1 > 0$):

$$\frac{\mathrm{d}^2}{\mathrm{d}\delta M^2}\left(\rho_{\mathrm{rn}}^2\right) = 2c_1 \cos\left(2\delta M + c_2\right) > 0, \tag{3.17}$$

hence, the minimum is obtained. The minimum is found by substituting $\delta M = -c_2/2$ in Eq. (3.11) and taking the square root, Eq. (3.22). We now discuss some special cases for $\delta\omega \in (-\pi, \pi]$.

*Case 1:* $\delta\omega = 0 \vee \delta\omega = \pi$, $\delta e = \delta i$

This solution is well known to be:

$$\rho_{\mathrm{rn,min}} = \rho_{\mathrm{rn}} = a\delta e = a\delta i. \tag{3.18}$$

The relative motion is a perfect circle in the radial-normal plane.

*Case 2:* $\delta\omega = 0$, $\delta e \neq \delta i$:

In this case, the motion in the radial-normal plane is elliptical, with semi-axes $a\delta e$ and $a\delta i$

and the minimum separation distance is given by:

$$\rho_{\mathrm{rn,min}} = \min\left(a\delta e, a\delta i\right). \tag{3.19}$$

*Case 3:* $\delta\omega \neq 0$, $\delta e = \delta i$:

Substituting the conditions in Eq. (3.15) we obtain:

$$\begin{aligned} c_2 &= -\tfrac{\pi}{2} + \delta\omega && \text{for } \delta\omega < 0 \\ c_2 &= \tfrac{\pi}{2} + \delta\omega && \text{for } \delta\omega > 0 \end{aligned} \tag{3.20}$$

and substituting $\delta M = -c_2/2$ in Eq. (3.11) we find:

$$\begin{aligned} \rho_{\mathrm{rn,min}} &= a\delta e\sqrt{1 + \sin\delta\omega} && \text{for } \delta\omega < 0 \\ \rho_{\mathrm{rn,min}} &= a\delta e\sqrt{1 - \sin\delta\omega} && \text{for } \delta\omega > 0. \end{aligned} \tag{3.21}$$

*Case 4:* $\delta\omega \neq 0$, $\delta e \neq \delta i$:

The solution to the general case was found previously as:

$$\rho_{\mathrm{rn,min}} = a\sqrt{\delta e^2 \cos^2\left(-\frac{c_2}{2}\right) + \delta i^2 \sin^2\left(-\frac{c_2}{2} - \delta\omega\right)}. \tag{3.22}$$

In [1], another general solution to the same problem was found. Defining

$$B_1 = 0.5\left(\delta e^2 + \delta i^2\right) \quad \text{and} \quad B_2 = -\Delta e_x \Delta i_x - \Delta e_y \Delta i_y \tag{3.23}$$

gives the general solution for the minimum distance:

$$\rho_{\mathrm{rn,min}} = a\sqrt{B_1 - \sqrt{B_1^2 - B_2^2}}, \tag{3.24}$$

which can also be defined completely in terms of the variables $\delta e$, $\delta i$ and $\delta\omega$ if $B_2$ is written as:

$$B_2 = -\Delta\mathbf{e}^T\Delta\mathbf{i} = -\delta e \delta i \cos|\delta\omega|\,. \tag{3.25}$$

We confirmed numerically that Eqs. (3.22) and (3.23) provide identical solutions. The recent work [4] includes the more general solution to the minimum distance problem in the radial-normal plane without requiring Assumption 3.1. In Section 3.3.3 we derive a similar solution using rational orbital elements.

### SIMPLIFIED MINIMUM DISTANCE IN CIRCULAR TOLERANCE WINDOWS

In the previous section we found a nonlinear relation between simplified minimum separation distance and relative orbital elements. In this section we investigate the relation between circular control windows on relative orbital elements and corresponding minimum separation distance, still under Assumption 3.1.

Circular (2-norm bounded) tolerance windows are convenient convex tolerance windows on relative eccentricity and inclination vectors. These tolerance windows are defined by the following sets:

$$S_e(\Delta\mathbf{e}_c, r_e) = \left\{\Delta\mathbf{e} \mid \|\Delta\mathbf{e} - \Delta\mathbf{e}_c\|_2 \le r_e\right\} \tag{3.26}$$

$$S_i(\Delta\mathbf{i}_c, r_i) = \left\{\Delta\mathbf{i} \mid \|\Delta\mathbf{i} - \Delta\mathbf{i}_c\|_2 \le r_i\right\}, \tag{3.27}$$

where $\Delta\mathbf{e}_c$ and $\Delta\mathbf{i}_c$ are the centers of the tolerance windows, and $r_e$ and $r_i$ are the radii of the tolerance windows on respectively $\Delta\mathbf{e}$ and $\Delta\mathbf{i}$.

We investigate the smallest minimum distance for relative eccentricity and inclination vectors constrained inside these circular tolerance windows under Assumption 3.1, which allows us to use the analytic expression for the separation distance found in the previous section. In addition, we impose another assumption:

**Assumption 3.2.** The inner product between relative eccentricity and inclination vectors is positive: $\Delta\mathbf{e}^T\Delta\mathbf{i} > 0$.

This assumption guarantees that the minimum separation distance is larger than zero and limits the analysis to only half of the design space:

$$\begin{gathered} \Delta\mathbf{e}^T\Delta\mathbf{i} = \delta e \delta i \cos|\delta\omega| > 0 \\ \Downarrow \\ \delta e > 0,\ \delta i > 0,\ |\delta\omega| < \pi/2 \\ \Downarrow \\ \rho_{\mathrm{rn,min}} > 0. \end{gathered} \tag{3.28}$$

We now investigate the problem of finding the minimum separation distance in the radial-normal plane, for relative eccentricity and inclination problems constrained inside the 2-norm bounded set centered on $\Delta\mathbf{e}_c$ and $\Delta\mathbf{i}_c$ with norm smaller than or equal to respectively $r_e$ and $r_i$. The resulting problem can be formulated as an optimization problem as follows:

**Problem 3.1.**

$$\begin{array}{ll} \text{minimize} & \rho_{\text{rn,min}} \\ \text{subject to} & \Delta\mathbf{e} \in S_e\left(\Delta\mathbf{e}_c, r_e\right) \\ & \Delta\mathbf{i} \in S_i\left(\Delta\mathbf{i}_c, r_i\right), \end{array}$$

in which the optimization variables are $\Delta\mathbf{e}$ and $\Delta\mathbf{i}$. Note that this optimization problem is not convex (i.e. the cost function is non-convex in the optimization variables). We did not find an analytic solution to this problem, but we do proof that the solution of this optimization problem always lies on the boundary of $S_e$ and $S_i$. This reduces the solution space of the optimization problem to two lines (i.e. the respective boundaries of $S_e$ and $S_i$). Both lines can be parametrized with a single variable allowing a visualization of the solution space. In order to proof that the solution always lies on (a subset of) the boundary (under Assumptions 3.1 and 3.2), it suffices to demonstrate the following three inequalities:

$$\frac{\partial \rho_{\text{rn,min}}}{\partial \delta e} \geq 0, \quad \frac{\partial \rho_{\text{rn,min}}}{\partial \delta i} \geq 0, \quad \frac{\partial \rho_{\text{rn,min}}}{\partial |\delta\omega|} \leq 0. \tag{3.29}$$

Using Eqs. (3.23)-(3.25) we can express:

$$\frac{\partial \rho_{\text{rn,min}}}{\partial \delta e} = \frac{a^2}{2\rho_{\text{rn,min}}}\left(\delta e - \frac{B_1 \delta e^2 - B_2^2}{\delta e\sqrt{B_1^2 - B_2^2}}\right), \tag{3.30}$$

since $a > 0$, $\delta e > 0$ and $\rho_{\text{rn,min}} > 0$ we have:

$$\begin{array}{rcl} \frac{\partial \rho_{\text{rn,min}}}{\partial \delta e} & \geq & 0 \\ & \Uparrow & \\ \delta e - \frac{B_1 \delta e^2 - B_2^2}{\delta e\sqrt{B_1^2 - B_2^2}} & \geq & 0 \\ & \Uparrow & \\ \sqrt{B_1^2 - B_2^2} - B_1 + \delta i^2 \cos^2|\delta\omega| & \geq & 0 \\ & \Uparrow & \\ \sqrt{B_1^2 - B_2^2} & \geq & B_1 - \delta i^2 \cos^2|\delta\omega| \\ & \Uparrow & \\ B_1^2 - B_2^2 & \geq & B_1^2 - 2B_1\delta i^2\cos^2|\delta\omega| + \delta i^4 \cos^4|\delta\omega| \\ & \Uparrow & \\ -B_2^2 & \geq & -B_2^2 - \delta i^4\cos^2|\delta\omega| + \delta i^4\cos^4|\delta\omega| \\ & \Uparrow & \\ 0 & \geq & \cos^4|\delta\omega| - \cos^2|\delta\omega|, \end{array} \tag{3.31}$$

and since $\cos|\delta\omega| \leq 1$ the last inequality is fulfilled, proving the first inequality in Eqs. (3.29). The proof for the second inequality is obtained by interchanging $\delta e$ with $\delta i$ in the above equations. To proof the third inequality we obtain the partial derivative with respect to $|\delta\omega|$:

$$\frac{\partial \rho_{\text{rn,min}}}{\partial |\delta\omega|} = -\frac{a^2 \delta e^2 \delta i^2 \cos|\delta\omega| \sin|\delta\omega|}{2\rho_{\text{rn,min}}\sqrt{B_1^2 - B_2^2}}, \tag{3.32}$$

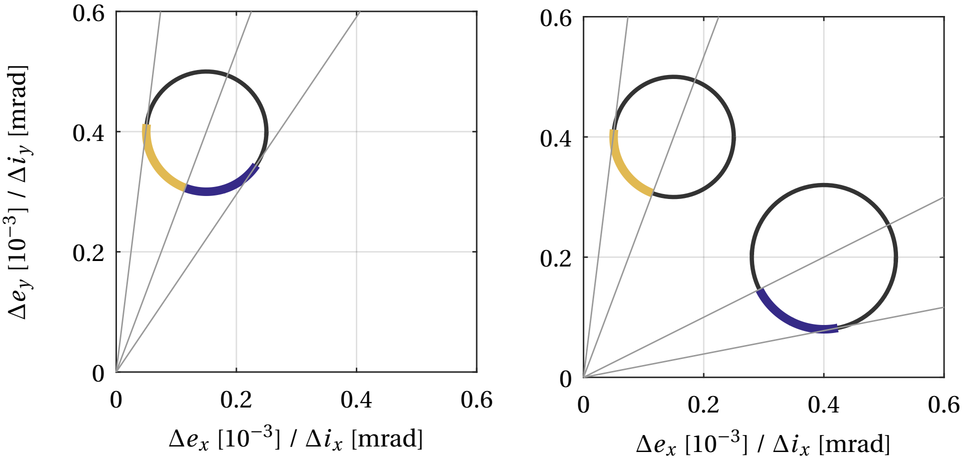

Figure 3.2: Control windows for relative eccentricity and inclination vectors, left: relative eccentricity vector lies within the circle, the inclination vector is arbitrary, right: relative eccentricity vector lies in one circle the relative inclination vector in the other circle.

and since $a > 0$, $\rho_{\text{rn,min}} > 0$ and $\sqrt{B_1^2 - B_2^2} > 0$ we obtain:

$$\frac{\partial \rho_{\text{rn,min}}}{\partial |\delta\omega|} \leq 0 \quad \Leftarrow \quad \cos|\delta\omega| \sin|\delta\omega| \geq 0 \quad \text{for } |\delta\omega| \leq 90^\circ. \tag{3.33}$$

The inequalities in Eqs. (3.29) do not just restrict the solution set to the boundary of the set, but to a specific part of the boundary. This can be seen from Figure 3.2. If we look at the left plot in Figure 3.2 and assume that the eccentricity vector is constrained to lie within the circle, the eccentricity vector that solves Problem 3.1 is restricted to lie on the light (golden) boundary if $\Delta\mathbf{i}$ is on the right-side of the line through the center of the tolerance window of $\Delta\mathbf{e}$ or on the dark (blue) boundary if $\Delta\mathbf{i}$ is on the left-side of the line through the center of the tolerance window. If both $\Delta\mathbf{e}$ and $\Delta\mathbf{i}$ are restricted to a circular window, the values that solve Problem 3.1 lie on respectively the golden and blue boundaries as indicated in the right-side plot of Figure 3.2.

### Particular solutions under restricted conditions

We present an (analytic) solution to Problem 3.1 under the following restriction:

**Assumption 3.3.**

$$\Delta\mathbf{e}_c = \Delta\mathbf{i}_c \quad \text{and} \quad r_e = r_i, \tag{3.34}$$

thus obtaining identical eccentricity and inclination vector control windows. Note that these restrictions have practical relevance since $|\delta\omega_c| = 0$ for the $e/i$-vector separation strategy. From Eq. (3.19) we see that we obtain no increase in the minimum separation distance by making $\delta e$ larger than $\delta i$ or vice versa for $\delta\omega = 0$.

The minimum distance for this particular $\ell_2$-norm bounded eccentricity and inclination vectors can be found by substituting

$$\delta e = \sqrt{r_e^2 + \delta e_c^2 - \sqrt{2} r_e \delta e_c} \quad \text{and} \quad \delta\omega = \sqrt{2}\frac{r_e}{\delta e} \tag{3.35}$$

into Eq. (3.22).

To summarize: for circular tolerance windows on relative eccentricity and inclination vectors we can find the minimum distance by solving Problem 3.1. From the analysis we know that this solution must lie on a subset of the boundary of the tolerance window. Under Assumption 3.3 we have found an analytical solution to the minimum distance problem if the eccentricity and inclination vectors are controlled inside identical circular tolerance windows.

### 3.3.3. MINIMUM DISTANCE IN RATIONAL ELEMENTS

Building on the work from [4] we derive the solution to the general minimum distance problem (without the need for Assumption 3.1) in terms of rational orbital elements. The radial-normal distance in rational elements is defined as:

$$\frac{\rho_{\mathrm{rn}}}{a\delta e} = \sqrt{\left(\varphi_a - \cos\delta M\right)^2 + \varphi_i^2 \sin^2\left(\delta M - \delta\omega\right)}. \tag{3.36}$$

There are several conditions that lead to a simplification of Eq. (3.36) impacting the solution of the minimum distance problem. These are discussed before the general solution is presented.

*Case 1:* $\varphi_a = 0$
This case is equivalent to Assumption 3.1 and the solution to the minimum distance problem in rational elements is given by:

$$\frac{\rho_{\mathrm{rn,min}}}{a\delta e} = \sqrt{0.5\left(1+\varphi_i^2\right) - \sqrt{0.25\left(1+\varphi_i^2\right)^2 - \varphi_i^2\cos^2\delta\omega}}. \tag{3.37}$$

*Case 2:* $\varphi_i = 0$
This case describes vanishing out-of-plane motion, and a nonzero minimum separation distance is achieved only if $\left|\varphi_a\right| > 1$. The minimum separation distance is equal to:

$$\frac{\rho_{\mathrm{rn,min}}}{a\delta e} = \max\left(0, \left|\varphi_a\right| - 1\right). \tag{3.38}$$

This case is not expected to occur in practice.
*Case 3:* $\cos\delta\omega = 0$
This case describes perpendicular relative eccentricity and inclination vectors. The satellite motion in the radial-normal plane is restricted to a line that is shifted by $\varphi_a$ in the radial direction. The minimum separation distance in this case is given by:

$$\frac{\rho_{\mathrm{rn,min}}}{a\delta e} = \frac{\varphi_a\varphi_i}{\sqrt{\varphi_i^2+1}}. \tag{3.39}$$

Note that normally one aims to avoid perpendicular relative eccentricity and inclination vectors.
*Case 4:* $\sin\delta\omega = 0$
This case describes (anti-)parallel relative eccentricity and inclination vectors. The solution is found by evaluating Eq. (3.36) at the points

$$\delta M \in \left\{0,\ \pi,\ \operatorname{atan2}\left(\frac{\sqrt{\varphi_i^4 - 2\varphi_i + 1 - \varphi_a^2}}{(\varphi_i+1)(\varphi_i-1)}, \frac{-\varphi_a}{\varphi_i^2-1}\right)\right\}, \tag{3.40}$$

which are solutions of $\mathrm{d}\rho_{\mathrm{rn}}/\mathrm{d}\delta M = 0$.

*Case 5:* General case
To obtain the general solution, we differentiate Eq. (3.36) with respect to $\delta M$ and equate to zero:

$$\frac{\mathrm{d}\rho_{\mathrm{rn}}}{\mathrm{d}\delta M}\frac{1}{a\delta e} = \frac{(\varphi_a - \cos\delta M)\sin\delta M + \varphi_i^2 \sin(\delta M - \delta\omega)\cos(\delta M - \delta\omega)}{\sqrt{(\varphi_a - \cos\delta M)^2 + \varphi_i^2 \sin(\delta M - \delta\omega)^2}} = 0. \tag{3.41}$$

The roots of Eq. (3.41) are given by:

$$\delta M = \operatorname{atan2}\left(\frac{\varphi_i^2 \sin\delta\omega\cos\delta\omega\,(-1+2x^2)}{x + 2x\varphi_i^2\sin^2\delta\omega - x\varphi_i^2 - \varphi_a}, x\right), \tag{3.42}$$

where $x$ are the real roots of a 4th order polynomial in the following coefficients:

$$\begin{aligned}
p_4 &= \varphi_i^4 - 2\varphi_i^2 + 4\varphi_i^2\sin^2\delta\omega + 1\\
p_3 &= 2\varphi_a\varphi_i^2 - 2\varphi_a - 4\varphi_a\varphi_i^2\sin^2\delta\omega\\
p_2 &= -\varphi_i^4 + 2\varphi_i^2 + \varphi_a^2 - 4\varphi_i^2\sin^2\delta\omega - 1\\
p_1 &= -2\varphi_a\varphi_i^2 + 2\varphi_a + 4\varphi_a\varphi_i^2\sin^2\delta\omega\\
p_0 &= -\varphi_i^4\sin^4\delta\omega + \varphi_i^4\sin^2\delta\omega - \varphi_a^2.
\end{aligned} \tag{3.43}$$

These equations can be used to find the minimum separation distance for any combination of relative orbital elements by first transforming the set of relative orbital elements into rational elements and then evaluating the relevant equation.

### 3.3.4. DESIGN SPACE AND IMPACT ON MINIMUM SEPARATION DISTANCE

One of the key benefits of the rational orbital elements is that they can be used to reduce the design space from four variables ($\Delta e_x, \Delta e_y, \Delta i_x, \Delta i_y$) or three variables ($\delta e, \delta i, \delta\omega$) to only two variables ($\varphi_i, \delta\omega$). This reduction allows a direction visualization of the design space in relation to the minimum distance constraint. Equations (3.37) to (3.42) allow to parametrize the design space in terms of $\varphi_i$ and $\delta\omega$ and evaluate these equations either for a fixed $\varphi_a$ or a range of realistic values for $\varphi_a$ to gain a complete picture of how a choice of (a set of) relative eccentricity and inclination vectors impacts the minimum separation distance.

Under Assumption 3.1 the rational minimum distance is only a function of $\varphi_i$ and

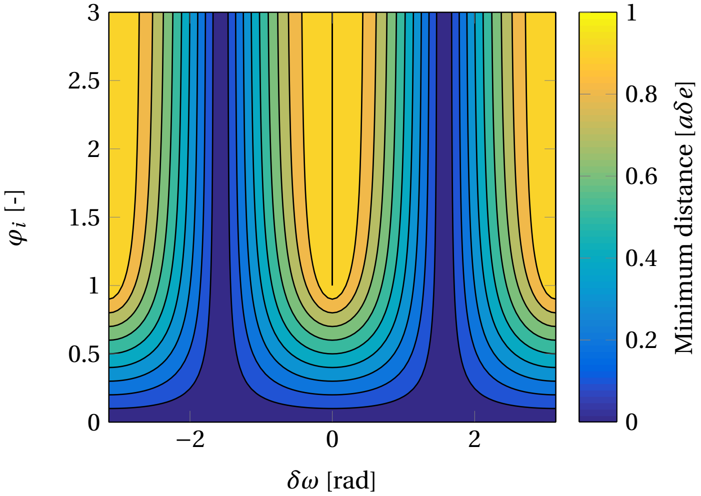

Figure 3.3: Minimum distance as a function of rational elements $\delta\omega$ and $\varphi_i$ for $\varphi_a = 0$.

$\delta\omega$, allowing us to directly visualize the minimum separation distance as a function of these variables. Figure 3.3 shows a contour plot of the rational minimum distance as function of $\varphi_i$ and $\delta\omega$. The plot clearly shows the vanishing minimum separation distance for perpendicular relative $e/i$ vectors. It further shows that a maximum separation distance is obtained for (anti-)parallel relative $e/i$-vectors. Lastly, the plot shows that the minimum separation distance becomes zero for small $\varphi_i$ and that increasing $\varphi_i$ to a value higher than ca. 1.5 has only a very small impact on the minimum separation distance.

By dropping Assumption 3.1 the minimum distance can be determined by solving Eqs. (3.37) to (3.40). However, if $\varphi_a$ is not fixed to a specific value, but allowed to vary in a certain range, the following optimization problem results:

**Problem 3.2.**

$$\begin{aligned} \text{minimize} \quad & \frac{\rho_{\text{rn,min}}}{a\delta e} \\ \text{subject to} \quad & \\ & \varphi_i \ \text{fixed} \\ & \delta\omega \ \text{fixed} \\ & \varphi_a \in \left[\varphi_{a,\text{min}}, \varphi_{a,\text{max}}\right] \end{aligned}$$

where the cost function is as per Eq. (3.36), or one of its simplifications in Eqs. (3.37)-(3.42). The only variable in this equation is $\varphi_a$ and we can solve the problem by a grid search over the domain of $\varphi_a$. Figure 3.4 shows an exemplary plot of the rational minimum distance as a function of $\varphi_i$ and $\delta\omega$ for $\varphi_{a,\text{min}} = -0.3$ and $\varphi_{a,\text{max}} = 0.3$. The influence of nonzero $\varphi_a$ is evident from the plot.

If a target minimum separation distance is given in designing a set of (convex) toler-

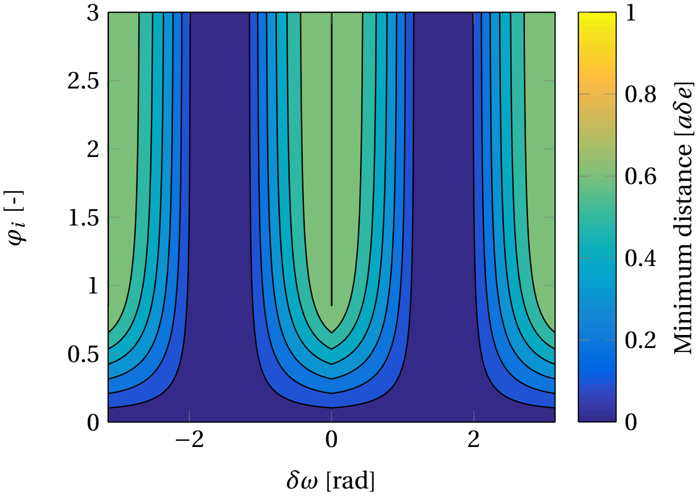

Figure 3.4: Rational minimum distance for $|\varphi_a| < 0.3$ as a function of rational elements $\delta\omega$ and $\varphi_i$

ance windows on the relative orbital elements, we can determine (e.g. from operational experience) a realistic window on $\varphi_a$, determine a range of values for $a\delta e$ (e.g. by analyzing the configuration space in terms of $\Delta e$), and then from Figure 3.4 (adjusted to the right window on $\varphi_a$) determine all possible combinations of $\varphi_i$ and $\delta\omega$ that satisfy the constraint. In going back from $\varphi_i$ and $\delta\omega$ to windows on $\Delta\mathbf{e}$ and $\Delta\mathbf{i}$ we have two additional degrees of freedom that we can use to design the tolerance windows. Section 3.5 discusses this transformation for two particular cases.

## 3.4. SENSOR CONE AVOIDANCE CONSTRAINT

Geostationary satellites carry payloads which are used most commonly for communication, Earth observation or navigation purposes. An observation or the transmission of a signal could be disturbed when an object, e.g. another satellite, passes through the field of view of a sensor. This problem was discussed in [5], where an analysis was presented showing that a non-negligible amount of such cases occur when multiple geostationary satellites are collocated in a single slot. No countermeasures were implemented.

In the recent past the, “standard” Attitude and Orbit Control System (AOCS) suite on three-axis stabilized geostationary satellites consisted of a combination of Earth and Sun sensors, complemented by a gyroscope. Nowadays most geostationary satellites are equipped with star sensors since these sensors provide reliable and accurate attitude measurements. These star sensors add another possibility for sensor interference, namely, when the sunlight reflected off one satellite enters the field of view of an active star sensor on another satellite.

This problem can be addressed in several ways. One option is to develop a star sensor that is robust enough to tolerate such cases. Star sensor manufacturers claim to have developed star sensors that can provide a reliable solution through such events (at least for a limited duration). However, operators are hesitant to accept these claims. Another possibility is a redundant star sensor setup with at least two “heads” in hot redundancy. The satellite can be commanded to switch sensors (or use information from only one sensor if attitude measurements from both sensors are used simultaneously) when a potential interference case occurs. This requires accurate and continuous orbit knowledge of all satellites in the fleet, and even then, a baseline strategy with frequent switching of star sensors is generally undesirable. A third option is to deal with this problem through the design of a relative motion guidance and control algorithm that avoids such cases altogether. The last option, if an increase in propellant consumption can be avoided, would not pose additional risk to the fleet of satellites and could already be applied to fleets of satellites currently in orbit, if the sensor geometry allows it.

Motivated by these use-cases, we investigated the possibilities of avoiding the field of view of sensors on other satellites in the fleet by designing a guidance (and control) method for the relative motion of a fleet of two or more satellites, tackling both problems of payload interference and star sensor interference simultaneously.

### 3.4.1. DEFINITION OF THE SENSOR CONE AVOIDANCE CONSTRAINT

The sensor cone constraint is to avoid the field-of-view (i.e. the sensor cone) of sensors on other satellites in the fleet. Figure 3.5 depicts the sensor cone constraint graphically. The sensor cone is defined by the set

$$K_s\left(\hat{\mathbf{b}}_s, \beta_s\right) = \left\{\boldsymbol{\rho} \in \mathbb{R}^3 \mid \boldsymbol{\rho}^T \hat{\mathbf{b}}_s \geq \|\boldsymbol{\rho}\|_2 \cos\beta_s\right\}, \tag{3.44}$$

for a sensor with bore-sight unit vector $\hat{\mathbf{b}}_s$ and half-cone angle $\beta_s$. The sensor cone avoidance constraint is then defined as:

$$\boldsymbol{\rho}^T \hat{\mathbf{b}}_s < \|\boldsymbol{\rho}\|_2 \cos\beta_s \tag{3.45}$$

where $\boldsymbol{\rho}$ is the position vector of a (follower) satellite in a reference frame attached to the (primary) satellite carrying the sensor. In the remainder of this section, Cartesian position vectors and sensor bore-sight vectors are defined in the RTN frame attached to the satellite carrying the sensor, unless otherwise stated. The satellite carrying the sensor is termed the *primary* satellite. Before analyzing the constraint in more detail, we limit the scope of the analysis. Three important assumptions are made:

**Assumption 3.4.** The satellite is three-axis stabilized and Earth-pointing, hence the orientation of the satellite in the RTN reference frame is fixed.

This assumption is reasonable since most modern GEO-satellites are three-axis stabilized and Earth-pointing, with solar arrays on drive mechanisms, such that the satellite body can maintain a fixed attitude in the RTN frame.

**Assumption 3.5.** The sensor geometry is invariant in a body fixed reference frame.

This assumption basically states that the sensor is rigidly attached to the satellite body and not mounted on some mechanism that can direct the orientation of the sensor.

**Assumption 3.6.** The satellites are considered to be points in space, i.e. the satellites have no dimensions.

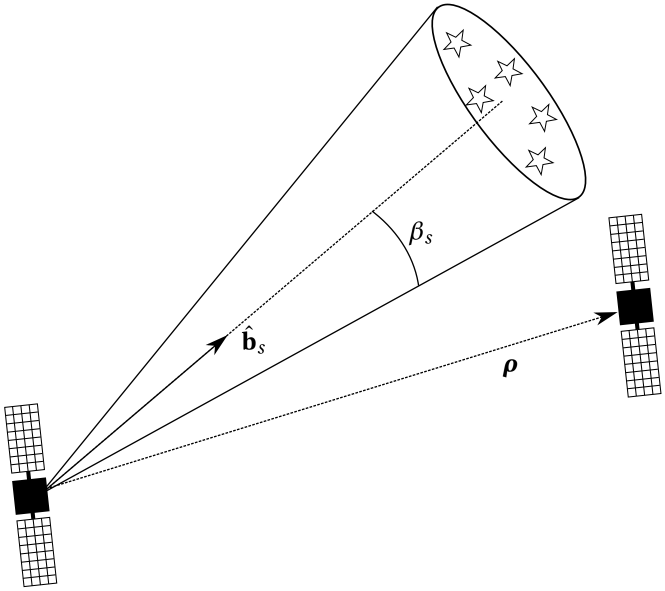

Figure 3.5: Visualization of the (relative) geometry of a sensor cone avoidance constraint

The implication of Assumptions 3.4 and 3.5 is that the sensor cone constraint is invariant in the RTN frame, which allows dealing with this constraint by relative orbit design. More specifically, it allows specifying time-invariant control windows on relative orbital elements that satisfy the sensor cone constraint. Assumption 3.6 avoids dealing with the satellite dimensions, which would unnecessarily complicate the problem. Instead, if the minimum distance between satellites is known, the satellites' dimensions can be dealt with by applying an angular margin in the constraint definition (which in practice is so small that it can be ignored altogether).

The subsequent analysis focuses on two types of sensors in particular. The first type is a star sensor and the second is a generic payload sensor pointing towards the Earth. Star sensors on Earth-pointing satellites ideally point (anti-)parallel to the angular momentum vector, which in case of GEO-satellites is towards the North or South. This results in only small variations in the pointing direction in an inertial reference frame, hence allowing the star sensor to track particular stars for longer periods of time, thereby improving measurement accuracy. Following this philosophy, we focused the analysis to star sensor bore-sight directions maximally 30° away from the North or South directions. In our examples, we look at North pointing sensors, however, (anti-)symmetry of the satellite's relative motion allows to draw similar conclusions for North and South-pointing star sensors. The sensor itself has a half-cone angle $\beta_s = 26°$, which is a typical value for a star sensor's sun exclusion angle [6], and hence a conservative assumption for the sensor cone constraint half-cone angle (i.e. the Sun is (much) brighter than the reflection of a part of the Sun). The geometry of the star sensor is visualized in Figure 3.6.

The second constraint originates from a general Earth-pointing payload sensor. This could be a set of repeaters on telecommunications satellite, a science instrument on an

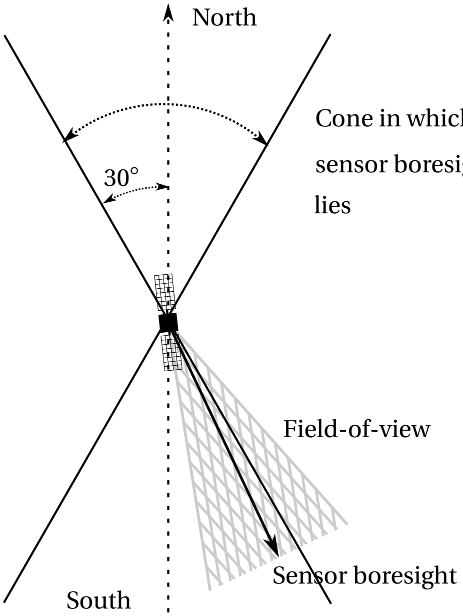

Figure 3.6: Potential star sensor boresight directions

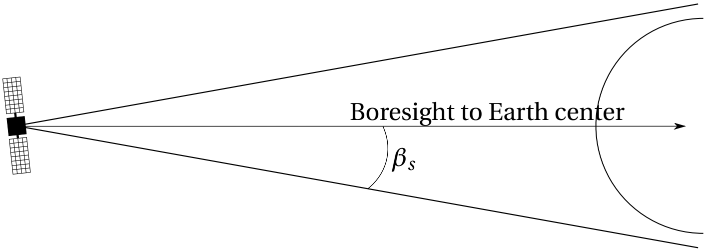

Figure 3.7: Earth sensor geometry

Earth observation mission or any other Earth pointing payload. The sensor bore-sight is in the direction of the Earth's center, with a half-cone angle $\beta_s = 9°$, thus covering the entire Earth. Most sensors will only service a specific region on the Earth. Thus by defining the sensor cone constraint to contain the entire Earth all sensors observing Earth or providing terrestrial services are included in a conservative manner. This constraint is visualized in Figure 3.7.

The analysis is performed for a pair of satellites in a geostationary slot, where only one of the satellites, the primary, carries either a star sensor, an Earth pointing sensor or both. A discussion is included on the validity of the results for larger fleets, where more than one satellite carries sensors, thereby constraining the relative motion of the other satellites.

## 3.4.2. ANALYSIS OF THE SENSOR CONE CONSTRAINT

Our aim is similar to that of section 3.3, namely, to investigate which combinations of relative orbital elements can be chosen such that the sensor cone avoidance constraints are respected. As indicated earlier, the sensor cone avoidance constraint is a non-convex constraint. The largest convex region in Cartesian space that respects the constraint is a half-space attached to the primary satellite. Any half-space defined by a normal vector in the dual cone $K_s^*$ of the sensor cone satisfies the constraint. However, these half-spaces only allow a natural orbital motion if the satellites are separated in terms of relative mean longitude. Thus we could deal with a sensor cone avoidance constraint by defining an appropriately oriented half-space attached to the primary satellite while at the same time enforcing a strict separation in mean longitude difference. This solution quickly exhausts the configuration space and therefore less restrictive solutions are sought (i.e. solutions that do no rely on a strict separation in mean longitude difference).

### SIMPLIFIED ANALYSIS FOR VANISHING RELATIVE MEAN LONGITUDE

To gain geometrical insight, we first investigate the problem under Assumption 3.1 and the following additional assumptions:

**Assumption 3.7.** Relative mean longitude is equal to zero: $\Delta L = 0$.

**Assumption 3.8.** The distance between the satellites is larger than zero ($\rho > 0$).

Assumption 3.7 ensures centered relative motion, while Assumption 3.8 avoids the trivial constraint violation when two satellites share the same position (a situation that has no practical relevance). Under these assumptions the relative motion lies on a 2:1 elliptical cylinder centered on the primary, as shown in Section 2.5.2. The sensor cone avoidance constraint is met when the sensor cone does not intersect with the relative orbit. This constraint can be formulated in terms of relative orbital elements by introducing the relative angular momentum vector $\delta\mathbf{h}$. The relative angular momentum vector is defined in the RTN frame of the primary and is perpendicular to the relative orbital plane and parametrized in terms of the relative eccentricity and relative inclination vectors (see also Eq. (2.48)):

$$\frac{\delta\mathbf{h}}{na^2} := \begin{pmatrix} -2\left(\Delta e_x \Delta i_y - \Delta e_y \Delta e_x\right) \\ \Delta e_x \Delta i_x + \Delta e_y \Delta i_y \\ -2\left(\Delta e_x^2 + \Delta e_y^2\right) \end{pmatrix} = \begin{pmatrix} -2\delta e \delta i \sin\delta\omega \\ \delta e \delta i \cos\delta\omega \\ -2\delta e^2 \end{pmatrix}. \tag{3.46}$$

Under Assumptions 3.1 and 3.7 the relative angular momentum vector can also be calculated in a manner equivalent to the usual orbital angular momentum vector:

$$\delta\mathbf{h} = \boldsymbol{\rho} \times \dot{\boldsymbol{\rho}}. \tag{3.47}$$

From these equations we clearly see that the orientation of the relative orbit is fully determined by the relative eccentricity and inclination vectors. The sensor cone avoidance constraint is met when the relative angular momentum vector lies in the union of the dual cone of the sensor cone and its negative, i.e. under Assumptions 3.1 and 3.7, all relative orbits for which

$$\delta\mathbf{h} \in \left\{K_s^* \cup -K_s^*\right\} \tag{3.48}$$

satisfy the cone avoidance constraint. We stress an important point here: satisfaction of the constraint is not dependent on the absolute orientation of the relative eccentricity and inclination vectors as given by $\left(\Delta e_x, \Delta e_y\right)$ and $\left(\Delta i_x, \Delta i_y\right)$, it is only depending on the magnitude of the relative eccentricity and inclination vectors ($\delta e$ and $\delta i$) and their relative orientation ($\delta\omega$). We can go one step further; scaling the relative angular momentum vector by a positive value does not alter its orientation, and thus if we scale the relative angular momentum vector as follows:

$$\frac{\delta \mathbf{h}}{\delta e^2 n a^2} = \begin{pmatrix} -2\frac{\delta i}{\delta e}\sin\delta\omega \\ \frac{\delta i}{\delta e}\cos\delta\omega \\ -2 \end{pmatrix} = \begin{pmatrix} -2\varphi_i \sin\delta\omega \\ \varphi_i\cos\delta\omega \\ -2 \end{pmatrix} = \delta\mathbf{h}_\varphi, \tag{3.49}$$

we can observe that satisfaction of the constraint is only dependent on the ratio $\varphi_i$ and $\delta\omega$, further motivating the value of rational orbital elements. Now for a particular relative state (and under Assumptions 3.1 and 3.7), it is straightforward to evaluate whether or not the constraint is satisfied by evaluating whether $\delta\mathbf{h}_\varphi \in \left\{K_s^* \cup -K_s^*\right\}$, or alternatively by evaluating if the following constraint is met:

$$\left|\delta\mathbf{h}_\varphi^T \hat{\mathbf{b}}_s\right| \geq \left\|\delta\mathbf{h}_\varphi\right\|_2 \cos\left(\frac{\pi}{2} - \beta_s\right). \tag{3.50}$$

For a given sensor bore-sight direction and half-cone angle, we can parametrize the region satisfying the constraint in terms of $\varphi_i$ and $\delta\omega$. Two exemplary graphs are given in Figure 3.8, where the light (yellow) area corresponds to satisfaction of the constraint, while the dark (blue) area corresponds to a violation of the constraint. A direct insight obtained from Figure 3.8 is that the configuration that is ideal from the point of view of relative separation distances with relative eccentricity and inclination vectors (anti-)parallel conflicts with the constraint of an Earth-pointing sensor. Note that if Eq. (3.48) is met, the sensor cone avoidance constraint is satisfied at any position in the (relative) orbit.

### SIMPLIFIED ANALYSIS FOR NONZERO MEAN LONGITUDE

Although the previous analysis provides valuable geometric insight, it is only valid under Assumptions 3.1 and 3.7, where especially the latter is too restrictive. We now investigate the more general case without Assumption 3.7. We limit the analysis to satellites inside the same geostationary slot which, for a minimum absolute eccentricity of zero, results in the following relative mean longitude window, see Eqs. (3.2):

$$\phi_{\min} \leq \Delta L \leq \phi_{\max}. \tag{3.51}$$

Let us assume we have chosen a set of relative eccentricity and inclination vectors that satisfy the constraint for $\Delta L = 0$. We intend to find out in what window around $\Delta L = 0$ the constraint remains satisfied. To that end, we first perform a conceptual exercise to further develop our geometrical understanding. We use the geometry in Figure 3.9 for this conceptual exercise. If the sensor cone avoidance constraint is satisfied at $\Delta L = 0$, the constraint will remain satisfied for $\Delta L$ in one of the following two domains:

$$\begin{array}{l} \Delta L \in \left\{0,\ \phi_{\max}\right\} \\ \Delta L \in \left\{\phi_{\min},\ 0\right\} \end{array}, \tag{3.52}$$

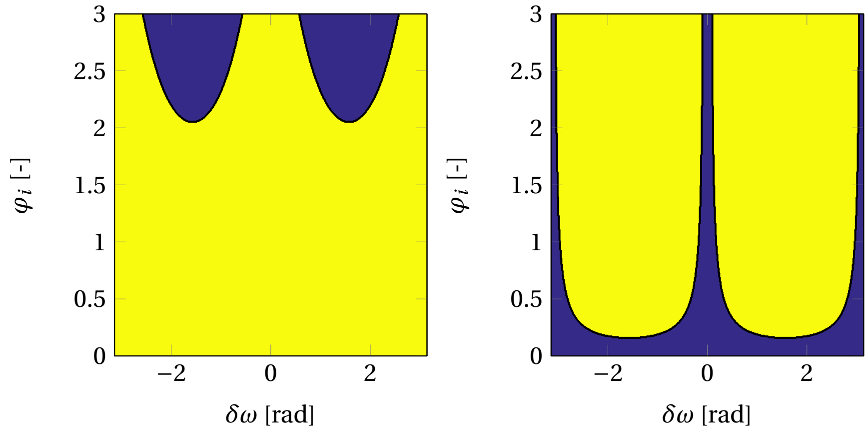

(a) North pointing sensor, $\beta = 26°$ (b) Earth pointing sensor, $\beta = 9°$

Figure 3.8: Yellow regions show the possible configurations respecting the sensor cone avoidance constraint under Assumptions 3.1 and 3.7.

i.e., we can move the relative orbit either in the direction of increasing or decreasing $\Delta L$ without ever violating the constraint. Identifying this direction gives us directly either the upper bound or lower bound on $\Delta L$ (which is the geostationary slot boundary). This can be done by an analysis of the geometry, or by evaluating the following expression:

$$\operatorname{sign}\left(\hat{\mathbf{b}}_c^T \cdot \delta\mathbf{h}\right) \cdot \operatorname{sign}\left(\hat{\mathbf{e}}_2^T \cdot \delta\mathbf{h}\right) = \begin{cases} -1 & \Rightarrow \quad \Delta L_{\max} = \phi_{\max} \\ 1 & \Rightarrow \quad \Delta L_{\min} = \phi_{\min} \end{cases}, \tag{3.53}$$

where $\hat{\mathbf{e}}_2 = (0,\ 1,\ 0)^T$ selects the tangential component of $\delta\mathbf{h}$. We define the bound found from Eq. (3.53) as the “closed-end”. We then start at the closed-end and keep increasing (or decreasing) the value of $\Delta L$ until the relative orbit coincides with the sensor cone and the constraint is violated. The largest (or smallest) $\Delta L$ at which the sensor cone avoidance constraint is violated is the other bound on $\Delta L$, which we define as the “open-end”. In performing this exercise, the relative orbit traces out a tube (the cross-section of this tube is the projection of the relative orbit onto the $x$–$z$ plane). Figure 3.9 shows the tube and the end-points for the case $\Delta L_{\max} = \phi_{\max}$. We used the term “open-end” as the sensor looks through this end of the tube.

The previous exercise, although conceptual, helps to create a geometric understanding of the constraint. We arrive at a more formal approach to finding the bound on $\Delta L$ (open-end) by solving the following optimization problem:

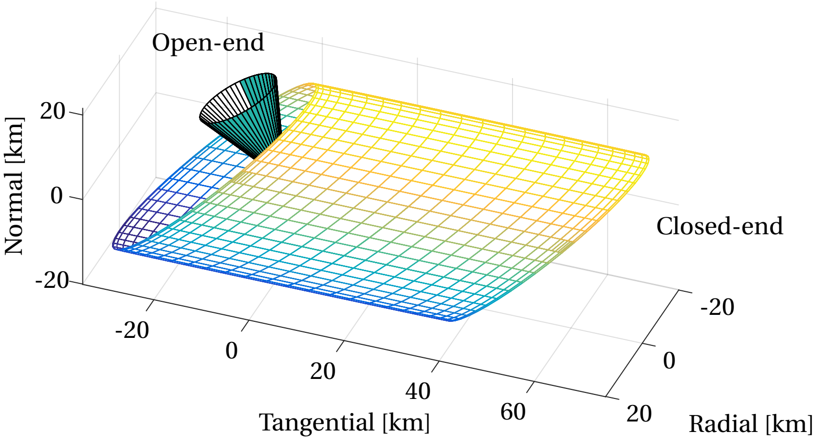

Figure 3.9: Tracing out the relative orbit between $\Delta L_{\text{min}}$ and $\Delta L_{\text{max}}$ forms a tube where the sensor looks through the open end

**Problem 3.3.**

$$\begin{aligned} \text{minimize} \quad & \sqrt{\Delta L^2} \\ \text{subject to} \quad & \Delta \mathbf{e} \text{ fixed} \\ & \Delta \mathbf{i} \text{ fixed} \\ & \Delta n = 0 \\ & L \in \{0,\ 2\pi\} \\ & \boldsymbol{\rho}^T \hat{\mathbf{b}}_s \geq \|\boldsymbol{\rho}\|_2 \, \|\hat{\mathbf{b}}_s\|_2 \cos\beta_s. \end{aligned}$$

The optimization variables in this problem are $L$ and $\Delta L$. The variable $\boldsymbol{\rho}$ is the relative position of the satellite in the RTN frame, which is a function of the relative orbital elements. The solution of the problem is the smallest (absolute) $\Delta L$ (and corresponding $L$) resulting in a violation of the constraint.

### GENERAL ANALYSIS OF SENSOR CONE AVOIDANCE CONSTRAINT

Let us take this analysis one step further. Instead of assuming fixed relative eccentricity and inclination vectors and a zero mean orbital motion, we look into a more realistic case. We assume that these relative orbital elements are varying inside (convex) control windows, similar to the control windows defined in Section 3.3.2 for the minimum distance constraint. Small variations in the relative eccentricity and inclination vectors and

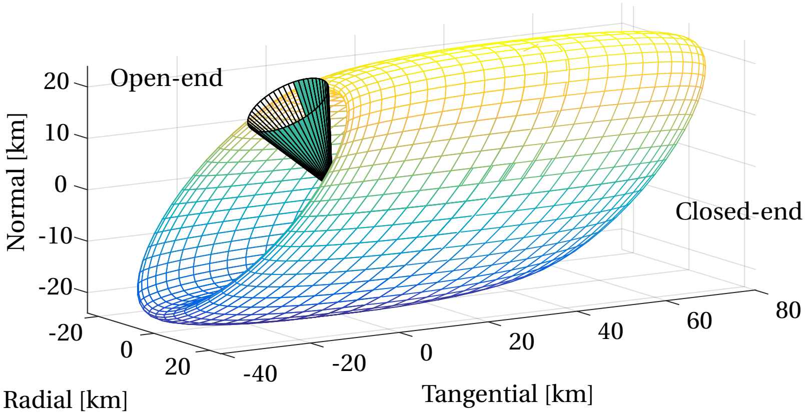

Figure 3.10: When eccentricity and inclination vectors vary inside a window, the tube becomes a torus where the sensor looks through the open end

mean orbital motion result in variations in the position, the size and the orientation of the relative orbital plane. We can conceptually visualize a 3-dimensional elliptical torus enclosing all of these relative orbits, as done in Figure 3.10. Dealing with the sensor cone avoidance constraint can thus be solved as a relative orbit design problem, rather than a relative orbit control problem. The design problem becomes an informed selection of control windows on relative orbital elements such that, when the relative state is maintained inside these control windows, the sensor cone avoidance constraint is guaranteed to be satisfied.

The selection of these control windows is discussed later. Here, it is assumed that we have selected a set of control windows on relative eccentricity and inclination vectors $S_e$, $S_i$ and realistic bounds on minimum and maximum relative orbital motion $S_n$. We formulate the following two problems (a. and b.):

**Problem 3.4.**

$$\begin{aligned} &\text{minimize} && \sqrt{\Delta L^2} \\ &\text{subject to} && \\ & && \Delta \mathbf{e} \in S_e \\ & && \Delta \mathbf{i} \in S_i \\ & && \Delta n \in S_n \\ & && L \in \{0,\ 2\pi\} \\ & && \boldsymbol{\rho}^T \hat{\mathbf{b}}_s \geq \|\boldsymbol{\rho}\|_2 \|\hat{\mathbf{b}}_s\|_2 \cos\beta_s \\ &\textbf{a.)} && \Delta L \leq 0, \\ &\textbf{b.)} && \Delta L > 0. \end{aligned}$$

The solution of Problem 3.4a gives us a lower bound on $\Delta L$, while the solution of Problem 3.4b gives an upper bound. In most cases, either Problem 3.4a or 3.4b will return infeasible in line with the “closed-end” of the tube. However, since $\Delta n$ is no longer zero, but allowed to vary inside $S_n$, we can no longer guarantee that a “closed-end” exists and hence we are required to solve both Problem 3.4a and 3.4b to find the window on $\Delta L$ satisfying a particular sensor cone avoidance constraint.

### 3.4.3. SENSOR CONE AVOIDANCE IN RATIONAL ELEMENTS

The sensor cone avoidance constraint is conceptually more difficult than the minimum separation distance constraint. The constraint depends not only on the relative eccentricity and inclination vectors, but also on the relative mean longitude, the sensor boresight direction and the sensor cone half-angle. The relative mean longitude is the most “sensitive” relative orbital element to control, since small differences in semi-major axes of the satellites cause a drift of the relative mean longitude. In that sense we can define a set of relative orbital elements to be “good” (with respect to the sensor cone avoidance constraint) if they allow a large window for the relative mean longitude to vary in. Thus, in designing the relative motion we seek those combinations of relative orbital elements that allow large variations of the relative mean longitude within the boundaries of the geostationary slot. Again, we first consider the relative motion under Assumption 3.1 since it is conceptually simpler. We further assume:

**Assumption 3.9.** The relative inclination vector has nonzero magnitude: $\varphi_i > 0$

and

**Assumption 3.10.** The tolerance window for $\Delta L$ is symmetric and centered at $\Delta L = 0$, such that $\Delta L_{\text{min}} = -\Delta L_{\text{max}}$. The primary satellite (the satellite carrying the sensor) is located at the center of the tolerance window at $\Delta L = 0$.

The first assumption is of little practical consequence since $\varphi_i = 0$ result in zero minimum separation distance in the radial-normal plane, which is something we should avoid anyhow. From a theoretical point of view this assumption avoids dealing with relative orbits that lie completely in the radial-tangential plane. This type of relative orbit could result in “theoretical” satisfaction of the constraint for arbitrary relative mean longitude (since by Assumption 3.6 the satellites have no dimensions). The second assumption makes the problem symmetric and allows us to argue that a tolerance window between $\Delta L_{\mathrm{min}}$ and $\Delta L$ is “equivalent to”, or “as good as” a tolerance window between $-\Delta L$ and $\Delta L_{\mathrm{max}}$ for some value of $\Delta L \in [\Delta L_{\mathrm{min}}, \Delta L_{\mathrm{max}}]$.

In Section 3.4.2 it was shown that the set of possible satellite positions having a fixed $\varphi_i$, fixed $\delta\omega$, zero $\varphi_a$ and an arbitrary $\delta M \in [0,\ 2\pi]$ trace out a tube for varying $\varphi_L$. If we now attach a sensor to the primary satellite, then for $\varphi_L = 0$ there are two possibilities; 1.) the relative orbit of the secondary satellite crosses the sensor cone and the constraint is violated, or 2.) the constraint is satisfied for the complete relative orbit of the secondary satellite. In case 1.) the largest continuous tolerance window on $\varphi_L$ is smaller than half of the tolerance window on $\Delta L$. This case is of little interest to us as satellites could be contained in such region by defining an appropriate half-space in Cartesian space containing the complete relative orbit. In case 2.) there are again two possibilities, a.) we can decrease $\varphi_L$ without ever violating the constraint, or b.) we can increase $\varphi_L$ without ever violating the constraint (i.e. under Assumptions 3.1 and 3.9 there is always an open-end and a closed-end, see also Figure 3.9). Now we can attach a metric to “how good” a certain combination of orbital elements is with respect to a sensor cone avoidance constraint, namely how far can we change $\varphi_L$ (in either positive or negative direction) before the constraint is violated. We can obtain the score of a combination of elements with respect to this metric by solving the following optimization problem:

**Problem 3.5.**

$$
\begin{array}{ll}
\text{minimize} & \sqrt{\varphi_L^2} \\
\text{subject to} & \varphi_i \text{ fixed} \\
 & \delta\omega \text{ fixed} \\
 & \varphi_a = 0 \\
 & \delta M \in \{0,\ 2\pi\} \\
 & \boldsymbol{\rho}^T \hat{\mathbf{b}}_s \geq \left\|\boldsymbol{\rho}\right\|_2 \left\|\hat{\mathbf{b}}_s\right\|_2 \cos\beta_s .
\end{array}
$$

The optimization variables in this problem are $\delta M$ and $\varphi_L$. The solution of the problem is the smallest (absolute) $\varphi_L$ (and corresponding $\delta M$) resulting in a violation of the constraint.

If we drop Assumption 3.1 and let $\varphi_a$ vary in $S_{\varphi_a}$ in line with with Problems 3.4a and b, we can no longer guarantee that a closed-end exists (i.e. the absence of either a lower- or upper bound on $\varphi_L$). Therefore, two optimization problems are required to be solved:

**Problem 3.6.**

$$
\begin{aligned}
\text{minimize} \quad & \sqrt{\varphi_L^2} \\
\text{subject to} \quad & \\
& \varphi_i \text{ fixed} \\
& \delta\omega \text{ fixed} \\
& \varphi_a \in S_{\varphi_a} \\
& \delta M \in \{0,\ 2\pi\} \\
& \boldsymbol{\rho}^T \hat{\mathbf{b}}_s \geq \|\boldsymbol{\rho}\|_2 \, \|\hat{\mathbf{b}}_s\|_2 \cos\beta_s \\
\textbf{a.)} \quad & \varphi_L \leq 0, \\
\textbf{b.)} \quad & \varphi_L > 0.
\end{aligned}
$$

If both Problems 3.6a and 3.6b are feasible, an upper and a lower bound on $\varphi_L$ exists, otherwise, we obtain the usual open- and closed-ends.

### 3.4.4. DESIGN SPACE AND IMPACT ON SENSOR CONE AVOIDANCE

To support the design of a set of (convex) tolerance windows on the relative orbital elements we parametrize again the design space in terms of $\varphi_i$ and $\delta\omega$ and show the objective value of Problem 3.5 or 3.6 as a function of these elements. We focus first on Problem 3.5, under the assumption $\varphi_a = 0$. The right side of Figures 3.11 and 3.12 show such plots for respectively an Earth-pointing sensor with a 9° half-angle and a North-pointing star sensor with a 26° half angle.

In order for such plot to be useful in designing a set of tolerance windows on orbital elements additional information is required: we need to know whether the open-end is facing in the positive or negative $\varphi_L$ direction. Note that this information is directly obtained from the solution of Problem 3.5, namely from the sign of $\varphi_L^\star$. The graphs on the left side of Figures 3.11 and 3.12 present this information. The information in this plot is encoded as follow; the white areas correspond to areas where a constraint violation occurs already at $\varphi_L = 0$, the light-gray areas correspond to areas where a violation occurs for $\varphi_L < 0$ and the dark gray areas correspond to areas where a violation occurs for $\varphi_L > 0$. The smallest $|\varphi_L|$ resulting in a constraint violation is read from the figure on the right side. An interesting and important observation from these figures is that the direction of the open-end switches instantly at $\delta\omega = -\pi/2$ and $\delta\omega = \pi/2$. If we select a tolerance windows on $e/i$-vectors that includes such a switching point, the result is that we have to include both an upper bound and a lower bound on $\Delta L$ to guarantee constraint satisfaction, whereas if such switching point can be avoided, we only have to deal with either an upper or a lower bound.

We also include results where $\varphi_a \in S_{\varphi_a}$. Similar to the minimum distance constraint we choose bounds between $\varphi_{a,\min} = -0.3$ and $\varphi_{a,\max} = 0.3$ in the examples in this section. Figures 3.13 and 3.14 show the achieved objective value of Problem 3.6 on the right side. On the picture on the left side we added an additional shade of gray; the darkest areas in the graph shows the region in which no “closed-end” exists. In these sections of the configuration space we need to include both an upper and a lower bound on $\varphi_L$ in order to satisfy the sensor cone constraint.

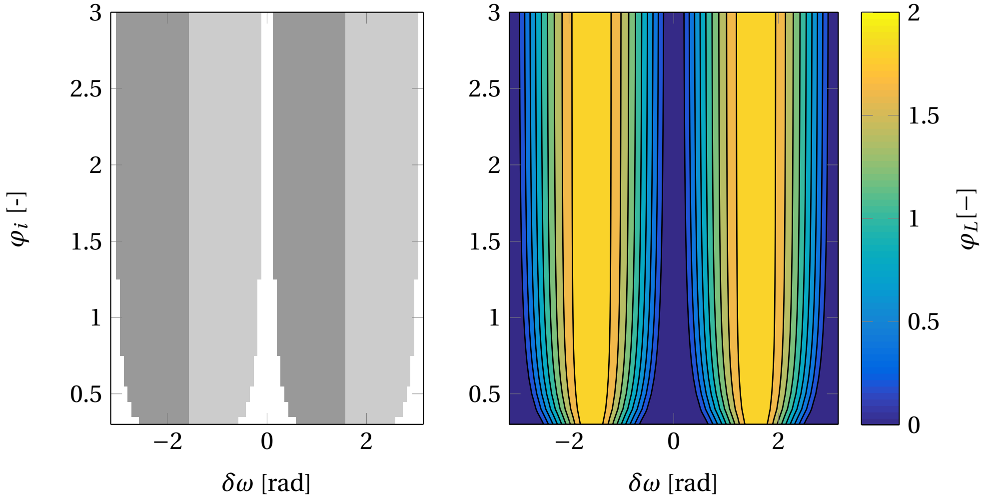

Figure 3.11: Solution to Problem 3.5 in terms of $\delta\omega$ and $\varphi_i$ for an Earth pointing sensor with a 9° half cone angle. The graph on the left side shows whether 1. the constraint is violated at $\varphi_L = 0$ (white), 2. the violation occurs for $\varphi_L < 0$ (light-grey) or 3. the violation occurs for $\varphi_L > 0$ (dark-grey). The graph on the right side shows the magnitude of $\varphi_L$.

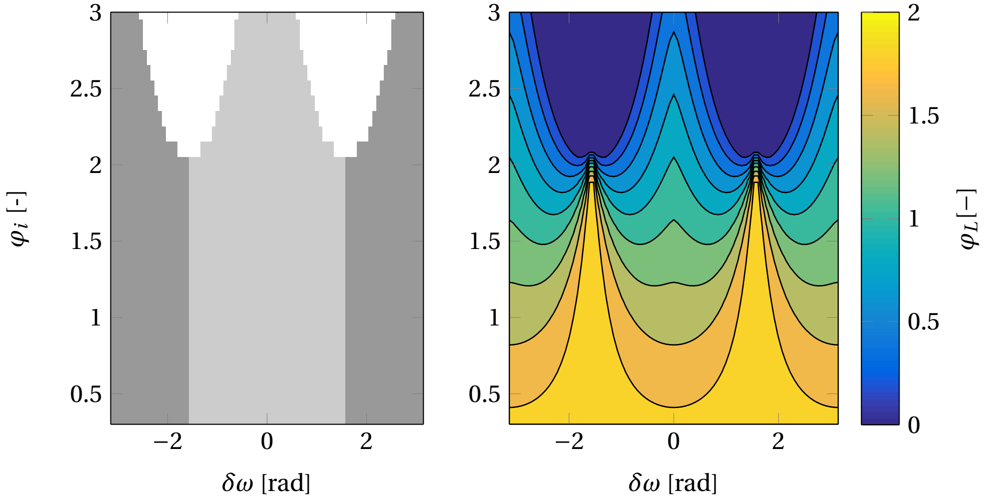

Figure 3.12: Solution to Problem 3.5 in terms of $\delta\omega$ and $\varphi_i$ for a North pointing star sensor with a 26° half cone angle. The graph on the left side shows whether 1. the constraint is violated at $\varphi_L = 0$ (white), 2. the violation occurs for $\varphi_L < 0$ (light-grey) or 3. the violation occurs for $\varphi_L > 0$ (dark-grey). The graph on the right side shows the magnitude of $\varphi_L$.

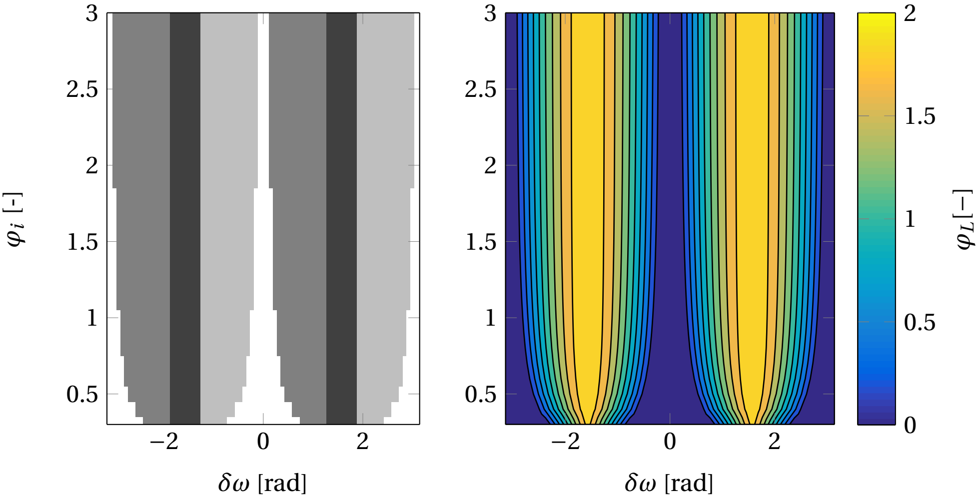

Figure 3.13: Solution to Problem 3.6 in terms of $\delta\omega$ and $\varphi_i$ for an Earth pointing sensor with a 9° half cone angle. The graph on the left side shows whether 1. the constraint is violated at $\varphi_L = 0$ (white), 2. the violation occurs for $\varphi_L < 0$ (light-grey), 3. the violation occurs for $\varphi_L > 0$ (dark-grey) or 4. the violation occurs for $\varphi_L < 0$ and $\varphi_L > 0$ (darkest-gray). The graph on the right side shows the magnitude of $\varphi_L$.

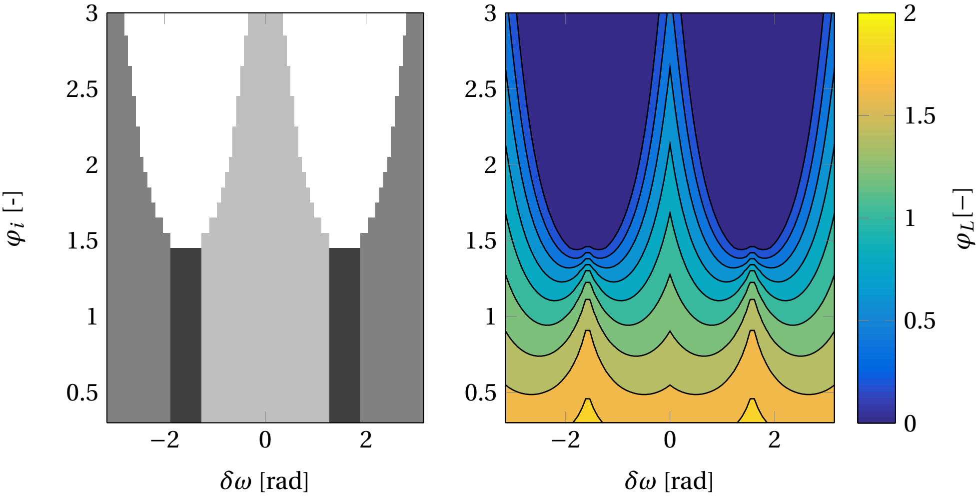

Figure 3.14: Solution to Problem 3.6 in terms of $\delta\omega$ and $\varphi_i$ for a North pointing star sensor with a 26° half cone angle. The graph on the left side shows whether 1. the constraint is violated at $\varphi_L = 0$ (white), 2. the violation occurs for $\varphi_L < 0$ (light-grey), 3. the violation occurs for $\varphi_L > 0$ (dark-grey) or 4. the violation occurs for $\varphi_L < 0$ and $\varphi_L > 0$ (darkest-gray). The graph on the right side shows the magnitude of $\varphi_L$.

## 3.5. TYPICAL CONVEX SETS IN RATIONAL ELEMENTS

In the analysis presented in this chapter we reduced the 4-dimensional design space of relative eccentricity and inclination vectors to the 2-dimensional design space in terms of $\varphi_i$ and $\delta\omega$. If we now use the results from this chapter to select a suitable set of $\varphi_i$ and $\delta\omega$, there are an infinite number of realizations of this set in terms of the relative eccentricity and inclination vectors. We can use this freedom to select tolerance windows that are well suited for control.

It might be more convenient to approach this problem the other way around. Select a shape, size and nominal (i.e. center of the window) eccentricity and inclination vector magnitude. We can leave the relative orientation unspecified. Now the transformation into rational space is unique up to the nominal $\delta\omega$, which can be chosen freely. Thus we have a set in rational space which we can move from left to right over the diagrams and find a position satisfying the constraints.

We investigate both approaches, each for one specific example. We limit ourselves to an analysis of how circular tolerance windows in $e/i$-space look in rational space and how a rectangle in rational space can be realized in $e/i$-space. We start with the circular $e/i$-windows. The center of a set can be parametrized using magnitude/phase notation for the relative eccentricity vector as

$$\Delta\mathbf{e}_c = \delta e_c \begin{bmatrix} \cos\delta\tilde{\omega}_c \\ \sin\delta\tilde{\omega}_c \end{bmatrix} \tag{3.54}$$

and for the relative inclination vector as

$$\Delta\mathbf{i}_c = \delta i_c \begin{bmatrix} \cos\delta\Omega_c \\ \sin\delta\Omega_c \end{bmatrix}. \tag{3.55}$$

Using this set center, we can define an $\ell_2$-norm bounded set in relative eccentricity and inclination vector space as follows:

$$S_e\left(\Delta\mathbf{e}_c, r_e\right) = \left\{\Delta\mathbf{e} \mid \|\Delta\mathbf{e} - \Delta\mathbf{e}_c\|_2 \leq r_e\right\} \tag{3.56}$$

$$S_i\left(\Delta\mathbf{i}_c, r_i\right) = \left\{\Delta\mathbf{i} \mid \|\Delta\mathbf{i} - \Delta\mathbf{i}_c\|_2 \leq r_i\right\}, \tag{3.57}$$

where $r_e$ and $r_i$ are the radii of the sets for respectively relative eccentricity and inclination vectors. We need to make one assumption for the following analysis to hold:

**Assumption 3.11.** The origin of the $e/i$ plane is not part of the sets $S_e$ and $S_i$ (or equivalently $\delta e > 0$ and $\delta i > 0$).

The rational elements $\delta\omega$ and $\varphi_i$ are fully defined by the relative eccentricity and inclination vectors as follows:

$$\delta\omega\left(\Delta\mathbf{e}, \Delta\mathbf{i}\right) = \operatorname{atan2}\left(\Delta e_y \Delta i_x - \Delta e_x \Delta i_y,\ \Delta e_x \Delta i_x + \Delta e_y \Delta i_y\right) \tag{3.58}$$

and

$$\varphi_i\left(\Delta\mathbf{e}, \Delta\mathbf{i}\right) = \frac{\delta i}{\delta e} = \frac{\sqrt{\Delta i_x^2 + \Delta i_y^2}}{\sqrt{\Delta e_x^2 + \Delta e_y^2}}. \tag{3.59}$$

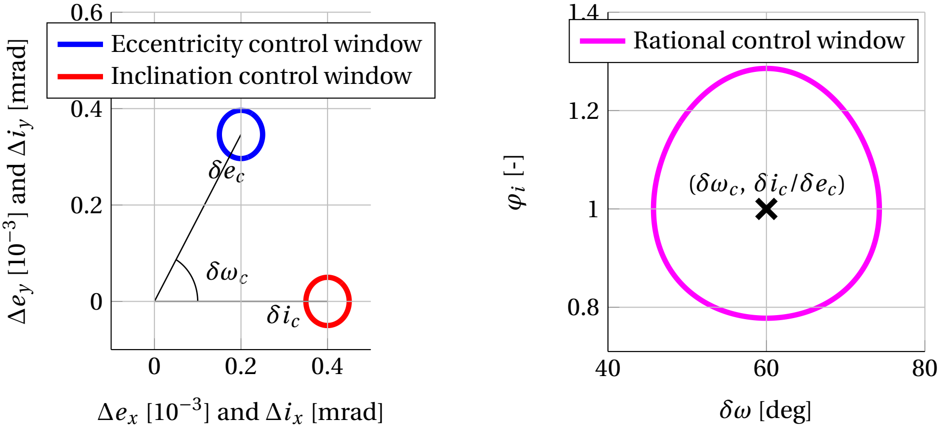

Figure 3.15: Exemplary transformation of circular relative $e/i$-windows into rational space.

Using these equations we can transform any pair of relative eccentricity and inclination vectors into $\delta\omega$ and $\varphi_i$. We can define the set of all possible combinations of $\delta\omega$ and $\varphi_i$ as follows:

$$S_\varphi = \left\{\varphi_i\left(\Delta\mathbf{e}, \Delta\mathbf{i}\right),\ \delta\omega\left(\Delta\mathbf{e}, \Delta\mathbf{i}\right) \mid \Delta\mathbf{e} \in S_e,\ \Delta\mathbf{i} \in S_i\right\}. \tag{3.60}$$

The boundary of the set $S_\varphi$ can be formulated analytically as follows:

$$\mathrm{bd}\ S_\varphi = \left\{ \varphi_i\left(\Delta\mathbf{e}, \Delta\mathbf{i}\right),\ \delta\omega\left(\Delta\mathbf{e}, \Delta\mathbf{i}\right) \mid \begin{array}{l} \Delta\mathbf{e}\left(\theta\right) = \Delta\mathbf{e}_c + \begin{bmatrix} r_e \cos\left(\theta + \delta\omega_c\right) \\ r_e \sin\left(\theta + \delta\omega_c\right) \end{bmatrix} \\ \Delta\mathbf{i}\left(\theta\right) = \Delta\mathbf{i}_c + \begin{bmatrix} r_i \cos\left(\theta + \pi\right) \\ r_i \sin\left(\theta + \pi\right) \end{bmatrix} \\ \theta \in [0,\ 2\pi) \end{array} \right\}, \tag{3.61}$$

since the set boundary is now fully parametrized by a single variable $\theta$ we can directly visualize the set $S_\varphi$ (under Assumption 3.11) for any choice of two-norm bounded sets in relative eccentricity and inclination vector space parametrized by $\delta e_c$, $r_e$ for the eccentricity vector and by $\delta i_c$, $r_i$ for the inclination vector and $\delta\omega_c$, the angle between relative eccentricity and relative inclination control window center. Since the set $S_\varphi$ is not dependent on $\delta\tilde{\omega}_c$ and $\delta\Omega_c$, but only on their difference $\delta\omega_c = \delta\tilde{\omega}_c - \delta\Omega_c$, we can freely chose either $\delta\tilde{\omega}_c$ or $\delta\Omega_c$.

We include an example of two-norm bounded sets in relative $e/i$-space and their transformation into rational space. Note that only one rational set results from a set in $e/i$-space, but there are infinitely many realizations of that rational set in $e/i$-space. Figure 3.15 shows the transformation of two circular relative eccentricity and inclination vector windows into rational space. The resulting shape in rational space resembles an egg.

We look at one example of transforming a set in rational space into $e/i$-space, namely, that of a rectangular box in rational space parametrized by:

$$\varphi_{i\min} \le \varphi_i \le \varphi_{i\max} \tag{3.62}$$

$$\delta\omega_c - \Delta\delta\omega = \delta\omega_{\text{min}} \le \delta\omega \le \delta\omega_{\text{max}} = \delta\omega_c + \Delta\delta\omega. \tag{3.63}$$

We are now looking for sets in $e/i$-space that realize the rectangular set in rational space. Since we go from a 2-dimensional space to a 4-dimensional space there are infinitely many possibilities for this realization. We look into one particular example, which we motivate as follows. If we would keep the inclination vector restricted to a point, the transformation of the rectangular set into $e/i$-space would be one-to-one. The resulting shape of the eccentricity set is a section of an annulus. We maintain this shape for the eccentricity, but we make it smaller. The resulting shape in inclination space is also an annular sector. We can parametrize this shape using its center ($\delta e_c$ and $\delta\tilde{\omega}_c$ for the eccentricity and $\delta i_c$ and $\delta\Omega_c$ for the inclination) and maximum deviation, symmetric in positive and negative direction ($\Delta\delta e$ and $\Delta\delta\tilde{\omega}$ for the eccentricity and $\Delta\delta i$ and $\Delta\delta\Omega$ for the inclination) so that:

$$\delta e_{\text{max}} = \delta e_c + \Delta\delta e \tag{3.64}$$
$$\delta e_{\text{min}} = \delta e_c - \Delta\delta e \tag{3.65}$$
$$\delta\tilde{\omega}_{\text{max}} = \delta\tilde{\omega}_c + \Delta\delta\tilde{\omega} \tag{3.66}$$
$$\delta\tilde{\omega}_{\text{min}} = \delta\tilde{\omega}_c - \Delta\delta\tilde{\omega} \tag{3.67}$$
$$\delta i_{\text{max}} = \delta i_c + \Delta\delta i \tag{3.68}$$
$$\delta i_{\text{min}} = \delta i_c - \Delta\delta i \tag{3.69}$$
$$\delta\Omega_{\text{max}} = \delta\Omega_c + \Delta\delta\Omega \tag{3.70}$$
$$\delta\Omega_{\text{min}} = \delta\Omega_c - \Delta\delta\Omega \tag{3.71}$$

Now we can infer that:

$$\Delta\delta\omega = \Delta\delta\tilde{\omega} + \Delta\delta\Omega \tag{3.72}$$

and

$$\delta\omega_c = \delta\tilde{\omega}_c + \delta\Omega_c \tag{3.73}$$

and so we can choose a nominal value for the relative eccentricity vector phase angle (or alternatively the relative inclination vector phase angle) and we can choose how to divide the available "space" between the relative eccentricity and inclination vector phase angle tolerance windows.

We also have

$$\varphi_{i\text{max}} = \frac{\delta i_{\text{max}}}{\delta e_{\text{min}}} \quad \text{and} \quad \varphi_{i\text{min}} = \frac{\delta i_{\text{min}}}{\delta e_{\text{max}}}. \tag{3.74}$$

And so we have two constraints on the magnitude of the windows, while we have four parameters for sizing the window, namely $\delta e_c$, $\Delta\delta e$, $\delta i_c$ and $\Delta\delta i$ (or alternatively $\delta e_{\text{min}}$, $\delta e_{\text{max}}$, $\delta i_{\text{min}}$, $\delta i_{\text{max}}$). We can "freely" choose two of the parameters, while the other two follow from Eqs. (3.64)-(3.67) and (3.74).

As a particular example we could choose freely $\delta e_{\text{min}}$ and $\delta\tilde{\omega}_c$ and we choose to enforce $\Delta\delta e = \Delta\delta i$ and $\Delta\delta\tilde{\omega} = \Delta\delta\Omega$ to obtain tolerance windows on relative eccentricity and inclination vectors that have identical tolerance magnitudes. By choosing $\delta e_{\text{min}}$ we are directly influencing the minimum distance that is guaranteed by the tolerance window, as well as the relative mean longitude window that results in sensor cone constraint satisfaction.

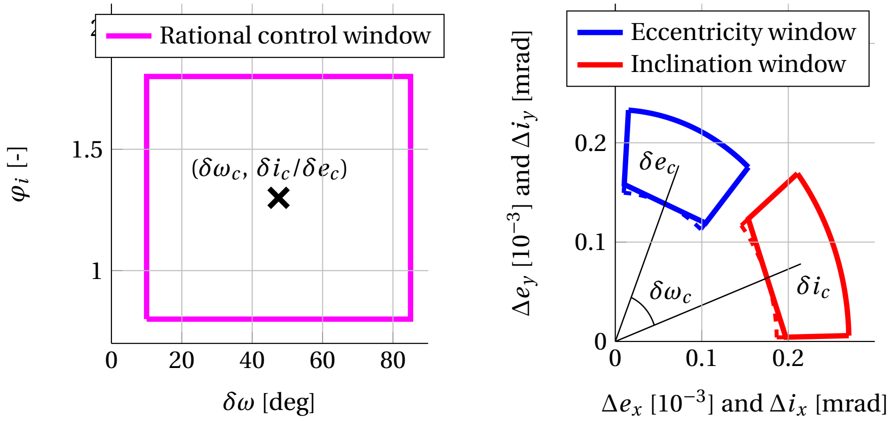

Figure 3.16: Exemplary transformation of rectangular rational window into relative $e/i$-space. The dashed line in the graph on the right-side is the original (non-convex) shape of the window. The convexified approximation is given by the solid lines.

Figure 3.16 shows an exemplary transformation of a rectangular window into $e/i$-space using the constraints $\Delta\delta e = \Delta\delta i$ and $\Delta\delta\tilde{\omega} = \Delta\delta\Omega$. We further set $\delta e_{\text{min}} = 1.5{\cdot}10^{-4}$ and $\delta\tilde{\omega}_c = 67.5°$. The resulting control window is not convex (see the dashed line in Figure 3.16). The set is convexified by approximating the lower arc by a straight line touching the arc in the center, and the convexified set is given by the solid line in Figure 3.16.

## 3.6. DESIGN PROCESS

This section presents a process for designing a guidance method that can deal with the geometric constraints introduced in this chapter. The goal is to find a guidance that deals with the constraints, while achieving good performance in terms of propellant consumption. The latter is only verified through simulations in which the control algorithms are included. The key idea here is that we design a guidance method in terms of relative orbital elements, which are integration constants in the Keplerian problem, hence natural orbital motion results.

1. **Constraint Identification**
   Identify the different geometric constraints (geostationary slot, sensor cone avoidance and minimum distance constraints) for all the satellites in the fleet.

2. **Constraint Mapping**
   Create a map (in rational elements) showing the level of satisfaction of each of the constraints as a function $\varphi_i$ and $\delta\omega$, one map for each constraint. If there are satellites imposing identical constraints (such as minimum distance or a constraint arising from an Earth-pointing sensor), one map is sufficient for all identical constraints.

3. **Tolerance Window Sizing**
   Based on the number of satellites and the size of the geostationary slot, select an

appropriate value for $\delta e_{\min}$. Based on the maneuver strategy (mainly the maneuver cycle duration) select an appropriate tolerance window size (possibly only for the eccentricity vector). If the maneuver cycle duration is to be determined we can try to find the largest maneuver cycle duration such that we can fulfill all constraints simultaneously.

4. **Definition of Rational Element Boundaries**
   Using the constraint values (e.g. minimum distance), the maneuver cycle duration and $\delta e_{\min}$ define suitable boundaries for each constraint in rational elements (in practice these are boundaries on $\varphi_L$ and the non-dimensional minimum distance).

5. **Identification of Constraint Satisfaction Regions**
   Using the rational element boundaries and the maps, identify the regions in rational space that satisfy all constraints simultaneously. We perform this step by overlaying all maps and indicating (binary color coding) which areas violate at least one constraint.

6. **Tolerance Window Selection**
   With the areas that satisfy the constraints indicated, we need to determine the tolerance window in rational space and find the tolerance windows in $e/i$-space that are a realization of the tolerance windows in rational space or vice-versa. We can choose to define tolerance windows that realize only a subset of the constraint satisfaction regions. Furthermore, for the control algorithms in the next chapter the tolerance windows on relative $e/i$-vectors should be convex sets that are formulated mathematically. We use only tolerance windows that can be described fully using linear and quadratic inequality constraints. Furthermore, the relative configuration in $e/i$-space could be rotated (by selecting either $\delta\Omega_c$ or $\delta\tilde{\omega}_c$) without affecting the satisfaction of constraints. Such rotations could be used, e.g., to align the tolerance window in a beneficial way to the natural inclination vector drift.

7. **Optional: Constraint Satisfaction Check**
   Although the above steps result in a rigorous (and perhaps slightly conservative) design, we can still perform checks on the tolerance windows to verify whether they indeed satisfy all geometric constraints (by solving Problem 3.4 for the selected tolerance windows), whether they satisfy the geostationary slot boundaries, whether they can be formulated as convex constraints that can be dealt with adequately by the solution algorithm, whether the tolerance windows are sufficiently spacious for the control algorithm, etc. If one or more checks fail the design is iterated until all constraints are satisfied simultaneously, or until we conclude that the constraints are conflicting and that the method outlined in this work does not provide a viable solution.

This is an exemplary design process that can be followed to come up with a successful design of a guidance for a fleet of satellites in a geostationary orbit. Since this short description is rather abstract we include a design example in which we go through each of the steps in more detail for a concrete case.

## 3.7. DESIGN EXAMPLE

In this section we include a design example that is meant to be both realistic and instructive. At the core of the example is a two-satellite fleet, where the leader satellite carries a star sensor and an Earth-pointing payload. The follower satellite's guidance should avoid the field of view of both the Earth pointing payload and the star sensor on the leader satellite. We then discuss how this problem changes if not only the leader satellite, but also the follower satellite carries an Earth-pointing payload and a star sensor. Lastly, we investigate how this problem changes if multiple follower satellites are collocated with the leader satellite.

We design the guidance for a fleet of satellites collocated at 19.2°E. We target a maneuver cycle duration of 7 days. The leader satellite is controlled using the SPP strategy with a mean eccentricity circle radius of $2{\cdot}10^{-4}$. The leader's longitude control strategy aims at maintaining a mean longitude window with a size of 0.525 mrad (or 0.03°). The leader's mean inclination is maintained smaller than 0.5 mrad (or 0.029°). The maximum mean-to-osculating variations for the different elements over a period of one year are given in Table 2.2. The follower satellite(s) is (are) controlled with respect to the leader satellite. The control windows in which the follower satellite(s) is controlled are the result of this design example. Two design options are developed in the following sections. Option 1 has circular $e/i$ tolerance windows, while option 2 is a realization of a rectangular window in rational space (both options were discussed in Section 3.5).

### 1. CONSTRAINT IDENTIFICATION

We start by an identification of the constraints. The first constraint is for the satellites to stay inside the geostationary slot. For this example we consider a large slot of ±0.1° in both longitude and latitude. The second constraint is to maintain a separation distance in the radial-normal plane that is larger than or equal to 5 km. The third constraint is for the follower satellite to avoid the field of view of an Earth-pointing sensor with a 9° half-cone angle. The fourth and last constraint is for the follower satellite to avoid the field of view of a star sensor on the leader satellite. The star sensor is pointing in North-East direction (boresight: $[0, \cos 30°, \sin 30°]^T$) with a 26° half cone-angle. The constraints are summarized in Table 3.1.

### 2. CONSTRAINT MAPPING

The next step in the design process is to create maps of the constraints in rational space. We do this for constraints C2, C3 and C4. In creating these maps we assume $|\varphi_a| < 0.1$, this value is based on experience. In the simulations in Chapter 5 we will justify this choice. Figure 3.17 shows the minimum distance (in units of $a\delta e$) as a function of $\delta\omega$ and $\varphi_i$. Figures 3.18 and 3.19 show rational element maps for the Earth-pointing payload and the star sensor. The left figure shows whether the open-end of the tube is in the negative $\varphi_L$-direction (light-grey), in the positive $\varphi_L$ direction (dark-grey), in both directions (darkest-grey) or if the constraint is violated already at $\varphi_L = 0$ (white). The right figure shows the magnitude of $\varphi_L$.

### 3. TOLERANCE WINDOW SIZING

This step is perhaps the most difficult one in the process as it crosses the boundary between guidance and control and requires the analyst's experience and judgment. We try

Table 3.1: Constraints on (Relative) Motion of the Fleet of Satellites

| | |
|---|---|
| **C1** | **Geostationary Slot Boundary**<br>The satellites shall stay inside the geostationary slot. A geostationary slot of ±0.1° in longitude and ±0.1° in latitude is used in this example |
| **C2** | **Minimum Distance**<br>The satellites shall maintain a minimum distance in the radial-normal plane larger than or equal to 5 km |
| **C3** | **Earth Sensor Cone Avoidance**<br>To avoid sensor interference with the leader satellite's payload a cone attached to the leader satellite pointing Earthwards shall be avoided by the follower satellite<br>Boresight unit vector: $[-1,\ 0,\ 0]^T$<br>Half-cone angle: 9° |
| **C4** | **Star Sensor Cone Avoidance**<br>To avoid sensor interference with the leader satellite's star sensor a cone attached to the leader satellite pointing North-East shall be avoided by the follower satellite<br>Boresight unit vector: $[0,\ \cos 30°,\ \sin 30°]^T$<br>Half-cone angle: 26° |

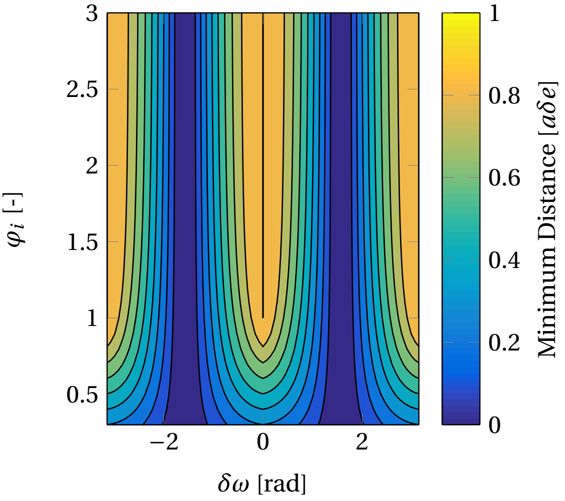

Figure 3.17: Rational Element Map for C2 - Minimum Distance

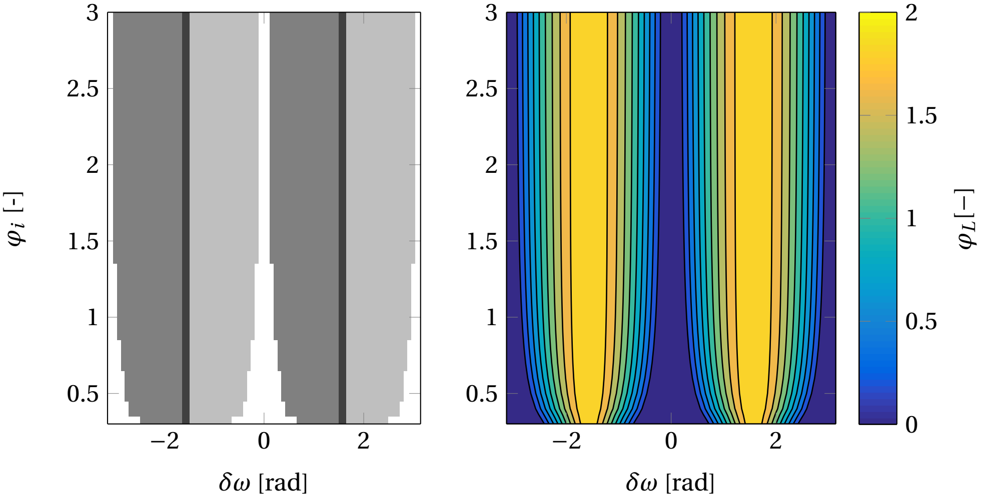

Figure 3.18: Rational Element Map for C3 - Earth pointing sensor. The graph on the left side shows whether 1. the constraint is violated at $\varphi_L = 0$ (white), 2. the violation occurs for $\varphi_L < 0$ (light-grey), 3. the violation occurs for $\varphi_L > 0$ (dark-grey) or 4. the violation occurs for $\varphi_L < 0$ and $\varphi_L > 0$ (darkest-gray). The graph on the right side shows the magnitude of $\varphi_L$.

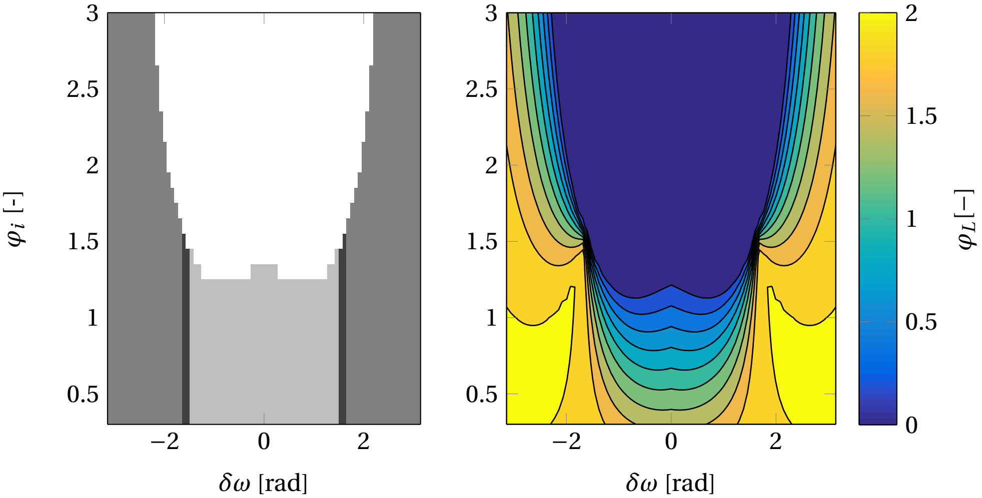

Figure 3.19: Rational Element Map for C4 - Star sensor pointing North-East. The graph on the left side shows whether 1. the constraint is violated at $\varphi_L = 0$ (white), 2. the violation occurs for $\varphi_L < 0$ (light-grey), 3. the violation occurs for $\varphi_L > 0$ (dark-grey) or 4. the violation occurs for $\varphi_L < 0$ and $\varphi_L > 0$ (darkest-gray). The graph on the right side shows the magnitude of $\varphi_L$.

Table 3.2: Contributors to the configuration space independent of the fleet's relative configuration

| | **Eccentricity** | **Inclination** | **Mean Longitude** |
|---|---|---|---|
| **Leader control window** | $2.00{\cdot}10^{-4}$ | $5.00{\cdot}10^{-4}$ | $5.25{\cdot}10^{-4}$ |
| **Osculating-to-mean** | $1.20{\cdot}10^{-4}$ | $5.35{\cdot}10^{-4}$ | - |
| **Uncertainty margin** | $2.50{\cdot}10^{-5}$ | $2.50{\cdot}10^{-5}$ | $2.00{\cdot}10^{-4}$ |
| **Sum** | $3.45{\cdot}10^{-4}$ | $1.06{\cdot}10^{-3}$ | $7.25{\cdot}10^{-4}$ |

to objectify this step of the process as much as possible. Since all rational elements are scaled with the magnitude of the relative eccentricity vector we would like to have $\delta e_{\text{min}}$ as large as possible. The limiting factor is the size of the geostationary slot. We analyze the geostationary slot size and allocate the available space to different contributors. The required latitude window is only dependent on the inclination of the satellites, while the longitude window is shared between contributions from the satellites' eccentricity and mean longitude. We can separate between contributions of the relative configuration and those that are independent of the relative configuration.

The independent contributors are the leader satellite's control window, the maximum osculating-to-mean variations and an uncertainty margin for the different orbital elements. Contributions due to the relative configuration are the control window of the follower satellite(s) and the nominal relative orbital elements (the relative orbital elements of the tolerance window's center). The independent contributors of the design example are listed in Table 3.2.

From the eccentricity and mean longitude contributions in Table 3.2 we can calculate how much of the longitude window we can allocate to the relative contributors. To compute the contribution of eccentricity to the longitude window we multiply the sum of the eccentricity contributions by four (recall that the eccentricity results in a 1:2 ellipse in the radial-tangential plane, with a semi-major axis of $2e$, hence a major axis of $4e$). Thus the independent contributors already use up 2.1 mrad (or 0.12°) of the 0.2° longitude window and 1.06 mrad or ±0.06° of the ±0.1° latitude window. The remaining space can be allocated to the relative contributors.

We exemplify this allocation with Figure 3.20 in which a schematic of the eccentricity vector configuration space is given. The mean eccentricity vector of the leader satellite is controlled inside its control window. Furthermore, margins for osculating-to-mean variations and uncertainty are added. The follower satellite is controlled to a nominal distance of $\delta e_c$ and is kept inside a relative element control window. Since the follower satellite is controlled relative to the leader satellite, the contributors of the leader also affect the follower satellite. If we now want to calculate the maximum eccentricity $e_{\text{max}}$ we count the independent contributors once and half of the value $\delta e_c$ and half of the follower relative control window radius. The mean longitude window $\Delta L_{\text{tot}}$ consists of the independent contributors (Table 3.2) and the size of the relative mean longitude window. To satisfy the geostationary slot boundaries the following inequality should be fulfilled:

$$4e_{\text{max}} + \Delta L_{\text{tot}} \leq 0.00349 \text{ rad } \left(= 0.2^\circ\right). \tag{3.75}$$

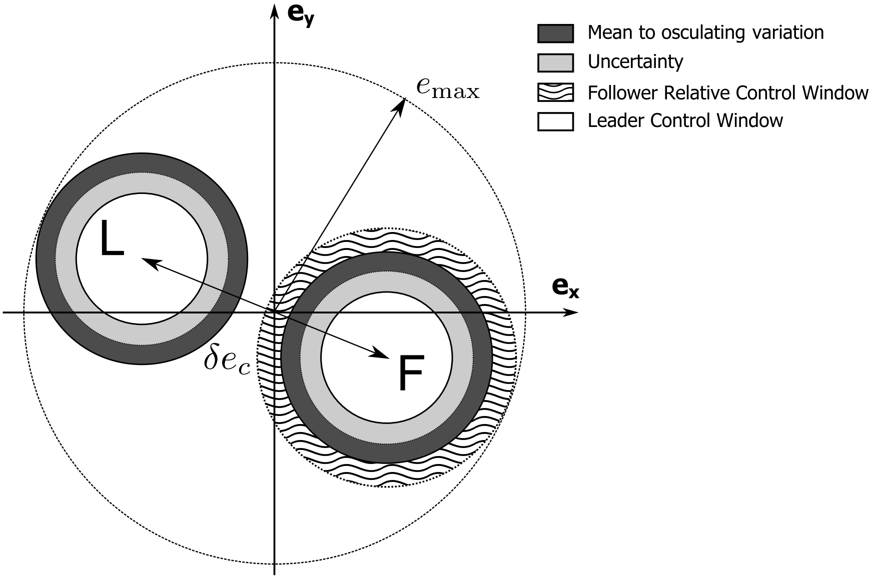

Figure 3.20: Configuration space allocation of a leader and a follower satellite.

In selecting $\delta e_{\min}$, the size of the eccentricity control window and the size of the relative mean longitude control window, the inequality in Eq. (3.75) should hold. Based on the preceding analysis we take $\delta e_{\max} = 4.5{\cdot}10^{-4}$ and a tolerance window radius of $r_e = 5{\cdot}10^{-4}$ (or $\Delta\delta e = 5{\cdot}10^{-4}$), such that $\delta e_c = 4{\cdot}10^{-4}$ and $\delta e_{\min} = 3.5{\cdot}10^{-4}$. These choices for $\delta e_c$ and $r_e$ allow a maximum tolerance window on relative mean longitude of roughly 0.5 mrad (so that $\Delta L_{\text{tot}} = 0.725 + 0.5 = 1.225$ mrad) for Eq. (3.75) to hold. This value is taken for design option 2, whereas a smaller value is taken for design option 1, as explained later in the design process. The values of the relative contributors are summarized in Table 3.3. The values for the inclination vector tolerance window are determined later in the process.

### 4. DEFINITION OF RATIONAL ELEMENT BOUNDARIES

The next step in the process is the definition of the rational element boundaries. To have a minimum distance of 5 km with a value of $\delta e_{\min} = 3.5{\cdot}10^{-4}$ we require a rational minimum distance $\geq 0.34$, see Eq. (3.36). We further impose that $\varphi_L$ at which constraint violation occurs is $\geq 0.5$ so that the relative mean longitude window ±0.175 mrad is in any case free of constraint violations.

Table 3.3: Relative configuration dependent contributors to the configuration space of the fleet

| | **Eccentricity** | **Inclination** | **Mean Longitude** |
|---|---|---|---|
| Option 1: | | | |
| **Relative control window size** | $5.00{\cdot}10^{-5}$ | $5.00{\cdot}10^{-5}$ | $3.50{\cdot}10^{-4}$ |
| **Nominal relative separation** | $4.00{\cdot}10^{-4}$ | $4.00{\cdot}10^{-4}$ | - |
| Option 2: | | | |
| **Relative control window size** | $5.00{\cdot}10^{-5}$ | $5.00{\cdot}10^{-5}$ | $5.00{\cdot}10^{-4}$ |
| **Nominal relative separation** | $4.00{\cdot}10^{-4}$ | $4.55{\cdot}10^{-5}$ | - |

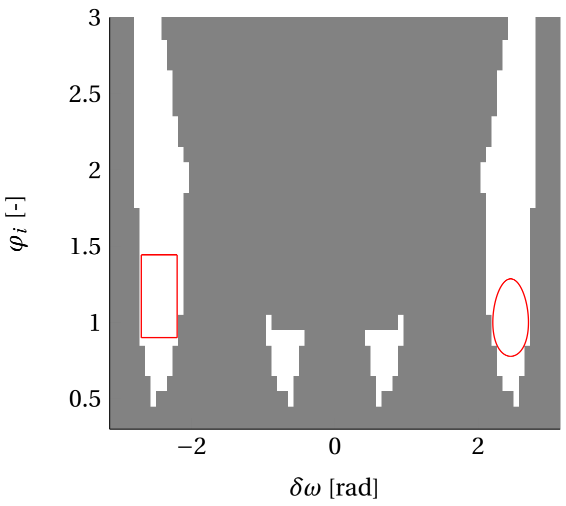

Figure 3.21: Rational element map showing simultaneous satisfaction of constraints C2, C3 and C4 (Table 3.1) in white. The indicated windows (red) show the tolerance window design in rational space for option 1 (right) and option 2 (left).

### 5. Identification of Constraint Satisfaction Regions

Using the maps in Figures 3.17 to 3.19 we can identify the regions in rational space that satisfy the constraints and in Figure 3.21 we show these regions in white, thereby completing the identification of constraint satisfaction regions.

### 6. Tolerance Window Selection

We are now ready to select the tolerance windows. We demonstrate this using both methods from Section 3.5. We start with option 1: if we select a tolerance window on the inclination vector that is identical to the eccentricity vector tolerance window ($\delta i_c = 0.4$ mrad and $r_i$ =0.05 mrad), we can use Eq. (3.61) to calculate the set boundary in rational space. By changing $\delta\omega_c$ we can move the set horizontally to find a region that satisfies the different constraints. The final choice is indicated in Figure 3.21 by the red shape on the right-hand side. The resulting value of $\delta\omega_c = 140.5°$ for design option 1. The values of

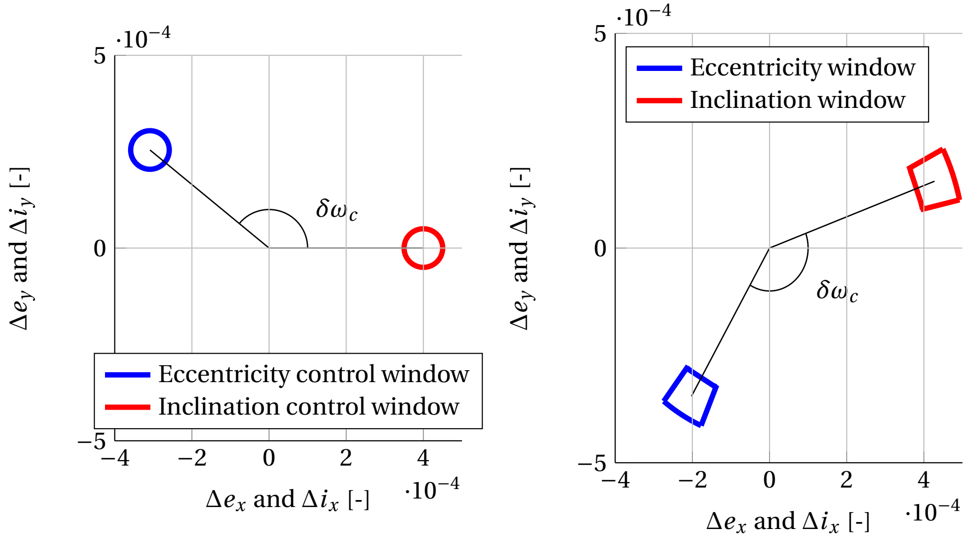

Figure 3.22: Control windows for relative eccentricity and inclination vectors, left: option 1, right: option 2.

the relative inclination vector size and control window are indicated in Table 3.3. Lastly, we have arbitrarily chosen $\delta\tilde{\omega}_c = 140.5°$, so that $\delta\Omega_c = 0°$.

Option 2, discussed in Section 3.5, is to choose a rectangular window in rational space and realize this window in relative $e/i$-space. Using Figure 3.21 we have selected the window in rational space indicated by the rectangular square on the left-side of the figure, by choosing $\varphi_{i\text{min}} = 0.9$, $\delta\omega_{\text{min}} = -154.7°$ and $\delta\omega_{\text{max}} = -126.1°$. The other boundaries follow from the choice of $\delta e_{\text{min}} = 3.5{\cdot}10^{-4}$ and $\Delta\delta e = 5{\cdot}10^{-5}$, and the constraint $\Delta\delta e = \Delta\delta i$ (see also Table 3.3, option 2). Furthermore, we chose $\delta\Omega_c = 40°$ so that the diagonal of the relative inclination vector control window is roughly in line with the natural secular inclination evolution over the simulation period. Figure 3.22 shows the control windows in relative $e/i$-space.

We left out a discussion on the relative mean longitude window until this point. If we look back to Figures 3.18 and 3.19 and we observe the left figures, we see that for design option 1, we have the tube's open-end in the positive $\Delta L$-direction for the star sensor and in the negative $\Delta L$-direction for the Earth sensor. The resulting implication is that we need to constrain the relative mean longitude in a window of $[-0.175, 0.175]$ mrad, hence the smaller longitude window in Table 3.3. For design option 2, we have the open-end of the tube in the positive $\Delta L$-direction for both sensors and thus we only need to constrain the relative mean longitude using an upper bound $\Delta L \leq 0.175$ mrad to satisfy the sensor cone constraints.

If we consider the same fleet of two satellites, but now both satellites carry the same Earth and star sensors, the design we obtained before would still work, given that we use the symmetric window for the relative mean longitude $\Delta L \in [-0.175, 0.175]$ mrad, for both of the design options. It will be demonstrated in Chapter 5 that only an upper, as in design option 2, won't satisfy the constraints when both satellites carry the same sensors.

If we consider, however, a fleet of more than two satellites, where each satellite is controlled with respect to the leader satellite only, the same configuration with circular control windows could still work if we reduce the tolerance window radius by a factor two and the relative mean longitude window also by a factor two: $\Delta L \in [-0.0875, 0.0875]$ mrad. In addition, the difference between the centers of the relative $e/i$ tolerance windows between two follower satellites should be at least as large as between a follower and the leader satellite. The reason that the tolerance windows need to be reduced by a factor two is because all follower satellites are controlled with respect to the leader satellite, but not with respect to each other. The tolerance windows on relative eccentricity and inclination vectors between two follower satellites are also circular, but with radius $2r_e$ and $2r_i$. For the tolerance windows based on the annular sector, the addition of two follower satellites is not so straightforward and can only be approached numerically. We therefore prefer circular tolerance windows for fleets with more than two satellites to simplify the associated analysis.

If one of the follower satellites imposes a constraint different than those from the leader satellite, the design process is exactly the same. The additional constraint is added and treated similar as the other constraints. With sensor cone constraints originating from multiple satellites (in most cases) only a symmetric mean longitude window guarantees simultaneous satisfaction of all constraints.

We leave out the last step of the process. Instead, the guidance worked out in this design example is used in Chapter 5 in simulations. It is verified that the design adequately deals with the various constraints.

## 3.8. CONCLUDING REMARKS

This chapter presented an analysis of three types of geometric constraints imposed on a fleet of collocated satellites:

1. The satellite(s) shall be kept inside the geostationary slot.
2. A minimum separation distance between the satellites shall be maintained.
3. A satellite shall avoid the (conic) field-of-view of a sensor (or multiple sensors) attached to another satellite in the fleet.

These constraints were analyzed in detail and a method was presented to design a set of tolerance windows respecting these constraints. The analysis and design focused on the identification of the (relative rational) orbital elements that satisfy the constraints for any value of the mean longitude.

The geostationary slot boundaries were translated into boundaries on the orbital elements. To respect the boundaries in longitude, a combination of eccentricity and mean longitude difference were required to be constrained. To satisfy the latitudinal boundaries, the inclination needed to be kept below the maximum latitude. The radial boundaries are normally respected as a result of satisfying the longitude boundaries.

To maintain a minimum separation distance, we choose to constrain the distance in the radial-normal plane. The tangential direction was omitted because this direction is usually subject to much larger uncertainty in orbit determination and prediction. The key to satisfying the minimum distance constraint was to design the relative $e/i$-configuration such that the constraint is respected. In addition to the $e/i$-vectors, a nonzero mean orbital motion difference has a small impact as well. For the simplified cases of zero mean orbital motion difference and circular tolerance windows that are identical in size and location in respectively the eccentricity and inclination plane, an analytic solution was provided for the minimum distance in the radial-normal plane. A general solution of the minimum distance problem in rational orbital elements was provided, i.e. a solution that did not rely on the assumption of zero mean orbital motion difference. The introduction of rational orbital elements allowed to parametrize the configuration space using only two variables, thus allowing a clear visualization of the minimum distance in terms of rational orbital elements.

The sensor cone avoidance constraint was formulated mathematically and analyzed in terms of relative orbital elements and rational relative orbital elements. This constraint required to actively control the relative mean longitude between two satellites to ensure satisfaction of the constraint, something that was not required with only a minimum distance constraint. The strategy for dealing with this constraint was again to design the relative motion of two satellites using the relative eccentricity and inclination vectors. A metric was defined to attach a value to “how good” a combination of relative eccentricity and inclination vectors was. This metric indicated the size of window in mean longitude difference that respected the sensor cone avoidance constraint. The design space was parametrized in terms of rational orbital elements and maps were created that visualize the chosen metric for combinations of rational orbital elements.

Since the design space in rational orbital elements is two-dimensional, whereas the design space in relative eccentricity and inclination vector space is four-dimensional, an area in rational space has infinitely many realizations in $e/i$-space. Two useful options were presented, one option to transform a set of circular relative $e/i$-windows into rational space and a second option for realizing a rectangular rational set in $e/i$-space.

A process was introduced to design a set of relative orbits that simultaneously satisfy the different geometric constraints. An elaborate example demonstrated the process to design a set of tolerance windows on relative eccentricity and inclination vectors and relative mean longitude difference that satisfy simultaneously the constraints to stay inside a geostationary slot, respect a minimum distance and avoid the field of view of both a star sensor and an Earth pointing sensor.

## REFERENCES

[1] E. M. Soop, *Handbook of Geostationary Orbits* (Microcosm and Kluwer, Dordrecht, 1994).

[2] S. HUBERT and J. SWALE, *Stationkeeping of a constellation of geostationary communications satellites,* in *Astrodynamics Conference* (American Institute of Aeronautics and Astronautics (AIAA), 1984).

[3] M. Eckstein, C. Rajasingh, and P. Blumer, *Colocation strategy and collision avoidance for the geostationary satellites at 19 degrees west,* in *International Symposium on Space Flight Dynamics* (1989).

[4] G. Gaias and J.-S. Ardaens, *Design challenges and safety concept for the AVANTI experiment,* Acta Astronautica **123**, 409 (2016).

[5] P. Wauthier and P. Francken, *The ASTRA co-location strategy for three to six satellites,* Revista Brasileira de Ciencias Mecanicas (ISSN 0100-7386), vol. 16, p. 163-171 **16**, 163 (1994).

[6] Jena Optronik, *Datasheet: Autonomous star sensor astro aps,* `http://www.jena-optronik.de/de/lageregelungssensoren/sternsensor-astro-aps.html`.

# 4

# SINGLE-SATELLITE STATION-KEEPING

*The further one goes, the less one knows.*

Lao Tzu

*We can know only that we know nothing.*
*And that is the highest degree of human wisdom.*

Leo Tolstoy

***Abstract***
*The station-keeping problem is defined together with a number of key constraints. A new method is introduced to solve the station-keeping problem. The method relies on using convex optimization techniques to calculate a sequence of maneuvers over a maneuver cycle. The resulting solution is processed into a maneuver plan that can be realized by a system with on-off thrusters. Various simulation results are presented to validate the methodology, to investigate long-term optimal strategies, to investigate the performance under various uncertainties and to evaluate the method in a receding horizon setting.*

Station-keeping of a single geostationary satellite is simply speaking maintaining the position of the satellite inside its assigned geostationary slot. Secondary goals are a minimization of propellant consumption and limiting the required number of thruster firings to an acceptable level. To perform station-keeping of geostationary satellites the key task is to determine the orbit control maneuvers for a certain time window, a so-called maneuver cycle. In geostationary satellite station-keeping this task is usually performed on-ground. A maneuver plan is calculated and uploaded to the satellite and executed on-board in open-loop. The station-keeping problem is a problem that has been solved (in various ways) already many years ago and many satellites are controlled successfully inside their geostationary slots. The current state-of-art methods are elegant in their simplicity, yet able to deal with the problem adequately.

Despite of the success of state-of-art methods, this chapter develops a new method for station-keeping of geostationary satellites. The primary motivation for introducing a new method arises from the need to be able to deal with the sensor cone avoidance constraints. The station-keeping method developed in this chapter forms the basis for the collocation control method developed in the next chapter. In addition to the usefulness for collocation, the method has a number of benefits for single-satellite station-keeping as well:

- It is is flexible in the sense that it can be applied to satellites with a classical chemical propulsion system with high thrust-to-mass ratio as well as to satellites with an electric propulsion system.
- The method can deal with arbitrary thruster configurations and is in that sense more general than the state-of-art methods
- The resulting maneuver plans can be realized by simple on-off thrusters.
- The method is shown to be propellant efficient, while using an acceptably small number of thruster firings.
- It can be configured such that the resulting maneuver plans resemble closely those derived from a classic method, which directly provides a valuable validation of the methodology.
- The method can be applied in an open-loop setting such as conventional methods, as well as in a closed-loop setting, in the form of a receding horizon controller.

The method is applied in a normal station-keeping scenario in which maneuvers are calculated for the duration of a maneuver cycle, as well as in a receding horizon control setting. In addition, the method is used with an optimization horizon of one year and as such, optimal guidance strategies are investigated as well as the influence of several parameters on the optimization problem solution.

## 4.1. INTRODUCTION TO STATION-KEEPING

The problem of station-keeping of a geostationary satellite is a guidance and control problem. We define the guidance problem as the formulation of desired state, as well as constraints on state and control variables such that, if these constraints are met, the resulting motion has desired characteristics. The control problem, or maneuver planning problem, is the calculation of orbit control maneuvers that satisfy the constraints coming from guidance. These two problems are treated together in this work.

### 4.1.1. DEFINITION OF THE STATION-KEEPING PROBLEM AND CONSTRAINTS

The key objectives of the station-keeping problem are 1.) stay inside the geostationary slot, while 2.) minimizing propellant consumption and 3.) do so with an acceptably small number of thruster firings. Of the state constraints that have been discussed in the previous chapter, only the constraint to stay inside the geostationary slot is relevant to single-satellite station-keeping (the other constraints are treated in the next chapter). In addition to constraints on the satellite state, several constraints on control are common. We provide a short summary of some of the most relevant constraints:

1. The thrust that can be delivered by a thruster is limited and hence an important constraint is the maximum thrust force $T \leq T_{\max}$.
2. Thruster firings are not allowed during specific time periods (e.g. during orbit determination, eclipses, weekends, etc.).
3. The thrusters have only a single (qualified) operational point and are on/off thrusters (i.e. thrust force cannot be modulated).
4. The thrusters have a minimum (or maximum) firing duration.

Such constraints can apply both to single-satellite station-keeping and to satellites collocated in a single slot. In developing a method for station-keeping it is key that these constraints can be dealt with in an appropriate manner.

### 4.1.2. THE STATUS QUO

The majority of geostationary satellites that are currently in orbit are chemically propelled satellites with a thruster configuration that is equivalent to the REF configuration described in Section 2.6. Here, we say equivalent, since generally many more thrusters are equipped, which are not pointing through the center of mass, such that angular momentum can be controlled as a by-product of making orbit maneuvers. The key advantage of the REF configuration is that it allows to decouple NS control and EW control. This decoupling is usually capitalized upon by satellite operators and separate strategies for NS and EW control are developed. Maneuvers are usually calculated analytically and satellites are controlled using fixed schedules (an exemplary schedule is given in one of the analysis cases presented at a later stage, Figure 4.3). The typical inputs to the algorithms calculating the maneuvers are the corrections to the orbital elements that shall be achieved by the maneuvers, together with the duration of the maneuver cycle. Hence it is the task of the guidance module to define the desired orbital elements and compare these to the current orbital elements (or propagated orbital elements) to calculate these orbital element corrections. The length of a maneuver cycle duration is typically determined by analyzing the longitude drift rate for EW maneuvers (which is a function of the satellite longitude) and the inclination drift rate for NS maneuvers. These drifts are then compared to the geostationary slot size to determine a maneuver cycle duration that is short enough to guarantee that the satellite can be controlled within the geostationary slot. Orbit prediction accuracy, especially in the along-track direction also plays a significant role. Further operational constraints can enter this analysis, such as having a maneuver cycle duration that synchronizes with the usual 5-day work week. Typical maneuver cycle durations are between 7 and 28 days. Other considerations made in the guidance module are typically to determine the long-term direction of the drift of the mean inclination vector and enforce inclination vector corrections in the same direction as the mean inclination vector drift such that propellant consumption for NS control is minimized. In EW direction the propellant consumption is usually minimized by controlling the mean eccentricity vector to a circle, such that the eccentricity vector points in the direction of the Sun (projected onto the equatorial plane). This strategy is called the SPP strategy and the general idea is as follows; in the absence of control the mean eccentricity vector would describe a circle over the course of a one-year period due to perturbations by SRP. The SPP strategy basically keeps this natural circle, but with a smaller radius such that the geostationary slot boundaries are respected. As such, the smallest amount of propellant is required for controlling the eccentricity vector. With the inclination vector and eccentricity vector corrections defined, the remaining elements to control are the mean longitude difference and drift rate (or mean orbital motion difference). Since the drift rate is the derivative of the mean longitude difference it suffices to discuss the mean longitude. A mean longitude correction is usually determined by propagating the orbit to the end of the maneuver cycle and comparing the propagated mean longitude with a desired mean longitude. The goal of the EW maneuvers is to achieve this desired mean longitude at the end of the maneuver cycle (which is then achieved through controlling the drift rate).

The fundamental equations for calculating the maneuvers based on a set of orbital element corrections are worked out by Eckstein in [1]. In this paper, the equations for calculating maneuvers are presented for one, two, or three EW maneuvers per cycle, as well as one or two NS maneuvers per cycle. Eckstein provides the equations for an idealized propulsion system and for a realistic propulsion system including deterministic cross-couplings, e.g., a north-pointing thruster introduces some deterministic thrust in radial and EW directions as a result of plume impingement or thruster misalignment. The equations rely on the cross-coupling coefficients to be small and cannot be generalized to propulsion systems with significantly different configurations than the typical REF configuration. As we use Eckstein's method with two EW maneuvers and a single NS maneuver for an idealized propulsion system as a reference case in later simulations we shortly state the equations for calculating the maneuvers. It is assumed that the desired corrections and maneuver cycle duration are known (i.e. provided by a guidance module). The equations from Eckstein are adapted to the orbital element set of Eq. (2.6) and the orbital element differences are the desired differences to be accomplished by the maneuvers. The corrections are calculated as impulsive $\Delta V$s and the maneuver locations are expressed using the right ascension of the geostationary slot center ($\alpha$). The magnitude of the NS maneuver is given by:

$$\Delta V^{\mathrm{NS}} = n_{\mathrm{geo}} a_{\mathrm{geo}} \sqrt{\Delta i_x^2 + \Delta i_y^2}, \tag{4.1}$$

while the location of the maneuver can be determined from the following two equations:

$$\sin \alpha^{\mathrm{NS}} = \frac{\Delta i_y}{\sqrt{\Delta i_x^2 + \Delta i_y^2}} \tag{4.2}$$

$$\cos\alpha^{\mathrm{NS}} = \frac{\Delta i_x}{\sqrt{\Delta i_x^2 + \Delta i_y^2}}. \tag{4.3}$$

In case of the NS maneuver, the actual orbit in the maneuver cycle in which the maneuver is executed is essentially arbitrary (from the point of view of achieving the desired inclination correction). We assume however that the maneuver is executed within the first orbit. Note that in a real-world case it is customary to place the execution of a NS maneuver one or two orbits before executing an EW maneuver so that the EW maneuver can correct for the undesired parasitic thrust of the NS maneuver in the radial-tangential plane.

The location of the first EW maneuver is within the first orbit after calculating and uploading the maneuver. The second EW maneuver is executed exactly half an orbit further so that mean longitude and eccentricity vector are controlled simultaneously in an effective manner. The first maneuver is executed at a right ascension defined by the following two equations:

$$\sin\alpha_1^{\mathrm{EW}} = s\frac{\Delta e_y}{\delta e} \tag{4.4}$$

and

$$\cos\alpha_1^{\mathrm{EW}} = s\frac{\Delta e_x}{\delta e}, \tag{4.5}$$

where $\delta e = \sqrt{\Delta e_x^2 + \Delta e_y^2}$ and $s$ is equal to the sign of the nominal longitude acceleration due to the geopotential (the factor $s$ is included only for safety so that the drift rate change due to the first maneuver is in the direction opposite of the longitude acceleration, which is beneficial when the second maneuver would fail). As mentioned before, the location of the second maneuver is given by:

$$\alpha_2^{\mathrm{EW}} = \alpha_1^{\mathrm{EW}} + \pi. \tag{4.6}$$

The magnitude of the maneuvers is determined such that their sum achieves the required longitude drift, while their difference achieves the desired eccentricity change:

$$\Delta V_1^{\mathrm{EW}} = -\frac{n_{\mathrm{geo}} a_{\mathrm{geo}}}{\Delta t_1 + \Delta t_2}\left(\frac{1}{3}\frac{\Delta L}{n_{\mathrm{geo}}} - \frac{1}{2}s\Delta t_2 \Delta e\right) \tag{4.7}$$

and

$$\Delta V_2^{\mathrm{EW}} = -\frac{n_{\mathrm{geo}} a_{\mathrm{geo}}}{\Delta t_1 + \Delta t_2}\left(\frac{1}{3}\frac{\Delta L}{n_{\mathrm{geo}}} + \frac{1}{2}s\Delta t_1 \Delta e\right). \tag{4.8}$$

The times $\Delta t_1$ and $\Delta t_2$ are the durations between the execution of respectively first and second maneuver and the end of the maneuver cycle:

$$\Delta t_1 = \Delta t_{\mathrm{MC}} - \frac{\mathrm{mod}\,(\alpha_1 - \alpha_0, 2\pi)}{n_{\mathrm{geo}}}, \tag{4.9}$$

where $\Delta t_{\mathrm{MC}}$ is the maneuver cycle duration, $\alpha_0$ is the right ascension of the geostationary slot at the Epoch of maneuver calculation and

$$\Delta t_2 = \Delta t_1 - \frac{\pi}{n_{\mathrm{geo}}}. \tag{4.10}$$

As such, these durations capture the influence of the change in drift rate of a maneuver on the mean longitude difference that is achieved at the end of the maneuver cycle.

In terms of station-keeping methods for electric propulsion satellites, we found Douglas et al. ([2]) to be a good source of information. In this paper the authors describe their experience in Telesat in station-keeping of a Boeing Satellite Systems (BSS) 702 platform with ion thrusters. The methods used for calculating the station-keeping maneuvers is captured in a series of patents by Anzel, assigned to BSS, [3], [4], [5], [6]. These methods are in essence relying on the same equations as the method by Eckstein, albeit worked out for a particular thruster configuration that has strong similarities to configuration B used in this work (Figure 2.18). Again, the equations rely on a set of orbital element differences to be achieved by the maneuvers, in a similar way as discussed before. A particular add-on compared the work of Eckstein is the use of the thrusters to simultaneously control orbit and angular momentum (i.e. the BSS 702 platform has the thrusters mounted on gimbaled platforms so that the thrusters can be pointed away from the center of mass to create control torques on the satellite [2]). This combined control of orbit and angular momentum was further developed and published in yet another series of patents by BSS, [7], [8]. Due to the much lower thrust force that an electric propulsion system provides, more frequent maneuvers are required. The work by Douglas ([2]) and Goebel ([9]) report that four burns per day are required for station-keeping. Another work by Casaregola ([10]) describes Eutelsats experience in operating geostationary satellites with electric propulsion. One of their satellite, SESAT-1, is equipped with the SPT-100 thrusters. This satellite requires two to four burns per day, on each day of a 7-day maneuver cycle.

What the current state-of-art methods share, whether for chemical or electric propulsion, is that the maneuver algorithms aim to achieve a predefined set of orbital element corrections and the actual maneuvers are calculated using the analytic solutions available for impulsive corrections. These tried-and-true solutions have been used successfully for decades. They are conceptually straightforward and extremely effective. What these methods cannot do, however, is account for constraints on state and control explicitly in the determination of orbit control maneuvers and it is this void that we aim to fill.

## 4.2. DEVELOPMENT OF A NOVEL STATION-KEEPING METHOD

The geometric constraints discussed in the previous chapter motivate the need for a control methodology that can maintain relative orbital elements within certain tolerance windows. The development of the LTV dynamics in Chapter 2 enables the formulation of such constraints in convex form. The satellite state at any point in time can be formulated as an affine function of the initial state and controlled accelerations and hence we can impose convex constraints on the satellite state which are then also convex in terms of the controlled accelerations (i.e. the composition of a convex function with an affine function is convex). The analysis of geometric constraints from Chapter 3 as well as the LTV dynamics presented in Chapter 2 motivated the focus on convex optimization techniques for determining maneuver plans for station-keeping of (a fleet of) geostationary satellites. In the remainder of this section we introduce a series of increasingly relevant optimization problems. Each subsequent problem addresses a shortcoming of the prior problem formulation. The solution of each problem is a maneuver plan for station-keeping of a geostationary satellite.

### 4.2.1. GENERAL PROBLEM FORMULATION AND CONVENTIONS

The planning of station-keeping maneuvers of GEO satellites can be formulated as an optimal control problem. We aim to formulate the station-keeping problem as a convex optimization problem in standard form [11, chap.4]:

**Problem 4.1.**

$$\begin{aligned} \text{minimize} \quad & f_0\left(\mathbf{z}\right) \\ \text{subject to} \quad & f_i\left(\mathbf{z}\right) \leq 0 \\ & \mathbf{A}\mathbf{z} = \mathbf{b}, \end{aligned} \tag{4.11}$$

with cost function $f_0$ and inequality constraints $f_i$ convex and the equality constraints $\mathbf{A}\mathbf{z} = \mathbf{b}$ affine. The solution of the optimization problem is the decision variable vector $\mathbf{z}^\star$ that minimizes the cost function while satisfying all constraints.

We will formulate a sequence of problems with increasing complexity that can be solved to determine station-keeping maneuvers for a geostationary satellite. Each of the problems we consider is formulated as a *convex* optimization problem. This important characteristic ensures that the problem solution, a minimum of the cost function satisfying the constraints, is in fact the global minimum. Further, crude bounds on the computation time can be derived from a complexity analysis of the problem and stable algorithms exist to robustly solve the optimization problem [11]. In every problem formulation the ultimate goal is to determine the thrust force exerted on the satellite by each of the thrusters over the duration of a maneuver cycle. The main decision variable vector is thus the thrust force vector $\boldsymbol{\tau}$ and the "planning horizon" is the maneuver cycle duration.

We repeat the affine equation for the dynamics for all $N$ future states $\mathbf{x}_{\text{tot}}$, Eq. (2.52), where we include the size of the vectors and matrices explicitly for clarity (assuming 6 states and 4 thrusters):

$$\mathbf{x}_{\text{tot}}^{6N\times 1} = \mathbf{F}^{6N\times 6}\mathbf{x}_0^{6\times 1} + \mathbf{H}^{6N\times 3N}\boldsymbol{\Gamma}^{3N\times 4N}\boldsymbol{\tau}_{\text{tot}}^{4N\times 1} + \mathbf{J}^{6N\times 3N}\mathbf{d}_{\text{tot}}^{3N\times 1}. \tag{4.12}$$

As an example, an optimization problem with a timestep of 1080 seconds and a planning horizon of 7 days requires $N = 560$ time intervals and $4N = 2240$ decision variables, comprised in the vector $\boldsymbol{\tau}_{\text{tot}}$.

Assuming a convex domain for $\boldsymbol{\tau}_{\text{tot}}$ allows to include any convex combination of $\mathbf{x}_{\text{tot}}$ and $\boldsymbol{\tau}_{\text{tot}}$ as cost function or inequality constraint and any affine combination of $\mathbf{x}_{\text{tot}}$ and $\boldsymbol{\tau}_{\text{tot}}$ as equality constraint. To obtain a certain state at a particular discrete point in time we can simply select the particular rows in $\mathbf{F}$, $\mathbf{H}$ and $\mathbf{J}$ corresponding to that state. As a general convention we use indices to refer to particular rows and columns of the matrices. As an example, to "select" the last state we use to following notation:

$$\mathbf{x}_{\text{tot}}\left(6N\right) = \mathbf{F}\left(6N,:\right)\mathbf{x}_0 + \mathbf{H}\left(6N,:\right)\boldsymbol{\Gamma}\boldsymbol{\tau}_{\text{tot}} + \mathbf{J}\left(6N,:\right)\mathbf{d}_{\text{tot}}. \tag{4.13}$$

We introduce another notational convention, namely to refer to the state vector (all 6 elements) at a particular discrete point in time $k$ by adding a subscript to $\mathbf{F}$, $\mathbf{H}$ and $\mathbf{J}$. Again we illustrate with an example. The notation

$$\mathbf{x}_k = \mathbf{F}_k\mathbf{x}_0 + \mathbf{H}_k\boldsymbol{\Gamma}\boldsymbol{\tau}_{\text{tot}} + \mathbf{J}_k\mathbf{d}_{\text{tot}} \tag{4.14}$$

refers to the $k^{\text{th}}$ discrete state vector. The subscript $k$ added to $\mathbf{F}$, $\mathbf{H}$ and $\mathbf{J}$ indicates that only those rows required to form $\mathbf{x}_k$ are "selected" from those matrices. The same convention can be applied to individual elements of the state vector such that e.g. $\Delta L_k$ is the mean longitude difference at the discrete node $k$.
The above equations provide us with the osculating satellite state. However, desired states are often defined in terms of mean states. To obtain the mean state $\mathbf{x}^{\text{m}}_{\text{tot}}$, we simply evaluate the mean-to-osculating transformation at the discrete time-points matching the discrete osculating state and subtract it from the osculating state:

$$\mathbf{x}^{\text{m}}_{\text{tot}} = \mathbf{F}\mathbf{x}_0 + \mathbf{H}\boldsymbol{\Gamma}\boldsymbol{\tau}_{\text{tot}} + \mathbf{J}\mathbf{d}_{\text{tot}} - \mathbf{x}^{\text{o2m}}_{\text{tot}}.. \tag{4.15}$$

Hence, in summary, we aim to formulate an optimization problem that solves the station-keeping problem. The thrust force variables over the discrete intervals are the optimization variables and we have access to the state at each discrete node, such that both state variables and thrust variables can be constrained.

### 4.2.2. BASIC FORMULATION

We start with a basic formulation in which the optimization variables are directly the accelerations over the discrete intervals ($\mathbf{u}_{\text{tot}}$). Note that from these accelerations we can directly obtain $\Delta\mathbf{V}$ by multiplying the acceleration with the length of the discrete interval. We include only a constraint on the final state and as such, this basic problem is equivalent to the conventional station-keeping problem of calculating a set of orbital element differences to be achieved at the end of a maneuver cycle.

The basic formulation of the convex optimization problem to calculate the station-keeping maneuvers is as follows:

**Problem 4.2.**

$$\begin{aligned} &\text{minimize} \quad \|\mathbf{u}_{\text{tot}}\|_1 \\ &\text{subject to} \end{aligned}$$

$$\mathbf{F}_N\mathbf{x}_0 + \mathbf{H}_N\mathbf{u}_{\text{tot}} + \mathbf{J}_N\mathbf{d}_{\text{tot}} - \mathbf{x}^{\text{o2m}}_N = \mathbf{x}^{\text{m}}_{N,\text{des}}.$$

Solving this problem gives the optimal acceleration profile $\mathbf{u}^{\star}_{\text{tot}}$ that brings us from initial state $\mathbf{x}_0$ at $t_0$ to the desired final state $\mathbf{x}_{N,\text{des}} = \mathbf{x}^{\text{m}}_{N,\text{des}} + \mathbf{x}^{\text{o2m}}_N$ at $t_N$.

The choice of the objective function significantly impacts the solution of the optimization problem. As the use of propellant in space is extremely costly, a general objective is to minimize propellant consumption. In addition, thrusters have a limited number of duty cycles which can range from hundreds to millions of firings depending on the type of thruster. Common operational practice and a limited number of thruster firings strongly favor a cost function that penalizes the $\ell_1$-norm of control since the formulation of an optimization problem with an $\ell_1$-norm of control action naturally results in a sparse solution with limited thruster firings and it explicitly minimizes propellant consumption. The solution resulting from this cost function has significant benefits over a cost function penalizing the $\ell_2$-norm of control. An $\ell_2$-norm penalizes large $\Delta V$s more (in a relative sense) than an $\ell_1$ norm would, resulting in a solution to the optimization problem with many small accelerations (usually a continuous acceleration profile) requiring more propellant and more thruster firings than a solution based on an $\ell_1$-norm in the cost function. Examples of thrust profiles resulting from an $\ell_2$-norm in the cost function can be found in [12].

The only constraints are defined as a desired final state to be achieved at the end of the maneuver cycle. Note that this optimization problem is very similar to the conventional method; the conventional method calculates a set of impulsive maneuvers ($\Delta V$s) to achieve a desired set of state differences. In conventional station-keeping usually only five states are constrained, while $\Delta n$ is left free. The degree of freedom thus gained can then be used to minimize propellant consumption. In the optimization problem formulation we can do exactly the same by simply eliminating the constraint related to $\Delta n$. Furthermore, the conventional method usually separates NS and EW maneuvers and allows these maneuver to take place only at certain specific days in the maneuver cycle. Again, we can enforce a similar schedule by splitting the optimization problem in two smaller problems, one problem for calculating NS maneuvers and one for calculating EW maneuvers. The smaller problems can be obtained by setting the relevant elements in $\mathbf{u}_{\text{tot}}$ equal to zero (or removing them completely from the decision vector, while also remove the corresponding columns in $\mathbf{H}$ and $\mathbf{\Gamma}$). In Section 4.4.1 a demonstration is given under these settings, and the results between a conventional scheme is compared to the solution of Problem 4.2.

### 4.2.3. THRUST AND THRUSTER CONFIGURATION

Two key limitations of Problem 4.2, and also of the conventional methods, are that 1.) the thrust force cannot be constrained and 2.) it is assumed that either the thrusters are aligned with East-West and North-South directions, or pure East-West and North-South maneuvers can be realized by the thruster configuration of the satellite, e.g. by firing two thruster simultaneously. In general, for a classical satellite with a chemical propulsion system in the REF configuration and a relatively large thrust-to-mass ratio this does not cause any issues. However, for satellites with an electric propulsion system with a much smaller thrust-to-mass ratio this can result in non-negligible errors in the predicted and achieved effect of a maneuver. The size of the error increases for larger thruster firing durations, and an approximation of this error can be derived from the results presented in Section 4.3.3. In addition, electric thrusters usually point away from North and South directions, creating the need to explicitly account for the thruster configuration in the problem definition. To counteract these limitations we can extend the optimization problem to include thrust force limitations and include the thruster configuration:

**Problem 4.3.**

$$\begin{aligned} &\text{minimize} \quad \|\boldsymbol{\tau}_{\text{tot}}\|_1 \\ &\text{subject to} \end{aligned}$$

$$\begin{aligned} \mathbf{F}_N\mathbf{x}_0 + \mathbf{H}_N\boldsymbol{\Gamma}\boldsymbol{\tau}_{\text{tot}} + \mathbf{J}_N\mathbf{d}_{\text{tot}} - \mathbf{x}_N^{\text{o2m}} &= \mathbf{x}_{N,\text{des}}^{\text{m}} \\ \boldsymbol{\tau}_{\text{tot}} &\leq \boldsymbol{\tau}_{\max} \\ -\boldsymbol{\tau}_{\text{tot}} &\leq \mathbf{0}. \end{aligned}$$

The independent variables are now directly the thrust forces of each thruster separately and can vary in the range $[0, \tau_{\max}]$ (the vector inequalities are element-wise inequalities). Of course $\tau_{\max}$ can vary between the different thrusters (or can be set to zero whenever a thrust is not allowed for other reasons such as during eclipses). The key advantage of this formulation is that it decreases the error in achieving the final state for satellites with a very low thrust-to-mass ratio.

### 4.2.4. STANDARD PROBLEM FORMULATION

One of the key advantages of formulating the station-keeping problem as an optimization problem is that it allows to constrain the satellite states at any of the discrete time-points. One major application is to explicitly constrain the satellite to stay inside the geostationary slot, which can be achieved by defining suitable bounds on the eccentricity, inclination and mean longitude deviation. We first define the problem in general terms; we then introduce some particular constraints.

**Problem 4.4.**

$$\begin{aligned} &\text{minimize} \quad \|\mathbf{W}_\tau\boldsymbol{\tau}_{\text{tot}}\|_1 \\ &\text{subject to} \end{aligned}$$

$$\begin{aligned} \mathbf{c}(\boldsymbol{\tau}_{\text{tot}}) &\leq \mathbf{c}_{\max} \\ \mathbf{A}\boldsymbol{\tau}_{\text{tot}} &= \mathbf{b} \\ \boldsymbol{\tau}_{\text{tot}} &\leq \boldsymbol{\tau}_{\max} \\ -\boldsymbol{\tau}_{\text{tot}} &\leq \mathbf{0} \end{aligned}$$

In this problem $\mathbf{c}(\boldsymbol{\tau}_{\text{tot}}) \leq \mathbf{c}_{\max}$ is a vector of inequality constraints while $\mathbf{A}\boldsymbol{\tau}_{\text{tot}} = \mathbf{b}$ are equality constraints. The inequality and equality constraints are respectively convex and affine in $\boldsymbol{\tau}_{\text{tot}}$. Since $\mathbf{x}_{\text{tot}}$ is affine in $\boldsymbol{\tau}_{\text{tot}}$, we can include also any convex or affine function of $\mathbf{x}_{\text{tot}}$ as inequality, respectively equality constraint in the problem. We further included a weighting matrix $\mathbf{W}_\tau$. This matrix is diagonal and can be used to add a relative importance to the different thrusters, or thrust components at different times.

To enforce an equality constraint on the osculating state at the $k^{\text{th}}$ discrete time we formulate:

$$\mathbf{A}\boldsymbol{\tau}_{\text{tot}} = \mathbf{H}_k\boldsymbol{\Gamma}\boldsymbol{\tau}_{\text{tot}} = -\mathbf{F}_k\mathbf{x}_0 - \mathbf{J}_k\mathbf{d}_{\text{tot}} + \mathbf{x}_{k,\text{des}} = \mathbf{b}_1 \tag{4.16}$$

and similarly to constrain the mean state at the $k^{\text{th}}$ discrete time we write:

$$\mathbf{A}\boldsymbol{\tau}_{\text{tot}} = \mathbf{H}_k\boldsymbol{\Gamma}\boldsymbol{\tau}_{\text{tot}} = -\mathbf{F}_k\mathbf{x}_0 - \mathbf{J}_k\mathbf{d}_{\text{tot}} + \mathbf{x}_k^{\text{o2m}} + \mathbf{x}_{k,\text{des}}^{\text{m}} = \mathbf{b}_2. \tag{4.17}$$

Inequality constraints could be added to enforce the geoslot boundaries through constraining the mean orbital motion deviation, the mean longitude deviation, the eccentricity and the inclination. For a particular discrete time $k$ these constraints are as follows:

$$\begin{aligned}
c_1\left(\boldsymbol{\tau}_{\text{tot}}\right) &= & -\Delta n_k &\leq -\Delta n_{\min} = c_{1,\max} && (4.18)\\
c_2\left(\boldsymbol{\tau}_{\text{tot}}\right) &= & \Delta n_k &\leq \Delta n_{\max} = c_{2,\max} && (4.19)\\
c_3\left(\boldsymbol{\tau}_{\text{tot}}\right) &= & \sqrt{e_{x,k}^2 + e_{y,k}^2} &\leq e_{\max} = c_{3,\max} && (4.20)\\
c_4\left(\boldsymbol{\tau}_{\text{tot}}\right) &= & \sqrt{i_{x,k}^2 + i_{y,k}^2} &\leq i_{\max} = c_{4,\max} && (4.21)\\
c_5\left(\boldsymbol{\tau}_{\text{tot}}\right) &= & -\Delta L_k &\leq -\Delta L_{\min} = c_{5,\max} && (4.22)\\
c_6\left(\boldsymbol{\tau}_{\text{tot}}\right) &= & \Delta L_k &\leq \Delta L_{\max} = c_{6,\max}, && (4.23)
\end{aligned}$$

for suitable choices of $\Delta n_{\min}$, $\Delta n_{\max}$, $e_{\max}$, $i_{\max}$, $\Delta L_{\min}$ and $\Delta L_{\max}$. Of course any other inequality constraint that is convex in $\boldsymbol{\tau}_{\text{tot}}$ or equality constraint that is affine in $\boldsymbol{\tau}_{\text{tot}}$ could be formulated and included in the optimization problem as well.

### 4.2.5. STANDARD SCALED PROBLEM

In order to improve the numerical solution of optimization problems it is good practice to scale the problem such that the different variables and constraints vary in more uniform ranges. Proper scaling enhances robustness and improves convergence of the optimization problem [13] and a proper scaling will make the problem reliably solvable for a large range of thrust-to-mass ratios and a large range of different constraints. As an example, consider a constraint that limits the absolute value of $\Delta n$. From Figure 2.5 we see that this variable has a magnitude in the order of 1e-9 rad/s. Depending on the solver's setting, the algorithm for solving the optimization problem might terminate if the constraints are met to within a tolerance of 1e-8. Now in this case, a constraint violation of $\Delta n$ will never be detected. To counteract such problems and to improve the convergence properties of the solution algorithms a scaling of the optimization is performed.

The decision variables (i.e. the concatenated thrust vector) are scaled so that the magnitude of each decision variable can vary in the range $[0,1]$. This is achieved by applying the following scaling law:

$$\begin{aligned}
\bar{\boldsymbol{\tau}} &= \mathbf{T}\boldsymbol{\tau} && (4.24)\\
&= \begin{pmatrix} 1/T_{1,\max} & & & \\ & 1/T_{2,\max} & & \\ & & 1/T_{3,\max} & \\ & & & 1/T_{4,\max} \end{pmatrix}\boldsymbol{\tau},
\end{aligned}$$

where $T_{i,\max}$ denotes the (maximum) thrust that the $i^{\text{th}}$ thruster can deliver. Note that we use a bar $\{\bar{\cdot}\}$ to indicate a scaled variable. The complete (concatenated) vector of thrusts in the range $k = 1,..,N$ is defined as:

$$\begin{aligned}\bar{\boldsymbol{\tau}}_{\text{tot}} &= \mathscr{T}\boldsymbol{\tau}_{\text{tot}} \\ &= \begin{pmatrix}\mathbf{T} & & \\ & \mathbf{T} & \\ & & \ddots\end{pmatrix}\boldsymbol{\tau}_{\text{tot}}.\end{aligned} \tag{4.25}$$

For the constraints the scaling might not be as unambiguous as for the thrust vector, but we aim to implement a similar idea. As discussed above, an inequality constraint generally has the following form:

$$c\left(\boldsymbol{\tau}_{\text{tot}}\right) \leq c_{\max}, \tag{4.26}$$

scaling this equation by $c_{\max}$ and assuming $c_{\max}$ is positive results in the following scaled constraint:

$$\bar{c}\left(\boldsymbol{\tau}_{\text{tot}}\right) = \frac{1}{c_{\max}} c\left(\boldsymbol{\tau}_{\text{tot}}\right) \leq 1. \tag{4.27}$$

To apply this simple scaling law we need to formulate a constraint such that this scaling leads to a desired scaled constraint (i.e. if the right hand side of Eq. (4.26) would be equal to zero this clearly would not work). We do this by formulating affine inequality constraints with an upper and lower bound such that the upper and lower bound have identical magnitude $c_{\max}$ (and after scaling these bounds are equal to one). The convex constraints we deal with are formulated so that they are allowed to vary in the range $[0, c_{\max}]$ (and after scaling $[0,1]$). We exemplify the scaling using the inequality constraints from the previous section. We define

$$c_{1,\max} = c_{2,\max} = \frac{\Delta n_{\max} - \Delta n_{\min}}{2}, \tag{4.28}$$

$$\Delta n_{k,\text{mid}} = \frac{\Delta n_{\max} + \Delta n_{\min}}{2}, \tag{4.29}$$

$$c_{5,\max} = c_{6,\max} = \frac{\Delta L_{\max} - \Delta L_{\min}}{2}, \tag{4.30}$$

and

$$\Delta L_{k,\text{mid}} = \frac{\Delta L_{\max} + \Delta L_{\min}}{2}. \tag{4.31}$$

The scaled constraints can now be formulated as follows:

$$\bar{c}_1(\boldsymbol{\tau}_{\text{tot}}) = \frac{-\left(\Delta n_k - \Delta n_{k,\text{mid}}\right)}{c_{1,\max}} \le 1 \tag{4.32}$$

$$\bar{c}_2(\boldsymbol{\tau}_{\text{tot}}) = \frac{\left(\Delta n_k - \Delta n_{k,\text{mid}}\right)}{c_{2,\max}} \le 1 \tag{4.33}$$

$$\bar{c}_3(\boldsymbol{\tau}_{\text{tot}}) = \frac{\sqrt{e_{x,k}^2 + e_{y,k}^2}}{e_{\max}} \le 1 \tag{4.34}$$

$$\bar{c}_4(\boldsymbol{\tau}_{\text{tot}}) = \frac{\sqrt{i_{x,k}^2 + i_{y,k}^2}}{i_{\max}} \le 1 \tag{4.35}$$

$$\bar{c}_5(\boldsymbol{\tau}_{\text{tot}}) = \frac{-\left(\Delta L_k - \Delta L_{k,\text{mid}}\right)}{c_{5,\max}} \le 1 \tag{4.36}$$

$$\bar{c}_6(\boldsymbol{\tau}_{\text{tot}}) = \frac{\left(\Delta L_k - \Delta L_{k,\text{mid}}\right)}{c_{6,\max}} \le 1 \tag{4.37}$$

If we consistently apply this logic in the formulation of the constraints we can define a diagonal scaling matrix for the constraints similar to the thrust vector scaling as follows:

$$\begin{aligned}\bar{\mathbf{c}}(\boldsymbol{\tau}_{\text{tot}}) &= \mathscr{C}\mathbf{c}(\boldsymbol{\tau}_{\text{tot}}) \qquad (4.38)\\ &= \begin{pmatrix} 1/c_{1,\max} & & \\ & 1/c_{2,\max} & \\ & & \ddots \end{pmatrix} \mathbf{c}(\boldsymbol{\tau}_{\text{tot}}) \le \mathbf{1}.\end{aligned}$$

Alternatively, Eqs. (4.18)-(4.23) can be scaled using the geostationary slot size as a guideline for the maximum variations in each orbital element. It is not important to use the exact variations of the orbital elements, we only need to guess roughly the order of magnitude, so that the scaled variables vary in the same order of magnitude. For example, the mean longitude difference $\Delta L$ can be scaled by a factor $180/(0.1° \cdot \pi) \approx 570\ \text{rad}^{-1}$. A similar value can be used for eccentricity and inclination, while a value about two orders of magnitude larger should be used for mean orbital motion difference.

An affine equality constraint can be scaled based on the expected variations of that constraint during a maneuver cycle under "normal" circumstances. It might be debatable what "normal" circumstances are, but in most cases some guidelines could be obtained from operational experience. Consider an affine constraint:

$$\mathbf{a}_i^T \boldsymbol{\tau}_{\text{tot}} = b_i. \tag{4.39}$$

If we define $b_{i,\min}$ and $b_{i,\max}$ as the expected variations of the $i^{\text{th}}$ constraint, with $\Delta b_i = \frac{1}{2}\left(b_{i,\max} - b_{i,\min}\right) \ne 0$, the scaled constraint can be defined as follows:

$$\frac{1}{\Delta b_i}\left(\mathbf{a}_i^T \boldsymbol{\tau}_{\text{tot}} - b_i\right) = 0, \tag{4.40}$$

or for all equality constraints together we arrive at:

$$\begin{aligned}\bar{\mathbf{a}}\left(\boldsymbol{\tau}_{\text{tot}}\right) &= \mathscr{B}\left(\mathbf{A}\boldsymbol{\tau}_{\text{tot}} - \mathbf{b}\right) \\ &= \begin{pmatrix} 1/\Delta b_1 & & \\ & 1/\Delta b_2 & \\ & & \ddots \end{pmatrix} \left(\mathbf{A}\boldsymbol{\tau}_{\text{tot}} - \mathbf{b}\right) = \mathbf{0}.\end{aligned} \tag{4.41}$$

Again, as an alternative, we could also scale the constraints using the geostationary slot size as a guideline for the maximum variations in each orbital element.

Now we are ready to define the scaled optimization problem:

**Problem 4.5.**

$$\begin{aligned} &\text{minimize} \quad \|\mathbf{W}_\tau \bar{\boldsymbol{\tau}}_{\text{tot}}\|_1 \\ &\text{subject to} \end{aligned}$$

$$\begin{aligned} \bar{\mathbf{c}}\left(\boldsymbol{\tau}_{\text{tot}}\right) &\leq \mathbf{1} \\ \bar{\mathbf{a}}\left(\boldsymbol{\tau}_{\text{tot}}\right) &= \mathbf{0} \\ \bar{\boldsymbol{\tau}}_{\text{tot}} &\leq \mathbf{1} \\ -\bar{\boldsymbol{\tau}}_{\text{tot}} &\leq \mathbf{0}. \end{aligned}$$

To retrieve the solution of the unscaled problem, the optimal decision variables need to be unscaled using the inverse of $\mathscr{T}$. Note that this is the scaled version of Problem 4.4. To obtain scaled versions of Problems 4.3 and 4.2, we can apply the scaling to the final state constraints and the thrust vector. Note further that the constraints are still formulated as a function of $\boldsymbol{\tau}_{\text{tot}}$, whereas this should actually be replaced by $\mathscr{T}^{-1}\bar{\boldsymbol{\tau}}_{\text{tot}}$. We keep the current formulation as it is significantly more readable. In general, in the results derived in this work, scaled versions of the optimization problems were used due to their superior numerical stability and convergence properties.

### 4.2.6. GUARANTEEING FEASIBILITY

An undesired characteristic of the formulation of Problem 4.5 is that no guarantees can be given on the feasibility of the problem. This undesired property can be eliminated by including slack variables in the formulation of the problem as follows [11]:

**Problem 4.6.**

$$\begin{aligned} &\text{minimize} \quad \|\mathbf{W}_\tau \bar{\boldsymbol{\tau}}_{\text{tot}}\|_1 + \|\mathbf{W}_a \mathbf{s}_a\|_1 + \sum_{j=1}^{M_c} w_{cj} \cdot \max\left(0, s_{cj} - 1\right) \\ &\text{subject to} \end{aligned}$$

$$\begin{aligned} \bar{\mathbf{c}}\left(\boldsymbol{\tau}_{\text{tot}}\right) &\leq \mathbf{s}_c \\ \bar{\mathbf{a}}\left(\boldsymbol{\tau}_{\text{tot}}\right) &= \mathbf{s}_a \\ \bar{\boldsymbol{\tau}}_{\text{tot}} &\leq \mathbf{1} \\ -\bar{\boldsymbol{\tau}}_{\text{tot}} &\leq \mathbf{0} \end{aligned}$$

In this problem $\mathbf{s}_a$ and $\mathbf{s}_c$ are the slack variables related to respectively the $M_a$ equality constraints $\bar{\mathbf{a}}(\boldsymbol{\tau}_{\text{tot}})$ and $M_c$ inequality constraints $\bar{\mathbf{c}}(\boldsymbol{\tau}_{\text{tot}})$. The matrix $\mathbf{W}_a$ is a diagonal (positive definite) matrix containing the $M_a$ weight factors on $\mathbf{s}_a$, and $w_{cj}$ are the $M_c$ weight factors on $\mathbf{s}_c$. The decision variables in the optimization problem are now $\bar{\boldsymbol{\tau}}_{\text{tot}}$, $\mathbf{s}_a$ and $\mathbf{s}_c$, and the optimal solution is $\bar{\boldsymbol{\tau}}^{\star}_{\text{tot}}$, $\mathbf{s}^{\star}_a$ and $\mathbf{s}^{\star}_c$. Due to the introduction of the slack variables, this optimization problem is always feasible. If a constraint cannot be met, or if a constraint is extremely costly in terms of propellant consumption, the problem definition allows a violation of the constraints, however, with an impact on the cost function. The weight factors can be used to add a measure of relative importance between the different constraints. If the weights on the constraints are high (i.e. if constraint violations are heavily penalized), the solution of Problem 4.6 is identical to the solution of Problem 4.5, given that Problem 4.5 is feasible.

Now if an autonomous implementation of the calculation of the maneuvers is desired, a guaranteed problem feasibility is an important property. By solving Problem 4.6 we obtain the optimal values of $\mathbf{s}^{\star}_a$ and $\mathbf{s}^{\star}_c$ of the problem and can, by analyzing the optimal slack variables, directly see if all constraints are met, and if not, which constraints are causing problems. An autonomous implementation of such algorithms would benefit from Fault Detection, Isolation and Recovery (FDIR) functionality and a good input for a possible FDIR would be these slack variables.

### 4.2.7. LONG HORIZON - MULTIPLE SHOOTING FORMULATION

If we can solve the optimization problem for a very large horizon we can investigate whether guidance strategies such as the sun-pointing perigee strategy are suggested by the optimization problem solution. Furthermore, we could investigate the dependency of the thruster configuration on the optimal station-keeping strategy. Due to the periodicity of the perturbations a period of one year is a suitable time-horizon for investigating optimal station-keeping strategies. Hence, we need to formulate and solve the optimization problem for a horizon of one year.

In order to do so, we can “simply” take Problem 4.5, determine all involved equations for a horizon of one year and attempt to solve the resulting problem. The main problem with this approach is that each state is dependent on all preceding controls and the matrices involved in the problem are large dense matrices which require loads of memory and computational power to formulate and solve the resulting problem. By formulating the problem using a multiple shooting transcription method we can significantly decrease the number of control variables that a state variable depends on, at the cost of introducing additional decision variables [14].

We motivate this idea with an example. Let us assume we have formulated an instance of Problem 4.4 with affine equality constraints on all states

$$\mathbf{a}(\boldsymbol{\tau}_{\text{tot}}) = \mathbf{F}\mathbf{x}_0 + \mathbf{H}\boldsymbol{\Gamma}\boldsymbol{\tau}_{\text{tot}} + \mathbf{J}\mathbf{d}_{\text{tot}} - \mathbf{x}_{\text{tot,des}} = \mathbf{0}. \tag{4.42}$$

The algorithm for solving the problem requires the Jacobian of the constraint functions (a matrix containing the partial derivatives of all constraints with respect to all decision variables). In this case, the Jacobian is simply

$$\frac{\mathrm{d}\mathbf{a}}{\mathrm{d}\boldsymbol{\tau}_{\mathrm{tot}}} = \mathbf{H}\boldsymbol{\Gamma}, \tag{4.43}$$

since the equation is affine in $\boldsymbol{\tau}_{\mathrm{tot}}$. The Jacobian is a $6N \times 4N$ dense matrix with lower-triangular structure, see Eq. (4.12). Solving a linear equation containing this matrix becomes increasingly costly for large $N$. We can reformulate this equation, by introducing additional decision variables. In this motivating example, we split the problem into two segments with respectively $n_1$ and $n_2$ discretization steps so that $n_1 + n_2 = N$. We refer to the discrete step at the end of the first shooting segment with $N_1$ and thus $\mathbf{x}_{N_1}$ is the state at the end of the first shooting interval. This state is added to the decision variable vector. The state constraints now become:

$$\mathbf{a}_1\left(\boldsymbol{\tau}_{\mathrm{ms1}}\right) = \mathbf{F}_{\mathrm{ms1}}\mathbf{x}_0 + \mathbf{H}_{\mathrm{ms1}}\boldsymbol{\Gamma}_{\mathrm{ms1}}\boldsymbol{\tau}_{\mathrm{ms1}} + \mathbf{J}_{\mathrm{ms1}}\mathbf{d}_{\mathrm{ms1}} - \mathbf{x}_{\mathrm{ms1,des}} = \mathbf{0} \tag{4.44}$$

and

$$\mathbf{a}_2\left(\boldsymbol{\tau}_{\mathrm{ms2}}\right) = \mathbf{F}_{\mathrm{ms2}}\mathbf{x}_{N_1} + \mathbf{H}_{\mathrm{ms2}}\boldsymbol{\Gamma}_{\mathrm{ms2}}\boldsymbol{\tau}_{\mathrm{ms2}} + \mathbf{J}_{\mathrm{ms2}}\mathbf{d}_{\mathrm{ms2}} - \mathbf{x}_{\mathrm{ms2,des}} = \mathbf{0}. \tag{4.45}$$

We used subscript "ms$i$" to refer to all elements in the $i^{\mathrm{th}}$ multiple shooting interval. Furthermore, we introduce an additional "defect" constraint:

$$\mathbf{a}_3\left(\boldsymbol{\tau}_{\mathrm{ms1}}\right) = \mathbf{F}_{N_1}\mathbf{x}_0 + \mathbf{H}_{N_1}\boldsymbol{\Gamma}_{\mathrm{ms1}}\boldsymbol{\tau}_{\mathrm{ms1}} + \mathbf{J}_{N_1}\mathbf{d}_{\mathrm{ms1}} - \mathbf{x}_{N_1} = \mathbf{0}, \tag{4.46}$$

to enforce that the new set of constraints is equivalent the original set of constraints. A defect constraint is a constraint that enforces continuity [14], i.e. it ensures that the final state at a multiple shooting segment is the same as the initial state at the next multiple shooting segment. We now have two shooting intervals with an additional constraint enforcing continuity between the segments. The Jacobian of the constraints now becomes a $(6N+6) \times (4N+6)$ matrix with a much more sparse structure:

$$\frac{\mathrm{d}\mathbf{a}}{\mathrm{d}\mathbf{z}} = \left[\begin{array}{cc|c} \mathbf{H}_{\mathrm{ms1}}\boldsymbol{\Gamma}_{\mathrm{ms1}} & \mathbf{0} & \mathbf{0} \\ \mathbf{0} & \mathbf{H}_{\mathrm{ms2}}\boldsymbol{\Gamma}_{\mathrm{ms2}} & \mathbf{F}_{\mathrm{ms2}} \\ \hline \mathbf{H}_{N_1}\boldsymbol{\Gamma}_{\mathrm{ms1}} & \mathbf{0} & \mathbf{0} \end{array}\right], \tag{4.47}$$

with the new optimization variables:

$$\mathbf{z} = \left[\begin{array}{cc|c} \boldsymbol{\tau}_{\mathrm{ms1}}^T & \boldsymbol{\tau}_{\mathrm{ms2}}^T & \mathbf{x}_{N_1}^T \end{array}\right]^T. \tag{4.48}$$

Note that the upper left block in the Jacobian has the same size as the Jacobian in Eq. (4.43), however, half of the matrix is filled with zeros. Now any attempt at solving a linear equation involving this Jacobian can benefit from the increased sparsity obtained through the introduction of the additional decision variables and can potentially be performed more efficiently. Additionally, due to the increased sparsity of the upper-left block, less memory is required to store that part of the matrix compared to Eq. (4.43) (if the sparse structure is capitalized upon).

We can split the problem into at most $N$ shooting segments, one for each discretization interval. However, introducing an additional shooting segment is penalized by an increase in problem size (more constraints, more decision variables), and additional matrices are now included in the Jacobian ($\mathbf{F}_{\text{ms2}}$ and $\mathbf{H}_{N_1}\boldsymbol{\Gamma}_{\text{ms1}}$ in the example). Furthermore, going from one to two shooting intervals significantly increases sparsity of the upper-left block (by a factor two). However, the sparsity gain decreases for an increasing number of shooting segments. The computational time of the problem formulation and solution depends on the number of shooting segments. The required computational time depends on 1.) forming and storing the matrices in the problem formulation, 2.) transcribing the problem into one that is solvable by the solver (using the software CVX [15]) and 3.) solving the problem (using MOSEK [16], an off-the-shelf solver).

We are now ready to formulate the optimization problem using a multiple shooting transcription. We use the scaled Problem 4.6 as a basis, but with a decision variable vector $\mathbf{z}$ that now includes the state at the start of each "shooting interval". The optimization problem formulation is as follows:

**Problem 4.7.**

$$\text{minimize} \quad \|\mathbf{W}_\tau \bar{\boldsymbol{\tau}}_{\text{tot}}\|_1 + \|\mathbf{W}_a \mathbf{s}_a\|_1 + \sum_{j=1}^{M_c} w_{cj} \cdot \max\left(0, s_{cj} - 1\right)$$

subject to

$$\begin{aligned}
\bar{\mathbf{c}}(\mathbf{z}) &\leq \mathbf{s}_c \\
\bar{\mathbf{a}}(\mathbf{z}) &= \mathbf{s}_a \\
\bar{\mathbf{a}}_{\text{def}}(\mathbf{z}) &= \mathbf{0} \\
\bar{\boldsymbol{\tau}}_{\text{tot}} &\leq \mathbf{1} \\
-\bar{\boldsymbol{\tau}}_{\text{tot}} &\leq \mathbf{0}
\end{aligned}$$

The key difference with Problem 4.6 is that now the individual constraints in $\bar{\mathbf{c}}(\mathbf{z})$ and $\bar{\mathbf{a}}(\mathbf{z})$ depend on $\mathbf{z} = [\bar{\boldsymbol{\tau}}_{\text{tot}}, \bar{\mathbf{x}}_{\text{ms}}]^T$ and the defect constraints $\bar{\mathbf{a}}_{\text{def}}(\mathbf{z})$ have been added to the problem. We still have $N$ discrete timesteps, which are now divided into $N_{\text{ms}}$ equally sized shooting intervals. Each shooting interval spans $n_{\text{ms}}$ timesteps so that $n_{\text{ms}} \cdot N_{\text{ms}} = N$.

The state equations for the $N_{\text{ms}}$ shooting intervals are defined as follows:

$$\mathbf{x}_{\text{ms}i} = \mathbf{F}_{\text{ms}i}\mathbf{x}_{N_{i-1}} + \mathbf{H}_{\text{ms}i}\boldsymbol{\Gamma}_{\text{ms}i}\boldsymbol{\tau}_{\text{ms}i} + \mathbf{J}_{\text{ms}i}\mathbf{d}_{\text{ms}i}, \quad \text{for} \quad i = 1, \ldots, N_{\text{ms}}, \tag{4.49}$$

so that the total state equation is given as:

$$\begin{aligned}
\mathbf{x}_{\text{tot}} &= \begin{pmatrix} \mathbf{F}_{\text{ms1}} & & \\ & \ddots & \\ & & \mathbf{F}_{\text{msN}_{\text{ms}}} \end{pmatrix} \begin{pmatrix} \mathbf{x}_0 \\ \vdots \\ \mathbf{x}_{N_{N_{\text{ms}}-1}} \end{pmatrix} + \begin{pmatrix} \mathbf{H}_{\text{ms1}}\boldsymbol{\Gamma}_{\text{ms1}} & & \\ & \ddots & \\ & & \mathbf{H}_{\text{msN}_{\text{ms}}}\boldsymbol{\Gamma}_{\text{msN}_{\text{ms}}} \end{pmatrix} \boldsymbol{\tau}_{\text{tot}} \\
&\quad + \begin{pmatrix} \mathbf{J}_{\text{ms1}} & & \\ & \ddots & \\ & & \mathbf{J}_{\text{msN}_{\text{ms}}} \end{pmatrix} \mathbf{d}_{\text{tot}} \\
&= \mathbf{F}_{\text{ms}}\mathbf{x}_{\text{ms}} + (\mathbf{H}\boldsymbol{\Gamma})_{\text{ms}}\boldsymbol{\tau}_{\text{tot}} + \mathbf{J}_{\text{ms}}\mathbf{d}_{\text{tot}}.
\end{aligned} \tag{4.50}$$

The additional defect constraints that are added to the problem are:

$$\mathbf{a}_{\mathrm{def}} = \mathbf{F}_{N_i}\mathbf{x}_{N_{i-1}} + \mathbf{H}_{N_i}\boldsymbol{\Gamma}_{\mathrm{ms}i}\boldsymbol{\tau}_{\mathrm{ms}i} + \mathbf{J}_{N_i}\mathbf{d}_{\mathrm{ms}i} - \mathbf{x}_{N_i} = \mathbf{0}, \quad \text{for} \quad i = 1, \ldots, N_{\mathrm{ms}}. \tag{4.51}$$

Now we can, as before, select the rows from Eq (4.50) to obtain the states that we would like to constrain and formulate the convex inequality and affine equality constraints on these states. Scaling of these constraints can be performed in a manner similar as demonstrated in Section 4.2.5. Note that every state is again an affine function of the decision variable vector **z**.

## 4.3. CONCEPT OF OPERATIONS

In describing the concept of operations we focus on the two topics of interest in this work, which are guidance and maneuver planning. This concept of operations is the envisioned method of operations using the ideas developed in this work. The architecture is similar as in Figure 2.19, except that the plant model is replaced by an actual satellite in a geostationary orbit. We separate between Operator Task (OT) and Automated Task (AT) as well as between tasks that are required only infrequently (e.g. once at the start of the mission, or once every year) and tasks that are required every Maneuver Cycle (MC). Whenever we mention an automated activity, it is assumed that the automation is implemented on-ground, unless otherwise stated.

### 4.3.1. GUIDANCE

This section discusses several important processes in the guidance module. Table 4.1 summarizes the most important tasks that were identified. The table shows the frequency of execution and whether a task is to be performed by an operator or fully automated. The operator tasks are essentially the strategic definition and configuration of the station-keeping strategy. The first task (OT1) is self-explanatory, the second task (OT2) includes several strategic decisions, some examples are:

- Is a SPP strategy flown?
- Are NS and EW control treated together, or separated?
- Should a (weekly) schedule be used?
- Do we enforce constraints on mean or osculating orbital elements?

The third operator task (OT3) is the specification of the actual schedule: on which days are maneuvers flown, which days are reserved for orbit determinations. In OT4 the constraints are defined on a general level. Examples of such "general" constraints are:

- The definition of orbital element boundaries based on the geostationary slot size and maneuver duration
- Whether or not to avoid maneuvers in eclipses
- The definition of the maneuver constraints based on the propulsion system characteristics.

These operator tasks are ideally performed only once for the duration of the mission. The first two automated tasks (AT1 and AT2) generate piece-wise polynomials that are used to determine respectively the mean-to-osculating transformations at any desired epoch and the perturbing accelerations for setting up the LTV dynamics. Since both are determined for the center of the geostationary slot, this can be done ahead of time, e.g. once at the start of the mission, or re-evaluated every year. The remaining tasks are executed every maneuver cycle. These tasks include the specification of the actual constraints to be respected during the upcoming maneuver cycle (AT3) and the specification of the cost function including weight functions (AT4). Once the start time of a particular maneuver cycle is known, the mean-to-osculating transformation and the perturbing accelerations for all discrete nodes in the upcoming maneuver cycle can be determined. These provide important inputs for the maneuver planning algorithm.

Table 4.1: Overview of the key guidance tasks in the envisioned concept of operations (OT: operator task, AT: automated task, MC: maneuver cycle).

| **Identifier** | **Task** | **Freq.** |
|---|---|---|
| OT1 | Set the maneuver cycle duration | < 1/yr |
| OT2 | Generalized strategy definition | < 1/yr |
| OT3 | Set the schedule for the maneuver cycle | < 1/yr |
| OT4 | Generalized constraint definition | < 1/yr |
| AT1 | Determine the osculating to mean transformation at the slot center in the form of piece-wise polynomials, as a function of time | < 1/yr |
| AT2 | Determine the perturbing accelerations experienced by the slot center in the form of piece-wise polynomials as a function of time | < 1/yr |
| AT3 | Specific constraint definition | 1/MC |
| AT4 | Specific cost function definition | 1/MC |
| AT5 | Evaluate piecewise polynomials for osculating-to-mean transformation at the discrete nodes for the upcoming maneuver cycle | 1/MC |
| AT6 | Evaluate piecewise polynomials for perturbing accelerations at the discrete nodes for the upcoming maneuver cycle | 1/MC |

### 4.3.2. MANEUVER PLANNING

The maneuver planning module is essentially an automated function that receives a great deal of input from the guidance module, together with an initial state and epoch as a result of an orbit determination. The execution of the maneuver planning is triggered from within the guidance module (e.g. when a new orbit determination solution is available) and is executed generally once per maneuver cycle. The maneuver planning module uses the guidance and orbit determination information to generate a maneuver plan. This process can be summarized into several steps:

1. Setup the affine equations representing the orbital dynamics
2. Formulate the variables entering the cost and constraints function mathematically
3. Formulate the optimization problem (we did this using CVX)

4. Parse the optimization problem and feed it to a numeric solver (CVX)
5. Solve the problem (MOSEK)
6. Process the solution into a maneuver plan that can be executed by the satellite

Note that we have introduced both CVX and MOSEK. These are external software that we used to support the formulation (CVX [17], [15]) and solution (MOSEK [16]) of convex optimization problems. These tools make it straightforward to parse and solve the optimization problems, such that, in order to solve the station-keeping problem, we focus on the formulation of the problem rather than parsing it and feeding it to an algorithm that can solve the problem.

In a real-world application the maneuver plan would be send to the satellite as a (sequence of) telecommand(s) and executed (in open-loop) on-board the satellite. In principle, the maneuver planning can be repeated whenever a new orbit determination solution is available. The maneuver plan can then simply be overwritten in the satellite. As such it is possible to implement the same process as a receding horizon controller, with the planning horizon determined by the maneuver cycle duration and the frequency of re-planning determined by the frequency at which new orbit determination solutions are available. We provide one exemplary application using receding horizon control.

### 4.3.3. MANEUVER IMPLEMENTATION

The maneuver plans resulting from solving the optimization problems are processed before they are implemented. This is required because we assume that the thrusters have only a single qualified operational point and are hence on/off thrusters. Since we penalize the $\ell_1$-norm of the thrust vector in the cost function, the resulting maneuver plans are always sparse (i.e. they contain only a small number of nonzero elements). The maneuver plans resulting from a conventional method require a similar processing. Conventional station-keeping methods calculate an impulsive $\Delta V$, which is applied by switching on the thruster for a duration, so that the $\Delta V$ is realized. Assuming a burn with constant thrust force $T_{\max}$ and assuming that the mass $m$ stays constant, the acceleration profile resulting from a finite burn in tangential direction over the interval $[t_1,\ t_2]$ is defined as:

$$u_t(t) = \begin{cases} \frac{T_{\max}}{m}, & t \in [t_1,\ t_2] \\ 0, & \text{otherwise.} \end{cases} \tag{4.52}$$

This burn can be approximated by an impulsive burn at $t_m = (t_2 + t_1)/2$ as:

$$u_t(t) = \Delta V_t \delta(t - t_m)\,\mathrm{d}t, \tag{4.53}$$

where $\Delta V_t = T_{\max}/m \cdot (t_2 - t_1)$ and $\delta(t - t_m)$ is the Dirac delta function.

The left side of Figure 4.1 shows the concept for a transition from an impulsive $\Delta V$ to a finite burn. In realizing the maneuver plans resulting from an optimization problem we use the following logic; if subsequent time intervals for a single thruster have a nonzero thrust, these are combined into a single burn, centered on a weighted average of the individual thrusts, with a magnitude equal to $T_{\max}$, and a duration such that the total impulse is equal to the sum of the individual elements. This process is visualized on the right side of Fig. 4.1. We can limit the number of subsequent intervals that are combined

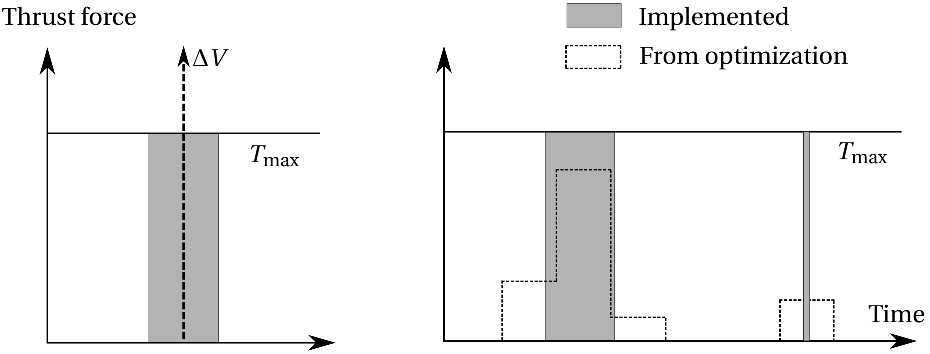

Figure 4.1: Implementation of finite thrust maneuver from impulsive $\Delta V$ (left) or from the solution of an optimization problem (right).

into a single burn so that the error resulting from this processing remains bounded. We found three subsequent segments (for a segment duration of 1080 s) a good trade-off between limiting the maximum error and allowing for long duration maneuvers (i.e. for satellite with low thrust-to-mass ratios).

A short analysis on the magnitude of the error introduced due to this processing is presented here. From Eq. (2.11) it is observed that both methods introduce an error in realizing changes to eccentricity and inclination vectors. The maneuver duration affects the change at a particular orbital element through a sinusoidal function of $\alpha$, hence we can provide an estimate of the error for both approaches. We investigate the effect of a tangential maneuver on $e_y$. An impulsive (superscript $I$) approximation is obtained as:

$$\Delta e_y^I = \frac{2}{V_{\text{geo}}} \sin \alpha_m \cdot \Delta V_t, \tag{4.54}$$

where $\Delta V_t = u_t \Delta t = u_t n_{\text{geo}} \Delta\alpha$. The effect of a finite burn (superscript $FB$) is calculated as:

$$\Delta e_y^{FB} = \frac{2}{V_{\text{geo}}} u_t n_{\text{geo}} \int_{\alpha-\Delta\alpha/2}^{\alpha+\Delta\alpha/2} \sin\alpha \cdot \mathrm{d}\alpha. \tag{4.55}$$

The relative error $e_{\Delta e_y}$ can be expressed analytically as

$$e_{\Delta e_y} = \frac{\Delta e_y^I - \Delta e_y^{FB}}{\Delta e_y^I} = \frac{\Delta\alpha - 2\sin\frac{\Delta\alpha}{2}}{\Delta\alpha}, \tag{4.56}$$

where the numerator has been specified so that a positive error results from a positive value for $\Delta\alpha$. An analysis of the other sinusoidal terms in Eq. (2.11) provides us with the exact same result. From Eq. (4.56) we find that the error that is made in case of calculating an impulsive maneuver is unbounded and depends on the maneuver duration. On the other hand, the maximum error that is made from the optimization problem solution is bounded through the length of the optimization interval. The maximum error is reached when processing an infinitesimally small maneuver, which can be interpreted

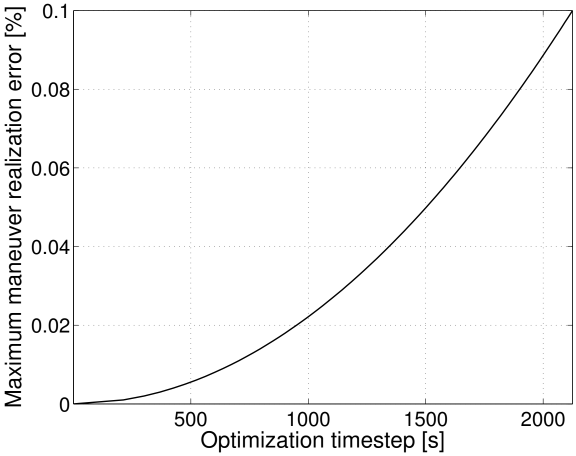

Figure 4.2: Maneuver realization error as a function of optimization timestep for a GEO satellite

impulsive. To guarantee an error smaller than a desired error tolerance $e_{\text{tol}}$ we solve the following equation for $\Delta\alpha$:

$$0 = \Delta\alpha\,(1 - e_{\text{tol}}) - 2\sin\frac{\Delta\alpha}{2}. \tag{4.57}$$

This equation is solved iteratively using Newton's method and the resulting $\Delta\alpha$ provides an upper bound for the optimization stepsize $\left(\Delta t = \Delta\alpha / n_{\text{geo}}\right)$ that guarantees an error smaller than the specified tolerance. The relation between the optimization timestep and the maximum error through maneuver realization is given in Figure 4.2 for errors up to 0.1%. We generally use optimization timesteps of 1080 s in most applications, resulting in a maneuver realization errors smaller than 0.023%. Figure 4.2 can be interpreted in another way. In case a maneuver is treated impulsively, the $x$-axis can be interpreted as maneuver duration with the $y$-axis showing the actual maneuver realization error. Hence the figure shows the benefits of the optimization based approach versus the conventional approach when maneuvers have long duration (e.g. when using low-thrust electric propulsion). Lastly, if the station-keeping algorithm calculates maneuvers that are shorter than the thruster's minimum on-time, these maneuvers are discarded, resulting in a maximum error equal to the minimum impulse bit.

## 4.4. SIMULATIONS, RESULTS AND ANALYSIS

In this section, we test the newly developed method. We start off with a comparison between the new method and the conventional scheme with two EW maneuvers and a single NS maneuver using a typical maneuver schedule for chemically propelled geostationary satellites. Another series of simulations investigates the solutions of the optimization problem with a one year horizon. These results are used to further validate the method by showing that the long horizon solution reproduces solutions (or strategies) known to be optimal, such as SPP. The sensitivity of the solution to certain constraint formulations is investigated, as well as the impact of the thruster configuration on the performance.

After the long horizon simulations we test the method in a more realistic scenario including orbit determination, actuation and modeling errors. We show that we can perform station-keeping in the presence of these errors and include a Monte-Carlo analysis to gain insight into the orbit prediction accuracy in terms of (relative) orbital elements. This orbit prediction accuracy is driving the achievable orbit control accuracy and hence the results obtained in this section provide a valuable source of information for the more challenging simulations in the next chapter, in which applications to a fleet of satellites are analyzed. The final simulation in this chapter demonstrates that if an orbit determination solution is available at a high frequency we can use the developed method as a receding horizon controller and substantially increase orbit control accuracy.

The simulations are performed using the simulation environment introduced in Section 2.7. Standard settings for the simulations are presented in Table 4.2 and these settings apply to all simulations unless otherwise stated.

Table 4.2: Standard simulation settings

| Aspect | Implementation |
|---:|:---:|
| Integrator | RK4 |
| Simulation timestep [s] | 108 |
| Optimization timestep [s] | 1080 |
| Order and degree Earth gravity | 10 |
| Sun gravity | yes |
| Moon gravity | yes |
| Solar radiation pressure | yes |
| Duration [days] | 364 |
| Longitude slot [deg] | 19.2 |

### 4.4.1. COMPARISON OF CONVENTIONAL AND NOVEL METHOD

We first demonstrate how the novel method for calculating station-keeping maneuvers functions in a scenario that is designed to resemble typical conventional operations. We configure the novel method such that the maneuver plans resulting from the optimization are very similar to a conventional operational scenario in which maneuvers are calculated according to a fixed schedule. We use a schedule in which EW maneuvers are calculated weekly, while NS maneuvers are calculated every fortnight. The schedule we use for this demonstration is given in Figure 4.3. On the first day an Orbit Determination (OD) is made, followed by a NS maneuver on day two. Day three and day ten are also used for OD, followed by EW maneuvers on day four and day eleven. The method is setup in such a way that thruster firings for NS maneuvers are constrained to take place only on the days marked by NS, and similarly EW maneuvers are allowed only on days marked with EW.

The goal of this scenario is to demonstrate that the novel method can reproduce the current state-of-art when configured to do so. This provides a valuable validation of the methodology (both for the modeling approach as well as for the method to calculate the station-keeping maneuvers) and establishes fidelity in the novel method. In order to

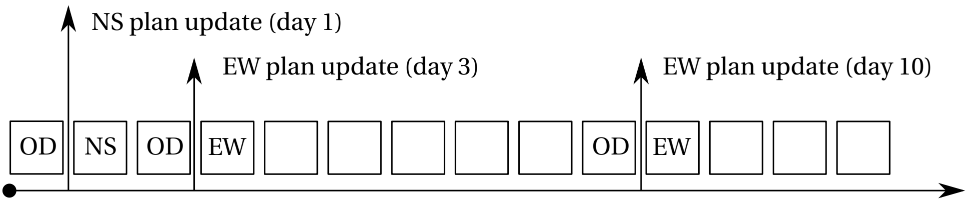

Figure 4.3: Typical 14 day maneuver schedule. Each box represents one day.

make the comparison, we have simulated side-by-side a conventional maneuver scheme and the novel method. The conventional scheme uses an analytic calculation of thruster pulses according to the method described in [18] (reproduced in Section 4.1.2), with two thruster pulses for EW maneuvers (separated by half an orbit) and a single pulse for NS maneuvers. The constraints on the final state are defined in an identical manner between the conventional method (*conv*) and the novel method (*cvx*). Both methods target a mean longitude of zero at the end of the EW maneuver cycle (7 days). The mean eccentricity at the end of the EW maneuver cycle is constrained to lie on an eccentricity circle following the classic SPP strategy. The inclination corrections target a zero mean inclination, to be achieved at the end of the day on which the NS maneuver is executed.

The novel method used a simplified version of the formulation in Problem 4.2; this was achieved by splitting up the problem into two smaller problems. The first problem considers only maneuvers in NS direction such that the optimization variables are only the acceleration components in NS direction $\mathbf{u}_{\text{tot,NS}}$, while the objective function simplifies to “minimize $\|\mathbf{u}_{\text{tot,NS}}\|_1$”. The constraints are defined as the desired mean inclination vector components at the end of day two in the cycle (i.e. only two constraints). This is achieved through a reduction of $\mathbf{F}_N$, $\mathbf{H}_N$, $\mathbf{J}_N$, $\mathbf{x}_N^{\text{o2m}}$ and $\mathbf{x}_{N,\text{des}}^{\text{m}}$ by selecting only the 4th and 5th rows, corresponding to the inclination vector components at $N$ (in this case $N$ corresponds to a time horizon of 1 day), while further reducing $\mathbf{H}_N$ by selecting the columns corresponding to the NS maneuvers (every 3rd column, starting at the 3rd column).

Similarly, the EW problem allows EW maneuvers ($\mathbf{u}_{\text{tot,EW}}$) on the first day after an EW plan update (see also Figure 4.3) with objective function “minimize $\|\mathbf{u}_{\text{tot,EW}}\|_1$”. The constraints are the desired mean longitude and eccentricity vector components to be achieved at the end of the EW maneuver cycle (the end of day 10, and day 3 in Figure 4.3). Now the 2nd, 3rd and 6th rows of the above matrices are selected at $N$ (here $N$ corresponds to a time horizon of 7 days), while further reducing $\mathbf{H}_N$ by selecting the columns corresponding to the EW maneuvers (every 3rd column, starting at the 2nd column). Both problems have the acceleration components over one day, in respectively NS and EW direction as optimization variables. The resulting optimization problems are very small and are setup, parsed and solved well under one second even with the parser-solver CVX in the loop.

The simulations contain no orbit determination, actuation or modeling errors (other than those induced by the LTV formulation of the dynamics). The satellites are modeled with a chemical propulsion system using the reference configuration with thrusters pointing in North, East and West directions (i.e. the NS maneuvers can be accomplished either with a North pointing thruster or with a South pointing thruster, we force both al-

Table 4.3: Initial osculating orbital elements

| **Parameter** | **Value** |
|---:|:---:|
| $\Delta n$ [rad/s] | -6.9E-09 |
| $e_x$ [-] | -8.9E-05 |
| $e_y$ [-] | 2.8E-04 |
| $i_x$ [rad] | 8.8E-04 |
| $i_y$ [rad] | -1.2E-04 |
| $\Delta L$ [rad] | 8.4E-05 |
| Epoch | 1 March 2010 10:00:00.0 UTC |

Table 4.4: Satellite parameters

| **Parameter** | **Value** |
|---:|:---:|
| Mass [kg] | 3000 |
| Surface area [m$^2$] | 120 |
| Solar reflection coefficient [-] | 1.2 |
| Max. thrust force [N] | 10 |
| Min. on-time [s] | 0.1 |

gorithms to use only a North pointing thruster to maximize comparability of the results).

The initial state (in osculating orbital elements) is given in Table 4.3. This initial state is chosen such that the mean initial state and the mean final state (after one year) are roughly the same (i.e. the mean eccentricity is already on the SPP circle, while the other elements have a mean of zero). Further relevant satellite parameters are summarized in Table 4.4.

Table 4.5: Propellant consumption and thruster firings over one year

| **method** | $\Delta V_{NS}$ [m/s] | $\Delta V_{EW}$ [m/s] | NS pulses | EW pulses |
|---:|:---:|:---:|:---:|:---:|
| *conv* | 47.972 | 3.039 | 26 | 104 |
| *cvx* | 47.968 | 3.036 | 26 | 104 |

The simulation was performed over a one year timeframe and the results present a side-by-side comparison of the conventional and novel methods. The main performance characteristics, namely number of thruster firings and propellant consumption, are presented in Table 4.5. From the table we observe that the performance is almost identical. Figures 4.4 and 4.5 present the location and magnitude of the orbit maneuvers. The figures show a remarkable resemblance. The maximum difference in magnitude of EW maneuvers was 0.0013 m/s. The maximum difference in location of the maneuver was equal to 0.53°. For NS maneuvers these figures are 0.0023 m/s and 0.16° respectively. From these results we conclude that the formulation of the problem as a

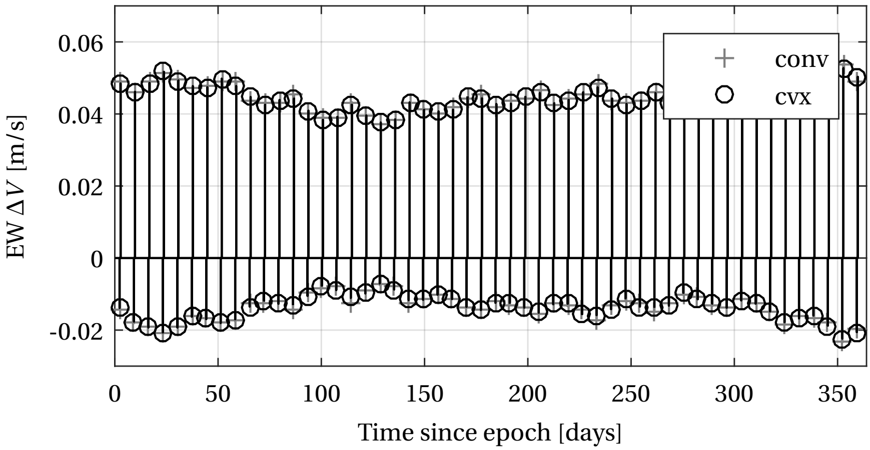

Figure 4.4: EW maneuvers in terms of $\Delta V$ of *conv* and *cvx* implementations over one year. A positive $\Delta V$ corresponds to a maneuver in the positive tangential direction, whereas a negative $\Delta V$ corresponds to a maneuver in the negative tangential direction.

convex optimization problem can reproduce thruster firings as if a state-of-art conventional method was used. This provides a critical validation of the concept.

The state trajectories in terms of synchronous orbital elements are given in Figures 4.6, 4.7 and 4.8. From these figures we can draw the same conclusion as before; namely both methods to calculate station-keeping maneuvers (although they are vastly different) produce almost identical results.

### 4.4.2. ANALYSIS OF LONG HORIZON PROBLEM SOLUTIONS

In this section, we solve Problem 4.7 for a horizon of one year, i.e. we solve an optimization problem to simultaneously determine the thruster pulses over a period of one year. The goals of this section are twofold. The first goal is to analyze the solution of the optimization problem and compare the results to tried-and-true guidance strategies for station-keeping of geostationary satellites. This can provide a further validation of the methodology. The second goal is investigate how sensitive the problem solution is to various parameters settings (e.g. thruster configuration) and constraint definitions. We focus on those settings that are relevant for the subsequent implementations of the novel method in more realistic simulation scenarios including orbit determination, actuation and modeling errors, both for a single satellite as well as for a fleet of collocated satellites.

Compared to the problem solved in Section 4.4.1 we now focus on a much more elaborate version of the problem:

- The time horizon is much larger (one year instead of one or two weeks).
- A single problem is solved (i.e. the problem is not split into smaller problems in respectively NS and EW direction).
- The thruster configuration is included.

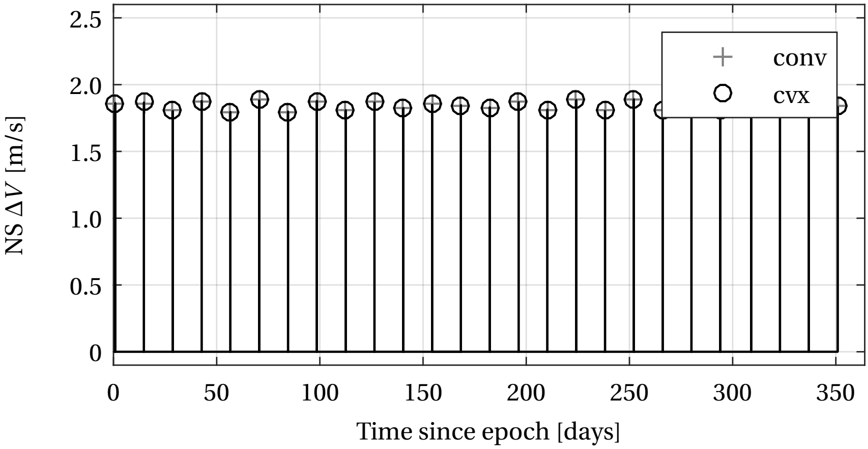

Figure 4.5: NS maneuvers in terms of $\Delta V$ of *conv* and *cvx* implementations over one year. A positive $\Delta V$ corresponds to a maneuver in the positive normal direction.

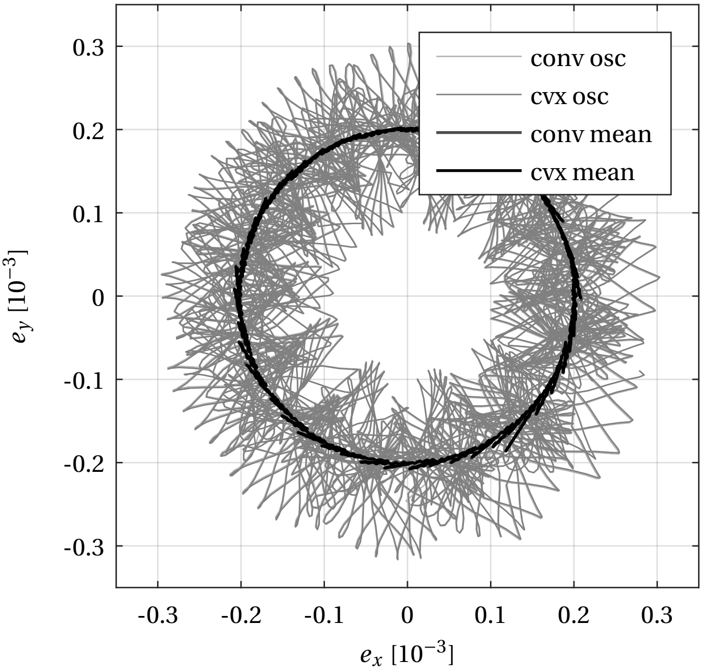

Figure 4.6: Mean and osculating eccentricity vector of *conv* and *cvx* implementations over one year. The differences between *conv* and *cvx* are not discernible.

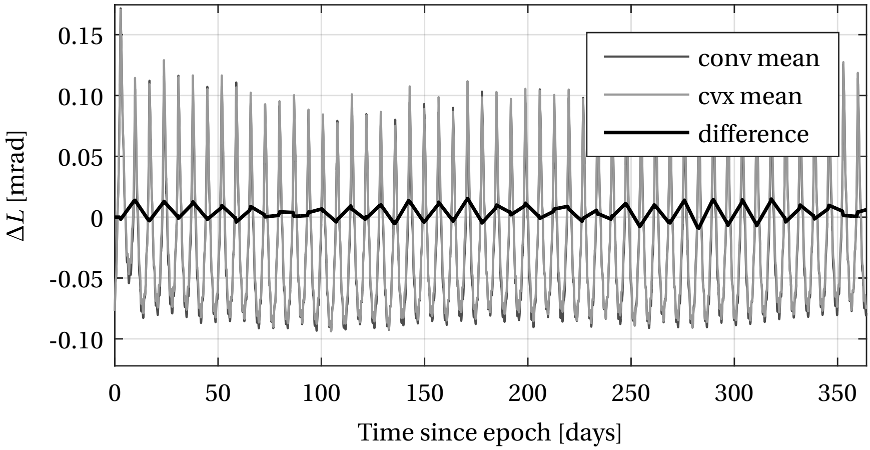

Figure 4.7: Mean longitude deviation of *conv* and *cvx* implementations and their difference over one year.

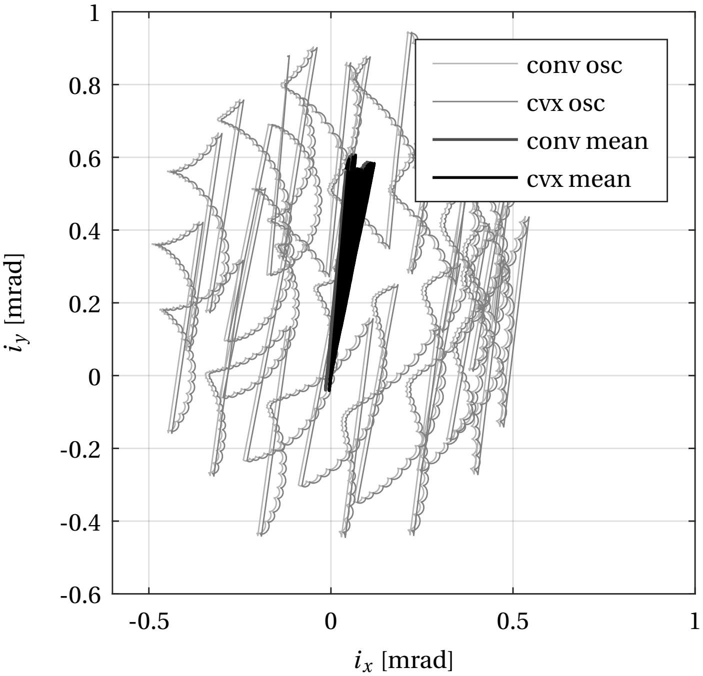

Figure 4.8: Mean and osculating inclination vector of *conv* and *cvx* implementations over one year. The differences between *conv* and *cvx* are hardly discernible.

- The maximum thrust force is constrained.
- The problem is scaled.
- The state is constrained at many more places than in Section 4.4.1.

The number of places at which we constrain the state is captured by a parameter that we call the Constraint Enforcement Ratio (CER). A CER of one would imply that state constraints are enforced at every discrete node in the optimization problem, while a CER of 10 would imply that constraints are enforced every $10^{\text{th}}$ timestep. The disadvantage of a large CER is that we have no (explicit) control over the state in the periods between two state constraints, while the disadvantage of a small CER is that parsing and solving the optimization problem requires more time and computational resources. Note that in the conventional case we have no control over the state at times other than the single point in time at which we apply the constraint. Being able to control the state at many more places is one of the key advantages of the novel method. We will investigate the impact of changing the CER such that we gain insight into the sensitivity of the algorithm to this parameter.

Another parameter that we can choose is how many discrete timesteps we include per multiple shooting segment. We have performed an analysis of the time it takes to setup the problem matrices, parse the problem (done by CVX) and solve the problem (done by an external solver, MOSEK). Without going into the details of this analysis we found as a general rule that it is a good idea to choose the number of discrete timesteps per multiple shooting segment equal to CER. Intuitively this makes sense, since we need to formulate and satisfy the defect constraint, Eq. (4.51), for the multiple shooting problem formulation. Thus, we have to calculate the state vector at these discrete times, and hence, we might as well formulate the constraints exactly at these discrete points in time. We further constrain the initial and final states to have identical mean values, such that the resulting strategy can be repeated year after year (i.e. otherwise we would always end up at the boundary of the control window and the results might look a little better than they would be in reality). The actual value of the initial and final state are left free for the optimizer to determine. This constraint ensures that the results are representative also if we are interested in scenarios that are longer that one year.

In these long-horizon problems we use a slightly larger timestep as in the other problems we investigate, in order to reduce the problem size to an acceptable level. We chose a timestep of 2160 seconds, such that exactly 40 timesteps fit into one day (or roughly one orbit). From Figure 4.2 we see that the maximum error thus made in realizing the thruster pulses is still smaller than 0.1%. We consider thruster configurations with four thrusters, and thus, with this choice of timestep we have $4 \cdot 40 \cdot 364 = 58240$ thrust force optimization variables to determine. In addition we have the state vectors at the end of each multiple shooting interval and the slack variables as optimization variables.

### ANALYSIS OF OPTIMAL STRATEGY FOR HIGH THRUST-TO-MASS RATIO

In this analysis we configure the optimization problem to use a high thrust chemical propulsion system in the reference configuration. We constrain either the osculating or mean eccentricity, inclination and mean longitude difference, either with or without enforcing a schedule. This leads to a total of four cases. The constraints are enforced once per orbit, i.e. the CER is equal to 40. Whenever we constrain mean orbital elements we reduce the tolerance window with the maximum mean-to-osculating variation of that element over the simulation horizon. A summary of the four cases used to setup Problem 4.7 is given in Table 4.6, where the cases are named using the identifier MS, meaning multiple shooting.

Before comparing the results of the four cases side-by-side, we investigate one case in more detail. Figures 4.9 to 4.12 show results from the MSC case. The state trajectories for the other cases look similar and hence we only need to analyze one of the four cases in detail to draw some more general conclusions regarding the optimal guidance strategy.

Table 4.6: Key simulation settings for long horizon simulations with high thrust-to-mass ratio.

| **Parameter** | **Unit** | **Value** | | | |
|---:|:---:|:---:|:---:|:---:|:---:|
| Case | | MSA | MSB | MSC | MSD |
| Tolerance on $e$ | $10^{-3}$ | 0.32 | 0.2 | 0.32 | 0.2 |
| Tolerance on $i$ | mrad | 1.22 | 0.69 | 1.22 | 0.69 |
| Tolerance on $\lvert\Delta L\rvert$ | mrad | 0.6 | 0.4 | 0.6 | 0.4 |
| Type of elements constrained | | Osculating | Mean | Osculating | Mean |
| CER | | 40 | 40 | 40 | 40 |
| Horizon | days | 364 | 364 | 364 | 364 |
| EW Schedule | | None | None | 1 out 14 | 1 out 14 |
| NS Schedule | | None | None | 1 out 14 | 1 out 14 |

Figure 4.9 shows the osculating inclination variation (light-grey) over a year. The NS maneuvers are shown in the figure by the thick (blue) line, while the tolerance window is indicated by the dashed (red) line. The important observation from this figure is that all inclination maneuvers achieve a change to the inclination vector that is (roughly) in the same direction. In terms of inclination control, conventional wisdom dictates that maneuvers should be made in the direction of the long-term secular variation of the inclination vector, and this is exactly what we see in Figure 4.9. All maneuvers are made in the same direction corresponding to the long-term (i.e. one year averaged) secular variation of the inclination vector, while the periodic variations are left uncontrolled.

Figure 4.10 shows the osculating eccentricity vector over one year as well as the implemented maneuvers and the tolerance window. We see very similar behavior of the eccentricity vector over the year as in Figure 4.6 in which a SPP strategy was used. To show that the optimization problem solution indeed suggests a SPP strategy, we show the difference between the eccentricity vector and the projection of the Sun onto the orbital plane in Figure 4.11. From this figure we see that the mean eccentricity vector closely follows the Sun vector over the one year period. Hence, also from the eccentricity control strategy we can see that the optimizer confirms the optimality of tried-and-true classical guidance strategies, or vice-versa, it provides a further validation that the novel methodology used to calculate station-keeping maneuvers is sound.

Figure 4.12 shows the osculating mean longitude difference over one year. In this figure we can recognize the typical parabolic longitude variations that are characteristic of a classical longitude control strategy when a schedule is imposed. We also see from this

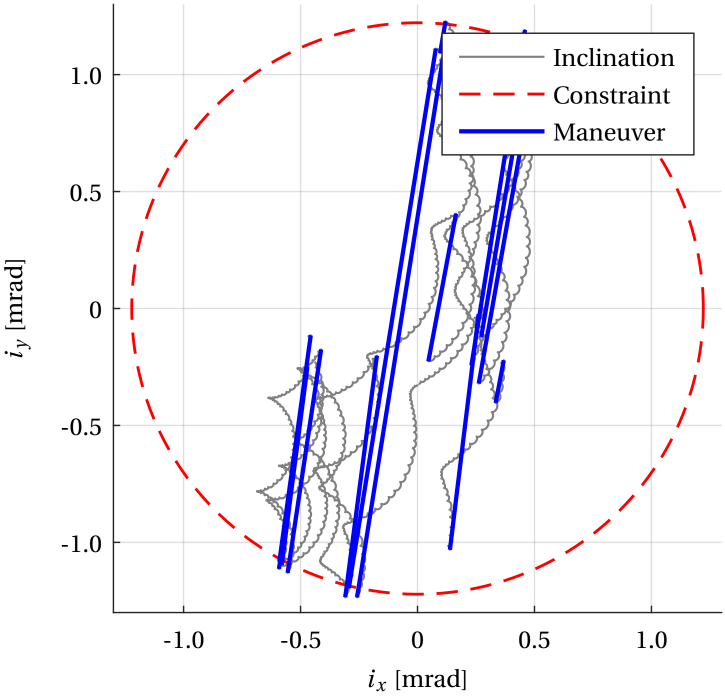

Figure 4.9: Osculating inclination vector over one year, case MSC.

figure that the constraints are violated at certain points in time. These violations result from the constraints being enforced only once every 40 discrete steps, while allowing violations in between. An analysis of the impact of a choice of CER is presented later in this chapter.

We now compare the four different cases in terms of propellant consumption and thruster firings. An overview of these results is given in Table 4.7. We first observe that the results are in close agreement with the results in Table 4.5 (which were based on a simulation using the full nonlinear equations of motion, while the results in this section are based only on the results of the optimization problem solution using the LTV approximation). We point out some interesting observations from this table; firstly, the $\Delta V_{NS}$ is almost identical in all cases, while the $\Delta V_{EW}$ is slightly higher in case the mean orbital elements are constrained (MSB and MSD). The reason is that the mean element constraints are slightly more restrictive since we reduced the tolerance window by the maximum expected osculating-to-mean variation to occur over the year. A much more interesting observation is the significant increase in number of thruster firings between cases MSA and MSB. This increase results from the constraint on mean eccentricity being active (n.b. with an active constraint we mean that the values on the left and right side

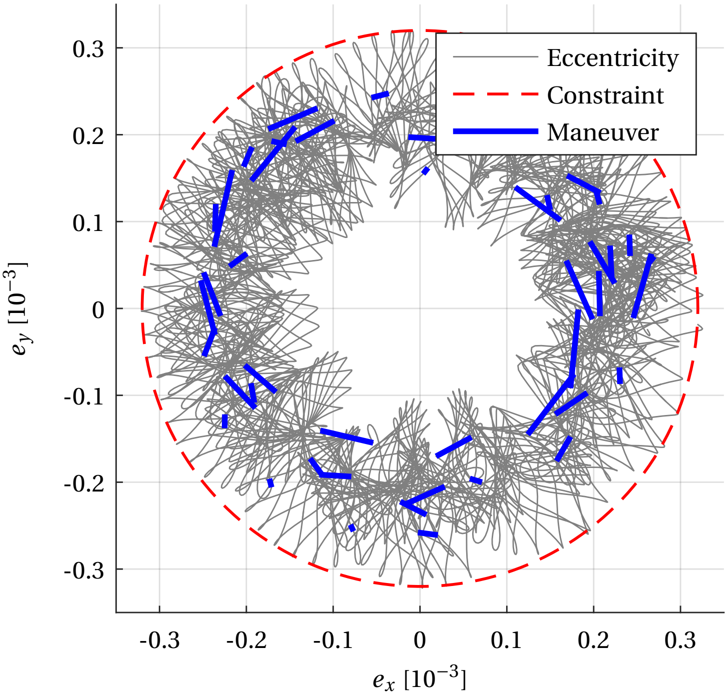

Figure 4.10: Osculating eccentricity vector over one year, case MSC.

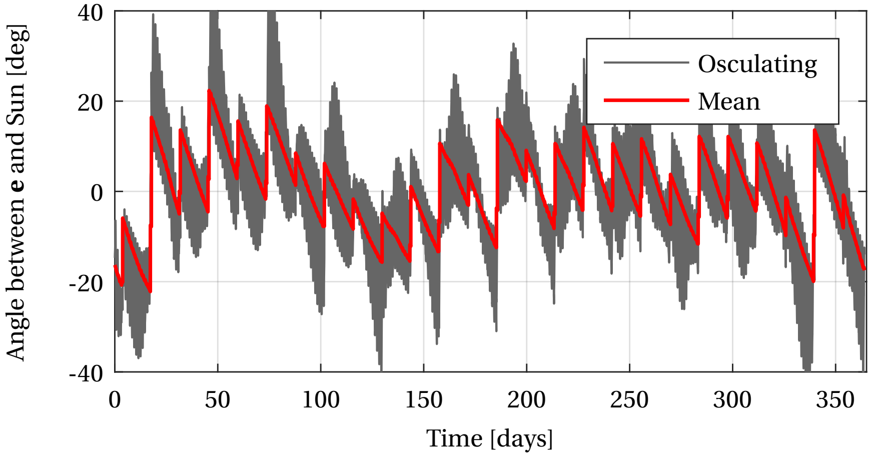

Figure 4.11: Angular difference between eccentricity vector and projected Sun vector, case MSC.

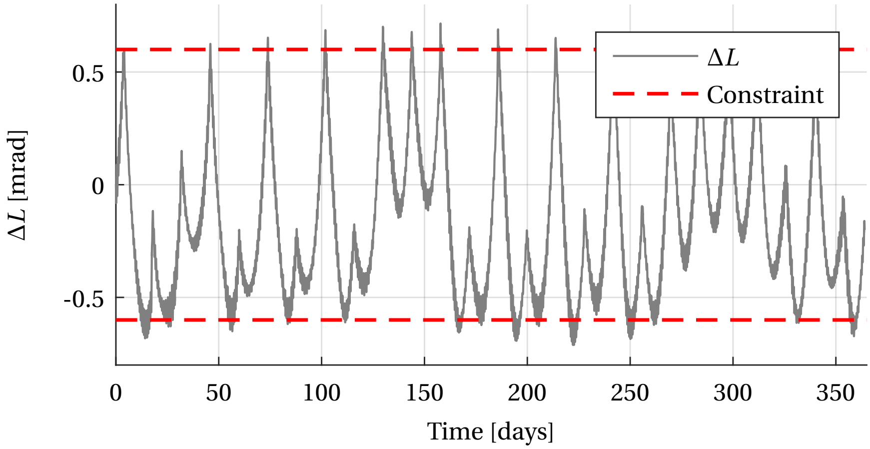

Figure 4.12: Osculating mean longitude difference, case MSC.

of an inequality constraint are roughly the same as the solution of the optimization problem) at (almost) every point in time in which the constraint is enforced. To show this we included Figure 4.13, displaying the mean eccentricity vector variations over one year, as well as the tolerance window. We see that the mean eccentricity lies almost completely on the constraint boundary and hence this constraint is active almost everywhere. Note that this is not the case when the osculating eccentricity is constrained, as evident from Figure 4.10. We further see that by imposing a schedule, we can reduce the number of required maneuver significantly (i.e. the cases where a schedule was enforced only needed respectively 59 and 66 of maneuvers per year for NS and EW station-keeping combined.

Table 4.7: Key results for long horizon simulations with high thrust-to-mass ratio.

| **Parameter** | **Unit** | **Value** | | | |
|---|---|---|---|---|---|
| Case | | MSA | MSB | MSC | MSD |
| $\Delta V_{NS}$ | m/s | 48.05 | 48.05 | 48.06 | 48.06 |
| $\Delta V_{EW}$ | m/s | 2.80 | 2.99 | 2.81 | 3.04 |
| NS Thruster firings | | 16 | 18 | 14 | 14 |
| EW Thruster firings | | 62 | 383 | 45 | 52 |

### SIZING ECCENTRICITY AND INCLINATION TOLERANCE WINDOWS

In this section we investigate case MSA from Table 4.6 again, while making changes to the size of the tolerance windows on eccentricity and inclination. We investigate what the impact of reducing or enlarging these windows is on the propellant consumption and number of thruster firings. Furthermore we show that we can reduce thruster firings by choosing suitable weight factors in the matrix $\mathbf{W}_{\tau}$.

Figures 4.14 and 4.15 show the propellant consumption and the number of thruster

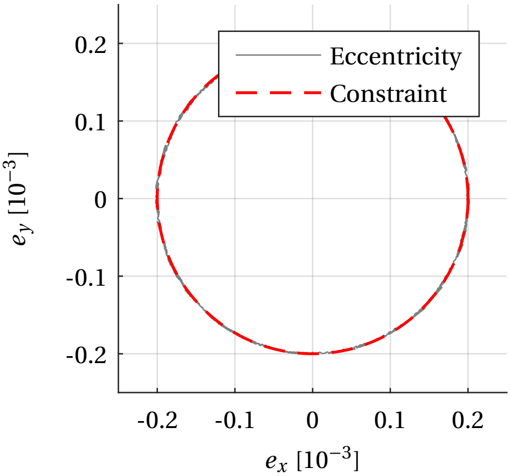

Figure 4.13: Mean eccentricity vector over one year, case MSB.

firings required for NS control. We observe from Figure 4.14 that the propellant consumption decreases with increasing size of the tolerance window, until the tolerance window reaches a size of approximately 0.5 mrad. This size coincides roughly with the size of the mean-to-osculating variations. This observation could be expected since for tolerance windows larger than 0.5 mrad the algorithm can “choose” a solution that only compensates for the secular variations while leaving the periodic variations uncontrolled. Also in terms of thruster firings we see a reduction with increasing control window size.

The graphs showing the propellant consumption and thruster firings for EW control are shown in Figures 4.16 and 4.17. In the propellant consumption plot we can identify three regions. Starting from the left, the first region corresponds to a control window

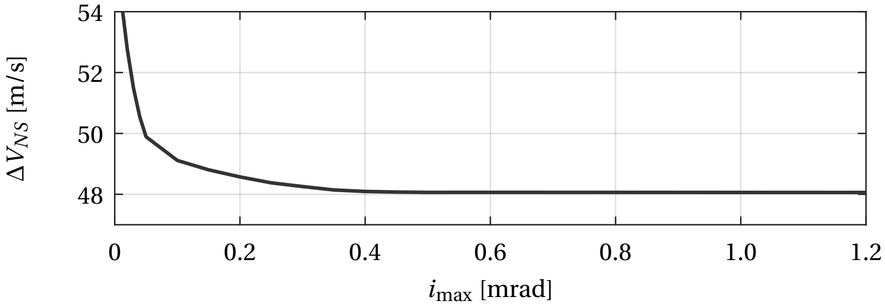

Figure 4.14: Required $\Delta V$ for NS control as a function of the tolerance window on inclination vector.

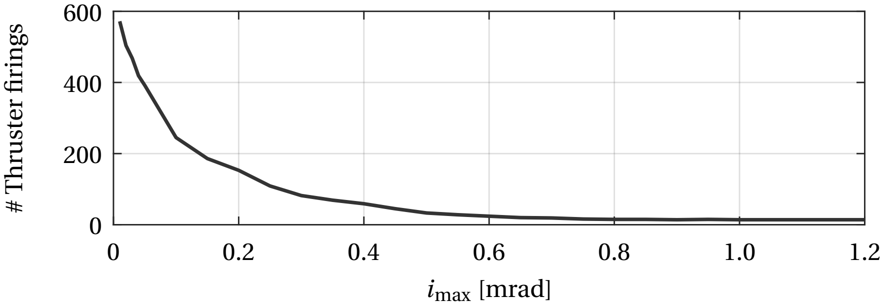

Figure 4.15: Number of thruster firings for NS control as a function of the tolerance window on inclination vector.

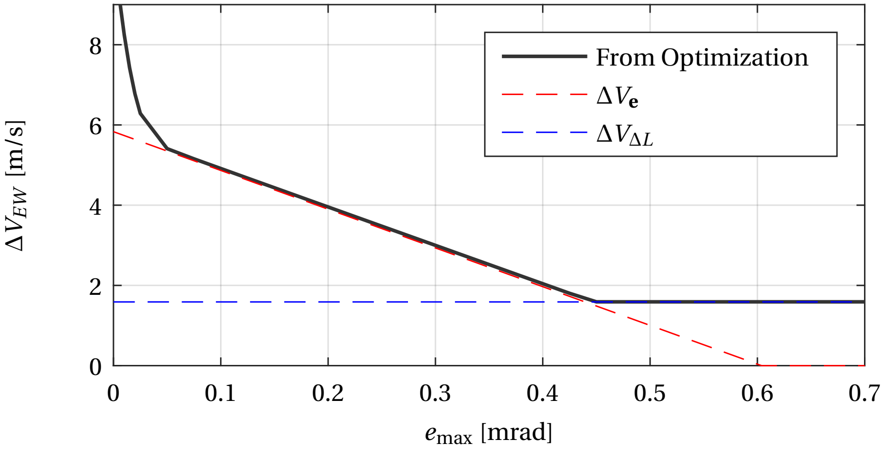

Figure 4.16: Required $\Delta V$ for EW control as a function of the tolerance window on eccentricity vector

that is so small that osculating-to-mean variations are actively controlled, leading to excessive and unnecessary propellant expenditure. In the region between approximately $0.5{\cdot}10^{-3}$ and $4.5{\cdot}10^{-3}$ the propellant consumption is dominated by eccentricity vector control. The region to the right of $4.5{\cdot}10^{-3}$ corresponds to the region where propellant consumption is dominated by controlling the mean longitude variations.

In the following paragraph we provide the analytical background, explaining the observed behavior. An analytic equation for the natural mean eccentricity vector circle radius in the absence of control is given by [19]:

$$r_e^{\text{natural}} = \frac{3}{2}\frac{1}{n_{\text{geo}}a_{\text{geo}}}C_R\left(\frac{A}{m}\right)P_s\frac{1}{n_s} \approx 0.011\left[\frac{\text{kg}}{\text{m}^2}\right]\cdot C_R\frac{A}{m} \tag{4.58}$$

where $n_s$ is the mean motion of the Sun. For the satellite characteristics used in the simulations this natural mean eccentricity circle has a radius of $5.3{\cdot}10^{-4}$. If the tolerance window is large enough, the satellite can follow its natural eccentricity circle and no propellant is required for eccentricity control. However, if the eccentricity is forced to a smaller circle with a radius $r_e^{\text{forced}}$, we can analytically determine the propellant that is required to compensate for this difference (assuming we always make "optimal" eccentricity maneuvers). For a natural drift over an infinitesimally small angle $\mathrm{d}\theta$ the eccentricity vector components drift as follows:

$$\mathrm{d}e_x^{\text{natural}} = -r_e^{\text{natural}}\sin\theta\,\mathrm{d}\theta \quad \text{and} \quad \mathrm{d}e_y^{\text{natural}} = r_e^{\text{natural}}\cos\theta\,\mathrm{d}\theta \tag{4.59}$$

we force this drift to be:

$$\mathrm{d}e_x^{\text{forced}} = -r_e^{\text{forced}}\sin\theta\,\mathrm{d}\theta \quad \text{and} \quad \mathrm{d}e_y^{\text{forced}} = r_e^{\text{forced}}\cos\theta\,\mathrm{d}\theta \tag{4.60}$$

and so we need to compensate the difference:

$$\Delta\,\mathrm{d}e_x = \Delta r_e\sin\theta\,\mathrm{d}\theta \quad \text{and} \quad \Delta\,\mathrm{d}e_y = \Delta r_e\cos\theta\,\mathrm{d}\theta \tag{4.61}$$

where $\Delta r_e = r_e^{\text{natural}} - r_e^{\text{forced}}$. To compensate for this infinitesimal difference we require (assuming an optimally placed maneuver in tangential direction):

$$d\Delta V = \frac{1}{2}n_{\text{geo}}a_{\text{geo}}\sqrt{\Delta\,\mathrm{d}e_x^2 + \Delta\,\mathrm{d}e_y^2} = \frac{1}{2}n_{\text{geo}}a_{\text{geo}}\Delta r_e\,\mathrm{d}\theta \tag{4.62}$$

Since the natural eccentricity makes a full revolution over the course of a year, the yearly propellant required for eccentricity vector control with SPP is equal to:

$$\Delta V_{\mathbf{e}} = \int_0^{2\pi}\frac{1}{2}n_{\text{geo}}a_{\text{geo}}\Delta r_e\,\mathrm{d}\theta = \pi n_{\text{geo}}a_{\text{geo}}\Delta r_e \tag{4.63}$$

and thus, if we constrain the (mean) eccentricity to be smaller than a certain value $e_{\max}^m$, the required propellant consumption for eccentricity control is equal to:

$$\Delta V_{\mathbf{e}} = \max\left(\pi n_{\text{geo}}a_{\text{geo}}\left(r_e^{\text{natural}} - e_{\max}^m\right),\, 0\right) \tag{4.64}$$

Since we are constraining the osculating eccentricity vector, we need to subtract $0.76{\cdot}10^{-4}$ from the osculating bound to get a representative forced mean eccentricity value from a bound on osculating eccentricity (i.e. from the results of case MSA we have calculated that the averaged mean eccentricity was $0.76{\cdot}10^{-4}$ smaller than the constraint boundary on osculating eccentricity). The red (diagonal) dashed line in Figure 4.16 shows the theoretical propellant consumption required for eccentricity control, as a function of a bound on the osculating eccentricity vector.

We can also determine the $\Delta V$ required for controlling the mean longitude in order to compensate for the tesseral gravity perturbations affecting the satellite in tangential direction (which we conveniently group under the term $u_t^{J_{22}}$ identified by the biggest contributor $J_{22}$). Since the satellite is not moving significantly with respect to the Earth the term $u_t^{J_{22}}$ is roughly constant and the $\Delta V$ required to compensate the tesseral gravity perturbations is given by:

$$\Delta V_{\Delta L} = \int u_t^{J_{22}} \, \mathrm{d}t = u_t^{J_{22}} \Delta t \tag{4.65}$$

where $\Delta t$ is $364 \cdot 86400$ s. For the 19.2°E slot used in these simulations, the $\Delta V_{\Delta L}$ is equal to 1.59 m/s for a period of 364 days. This is the blue (horizontal) dashed line in Figure 4.16.

Since the maneuvers to compensate for mean longitude can be used to simultaneously control eccentricity and vice versa, the total propellant required for EW control can be approximated by the maximum of these two contributors:

$$\max\left(\Delta V_{\Delta L},\, \Delta V_{\mathbf{e}}\right) \tag{4.66}$$

Looking again at Figure 4.16 we see that the solution to the optimization problem corresponds almost perfectly to these analytically determined components. The only exception is for very small tolerance windows, since in this case, the periodic variations of the eccentricity vector need to be compensated as well and the analytic method fails to provide a reliable solution.

The dark line in Figure 4.17 shows the number of thruster firings for EW control resulting from the optimization problem solution when no weight matrix is used. We observe a large number of thruster firings for small bounds, which is expected, due to the need to control the periodic variations of the eccentricity vector. The thruster firings then reduce to a number well below a 100. However, around $4.5{\cdot}10^{-4}$ we see a sudden increase in thruster firings. This increase corresponds exactly to the tolerance window size at which the mean longitude variations start to dominate the propellant budget. The number of thruster firings increases significantly because, as far as the optimizer is concerned, there is no better or worse place along the orbit to execute thruster firings for controlling the mean longitude. All tangential maneuvers have an equal effect on the mean longitude and hence the optimizer has no incentive to return a sparse solution with little thruster firings. This is where the weight matrix $\mathbf{W}_\tau$ can play an important role. By default, $\mathbf{W}_\tau$ is an identity matrix, with size equal to the number of thrust force variables in the optimization problem (here it is 58240 by 58240). Each element on the diagonal corresponds to a thrust force variable of a particular thruster over a particular discrete timestep. By setting the weight factors corresponding to all EW thruster firings at one discrete timestep per orbit to a value less than one, the optimizer is incentivized to place thruster firings to reduce the mean longitude at these timesteps. If we choose a weight just below one this will have no noticeable impact on the propellant consump-

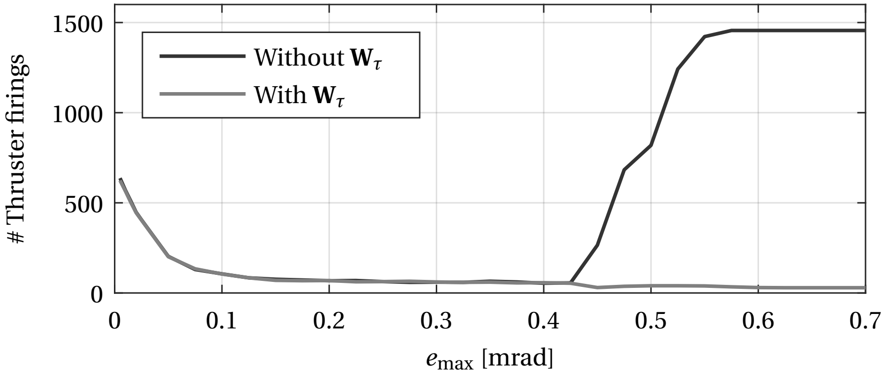

Figure 4.17: Number of thruster firings for EW control as a function of the tolerance window on eccentricity vector.

tion. In addition we can "stimulate" the optimizer to execute maneuvers according to a certain schedule by making the weights relating to a particular day (or other period) smaller than unity as well.

We have chosen a weight matrix in which the weights for all thrusters on the first day of every fortnight were equal to 0.999. In addition, the weights for the first discrete timestep per orbit have been reduced by 0.0001 (such that a weight of one is reduced to 0.9999 and a weight of 0.999 is reduced to 0.9989). This gives the optimizer an incentive to follow a schedule, however, the schedule is not mandatory as before. At the same time, we avoid the distribution of thruster firings for mean longitude control over many intervals. The result is shown by the light line in Figure 4.17. We see that in the period where the eccentricity control dominates the propellant consumption, no noticeable change is observed, while in the period where the mean longitude control dominates the EW propellant consumption a major reduction in thruster firings was achieved. The propellant consumption for all cases with and without $\mathbf{W}_\tau$ was almost identical, the maximum cumulative difference in propellant consumption over the complete analysis period was 1.2 mm/s.

### ANALYSIS OF OPTIMAL STRATEGY FOR LOW THRUST-TO-MASS RATIO

The one-year horizon optimization problem is using a 3000 kg satellite carrying four 80 mN thrusters. The thruster configuration is represented by Eq. (2.51), with $\gamma = 45°$, while $\beta$ is varied between 0 and 90°. We show results in terms of propellant consumption and thruster firings. We show also the propellant consumption and thruster firings for different eccentricity vector control window sizes to demonstrate that for typical electric propulsion systems, the SPP no longer results in significant propellant savings and can be forfeited. The space in the eccentricity plane thus gained can be used for collocating more satellites in one slot.

Figure 4.18 shows the propellant consumption as a function of $\beta$. The important observation from this graph is that it is roughly flat for $\beta$ between 5° and 90°, with a $\Delta V$ of around 68.02 m/s. If we assume that control of mean longitude difference and

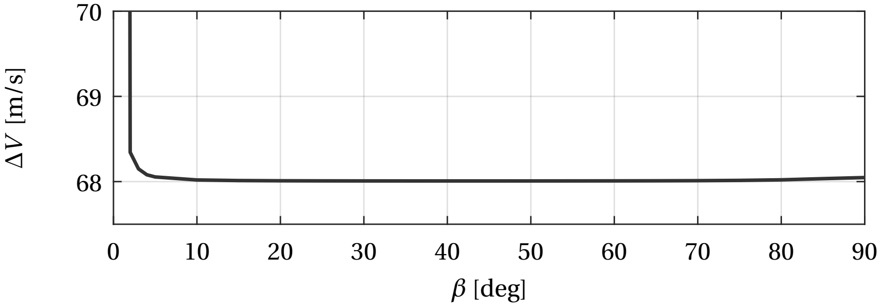

Figure 4.18: Required $\Delta V$ as a function of the thruster configuration, parametrized by $\beta$ for $\gamma = 45°$.

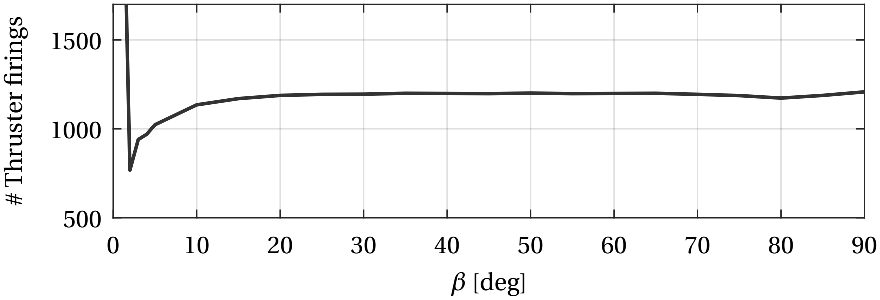

Figure 4.19: Number of firings as a function of the thruster configuration, parametrized by $\beta$ for $\gamma = 45°$.

eccentricity can be achieved completely as a by-product of inclination control, we can provide an approximate lower bound on the propellant consumption by taking the NS propellant consumption from Table 4.7 and dividing this number by $\cos\gamma$. The resulting lower bound on propellant consumption is equal to 67.97 m/s. We almost achieve this lower bound (a slight efficiency loss can be expected due to the lower thrust level, and hence longer thrust arcs), thus establishing fidelity in the approach to also find good solutions for a range of thruster configurations with low thrust. For values of $\beta$ below 5°, the propellant consumption increases rapidly for decreasing $\beta$. The underlying reason is that for small $\beta$ the thrusters deliver only a small thrust component in tangential direction and if this component gets too small the mean longitude difference cannot be controlled efficiently anymore, leading to a waste of propellant.

Figure 4.19 shows the number of thruster firings for varying $\beta$. From this figure we observe that for $\beta$ larger than 10°, roughly four thruster firings per day are required to simultaneously control inclination vector, eccentricity vector and mean longitude. The number of thruster firings is much larger than in the setup with the high thrust chemical propulsion system. The reason for this increase is that the thrust force is so small that thruster firings have much longer burn arcs. The longer the arc, the larger the efficiency loss (since we do not thrust at the optimal location). To counteract this efficiency loss the optimizer chooses to use thruster firings around every "optimal" location (from the point of view of controlling the inclination vector). With the locations of the firings fixed and the total impulse determined by the total size of inclination control maneuvers, the optimizer "just" distributes this total impulse over four thruster firings to control simultaneously three other variables: eccentricity vector and mean longitude.

At around $\beta = 2°$ an interesting observation is made from Figure 4.19. The number of thruster firings is reduced almost by a factor of two. The reason is that at $\beta \approx 2°$, the total amount of tangential thrust that is delivered as a by-product of inclination control is roughly equal to the amount of propellant required for mean longitude control. In this case the most efficient strategy is to use only two firings to achieve the necessary inclination vector change and simultaneously the required mean longitude drift. The total thrust is distributed over these two firings to achieve the required eccentricity vector change.

We further included Figure 4.20 in this section to show that for a typical low thrust propulsion configuration (configuration B is used in the example, but the result extends to any configuration with $\beta$ between 10° and 90°), the size of the eccentricity window does not have a significant influence on the propellant consumption, which allows us to forfeit the SPP strategy without a penalty on propellant consumption (unless we make the window so small that we actively need to control mean-to-osculating variations).

### IMPACT OF CONSTRAINT ENFORCEMENT RATIO

A key question to answer is how often we need to apply tolerance window constraints in order to avoid excessive constraint window violations in between the points at which the constraints are applied. This section therefore investigates the relation between the tolerance window violations and the CER. In general we expect that the more discrete points we apply the constraints to, the smaller the constraint violations will be, with the best case a CER of one, such that the constraints are enforced at every discrete point in time. The disadvantage of a small CER is that the optimization problem requires more

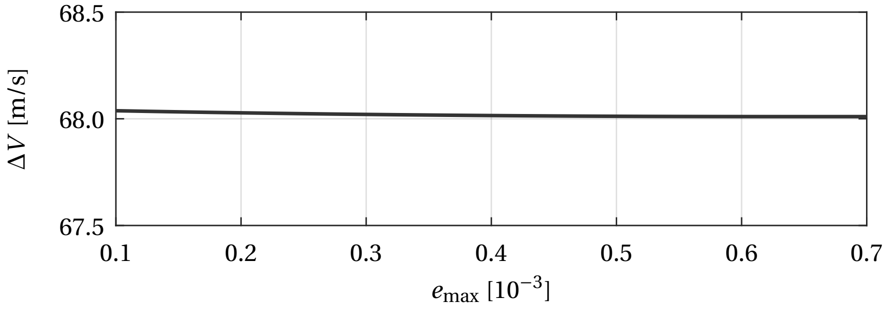

Figure 4.20: Propellant required as a function of the tolerance window on eccentricity vector: for typical electric propulsion configurations the SPP strategy is no longer required to save propellant.

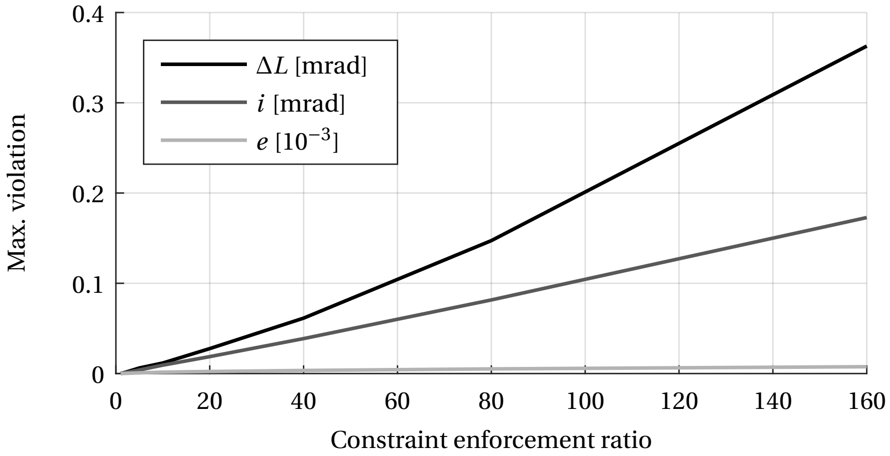

Figure 4.21: Tolerance window violations of mean orbital elements as a function of CER.

computational resources to setup and solve.

We setup the optimization problem as before in case MSB, with the same tolerances on the mean elements. As before we have used an optimization timestep of 2160 seconds, such that we have roughly 40 discrete points per orbit. We have investigated CER's between 1 and 160, meaning that the constraints have been enforced between 40 times per orbit and once every 4 orbits. The resulting maximum constraint violations over the one year simulation horizon are given in Figure 4.21 for the following mean orbital elements: mean longitude, inclination and eccentricity. From the results we clearly see that tolerance window violations on the mean elements are significantly smaller when we apply the constraints more often. Based on these results we choose a CER such that constraints on tolerance windows are enforced at least eight times per day for the simulations in the subsequent sections and in Chapter 5. The expected tolerance window violations are smaller than 0.01 mrad in the absence of uncertainty for these settings.

### 4.4.3. NOVEL METHOD WITH STATE CONSTRAINTS AND UNCERTAINTY

In the previous sections we have shown that the novel method produces reliable results. The method can be configured such that a conventional maneuver scheme results with identical performance and near-identical state trajectories. Using the long horizon problem formulation we have shown how the method retrieves classic guidance strategies. We have also shown that we can easily deal with different thruster configurations and thrust-to-mass ratios. We have investigated some important sensitivities with respect to different parameter settings.

In this section we are applying the method in a more realistic simulation scenario in which maneuver plans are determined using the optimization-based method, but the implementation of the maneuver plans relies on high fidelity simulations of the satellite and orbital dynamics. The simulations include various types of uncertainty, namely orbit determination errors, thrust force magnitude and direction errors and modeling errors of the SRP perturbation. Further modeling errors result from the fact that the optimization relies on the LTV dynamics, while the simulation relies on a numerical integration of the nonlinear equations of motion. The errors that we introduce are pessimistic in magnitude; if we can deal with errors of this size, we can deal with smaller errors as well.

This section is a core section investigating the merits of the new method. The goal is to show several advantages of the new method in a realistic simulation scenario. We aim to show the versatility of the algorithm to be used for chemical propulsion and electrical propulsion satellites, as well as the possibility to include state constraints and control constraints at any point in time. We further investigate how the state knowledge decreases over time, and discuss why our state prediction is worse for satellites with a large thrust-to-mass ratio than for satellites with low thrust-to-mass ratio (under identical assumptions on the uncertainty). An overview of simulation settings (in addition to Table 4.2) used for the analysis in the remainder of this chapter and the next chapter are given in Table 4.8. The implementation and magnitude of the errors was presented in Section 2.8.

We study three simulation cases with the three different thruster configurations from Section 2.6. The main settings of each case are summarized in Table 4.9, with identifier SS to note that we used a single shooting formulation (Problem 4.6), as opposed to the multiple shooting formulation in the previous section. We include final state constraints on the mean eccentricity and inclination vectors. In the case of SSREF the final mean

Table 4.8: Additional simulation settings for simulation including uncertainty. The errors are implemented as presented in 2.8.

| **Aspect** | **Implementation** |
|---:|:---:|
| Include orbit determination errors | Yes |
| Include thruster errors | Yes |
| Include SRP modeling errors | Yes |
| Include maximum thrust force constraint | Yes |
| Allow eclipse firings | No |

Table 4.9: Simulation settings for SSREF, SSA and SSB simulation cases

| Parameter | Unit | Value | | |
|---|---|---|---|---|
| Case | | SSREF | SSA | SSB |
| Thruster configuration | | REF | A | B |
| Thrust magnitude | N | 10 | 0.08 | 0.08 |
| Constraint on **e** | | Fixed final **e** | Fixed final **e** | Fixed final **e** |
| Constraint on **i** | | Fixed final **i** | Fixed final **i** | Fixed final **i** |
| SPP | | Yes | No | No |
| Tolerance on $\lvert\Delta L\rvert$ | mrad | 0.4 | 0.4 | 0.4 |
| Type of elements constrained | | Mean | Mean | Mean |
| Maneuver cycle | days | 7 | 7 | 7 |
| Schedule | | 6 out 7 | 6 out 7 | 6 out 7 |
| Use $\mathbf{W}_\tau$ | | Yes | No | No |
| Monte-Carlo runs | | 10 | 10 | 10 |

eccentricity vector is constrained using a SPP strategy with an eccentricity circle radius of $2 \cdot 10^{-4}$. In cases SSA and SSB, the final mean eccentricity vector is constrained to zero, i.e. in the previous section we demonstrated that a SPP has no added value for typical electric propulsion thruster configurations. In all three cases the final mean inclination vector is constrained to zero as well. Each case includes a schedule in which thruster firings are allowed 6 out of 7 days (with the 7th day reserved for orbit determination). In the case of SSREF a weighting matrix $\mathbf{W}_\tau$ is used to incentivize the optimizer to execute maneuvers on the first day of the cycle. To investigate the impact of the various random errors that were implemented, each case was simulated 10 times, giving us a total of $10 \cdot 52 = 520$ maneuver cycles per simulation case, which are used for the statistical analysis performed later in this section. The optimization problem used for these simulations is Problem 4.6, such that feasibility is still guaranteed even if the satellite state is outside of the constraint boundaries.

The main results of the simulations are summarized in Table 4.10. Firstly, we see from the table that even under influence of the various types of uncertainty, the performance in terms of propellant consumption and thruster firings is very good. In case SSREF the propellant consumption deviates no more than 0.42 m/s from the results excluding uncertainty (see Table 4.5). In terms of number of thruster firings we would expect around 208 thruster firings, an average of four firings per maneuver cycle, two EW firings and two NS firings. The results in Table 4.10 are closely meeting the expectation. The main difference between these performance numbers and those in Table 4.5 result from the fact that here we are applying a 7-day maneuver cycle also to NS control, as well as having two thrusters to perform NS maneuvers instead of a single thruster. Taking these changes into account the thruster firing results are in line with expectations. In cases SSA and SSB we have a propellant consumption that is very close to the theoretical minimum of 67.6 m/s (which is the propellant required for control of the secular variations of the inclination vector divided by cos 45° due to the off-pointing of the thrusters). In terms of thruster firings we expect an average of 4 thruster firings per day. With firings allowed on six out of seven days, this would result in an expected 1248 thruster firings. This value is almost exactly matched by SSA. In case SSB the value is slightly lower, as could be expected based on inspection of Figure 4.19.

The maximum longitude deviation from the slot center reveals a much larger deviation for SSREF than for the other two cases, even though a similar tolerance on the mean longitude was used. This difference has two root causes. The first and most obvious one is that SSREF uses a SPP strategy and hence the eccentricity induces longitude variations that are significantly higher than in the other cases (approximately 0.023 deg). The second cause stems from the impact of maneuver errors on the prediction accuracy of the orbital elements. Since SSREF uses significantly less maneuvers, these maneuvers are on average much larger than in the other cases and a maneuver error will also be much larger. In cases SSA and SSB more maneuvers are used to achieve similar changes to the orbital elements. Since the errors in separate maneuvers are statistically independent (for the error model that we choose to implement), the resulting errors in orbital elements are smaller. The same is true for the maximum latitude, but to a lesser extent.

Table 4.10: Key simulation results of cases SSREF, SSA and SSB

| **Parameter** | **Unit** | **Value** | | |
|---:|:---:|:---:|:---:|:---:|
| Case | | SSREF | SSA | SSB |
| Mean $\Delta V$ | m/s | 51.23 | 68.18 | 68.05 |
| Max. $\Delta V$ | m/s | 51.43 | 68.23 | 68.11 |
| Mean firings | | 211 | 1240 | 1129 |
| Max. firings | | 214 | 1245 | 1136 |
| Max. longitude deviation | deg | 0.080 | 0.046 | 0.040 |
| Max. latitude | deg | 0.041 | 0.032 | 0.032 |

In the sequel, we investigate the orbit prediction error in terms of orbital elements in more detail. We have included several errors sources, namely, orbit determination errors, maneuver errors (in magnitude and direction) and modeling errors (mismodeling of the SRP force and the LTV approximation of the nonlinear dynamics). We study the combined effect of these errors. Figures 4.23 to 4.26 show the Root Mean Square (RMS) of the error evolution over the maneuver cycle duration (the RMS was obtained from 10 Monte-Carlo simulations, each containing 52 maneuver cycles).

From Figures 4.23 to 4.25 we can make an interesting observation, namely, for the SSREF case, the error increases most significantly over the first day. This is due to maneuver errors, which, due to the schedule (incentivized by $\mathbf{W}_\tau$), take place mostly on the first day of the maneuver cycle. In cases SSA and SSB, the increase in error is much more continuous over the maneuver cycle. The initial errors are due to orbit determination, while the (roughly linear) increase in error over the maneuver cycle is due to a combination of SRP errors and the LTV approximation. These errors are most obvious in terms of the eccentricity and are mostly due to the SRP errors that we introduced in the simulations. In the case of SSREF, we observe that the error in $\Delta n$ hardly increases after the first day, indicating that this error depends mostly on the maneuver errors and is hardly affected by the other error terms.

From Figures 4.23 to 4.26 we can conclude that the errors in mean longitude difference are significantly larger than the errors in the other elements. Firstly the orbit determination errors are significantly larger for the mean longitude than any of the other elements, and secondly, the error in mean longitude grows linearly as a result of a consistent error in mean motion. It is clear from Figure 4.26 that the choice to guarantee minimum distance between two satellites by relying only on their relative eccentricity and inclination vector configurations is wise. Especially for larger prediction horizons, the knowledge of the mean longitude difference is poor. This is an important observation in order to be able to deal with geometric constraints successfully. The sensor cone avoidance constraints discussed in Chapter 3 require active control of the mean longitude between two satellites and large uncertainty in the knowledge of this parameter can be prohibitive in dealing with these constraints. The usual countermeasure is to reduce the maneuver cycle duration, which would necessitate additional orbit determinations. Another countermeasure is to include a constraint on the final mean longitude that is far away from the normal boundary. As evident from Figure 4.26, for each of the thruster configurations, the mean longitude prediction error is largest at the end of the maneuver cycle. By including a constraint on the mean longitude far away from the normal boundary, to be achieved at the end of the cycle, the constraint violations of mean longitude during the rest of the cycle will reduce significantly as well. Since mean longitude control is usually achieved as a by-product of either eccentricity control (for the REF configuration) or inclination control (for configurations A and B), no increase in propellant is expected if a tighter constraint on the final mean longitude is introduced (in fact, we may see a slight reduction in the propellant consumption, since the constraint violations at the end of the maneuver cycle, and hence at the start of the next maneuver cycle, are smaller or completely absent). In case of single-satellite station-keeping we can generally deal with the constraint violations. However, in case of collocating a fleet of satellites such violations can have larger consequences. In the next section and in the next chapter, we will introduce tighter constraints on the final state as a baseline.

Another observation from Figure 4.26 is that the mean longitude difference prediction error is larger for thruster configuration A than for configuration B. The reason for this increase in prediction error is that the thrust force component in tangential direction (which is the only direction contributing to mean longitude drift) is much larger with configuration A. Every thruster firing introduces an error in thrust force magnitude, which has a significant component in tangential direction. In the case of thruster configuration B the contribution in tangential direction is much smaller, resulting in better orbit prediction accuracy in this direction. Hence the general observation is that the particular thruster configuration that we chose can have an impact on the orbit prediction error.

### 4.4.4. NOVEL METHOD AS RECEDING HORIZON CONTROLLER

Motivated by the large uncertainties for longer prediction horizons we investigate the implementation in the form of a Receding Horizon Controller (RHC). We aim to show that with this setup we can maintain very tight bounds on the mean orbital elements with only a minor increase in propellant consumption. A potential use-case arises only if accurate orbit control is mandatory, for example, when a large number of satellites

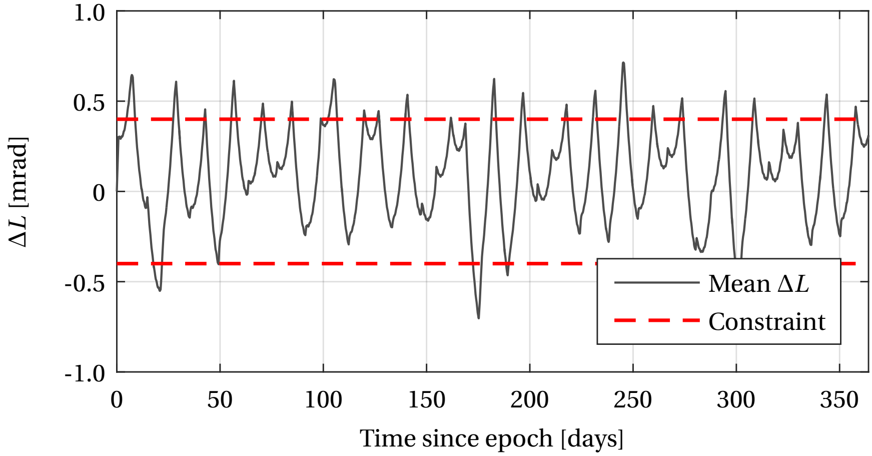

Figure 4.22: Mean longitude difference of SSREF

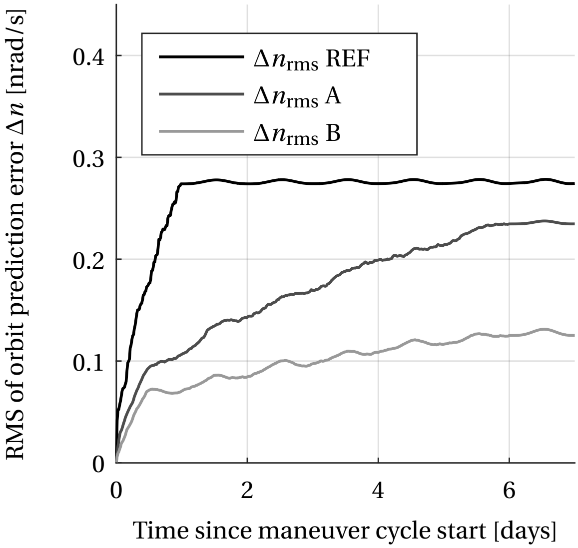

Figure 4.23: Orbit prediction errors in mean motion difference $\Delta n$

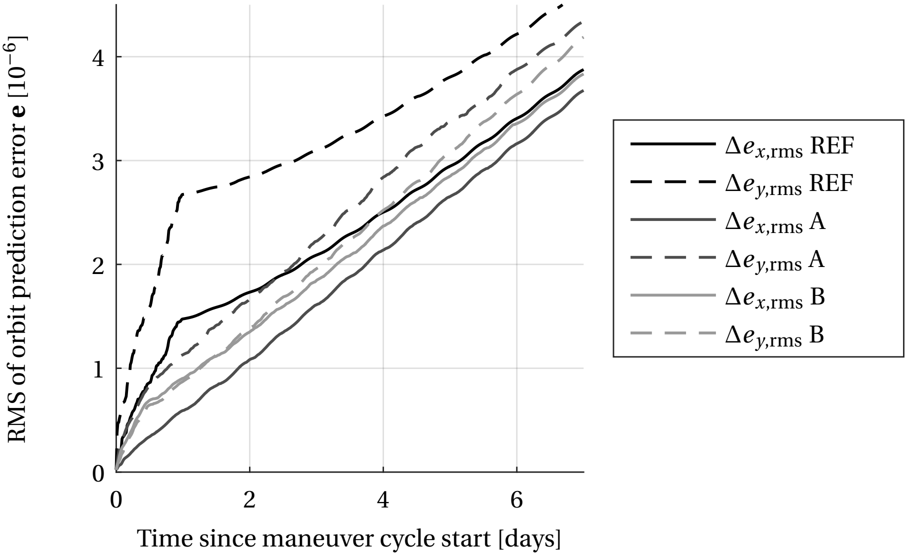

Figure 4.24: Orbit prediction errors in eccentricity vector **e**

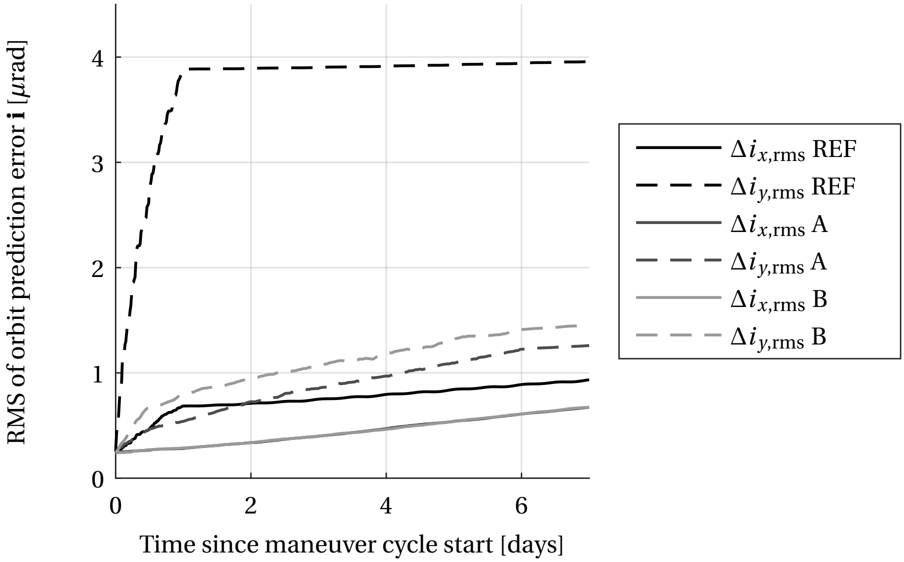

Figure 4.25: Orbit prediction errors in inclination vector **i**

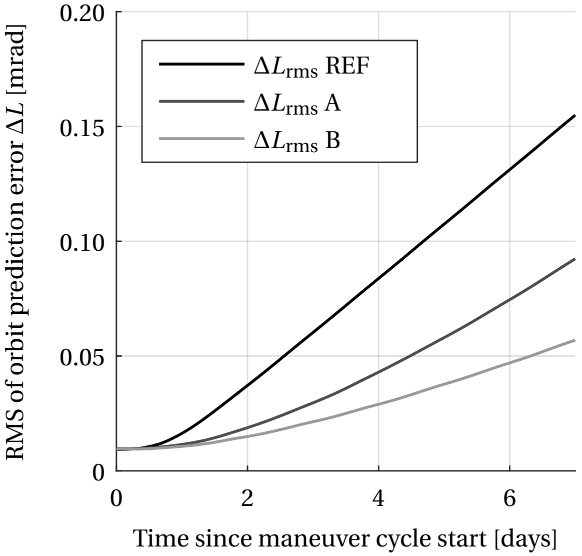

Figure 4.26: Orbit prediction errors in mean longitude difference $\Delta L$

are collocated in a single slot. The simulation settings are those in Tables 4.2 and 4.8. The key difference with previous simulations is a shorter maneuver cycle duration: we reduced the maneuver cycle duration from seven days to one day. Note that we need to include at least one orbit in the maneuver cycle, such that the control algorithm has a chance of achieving the desired orbital elements using maneuvers at those locations that are most efficient. Furthermore, no SPP strategy is used and the control windows on the (relative) orbital elements are much more stringent than before: the tolerance window on $\Delta L$ is reduced by a factor four, and small tolerance windows on eccentricity and inclination vectors were introduced that were previously absent. The frequency of re-planning is set to 6 hours, such that only the first quarter of a devised maneuver plan is actually executed, after which a new plan is calculated. The simulation cases and settings are summarized in Table 4.11.

We investigated the receding horizon controller for the three different propulsion system configurations used in this work. We show that in the presence of all those uncertainties we can still maintain very tight bounds on all relevant states. A summary of the achieved performance is given in Table 4.12. For the chemical propulsion case (RHCREF) we see an extremely large (relative) increase in number of thruster firings, which is something most chemical propulsion systems are not designed for. In the case of the electric propulsion configurations, we see only a minor (relative) increase in thruster firings and a RHC implementation can be feasible. The propellant consumption is hardly affected in any of the cases. Note that for case RHCREF the increase is mainly due to the fact that no SPP strategy was followed in these simulations.

Figures 4.27, 4.28 and 4.29 show the simulation results for the RHCA case. The state trajectories for the other two cases look very similar. We observe from these figures that the constraints on the mean orbital elements are maintained with sufficient margin. The state trajectories are at no point in time close to the boundaries of the tolerance windows, which is mainly due to the final state constraint. Especially in terms of mean longitude difference the control accuracy is remarkable. This control accuracy is achieved because of the combination of the short planning horizon together with the frequent replanning. A mean longitude prediction error (other than the initial error due to OD) is established over time due to an error in the predicted drift rate. By allowing "only" six hours before applying a form of feedback, this state can be controlled accurately as well.

The key enabler for an implementation of such scheme is the availability of frequent (or continuous) orbit determination solutions. An on-board GNSS receiver could provide the required capability. Such a GNSS receiver would make near continuous measurements, which could be used in an on-board filter to achieve real-time orbit determination solutions, or alternatively, the raw measurements could be sent to the ground station to perform a precise orbit determination on-ground. The maneuver planning could be implemented either on-board or on-ground. A geostationary satellite benefits from the possibility to have 24/7 contact using a single ground station and hence does not have a strong need for on-board autonomy.

Table 4.11: Simulation settings of RHC cases

| Parameter | Unit | Value | | |
|---|---|---|---|---|
| Case | | RHCREF | RHCA | RHCB |
| Thrust magnitude | N | 10 | 0.08 | 0.08 |
| Tolerance on $e$ | | 0.05 | 0.05 | 0.05 |
| Tolerance on $i$ | mrad | 0.05 | 0.05 | 0.05 |
| Tolerance on $\|\Delta L\|$ | mrad | 0.1 | 0.1 | 0.1 |
| Final state constraint $e$, $i$ and $\Delta L$ | | zero | zero | zero |
| Type of elements constrained | | Mean | Mean | Mean |
| Planning horizon | days | 1 | 1 | 1 |
| Replanning frequency | $\text{day}^{-1}$ | 4 | 4 | 4 |

Table 4.12: Simulation results of RHC cases

| Parameter | Unit | Value | | |
|---|---|---|---|---|
| Case | | RHCREF | RHCA | RHCB |
| $\Delta V$ | m/s | 53.10 | 68.14 | 68.45 |
| # of Firings | | 1546 | 1543 | 1684 |

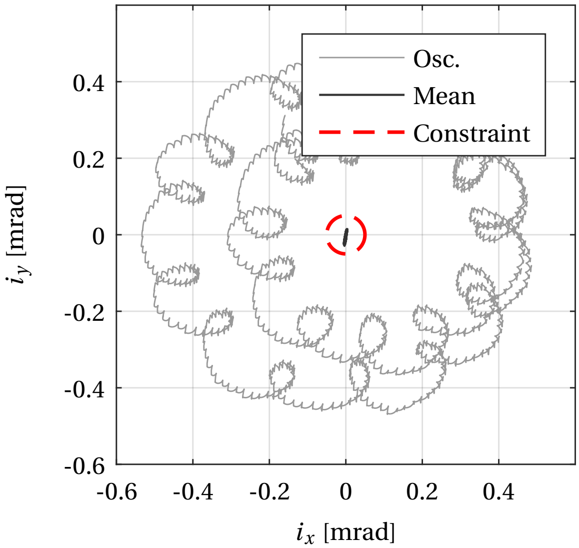

Figure 4.27: Inclination vector over one year, RHCA simulation.

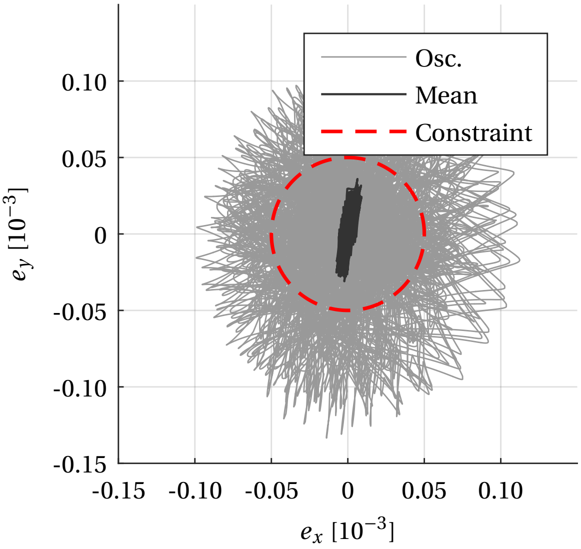

Figure 4.28: Eccentricity vector over one year, RHCA simulation.

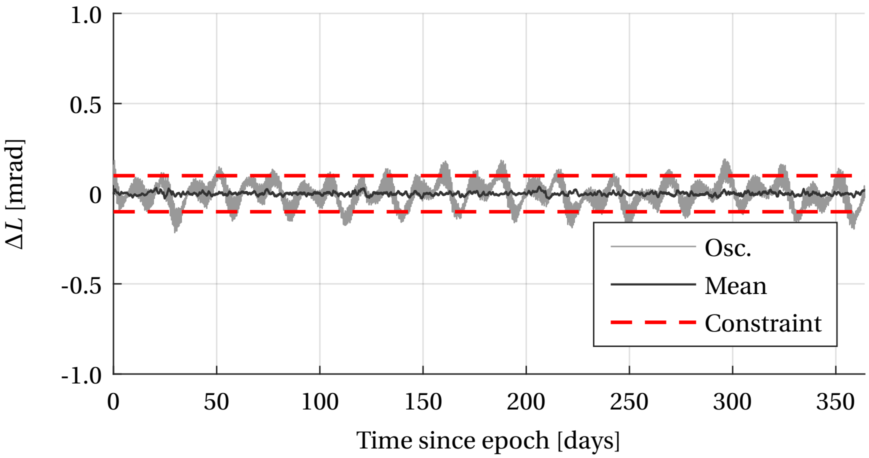

Figure 4.29: Longitude difference of RHCA simulation.

## 4.5. CONCLUDING REMARKS

This chapter presented the definition and solution to the problem of station-keeping of a geostationary satellite. Conventional methods for station-keeping usually rely on an analytic determination of maneuvers, based on the approximation of these maneuvers by impulsive $\Delta V$'s. In contrast to these methods we have developed a novel station-keeping method based on convex optimization. The formulation of the station-keeping problem as a convex optimization problem was enabled by the LTV formulation of the satellite dynamics. A sequence of increasingly complex problems was defined, culminating in the formulation of Problems 4.6 and 4.7. Both multiple shooting and single shooting approaches were applied, where the first is conceptually simpler, whereas the latter resulted in a reduction of computational effort, especially useful for larger problems.

The maneuver plans resulting from the solution of one of the convex optimization problems were not directly suitable for implementation using typical on/off thrusters. The method for processing these maneuver plans was introduced and an analysis was performed to obtain a bound on the errors introduced through this processing. The same analysis was used to determine the accuracy of the realization of a maneuver that was calculated under the assumption of an impulsive velocity increment. It was shown that the error, resulting from the use of an electric propulsion system, can become significant for long duration burns.

In the first simulation case, the station-keeping problem was configured to resemble a conventional approach with two EW maneuvers per week, and one NS maneuver per fortnight. This configuration allowed a validation of the methodology by comparing the results obtained from the new method to results obtained using a conventional approach. A remarkable similarity was shown both in the location and size of the maneuvers, as well as in the resulting state trajectories. These findings established fidelity in the new method.

The multiple shooting approach was used to formulate several station-keeping problems with a horizon of one year. The solutions of these problems were analyzed to further validate the methodology and to investigate the impact of certain parameters on the optimal strategy. The method confirmed tried-and-true strategies such as SPP. Other results obtained from these investigations are as follows:

- The analysis showed how the required $\Delta V$ and number of thruster firings were related to the size of the tolerance windows on inclination and eccentricity vectors.
- It was found that the SPP strategy has no benefits for typical electric propulsion thruster configurations.
- The number of thruster firings can be reduced significantly by using a weighting matrix, without (significantly) impacting the performance of the method.

The impact of the constraint enforcement ratio on the magnitude of the violations of the tolerance windows was also investigated.

The method was tested in a realistic simulation scenario including errors due to orbit determination, maneuver errors and modeling errors, both for a satellite with a chemical propulsion system and for two satellites with different electric propulsion system configurations. It was found that the performance of the method (in terms of propellant consumption and number of thruster firings) was hardly influenced by the various types of errors. Additionally, the impact of these errors on the state prediction accuracy was investigated by running each one year simulation ten times and comparing the predicted state trajectories to the actual state trajectories. This analysis showed that the prediction accuracy of the mean longitude difference is poor, confirming that it is a good choice not to rely on the tangential direction for ensuring a minimum separation distance. Another important observation for the electric propulsion configurations was that the state prediction error, especially in terms of mean longitude difference and mean motion difference, depends on the thruster configuration. Two exemplary thruster configurations were studied to arrive at this conclusion.

The final simulations demonstrated the method in a receding horizon controller setting. This implementation allowed to accurately control the state trajectories within small tolerance windows. In the simulation cases with electric propulsion systems, only a small increase in $\Delta V$ and number of thruster firings was observed. The simulations with the chemical propulsion system showed a very steep increase in the number of thruster firings, to a level comparable to the required thruster firings using an electric propulsion system. The increase in $\Delta V$ for the chemical propulsion system was small and resulted mainly from the omission of the SPP strategy. A receding horizon control implementation is only feasible if frequent orbit determination solutions are available.

The simulation scenarios have shown several aspects of the station-keeping method. Here, we summarize the positive characteristics:

- It was demonstrated that it can be used successfully to perform station-keeping of a geostationary satellite.
- The performance, both in terms of $\Delta V$ usage and number of thruster firings, is similar to conventional methods.
- The method can be used to both high thrust-to-mass chemical propulsion systems as well as low-thrust-to-mass electric propulsion systems with various thruster configurations.

- Implementing convex constraints on control is straightforward, making it easy to deal with constraints such as, e.g., avoid firings during eclipses or allow firings only at certain days of a maneuver cycle.
- The satellite state can be constrained at any discrete node in the optimization problem, allowing much more control over the state trajectory than using conventional methods.
- The method can be implemented as a receding horizon controller, allowing very accurate control of the satellite state.
- The formulation of the problem as a convex optimization problem with a guaranteed feasibility makes the method suitable for automation.

Despite all these strong characteristics the method also has some disadvantages in comparison to conventional methods. Both the conceptual and computational complexity of the method are much higher compared to conventional methods. An operator has no explicit control over the number of thruster firings that results from a solution of the station-keeping problem. A processing was required before the resulting maneuver plans could be implemented and small errors arise due to this processing. The magnitude of this error was shown to depend on the length of the discretization interval. It was not possible with the novel method to deal with the minimum on-time of a thruster explicitly. Instead, small thrusts were simply discarded, also leading to small errors, with maximum magnitude that is half of the minimum impulse bit.

## REFERENCES

[1] M. Eckstein, C. Rajasingh, and P. Blumer, *Colocation strategy and collision avoidance for the geostationary satellites at 19 degrees west,* in *International Symposium on Space Flight Dynamics* (1989).

[2] T. Douglas, C. Kelly, and A. Grise, *On-orbit stationkeeping with ion thrusters telesat canada's bss702 experience,* in *Space OPS 2004 Conference* (American Institute of Aeronautics and Astronautics (AIAA), 2004).

[3] B. Anzel, *Method for satellite station keeping,* (1991), uS Patent 5,020,746.

[4] B. Anzel, *Method and apparatus for a satellite station keeping,* (1995), uS Patent 5,443,231.

[5] B. Anzel, *Method and apparatus for a satellite station keeping,* (1998), uS Patent 5,810,295.

[6] B. Anzel, Y. Ho, and R. Noyola, *Fuel efficient methods for satellite stationkeeping and momentum dumping,* (2000), uS Patent 6,015,116.

[7] Y. Ho, *System and methods for simultaneous momentum dumping and orbit control,* (2011), uS Patent 7,918,420.

[8] Y. Ho, J. Kurland, and D. Uetrecht, *System and methods for simultaneous momentum dumping and orbit control,* (2013), uS Patent 8,439,312.

[9] D. Goebel, M. Martinez-Lavin, T. Bond, and A. King, *Performance of XIPS electric propulsion in on-orbit station keeping of the boeing 702 spacecraft,* in *38th AIAA/ASME/SAE/ASEE Joint Propulsion Conference & Exhibit* (American Institute of Aeronautics and Astronautics (AIAA), 2002).

[10] C. Casaregola, *Electric propulsion for commercial applications: In-flight experience and perspective at eutelsat,* IEEE Trans. Plasma Sci. **43**, 327 (2015).

[11] S. Boyd and L. Vandenberghe, *Convex Optimization* (Cambridge University Press, 2004).

[12] D. Losa, *High vs Low Thrust Station Keeping Maneuver Planning for Geostationary Satellites,* Ph.D. thesis, École Nationale Supérieure des Mines de Paris (2007).

[13] J. Betts, *Very low-thrust trajectory optimization using a direct {sqp} method,* Journal of Computational and Applied Mathematics **120**, 27 (2000).

[14] *3. Optimal Control Preliminaries,* in *Practical Methods for Optimal Control and Estimation Using Nonlinear Programming* (Society for Industrial & Applied Mathematics (SIAM), 2010) pp. 91–121.

[15] M. Grant and S. Boyd, *CVX: Matlab software for disciplined convex programming, version 2.0 beta,* `http://cvxr.com/cvx` (2013).

[16] E. Andersen, B. Jensen, J. Jensen, R. Sandvik, and U. Worsøe, *MOSEK version 6,* Tech. Rep. (Technical Report TR–2009–3, MOSEK, 2009).

[17] M. Grant and S. Boyd, *Graph implementations for nonsmooth convex programs,* in *Recent Advances in Learning and Control,* Lecture Notes in Control and Information Sciences, edited by V. Blondel, S. Boyd, and H. Kimura (Springer-Verlag Limited, 2008) pp. 95–110, `http://stanford.edu/~{}boyd/graph_dcp.html`.

[18] M. Eckstein, *Geostationary orbit control considering deterministic cross coupling effects,* in *$41^{st}$ congress of the International Astronautical Federation* (1990) Dresden, IAF Paper 90-326.

[19] H. Li, *Geostationary Satellites Collocation* (Springer, 2014).

# 5

# STATION-KEEPING OF COLLOCATED SATELLITES

*Collaboration is not about giving up our individuality;*
*it is about realizing our greater potential.*

Joshep Rain

*Our future lies not in competition, but in responsible, interdependent cooperation.*

Joshep Rain

***Abstract***
*Collocating a fleet of satellites requires a coordinated approach. This is even more true if not only minimum distance constraints, but also sensor cone avoidance constraints are present. The station-keeping method is extended to calculate maneuvers for a fleet of geostationary satellites using a leader follower hierarchy. An alternative problem formulation includes the various error sources to achieve a more robust satisfaction of the constraints. Simulation results present the performance and applicability of the method for an inhomogeneous fleet, a large homogeneous fleet as well as fleets subject to sensor cone avoidance constraints.*

In this chapter we formulate and analyze a maneuver planning algorithm for a fleet of satellites that are collocated in a single geostationary slot. The analysis and design of the guidance method discussed in Chapter 3 is combined with the method for station-keeping that was presented in Chapter 4. We require only small adaptations of the method from Chapter 4 to be applicable to collocation and hence the theoretical developments in this chapter are kept to a minimum. We do develop an extension of the method so that several error sources can be accounted for in the problem formulation, resulting in a more robust solution. Most of all, we spend time on studying applications of the method. We demonstrate how the station-keeping method can be used together with the design of a suitable guidance to simultaneously satisfy the geometric constraints that motivated this research.

## 5.1. INTRODUCTION TO COLLOCATION

The uniqueness of the geostationary orbit renders it a scarce natural resource. To manage the distribution of this resource, the orbit has been divided into a limited number of slots. These slots, especially above key areas, such as highly populated or highly developed countries, are extremely valuable. To make most use of a slot, operators collocate multiple satellites within a single slot. Since a single collision in a geostationary slot could potentially render the entire orbit unusable, it is of crucial importance to avoid close approaches between (collocated) geostationary satellites. This requires a coordinated approach to controlling the satellite orbits, requiring methods to analyze and control the relative motion of the satellites.

### 5.1.1. DEFINITION OF THE COLLOCATION PROBLEM AND CONSTRAINTS

The main objectives of the collocation problem include the station-keeping objectives that were defined in the previous chapter. In collocation an operator still aims to 1.) keep the satellites in the slot, 2.) minimize propellant expenditure and 3.) limit the number of thruster firings. In addition to these objectives, the collocation problem has two other important objectives, the first and foremost is to maintain safe separation distances between satellites, while the second objective is to avoid the satellites from interfering with each other, whether this be radio frequency interference, or interference through entering the field of view of a star sensor or an optical payload. The maneuver constraints from Section 4.1.1 still apply, while “new” constraints are introduced, which are of geometric nature. The two geometric constraints that are included are the minimum distance constraint and the sensor cone avoidance constraint. In Chapter 3 we have worked out methods for analyzing and designing a set of convex tolerance windows on relative orbital elements such that these geometric constraints are satisfied. The design of these tolerance windows is tested in this chapter to confirm that indeed they result in satisfaction of the constraints.

### 5.1.2. CURRENT OPERATIONAL PRACTICE

Several methods for collocating satellites in a geostationary slot exist. Soop ([1]) categorizes the different methods essentially into four approaches:

1. No collision avoidance measures: in the old days of geostationary operations, the

collision probability of two satellites in a geostationary slot was assumed to be extremely low (based on a volume integral over the geostationary box) and collision avoidance was neglected. Nowadays this approach is no longer acceptable.

2. Uncoordinated collocation with collision checking: the fleet is monitored for potential collisions and a reactive strategy is implemented to avoid close approaches. This means that a collision avoidance maneuver is executed when a conjunction with an unacceptably high probability of collision occurs.

3. Collocation by separation: different satellites in a slot are allocated to different regions usually defined in terms of orbital elements. These regions are chosen such that no collisions occur when the satellites stay inside these regions. This approach requires no coordination between the control strategies of the satellites, but large regions are required since they need to allow for drift of the elements, the (short) periodic variations and the errors in orbit determination, actuation and modeling.

4. Coordinated station-keeping: the collocation strategy and maneuver executions are coordinated between the satellites. The separations are defined in terms of relative orbital elements. Since the satellites experience roughly the same accelerations and the periodic variations of the orbital elements are almost identical, these need not be included as additional margin in the definition of the regions for the relative orbital elements. It can be advantageous to designate one satellite the fleet leader (or master), and implement an optimal strategy for controlling the leader.

It may be clear from the content of Chapter 3 that we focused on the fourth approach. The control windows are defined in terms of relative orbital elements, thus requiring a coordinated approach. Soop ([1]) further specifies several separation methods which he calls modes. A total of six different modes are described in detail. The first four modes rely on achieving a separation between satellites in the radial-tangential plane only, either by separating the satellites in longitude, eccentricity or both. The last two modes use also the normal direction and Soop ([1]) provides the equations for calculating the minimum distance in the radial-normal plane and in three dimensions under the assumptions of zero mean longitude difference and zero semi-major axis difference.

As evident from the analysis in Section 4.4.3, the errors in orbit prediction are most dominant in the mean longitude difference. This was already realized by Eckstein in his 1989 paper on a collocation strategy minimizing the need for collision avoidance maneuvers [2]. In this paper Eckstein presents collocation strategies which use separations in longitude, in eccentricity vector and by combining the effects of eccentricity and inclination vectors. Eckstein identifies as “safest” strategy for collocation the eccentricity/inclination vector separation strategy. This strategy relies on the satellites in the fleet having relative eccentricity and inclination vectors that are (anti-)parallel and the minimum distance is guaranteed using only the radial-normal plane. Eckstein simulates side-by-side this coordinated approach and an uncoordinated approach for satellites that are subject to orbit determination and maneuver errors. The results are a significant reduction in close approaches when a coordinated approach is used. It may come as no surprise that the eccentricity/inclination vector separation strategy remains the state-of-art method for collocating geostationary satellites.

One of the downsides of this strategy is that sensor interference is not mitigated as part of the strategy (i.e. it was never an objective). The occurrence of such interference events is frequent, and increases as the number of satellites in the slot increases [3]. A solution that is able to deal with the geometric constraints of minimum distance and the sensor cone avoidance constraints simultaneously has not been proposed to date. We fill this gap by presenting a method that does not only deal with the minimum distance constraint, but also successfully mitigates violations of sensor cone avoidance constraints, based on carefully selected relative control windows according to the method presented in Chapter 3.

## 5.2. CONVEX OPTIMIZATION BASED METHOD

We build on the method introduced in Chapter 4 and extend it towards collocated satellites. The collocation problem is formulated as a convex optimization problem and solved accordingly.

### 5.2.1. OPERATIONAL ARCHITECTURE

Following the concept of operations introduced in Section 4.3 we discuss the extensions that are required for collocating a fleet of satellites. The design of the guidance discussed in Chapter 3 introduces the need to constrain the relative states defined in relative orbital elements. Several different architectures allow for such constraints. The simplest option would be to constrain the absolute states of all satellites such that the relative state constraints are met. This would be in line with Soop's third approach: collocation by separation. As pointed out before, this quickly exhausts the configuration space and severely limits the amount of satellites that can be collocated in a single slot. We therefore choose to implement a leader/follower architecture. One satellite in the fleet is designated as a formation leader and this satellite is controlled using a method such as introduced in the previous chapter on single-satellite control. The other satellites in the fleet, the follower satellites, control their state relative to the leader satellite. An advantage is that the leader state trajectory includes maneuvers that are, if the leader's strategy is optimal, executed at optimal locations. If the other satellites follow this trajectory at some offset in terms of synchronous orbital elements (except for $\Delta n$), similar maneuvers result naturally for the other satellites. All satellites in the fleet experience very similar perturbations, most of which cancel out when forming the relative states (remember that we approximate the perturbations by those affecting the slot center). Hence, only the secular effects of the differential perturbations between satellites need to be corrected for. Using a similar argument, if controlling the relative states, no mean-to-osculating transformation is required (we determine the mean-to-osculating transformation by approximating the periodic perturbations at the geostationary slot center, and hence this mean-to-osculating transformation is identical for all satellites in the fleet).

In order to form the relative state and formulate the relative state constraints, the follower satellites need to know the (predicted) leader state. If the method from Chapter 4 is used to determine the leader maneuver plan, a by-product of solving the optimization

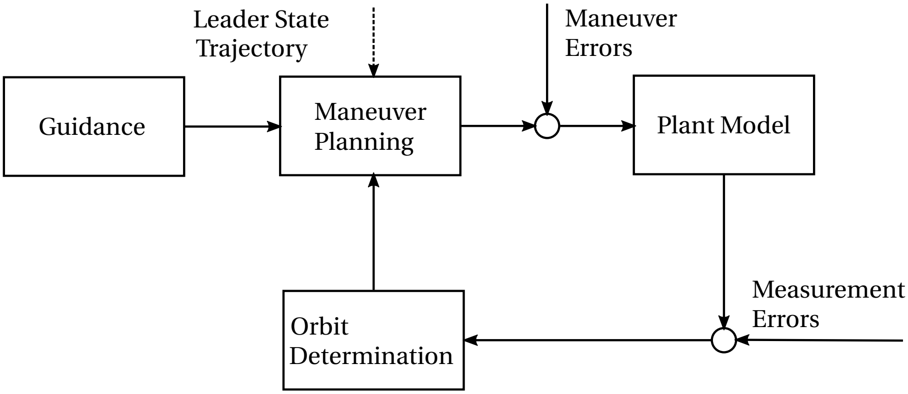

Figure 5.1: High level simulation architecture for a follower satellite

problem is the predicted state trajectory at the discrete nodes. This can be used directly as an input to the follower satellites' maneuver planning module. The relative state can be formed and the relative state constraints can be formulated. Figure 5.1 presents a high level architecture for a follower satellite. In the next section, the formulation of the optimization problem and constraints is discussed.

### 5.2.2. GENERAL PROBLEM FORMULATION

The collocation problem usually includes a mixture of both absolute state constraints (e.g. stay inside the geostationary slot) and relative state constraints (e.g. maintain a specific relative eccentricity/inclination vector configuration). As a starting point we can use the scaled problem formulation with guaranteed feasibility from Chapter 4, Problem 4.6, repeated here for convenience:

**Problem 5.1.**

$$\begin{aligned}\text{minimize} \quad & \|\mathbf{W}_\tau \bar{\boldsymbol{\tau}}_{\text{tot}}\|_1 + \|\mathbf{W}_a \mathbf{s}_a\|_1 + \sum_{j=1}^{M_c} w_{cj} \cdot \max\left(0, s_{cj} - 1\right) \\ \text{subject to} \quad & \end{aligned}$$

$$\begin{aligned} \bar{\mathbf{c}}\left(\boldsymbol{\tau}_{\text{tot}}\right) &\leq \mathbf{s}_c \\ \bar{\mathbf{a}}\left(\boldsymbol{\tau}_{\text{tot}}\right) &= \mathbf{s}_a \\ \bar{\boldsymbol{\tau}}_{\text{tot}} &\leq \mathbf{1} \\ -\bar{\boldsymbol{\tau}}_{\text{tot}} &\leq \mathbf{0}. \end{aligned}$$

The difference with the single-satellite station-keeping problem is in the definition of the constraints. The absolute (scaled) state constraints for staying inside the geostationary slot can be implemented similar to those used in Chapter 4. Alternatively they can be omitted altogether if the combination of the leader state trajectory and the relative state constraints is defined such that the geostationary slot boundaries are respected for every choice of relative state within the allowed tolerance windows. If $\mathbf{x}_k^L$ defines the leader state at time $k$, the relative state is simply defined as:

$$\Delta\mathbf{x}_k = \mathbf{x}_k^F - \mathbf{x}_k^L, \tag{5.1}$$

or for the total state trajectory at all $N$ discrete points in time:

$$\begin{aligned}\Delta\mathbf{x}_{\text{tot}} &= \mathbf{x}_{\text{tot}}^F - \mathbf{x}_{\text{tot}}^L \\ &= \mathbf{F}\mathbf{x}_0^F + \mathbf{H}\mathbf{\Gamma}^F\boldsymbol{\tau}_{\text{tot}}^F + \mathbf{J}\mathbf{d}_{\text{tot}}^F - \mathbf{x}_{\text{tot}}^L,\end{aligned} \tag{5.2}$$

with superscript $F$ for those vectors and matrices different between leader and follower satellites. We consider several types of constraints on relative states for the collocation problem which we can separate depending on the particular orbital element that is involved. We usually constrain only the relative eccentricity vector, the relative inclination vector and the relative mean longitude of the satellites.

The typical constraints for relative eccentricity and inclination vectors were discussed in Chapter 3. We focus on two typical constraints, which are either a circular tolerance window, centered on some nominal relative eccentricity or inclination vector, or a convexified annular sector (see Section 3.5), which is defined as the intersection between three affine inequality constraints and a two-norm constraint centered on the origin of the relative eccentricity or inclination plane. We also include an equality constraint for the relative eccentricity or inclination vector to a target value at a particular point in time. For the relative mean longitude, we consider affine equality and/or affine inequality constraints.

In the sequel, we provide some examples of the constraints that are implemented in the application cases in this chapter. We would like to constrain the relative eccentricity vector at the $k^{\text{th}}$ discrete step to lie within a circle with radius $r_e$, centered on some nominal relative eccentricity vector defined by $\Delta e_{x,k}^{\text{nom}}$ and $\Delta e_{y,k}^{\text{nom}}$. This constraint is convex in the optimization variables $\boldsymbol{\tau}_{\text{tot}}$ and is formulated as follows:

$$\bar{c}_1\left(\boldsymbol{\tau}_{\text{tot}}\right) = \frac{\sqrt{\left(\Delta e_{x,k} - \Delta e_{x,k}^{\text{nom}}\right)^2 + \left(\Delta e_{y,k} - \Delta e_{y,k}^{\text{nom}}\right)^2}}{r_e} \leq 1, \tag{5.3}$$

where $\Delta e_{x,k}$ and $\Delta e_{y,k}$ are obtained by selecting the corresponding rows from Eq. (5.2). In a similar manner, a constraint on the relative inclination is formulated as:

$$\bar{c}_2\left(\boldsymbol{\tau}_{\text{tot}}\right) = \frac{\sqrt{\left(\Delta i_{x,k} - \Delta i_{x,k}^{\text{nom}}\right)^2 + \left(\Delta i_{y,k} - \Delta i_{y,k}^{\text{nom}}\right)^2}}{r_i} \leq 1. \tag{5.4}$$

Contraints on the relative mean longitude are similar as for a single satellite:

$$\bar{c}_3\left(\boldsymbol{\tau}_{\text{tot}}\right) = -\frac{\left(\Delta L_k - \Delta L_{k,\text{mid}}\right)}{c_{3,\max}} \leq 1 \tag{5.5}$$

$$\bar{c}_4\left(\boldsymbol{\tau}_{\text{tot}}\right) = \frac{\left(\Delta L_k - \Delta L_{k,\text{mid}}\right)}{c_{4,\max}} \leq 1, \tag{5.6}$$

with scaling factors determined by the size of the relative mean longitude window:

$$c_{3,\max} = c_{4,\max} = \frac{\Delta L_{\max} - \Delta L_{\min}}{2}, \tag{5.7}$$

the window center is given by

$$\Delta L_{k,\text{mid}} = \frac{\Delta L_{\max} + \Delta L_{\min}}{2}. \tag{5.8}$$

In some cases we also define affine inequality constraints on the relative eccentricity and inclination vectors, for example, when we require to constrain the relative $e/i$-vectors inside annular sectors, as per the guidance design example in Chapter 3. In this case, a constraint is defined as follows:

$$\bar{c}_5\left(\boldsymbol{\tau}_{\text{tot}}\right) = a_e \Delta e_{x,k} + b_e \Delta e_{y,k} \leq 1, \tag{5.9}$$

or, for a constraint on the inclination vector:

$$\bar{c}_6\left(\boldsymbol{\tau}_{\text{tot}}\right) = a_i \Delta i_{x,k} + b_i \Delta i_{y,k} \leq 1, \tag{5.10}$$

where $a_e$, $b_e$, $a_i$ and $a_i$ are chosen such that the desired constraint arises. As before we define these constraints at every CER discrete nodes. In addition, we separately define a constraint on the final state, which is usually tighter than the other constraints. The reason for doing this is to reduce the impact of the various error sources (orbit determination, maneuvers, modeling) on the dissatisfaction of the constraints, as discussed in more detail later in the simulations and analysis section.

### 5.2.3. ROBUSTIFIED PROBLEM FORMULATION

The optimization method introduced before can be robustified by accounting for the different types of uncertainty affecting the station-keeping process in the solution of the optimization problem. In this section we develop a method that accounts for uncertainty in orbit determination errors, errors due modeling the dynamics as a LTV system, errors due to SRP model mismatch, thrust force magnitude errors and errors in thrust direction. Our aim in robustifying the process is to achieve a 3-sigma probability that a satellite stays inside some predefined tolerance windows at those times where constraints are enforced. We will first discuss the methods used to assess the 3-sigma error bounds of the different sources of errors. We then develop the formulation of the optimization problem taking these errors into account.

#### ORBIT DETERMINATION ERRORS

In Section 2.8 the orbit determination errors affecting the system were presented. Since the orbit dynamics are well-described by an LTV-system with a constant system matrix **A**, the orbit determination covariance matrix can be propagated linearly to achieve the orbit prediction covariance matrix at any time in the future. For a state transition matrix $\boldsymbol{\Phi}(t, t_0)$, the covariance at time $t$ is as follows:

$$\mathbf{C}(t) = \boldsymbol{\Phi}(t, t_0)\,\mathbf{C}(t_0)\,\boldsymbol{\Phi}^T(t, t_0). \tag{5.11}$$

In terms of the synchronous orbital elements defined in Eq. (2.6) the state transition matrix has a very simple structure:

$$\boldsymbol{\Phi}\left(t, t_0\right) = \begin{pmatrix} 1 & 0 & 0 & 0 & 0 & 0 \\ 0 & 1 & 0 & 0 & 0 & 0 \\ 0 & 0 & 1 & 0 & 0 & 0 \\ 0 & 0 & 0 & 1 & 0 & 0 \\ 0 & 0 & 0 & 0 & 1 & 0 \\ \Delta t & 0 & 0 & 0 & 0 & 1 \end{pmatrix}, \tag{5.12}$$

with $\Delta t = t - t_0$. Thus, the error in the first five states remains constant, while an error in the mean longitude $\Delta L$ increases linearly with time. The rate of change of the error in $\Delta L$ is dependent only on the initial error in $\Delta n$. The standard deviation of the orbital elements at time $t$ due to an initial orbit determination error at $t_0$ is equal to:

$$\boldsymbol{\sigma}^{\mathrm{OD}}_{\Delta\mathbf{x}(t)} = \left.\begin{pmatrix} \sigma_{\Delta n} \\ \sigma_{e_x} \\ \sigma_{e_y} \\ \sigma_{i_x} \\ \sigma_{i_y} \\ \sigma_{\Delta L} \end{pmatrix}^{\mathrm{OD}}\right|_{t=t_0} + \Delta t \left.\begin{pmatrix} 0 \\ 0 \\ 0 \\ 0 \\ 0 \\ \sigma_{\Delta n} \end{pmatrix}^{\mathrm{OD}}\right|_{t=t_0} . \tag{5.13}$$

We used the linear transformation of Eq. (2.43) to convert the covariance matrix from RTN coordinates into synchronous orbital elements for a variety of values of the mean longitude $L$. We approximated the standard deviations of the individual elements in Eq. (5.13) using only the diagonal elements of the covariance matrix in orbital elements and average the standard deviations over one orbit (i.e. values of $L$ between 0 and $2\pi$). The resulting standard deviations are given in Table 5.1. The standard deviation of the error contribution due to orbit determination is then computed from Eq. (5.13). To obtain the standard deviation of the state vector at all discrete times in the optimization problem simultaneously we evaluate Eq. (5.13) at the discrete nodes $t_k$ and concatenate the standard deviations to obtain $\boldsymbol{\sigma}^{\mathrm{OD}}_{\Delta\mathbf{x}_{\mathrm{tot}}}$.

Table 5.1: Standard deviations of orbit determination errors in synchronous orbital elements

| Element | $\sigma^{\mathrm{OD}}$ |
|---|---|
| $\Delta n$ [rad/s] | 4.4E-12 |
| $e_x$ [-] | 5.8E-8 |
| $e_y$ [-] | 5.8E-8 |
| $i_x$ [rad] | 4.9E-7 |
| $i_y$ [rad] | 4.9E-7 |
| $\Delta L$ [rad] | 8.7E-6 |

### MODELING ERRORS

The dominant dynamics modeling errors result from the approximation of the nonlinear dynamics by the LTV system in Eq. (2.13) and the errors introduced in approximating the SRP as defined in Section 2.8. An analysis of the accuracy of the LTV system was performed in Section 2.3.4. By comparing the errors in eccentricity, inclination and mean longitude we found that the errors grow roughly linear with time. To characterize the accuracy of the modeling errors in terms of synchronous orbital elements, we have performed a Monte-Carlo analysis for an optimization timestep of 1080 seconds for randomly generated initial states as in Section 2.3.4. The results of this analysis are presented in this section in order to derive a simple linear model of the uncertainty due to the LTV approximation of the dynamics. We performed a similar exercise to estimate the uncertainty resulting from SRP modeling errors and also derive a linear approximation of the standard deviation of the resulting error in terms of synchronous orbital elements. Hence we approximate the standard deviation of the error in orbital elements due to modeling errors as a linear function of time.

Table 5.2 presents the results of this analysis: the time-rate-of-change of the standard deviation of the errors in orbital elements due to the LTV dynamics and SRP mismodeling are given. To obtain an approximation of the standard deviation of the errors due to LTV or SRP mismodeling at time $t$, we multiply the entry from Table 5.2 with the time since the last orbit determination epoch $\Delta t = t - t_0$.

$$\boldsymbol{\sigma}^{\mathrm{LTV/SRP}}_{\Delta\mathbf{x}(t)} = \frac{\mathrm{d}}{\mathrm{d}t}\begin{pmatrix}\sigma_{\Delta n}\\ \sigma_{e_x}\\ \sigma_{e_y}\\ \sigma_{i_x}\\ \sigma_{i_y}\\ \sigma_{\Delta L}\end{pmatrix}^{\mathrm{LVT/SRP}} \cdot \Delta t. \tag{5.14}$$

As before, to obtain the standard deviation of LTV and SRP modeling errors at each discrete node we evaluate Eq. (5.14) at every $t_k$ and concatenate the standard deviations to obtain $\boldsymbol{\sigma}^{\mathrm{LTV}}_{\Delta\mathbf{x}_{\mathrm{tot}}}$ and $\boldsymbol{\sigma}^{\mathrm{SRP}}_{\Delta\mathbf{x}_{\mathrm{tot}}}$.

Table 5.2: Time derivative of a linear approximation of the standard deviation of the error due LTV dynamics model and SRP mismodeling.

| Element | Unit | $\frac{\mathrm{d}}{\mathrm{d}t}\left(\sigma^{\mathrm{LTV}}\right)$ | $\frac{\mathrm{d}}{\mathrm{d}t}\left(\sigma^{\mathrm{SRP}}\right)$ |
|---|---|---|---|
| $\Delta n$ | rad/s/day | 4.29E-12 | 2.3E-14 |
| $e_x$ | 1/day | 1.02E-07 | 4.86E-7 |
| $e_y$ | 1/day | 1.26E-07 | 5.00E-7 |
| $i_x$ | rad/day | 3.25E-07 | 7.14E-10 |
| $i_y$ | rad/day | 1.58E-07 | 2.86E-10 |
| $\Delta L$ | rad/day | 9.76E-07 | 1.00E-6 |

### THRUST ERRORS

Thrust force magnitude errors (TM) are separately treated from thrust direction errors (TD). We investigate how these errors affect our knowledge of the orbital elements, starting with a thrust force magnitude error. The influence of a maneuver on the orbital elements is captured by:

$$\mathbf{H}\boldsymbol{\Gamma}\boldsymbol{\tau}_{\text{tot}}, \tag{5.15}$$

where the $j^{\text{th}}$ element of $\boldsymbol{\tau}_{\text{tot}}$ is referred to as $\tau_j$. An uncertainty in this variable was modeled as a multiplicative uncertainty (Section 2.8):

$$\tau_j = \tau_{j,\text{nom}}\left(1+\Delta_\tau\right), \quad \text{with} \quad \Delta_\tau = \mathcal{N}\left(0, \sigma_{\tau_j}\right). \tag{5.16}$$

This thrust uncertainty $\tau_{j,\text{nom}}\Delta_\tau$, will affect all orbital elements in $\mathbf{x}_{\text{tot}}$ corresponding to the nonzero entries in the $j^{\text{th}}$ column of matrix $\mathbf{H}\boldsymbol{\Gamma}$, which we refer to as $\mathbf{H}\boldsymbol{\Gamma}\left(:,j\right)$. The uncertainty in $\mathbf{x}_{\text{tot}}$ due to the $\tau_{j,\text{nom}}\Delta_\tau$ can be evaluated as:

$$\Delta\mathbf{x}_{\text{tot},j} = \mathbf{H}\boldsymbol{\Gamma}\left(:,j\right)\tau_{j,\text{nom}}\Delta_\tau, \tag{5.17}$$

with standard deviation (element-wise):

$$\boldsymbol{\sigma}^{\text{TM}}_{\Delta\mathbf{x}_{\text{tot},j}} = \left|\mathbf{H}\boldsymbol{\Gamma}\left(:,j\right)\right|\tau_{j,\text{nom}}\sigma_{\tau_j}. \tag{5.18}$$

The total standard deviation due to all thrusts combined can be calculated by summing over all thrusts either linearly (L):

$$\boldsymbol{\sigma}^{\text{TM,L}}_{\Delta\mathbf{x}_{\text{tot}}} = \sum_j \left|\mathbf{H}\boldsymbol{\Gamma}\left(:,j\right)\right|\tau_{j,\text{nom}}\sigma_{\tau_j}, \tag{5.19}$$

or, if we assume that the errors of different thruster firings are statistically independent of each other (as we have implemented in our simulations, see Section 2.8), we can sum quadratically (Q):

$$\boldsymbol{\sigma}^{\text{TM,Q}}_{\Delta\mathbf{x}_{\text{tot}}} = \sqrt{\sum_j \left(\mathbf{H}\boldsymbol{\Gamma}\left(:,j\right)\tau_{j,\text{nom}}\sigma_{\tau_j}\right)^2}. \tag{5.20}$$

In the simulations we used a 3-$\sigma$ thrust magnitude error of 5%, such that $\sigma_{\tau_j} = 0.0167$ for each thruster firing. Note that both Eq. (5.19) and Eq. (5.20) are convex functions of the independent variables $\boldsymbol{\tau}_{\text{tot}}$.

Thrust direction errors are treated in a similar fashion as thrust magnitude errors. We first establish that a thrust direction error (for the errors considered in this work) results in an erroneous thrust in the plane perpendicular to the thrust vector, but has no significant impact on the magnitude of the thrust vector in the intended direction. For a maximum off-angle of the thrust vector of 1.5° the reduction of thrust $\tau_{j,\text{nom}}$ in the intended direction is:

$$\left(1-\cos 1.5^\circ\right)\cdot\tau_{j,\text{nom}} = 3.2\cdot 10^{-4}\cdot\tau_{j,\text{nom}}, \tag{5.21}$$

while in the plane perpendicular to the thrust vector a parasitical thrust of

$$\sin\left(1.5^\circ\right)\cdot\tau_{j,\text{nom}} \approx 1.5\frac{\pi}{180}\cdot\tau_{j,\text{nom}} = 0.026\cdot\tau_{j,\text{nom}} \tag{5.22}$$

occurs. We neglect the impact of a thrust direction error on the thrust force in the intended direction and approximate the thrust direction error in the direction perpendicular to the thrust direction as a linear function of the attitude error, such that a thrust error resulting from an attitude error with $\Delta_a = \mathcal{N}\left(0, \sigma_{a_j}\right)$ has a magnitude given by the random variable $\tau_{j,\text{nom}}\Delta_a$. This approximation is conservative as a rotation around the thrust vector itself does not contribute to a thrust direction error (i.e. only the perpendicular components do).

In order to project the thrust direction uncertainty of a thruster onto radial, tangential and normal directions we use:

$$\Gamma^{\perp}_{ij} = \frac{\sqrt{2}}{2}\sqrt{1-\Gamma^2_{ij}}, \tag{5.23}$$

where $ij$ refers to the $ij^{\text{th}}$ element of the matrix. This results in the following matrix for our definition of $\Gamma$ (Eq. 2.51):

$$\Gamma^{\perp} = \frac{\sqrt{2}}{2m}\begin{pmatrix} \sqrt{1-\sin^2\gamma\cos^2\beta} & \sqrt{1-\sin^2\gamma\cos^2\beta} & \sqrt{1-\sin^2\gamma\cos^2\beta} & \sqrt{1-\sin^2\gamma\cos^2\beta} \\ \sqrt{1-\sin^2\gamma\sin^2\beta} & \sqrt{1-\sin^2\gamma\sin^2\beta} & \sqrt{1-\sin^2\gamma\sin^2\beta} & \sqrt{1-\sin^2\gamma\sin^2\beta} \\ \sin\gamma & \sin\gamma & \sin\gamma & \sin\gamma \end{pmatrix}, \tag{5.24}$$

such that

$$\mathbf{u}^{\perp} = \Gamma^{\perp}\boldsymbol{\tau}. \tag{5.25}$$

We also define $\mathbf{\Gamma}^{\perp}$ similar to Eq. (2.53):

$$\mathbf{\Gamma}^{\perp} = \begin{pmatrix} \Gamma^{\perp} & & \\ & \Gamma^{\perp} & \\ & & \ddots \end{pmatrix}. \tag{5.26}$$

As for the thrust magnitude errors, we describe the effect of a thrust direction error of an individual thruster firing by $\tau_{j,\text{nom}}\Delta_a$. This error affects all orbital elements in $\mathbf{x}_{\text{tot}}$ corresponding to the nonzero rows of the $j^{\text{th}}$ column of matrix $\mathbf{H\Gamma}^{\perp}$. The uncertainty in $\mathbf{x}_{\text{tot}}$ due to $\tau_{j,\text{nom}}\Delta_a$ can be evaluated as:

$$\Delta\mathbf{x}_{\text{tot},j} = \mathbf{H\Gamma}^{\perp}\left(:,j\right)\tau_{j,\text{nom}}\Delta_a, \tag{5.27}$$

with standard deviation (element-wise):

$$\boldsymbol{\sigma}^{\text{TD}}_{\Delta\mathbf{x}_{\text{tot},j}} = \left|\mathbf{H\Gamma}^{\perp}\left(:,j\right)\right|\tau_{j,\text{nom}}\sigma_{a_j}. \tag{5.28}$$

Again, the total standard deviation due to all thrusts combined can be calculated by summing over all thrusts either linearly:

$$\boldsymbol{\sigma}^{\text{TD,L}}_{\Delta\mathbf{x}_{\text{tot}}} = \sum_j \left|\mathbf{H\Gamma}^{\perp}\left(:,j\right)\right|\tau_{j,\text{nom}}\sigma_{a_j}, \tag{5.29}$$

or quadratically:

$$\boldsymbol{\sigma}^{\text{TD,Q}}_{\Delta\mathbf{x}_{\text{tot}}} = \sqrt{\sum_j \left(\mathbf{H\Gamma}^{\perp}\left(:,j\right)\tau_{j,\text{nom}}\sigma_{a_j}\right)^2}. \tag{5.30}$$

We demonstrate both linear and quadratic summations of the thrust force and magnitude errors in the simulations in section 5.3.4.

### ROBUSTIFIED OPTIMIZATION PROBLEM

Using simplified error models, we have obtained a set of functions that describe the standard deviation of the synchronous orbital elements at every discrete node in the optimization depending on the various contributors. A conservative approximation of the total standard deviation of a satellite's total state vector is then:

$$\boldsymbol{\sigma}_{\Delta\mathbf{x}_{\text{tot}}} = \boldsymbol{\sigma}^{\text{OD}}_{\Delta\mathbf{x}_{\text{tot}}} + \boldsymbol{\sigma}^{\text{LTV}}_{\Delta\mathbf{x}_{\text{tot}}} + \boldsymbol{\sigma}^{\text{SRP}}_{\Delta\mathbf{x}_{\text{tot}}} + \boldsymbol{\sigma}^{\text{TM,L}}_{\Delta\mathbf{x}_{\text{tot}}} + \boldsymbol{\sigma}^{\text{TD,L}}_{\Delta\mathbf{x}_{\text{tot}}}, \tag{5.31}$$

in case of linearly added thrust uncertainties, or

$$\boldsymbol{\sigma}_{\Delta\mathbf{x}_{\text{tot}}} = \sqrt{\left(\boldsymbol{\sigma}^{\text{OD}}_{\Delta\mathbf{x}_{\text{tot}}}\right)^2 + \left(\boldsymbol{\sigma}^{\text{LTV}}_{\Delta\mathbf{x}_{\text{tot}}}\right)^2 + \left(\boldsymbol{\sigma}^{\text{SRP}}_{\Delta\mathbf{x}_{\text{tot}}}\right)^2 + \left(\boldsymbol{\sigma}^{\text{TM,Q}}_{\Delta\mathbf{x}_{\text{tot}}}\right)^2 + \left(\boldsymbol{\sigma}^{\text{TD,Q}}_{\Delta\mathbf{x}_{\text{tot}}}\right)^2}, \tag{5.32}$$

when we assume that all errors are independent from each other and the standard deviations can be added quadratically. Note that the equations are convex functions in the optimization variables $\boldsymbol{\tau}_{\text{tot}}$, both for a linear and a quadratic addition of the thrust magnitude and thrust direction errors. The other components of the error are independent of the optimization variables.

In the collocation problem we enforce constraints on the relative orbital elements and both leader and follower satellites contribute to the uncertainty in the relative orbital elements. The contribution of the leader satellite is a function of the leader's orbit control maneuver, but not of the optimization problem variables in the collocation problem (which are the thrust force variables of the follower satellite). The standard deviations of the leader and follower state trajectory in each orbital element at each of the discrete nodes are calculated using Eq. ( 5.31) or Eq. (5.32). The combined uncertainty in the relative orbital elements is then:

$$\boldsymbol{\sigma}_{\Delta\mathbf{x}_{\text{tot}}} = \boldsymbol{\sigma}^{F}_{\Delta\mathbf{x}_{\text{tot}}} + \boldsymbol{\sigma}^{L}_{\Delta\mathbf{x}_{\text{tot}}} \tag{5.33}$$

in case of linear addition, or

$$\boldsymbol{\sigma}_{\Delta\mathbf{x}_{\text{tot}}} = \sqrt{\left(\boldsymbol{\sigma}^{F}_{\Delta\mathbf{x}_{\text{tot}}}\right)^2 + \left(\boldsymbol{\sigma}^{L}_{\Delta\mathbf{x}_{\text{tot}}}\right)^2} \tag{5.34}$$

in case of quadratic addition. The superscripts $L$ and $F$ refer to leader and follower satellites. Note that these standard deviations remain convex functions of the optimization variables.

The typical constraint windows that we implement are bounds that are either affine or quadratic functions of the satellite state. We "robustly" enforce these constraints by "forcing" the optimization problem to stay three standard-deviations away from the boundary, hence essentially applying tighter (and time, state and and control dependent) bounds. For affine state constraints we can use affine combinations of the standard deviations of the (relative) orbital elements to robustly enforce a constraint.

The quadratic bounds in the station-keeping and collocation problems essentially keep the (relative) eccentricity or inclination vector inside a circular window. To apply such a constraint in a robustified manner we reduce the radius of the circular boundary, such that the satellite state stays inside reduced circular window with a probability exceeding 99.7%. As an example, if $\sigma_{\Delta e_{x,k}}$ and $\sigma_{\Delta e_{y,k}}$ are the standard deviations of the errors of the eccentricity vector components, the eccentricity vector will be in a circle with a radius of

$$3\sigma_{\delta e_k} = 3\sqrt{\left(\sigma_{\Delta e_{x,k}}\right)^2 + \left(\sigma_{\Delta e_{y,k}}\right)^2}. \tag{5.35}$$

with a probability ≥ 99.7% (assuming Gaussian errors, the probability reduces to 99.7% only in case $\Delta e_x$ and $\Delta e_y$ are fully correlated). Note that the value in Eq. (5.35) is not actually a standard deviation, however, we still used the $\sigma$-symbol. If we reduce the tolerance window radius by this value, the probability that the relative eccentricity vector stays inside the tolerance windows is then also ≥ 99.7%.

As examples of robustified constraint formulations we provide the "robustified" versions of Eqs. (5.3) and (5.4):

$$\bar{c}_1\left(\boldsymbol{\tau}_{\text{tot}}\right) = \frac{\sqrt{\left(\Delta e_{x,k} - \Delta e^{\text{nom}}_{x,k}\right)^2 + \left(\Delta e_{y,k} - \Delta e^{\text{nom}}_{y,k}\right)^2}}{r_e} + \frac{3\sigma_{\delta e_k}}{r_e} \leq 1 \tag{5.36}$$

and

$$\bar{c}_2\left(\boldsymbol{\tau}_{\text{tot}}\right) = \frac{\sqrt{\left(\Delta i_{x,k} - \Delta i^{\text{nom}}_{x,k}\right)^2 + \left(\Delta i_{y,k} - \Delta i^{\text{nom}}_{y,k}\right)^2}}{r_i} + \frac{3\sigma_{\delta i_k}}{r_i} \leq 1. \tag{5.37}$$

in which $\sigma_{\delta e_k}$ and $\sigma_{\delta i_k}$ represent the uncertainty in the relative orbital elements, resulting from the combined leader and follower uncertainties from Eq. (5.33) or Eq. (5.34).

The constraints are applied in a similar manner at each discrete node in the optimization problem, except at the final time. At this time the tolerance window is reduced even further, namely by three standard deviations of the combined orbit determination error of the leader and follower satellites (either linearly or quadratically). This is done to ensure that the constraint is not violated at the initial time of the next maneuver cycle, at which the tolerance windows is reduced by the orbit determination uncertainty (at the initial discrete node, no maneuvers have taken place and the standard deviations of the state error are only due to the orbit determination errors of leader and follower satellites).

## 5.3. SIMULATIONS, RESULTS AND ANALYSIS

We present the results of simulations for a variety of applications, each chosen for specific reasons. We start with an inhomogeneous fleet of four satellites in a ±0.1° slot. With this simulation case we show that we can apply the method for controlling a fleet of satellites in which each satellite has different characteristics. We show that we can maintain a minimum separation distance in a manner similar to the current operational practice. The next application case demonstrates that the method easily scales to larger fleets by showing an application with a large fleet of 16 satellites in a small ±0.05° slot. To be able to control that many satellites inside a small slot we have reduced the maneuver cycle duration to a single day. The subsequent applications build on the guidance design example introduced in Chapter 3 and show how we can deal with sensor cone avoidance constraints in addition to the minimum distance constraint. The last case study uses the robustified formulation of the collocation problem. We show that this formulation allows us to guarantee that we stay inside certain pre-defined tolerance windows. The advantages and disadvantages of the robustified formulation are discussed. All simulations included in this chapter include errors due to orbit determination, actuation and modeling.

### 5.3.1. INHOMOGENEOUS FLEET OF FOUR SATELLITES

In Chapter 3 we have shown how a minimum distance can be guaranteed if we can maintain the relative eccentricity and relative inclination vectors inside certain (convex) tolerance windows. Here, we use these tolerance windows and simulate the station-keeping of a fleet of four satellites in a geostationary slot. The calculation of the station-keeping maneuvers of the follower satellites is done by solving Problem 5.1. The goals are to maintain a certain minimum separation distance between the satellites while staying inside a geostationary slot of ±0.1°. One satellite is the designated fleet leader, while the other three follower satellites are controlled with respect to the leader satellite. We show a simulation case including the different forms of uncertainty discussed before, for satellites that all have either a different propulsion system from the leader satellite or a different surface area exposed to SRP, or both. We aim to show that the method we have developed in the previous chapter, and extended towards multiple satellites in this chapter, can be used to control a fleet of satellites such that minimum distances can be guaranteed while staying inside the geostationary slot. We show that there are no propellant consumption penalties compared to the case with a single geostationary satellite.

An overview of the key simulation parameters is given in Table 5.3. The leader satellite is equipped with an electric propulsion system in configuration B. The follower satellites each have different propulsion systems. The first follower satellite has a chemical propulsion system in the reference configuration while the other two follower satellites

Table 5.3: Key simulation settings for the simulations with an inhomogeneous fleet of four satellites

| **Parameter** | **Unit** | **Value** | | | |
|---|---|---|---|---|---|
| Satellite | | L | F1 | F2 | F3 |
| Thruster configuration | | B | REF | A | B |
| Thrust force | N | 0.08 | 10 | 0.08 | 0.08 |
| $A_s$ | $m^2$ | 90 | 120 | 120 | 120 |
| SPP | | Yes | - | - | - |
| Tolerance on **e** | $10^{-3}$ | - | 0.05 | 0.05 | 0.05 |
| Tolerance on **i** | mrad | - | 0.05 | 0.05 | 0.05 |
| Tolerance on $\|\Delta L\|$ | mrad | 0.3 | 0.3 | 0.3 | 0.3 |
| Tolerance on final **e** | $10^{-3}$ | fixed final **e** | 0.025 | 0.025 | 0.025 |
| Tolerance on final **i** | mrad | fixed final **i** | 0.025 | 0.025 | 0.025 |
| Tolerance on final $\|\Delta L\|$ | mrad | fixed final $\Delta L$ | 0.075 | 0.075 | 0.075 |
| Elements constrained | | Mean | Relative | Relative | Relative |
| Maneuver cycle | days | 7 | 7 | 7 | 7 |
| Schedule | | 6 out 7 | 6 out 7 | 6 out 7 | 6 out 7 |
| Use $\mathbf{W}_\tau$ | | No | No | No | No |

have an electric propulsion system in configuration A and B respectively. The leader's surface area exposed to solar radiation (90 $m^2$) is smaller than that of the follower satellites (120 $m^2$). Each satellite has a maneuver cycle of 7 days, where maneuvers are allowed 6 out of 7 days, with the $7^{th}$ day being reserved for orbit determination.

The leader satellite's eccentricity vector is constrained to follow a circle with the eccentricity vector pointing in the direction of the Sun (as per SPP) with a radius of $2{\cdot}10^{-4}$. Only the final eccentricity and inclination vectors (those at the end of each maneuver cycle) are constrained for the leader. The mean longitude difference is constrained to a ±0.3 mrad window around the slot center, while the final mean longitude difference is constrained to zero. The configuration in the eccentricity and inclination plane was chosen according to the eccentricity/inclination vector separation strategy, with identical configurations of relative eccentricity and inclination vectors. The actual configuration is clearly visible from the results that follow shortly. The tolerance windows on eccentricity and inclination vectors are circular with their radius given in Table 5.3. The relative mean longitude difference is constrained in a 0.3 mrad window centered on the leader's mean longitude difference. The final state is constrained to a smaller window (half the size for eccentricity and inclination and a factor 4 smaller for relative mean longitude). Constraining the final state in smaller windows significantly reduces overall constraint violations without significant impact on the propellant consumption. In fact, we observed a slightly positive impact on the propellant consumption, which can be explained as follows: without the smaller window in final state, the optimizer often generates a trajectory close to (or on) the constraint boundary. The effect of the various errors can push the trajectory over the boundary. Now the next maneuver cycle will start with a state outside of the tolerance windows. Due to the use of the slack variables, the optimization problem is still feasible, but the optimizer will try to bring the state back inside the tolerance windows as quickly as possible (since the cost associated to violating the constraints is rather high). The result is that some small maneuvers might be made at non-optimal locations. Including a final state constraint with a smaller tolerance counters this undesired situation.

The theoretical minimum distance for arbitrary relative eccentricity and inclination vectors inside the defined tolerance windows can be calculated using Eqs. (3.22) and (3.35). For the tolerance window definitions in this example, the theoretical minimum distance between leader and follower satellites (either F1 or F3) is equal to 9.67 km, while the theoretically achievable minimum distance between two follower satellites (either F1/F2 or F2/F3) is equal to 6.74 km. To calculate the minimum distance between two follower satellites we substituted twice the radius of the tolerance window in Eq. (3.35).

The performance results of the simulations are given in Table 5.4. In terms of propellant consumption, all four satellites show excellent performance, very much in line with the results for a single satellite. Although the differences are small, the obtained results for the fleet were slightly better than for a single satellite (Table 4.10). The addition of the final state constraint on $\Delta L$ made control of the leader satellite slightly more efficient (i.e. no maneuver cycle started with a longitude outside of the tolerance window). Furthermore, for the follower satellites, the small window on inclination vector allowed for small variations of the actual inclination vector variations compared to the predicted inclination vector variations based on Kamel's theory (which included Earth gravity perturba-

Table 5.4: Key results for the simulations with an inhomogeneous fleet with four satellites

| **Parameter** | **Unit** | **Value** | | | |
|---:|:---:|:---:|:---:|:---:|:---:|
| Satellite | | L | F1 | F2 | F3 |
| $\Delta V$ | m/s | 67.88 | 50.98 | 68.00 | 67.72 |
| Firings | | 1248 | 612 | 1251 | 1160 |
| Max. longitude deviation | deg | 0.062 | 0.071 | 0.078 | 0.064 |
| Max. latitude | deg | 0.041 | 0.044 | 0.043 | 0.040 |

tions up to 3rd order and degree and Sun and Moon gravity only). In terms of thruster firings, all three electric propulsion satellites were behaving as expected, while an increase in thruster firings for F1 is observed compared to a single satellite. This might have been expected as the trajectory is controlled relative to that of a leader satellite with an electric propulsion system. Hence the “reference” trajectory has many small maneuvers inside and maintaining the satellite state inside a tolerance window around this reference trajectory required more maneuvers than in the single-satellite case. The maximum longitude and latitude deviations show that all four satellite stayed inside the geostationary slot with ample margin.

In terms of state trajectories, we choose to show the absolute osculating eccentricity and inclination vectors of the fleet in Figures 5.2 and 5.3, as well as the relative state trajectories of the eccentricity vector (Figure 5.4), inclination vector (Figure 5.5) and mean longitude deviation (Figure 5.6). The constraints that were imposed on these relative state trajectories are given by the dashed lines. From these figures we observe minor violations of the state constraints over the course of the simulations. This was expected since we enforce these constraints only every 10th discrete step. In addition, the errors that we introduced cause orbit prediction errors and the accuracy of control cannot be better than the orbit prediction accuracy. Such minor violations of the constraints can be accounted for in the design of the nominal configuration and tolerance window sizing (in fact, the theoretical minimum distance of 6.74 km provides ample margin for errors). The important results are 1.) all satellites stayed inside the geostationary slot (see Figures 5.7 and 5.8), while 2.) the minimum distance in the radial-normal plane that was observed during the simulation between all pairs of satellites was between F1 and F2 and was equal to 8.61 km, as seen from Figure 5.9, depicting the relative trajectory of F2 in the radial-normal plane attached to F1.

### 5.3.2. HOMOGENEOUS FLEET OF SIXTEEN SATELLITES

We intend to show that with the method developed in this work we can safely collocate many more satellites in a single small slot. We demonstrate the collocation of 16 satellites in a small ±0.05° slot. To increase the accuracy of control (or alternatively; to reduce the orbit prediction errors), we use a maneuver cycle duration of only one day. The 16 satellites are assumed to be of identical build, with an electric propulsion system in configuration B. The satellite characteristics and simulation settings are the same as for F3 in Table 5.3 with some exceptions: the tolerance windows have been reduced by a factor two compared to the inhomogeneous fleet, the leader no longer follows a SPP strategy

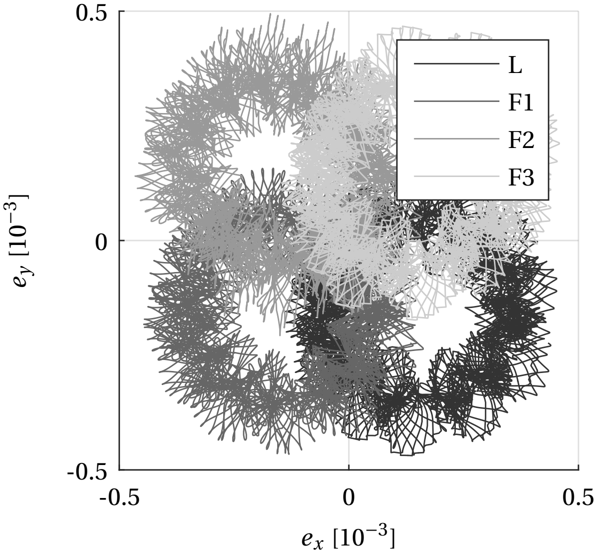

Figure 5.2: Osculating eccentricity vectors for the simulations with an inhomogeneous fleet with four satellites.

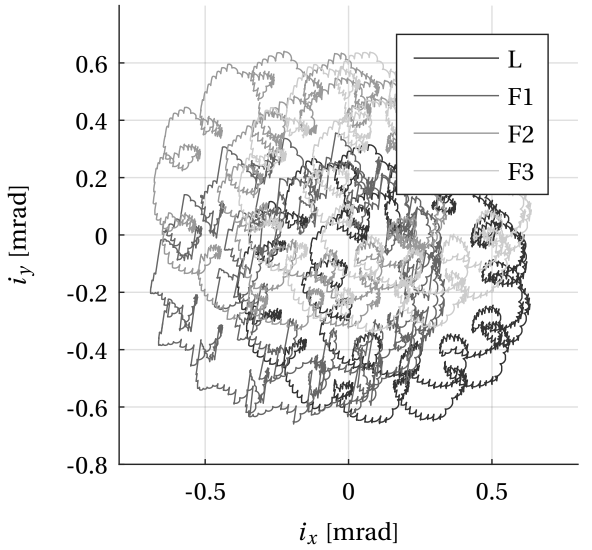

Figure 5.3: Osculating inclination vectors for the simulations with an inhomogeneous fleet with four satellites.

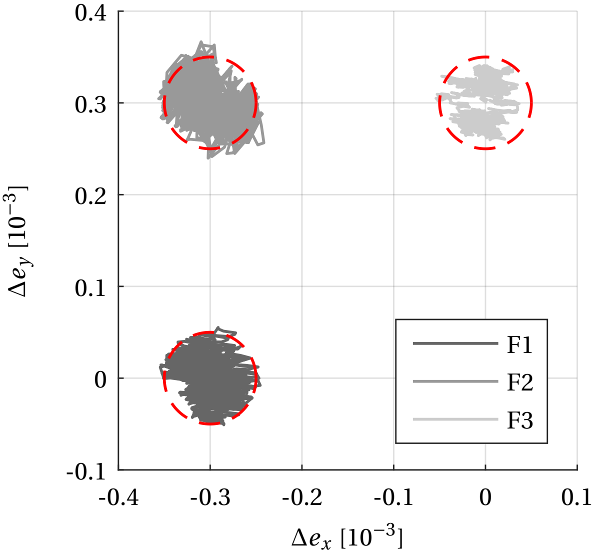

Figure 5.4: Relative eccentricity vectors for the simulations with an inhomogeneous fleet with four satellites

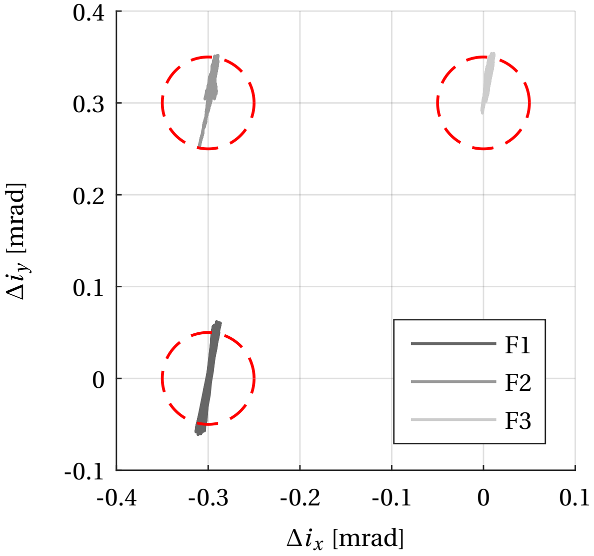

Figure 5.5: Relative inclination vectors for the simulations with an inhomogeneous fleet with four satellites

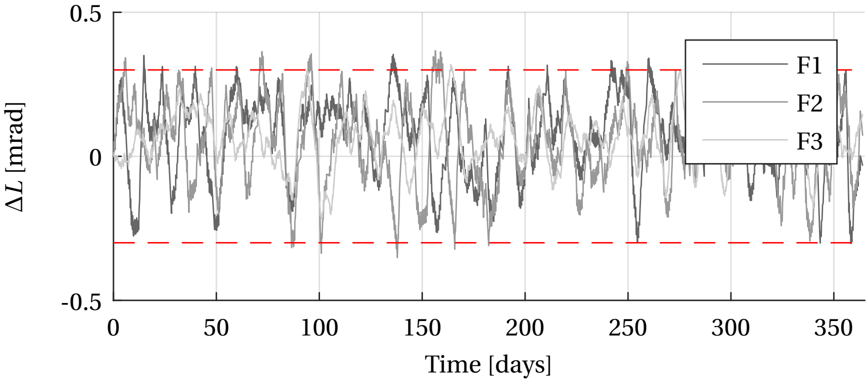

Figure 5.6: Relative longitudes for the simulations with an inhomogeneous fleet with four satellites

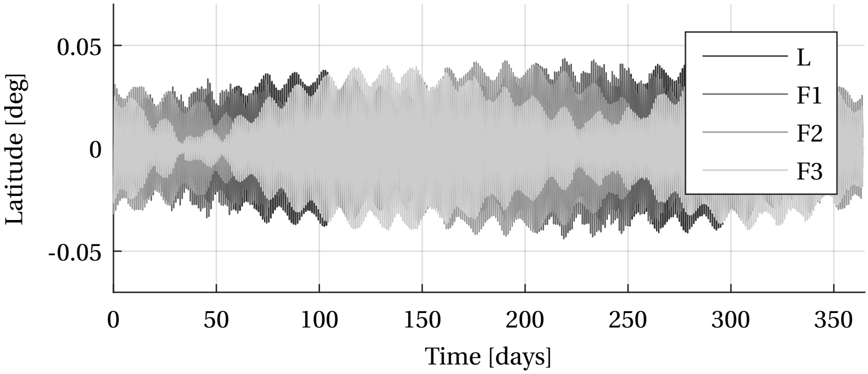

Figure 5.7: Latitudes for the simulations with an inhomogeneous fleet with four satellites

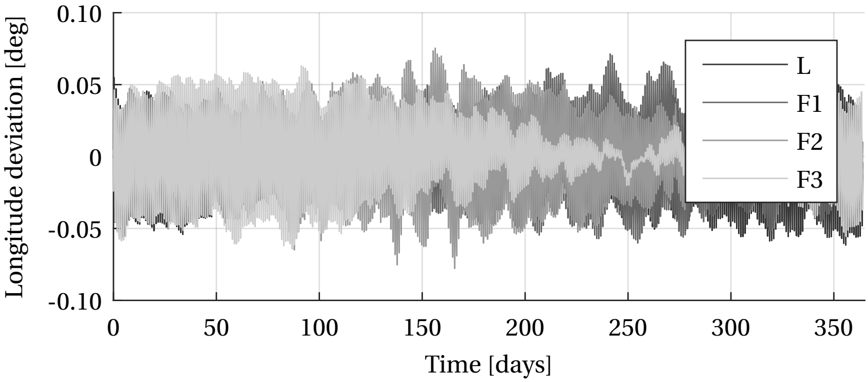

Figure 5.8: Longitudes for the simulations with an inhomogeneous fleet with four satellites

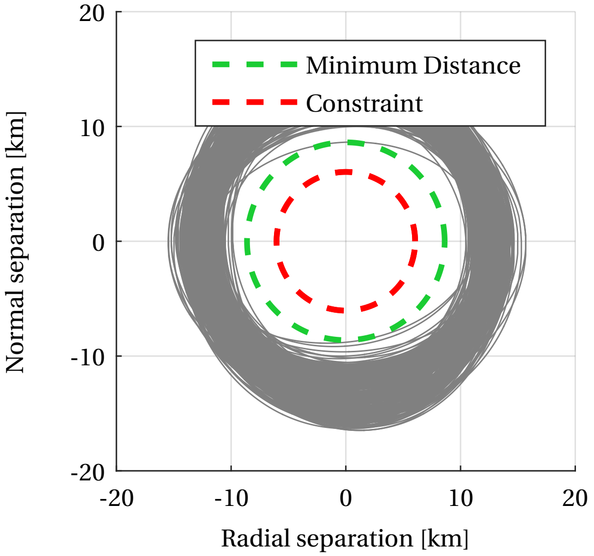

Figure 5.9: Relative motion of F1 and F2 of the inhomogeneous fleet in the radial-normal plane. The achieved minimum distance is equal to 8.61 km.

and no schedule is imposed. The reason that no SPP strategy is used is that none of the satellites in the fleet have a chemical propulsion system. The analysis in Section 4.4.2 showed that the SPP strategy is not required for the electric propulsion configurations studied in this work. A schedule is omitted because the propagation horizon is only one day.

The actual relative eccentricity and inclination vector configuration follows again the typical separation strategy and can be seen from Figures 5.10 and 5.11. We have further reduced the CER to one such that tolerance window violations are a result only of state prediction errors. Note that since we reduced the maneuver cycle duration to a single day, we can also significantly reduce the required minimum separation distance, since the orbit prediction errors are much smaller. We rely only on eccentricity and inclination vectors to achieve a minimum separation distance. Figures 4.24 and 4.25 show very small uncertainty in these elements during the first day (for configuration B in this case). The configuration of relative $e/i$-vectors gives us a theoretical minimum separation distance between the leader satellite and any follower satellite in the fleet that is larger than or equal to 3.57 km and between any two follower satellites it is larger than or equal to 2.13 km (using Eqs. (3.22) and (3.35) with $\delta e_c = \delta i_c = 1.2{\cdot}10^{-4}$ and $r_e = r_i = 0.25{\cdot}10^{-4}$ or $r_e = r_i = 0.5{\cdot}10^{-4}$).

Table 5.5 presents the simulation results. Instead of listing the individual $\Delta V$ and number of firings for each satellite, we provide the mean numbers and the maximum numbers. From the table we observe a slight increase in propellant consumption and

Table 5.5: Key simulation results for the simulations with a homogeneous fleet of 16 satellites

| Parameter | Unit | Value |
|---:|:---:|:---:|
| Mean $\Delta V$ | m/s | 68.23 |
| Max. $\Delta V$ | m/s | 69.36 |
| Mean firings | | 1468 |
| Max. firings | | 1504 |
| Max. longitude deviation | deg | 0.046 |
| Max. latitude | deg | 0.045 |

thruster firings as compared to Table 5.4. By decreasing the maneuver cycle duration, we increased the frequency of feedback and thus we increased the response to errors. This explains the increased thruster firings and the slight increase in propellant consumption. We further see from Table 5.5 that all satellites managed to stay inside the geostationary slot. Figures 5.10 and 5.11 show the control of the relative eccentricity and inclination vectors. We see only small violations of the boundaries, in line with the small orbit prediction errors that we expect during the one-day maneuver cycle duration. We further determined the minimum distance between all 120 pairs of satellites over the simulation duration (one year). We found that in this particular simulation the minimum distance occurred between the leader satellites and F6 and was equal to 3.56 km (the projected trajectory is given in Figure 5.12). This is noteworthy for two reasons: first, it is slightly smaller than the theoretical minimum of 3.57 km, and second, the smallest distance occurred between the leader satellite and a follower satellite and not between two follower satellites. From Figure 5.10 we infer that the eccentricity window is used almost completely over the year, and it is well possible that a close-to-worst-case orientation of relative eccentricity and inclination vectors occurs. If we include the small errors it is well possible that we observe a minimum distance that is slightly smaller than the theoretical worst-case. Another explanation is that the theoretical worst-case calculated using Eqs. (3.22) and (3.35) ignores a nonzero semi-major axis difference in calculating the minimum separation distance. Allowing for a small variation in relative semi-major axis would reduce the theoretical minimum separation distance (we have included the effect of a nonzero semi-major axis difference in the upcoming application cases based on the guidance design example from Chapter 3). The observation that the minimum separation distance occurred between the leader satellite and a follower satellite could result from the fact that all satellites have similar characteristics and thus the maneuvers tend to be executed at roughly the same locations in orbit. Each follower satellite gets, as an input, the same predicted leader state and any errors in this predicted leader state trajectory thus affect each of the follower satellites in a similar way. The resulting follower state trajectories are very similar to each other, thereby reducing the relative state variations between the follower satellites. This very similar behavior between the follower satellites can be seen also from the relative inclination vectors in Figure 5.11.

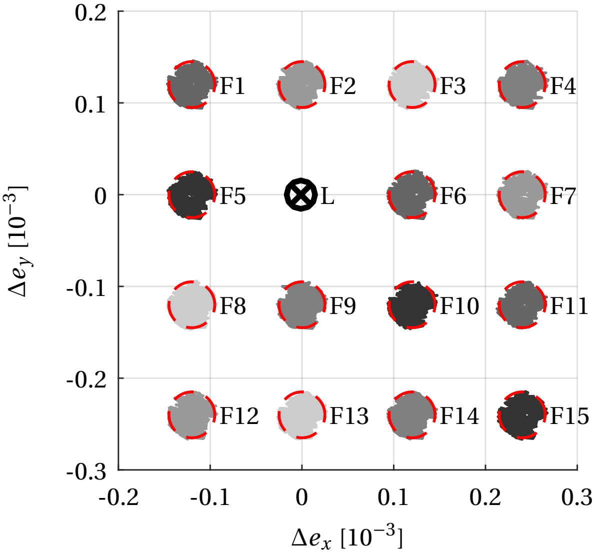

Figure 5.10: Relative eccentricity vectors for the simulations with a homogeneous fleet of 16 satellites

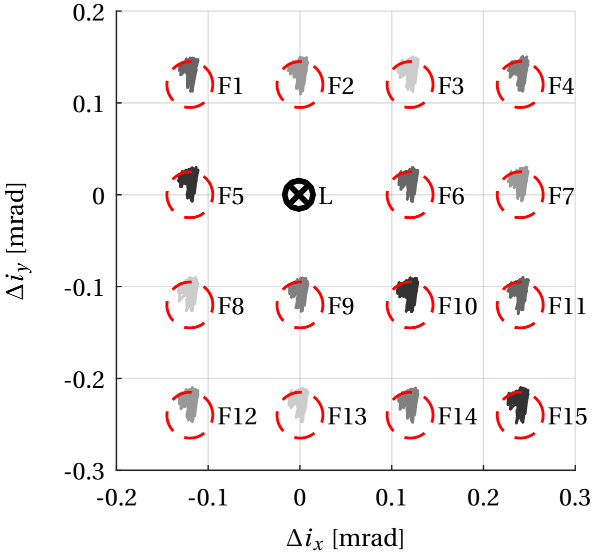

Figure 5.11: Relative inclination vectors for the simulations with a homogeneous fleet of 16 satellites

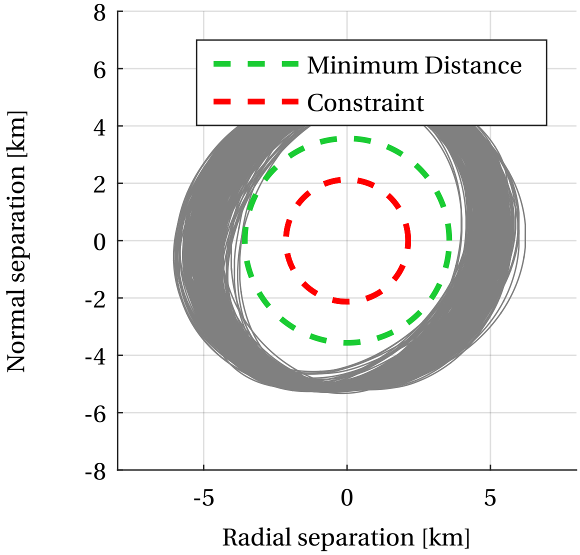

Figure 5.12: Relative motion between L and F6 in the radial-normal plane. The minimum distance is equal to 3.56 km

### 5.3.3. MANEUVER PLANNING WITH GEOMETRIC CONSTRAINTS

This section integrates the newly developed theory regarding control windows that simultaneously satisfy sensor cone avoidance constraints as well as minimum distance constraints and the convex optimization-based method for controlling the satellites. The addition of the sensor cone avoidance constraints requires us to actively control the relative mean longitude difference between the satellites, whereas this was not necessary to guarantee minimum distances or to stay inside the geostationary slot. The control methodology developed in this work is a key enabler to achieve simultaneous satisfaction of the various geometric constraints, as it allows also to explicitly constrain the relative mean longitude difference between the satellites. We setup an application case based on the guidance design example discussed in Chapter 3.

We investigate the two cases presented in Section 3.7. The first case presented in this section has its $e/i$ control windows derived from the rectangular rational window. The satellites are equipped with a chemical propulsion system. Since we observed large errors in controlling the mean longitude using a chemical propulsion system (Section 4.4.3), we investigate maneuver cycles of one week and 3.5 days. The second case we investigate has circular $e/i$ tolerance windows. For this case we study a fleet of four satellites, where all of the satellites carry an identical Earth pointing sensor and a star sensor. In this case, the satellites carry electric propulsion systems, and the maneuver cycle duration is set to one week.

#### RECTANGULAR RATIONAL WINDOW

We first investigate the case with the rectangular rational window. We study a two-satellite fleet where the leader satellite is equipped with two sensors, an Earth-pointing payload and a star sensor. Further details on the sensors, as well as the tolerance window definitions were discussed in Section 3.7. Table 5.6 provides a summary of the relevant simulation settings. We emphasize that we used the rational orbital elements only for the design of the tolerance windows and for the analysis of the results. The rational elements are not used for the maneuver planning itself.

As evident from Table 5.6, we have two satellites of identical build with identical propulsion systems. The fleet leader flies a SPP strategy. The leader is controlled to achieve a desired mean longitude difference and desired eccentricity and inclination vectors at the end of the maneuver cycle. In addition, the absolute mean longitude difference is kept between bounds. The constraints are defined in terms of mean elements. The follower satellite aims to achieve its eccentricity and inclination vectors within the annular sectors defined in Section 3.7, its mean longitude difference between an upper and a lower bound and the relative mean longitude below an upper bound only (indicated using a lower bound of $-\infty$ in Table 5.6). The constraints on the final states have the same shape but are made smaller by the factor indicated in the table (similar as done in the previous two application cases). The simulations have been performed for a maneuver cycle duration of 3.5 days (with 50 Monte-Carlo runs) and a maneuver cycle duration of 7 days (a single run was sufficient to show that the sensor cone avoidance constraints were violated). Note that we have chosen 3.5 days because of the synchronicity with the usual 7-day week (i.e. this would allow an operator to check and command a maneuver plan always during normal working days and avoid weekends). No schedule has been enforced in the simulations, but a weight matrix has been used to stimulate the

Table 5.6: Key settings for simulations with a rectangular rational window

| **Parameter** | **Unit** | **Value** | |
|---:|:---:|:---:|:---:|
| Satellite | | L | F1 |
| Thruster configuration | | REF | REF |
| Thrust force | N | 10 | 10 |
| A | $m^2$ | 120 | 120 |
| SPP | | yes | - |
| Constraint on **e** | $10^{-3}$ | - | annular sector |
| Constraint on **i** | mrad | - | annular sector |
| Window on abs $\Delta L$ | mrad | $[-0.175, 0.35]$ | $[-0.5, 0.5]$ |
| Window on rel $\Delta L$ | | - | $[-\infty, 0.175]$ |
| Constraint on final **e** | $10^{-3}$ | fixed final **e** | 0.5·annular sector |
| Constraint on final **i** | mrad | fixed final **i** | 0.5·annular sector |
| Window on final $\Delta L$ | mrad | fixed final $\Delta L$ | $0.25 \cdot [-\infty, 0.175]$ (rel) |
| Type of elements constrained | | mean | relative |
| Maneuver cycle | days | 3.5 and 7 | 3.5 and 7 |
| Schedule | | No | No |
| Use $\mathbf{W}_\tau$ | | Yes | Yes |

optimizer to place maneuvers on the first day of the maneuver cycle.

We first present the results of the 3.5 day maneuver cycle and demonstrate that we were successfully able to satisfy all constraints over the one year simulation. We have repeated the simulation 50 times. Every single case was successful and the average and worst-case performance results are presented. We then show that if the follower satellite were to be equipped with the same sensors as the leader satellite, constraint violations would occur. We show that this is in line with expectation based on the plots that were presented in Chapter 3. Lastly we show that for a 7-day maneuver cycle, the orbit prediction (and control) errors in terms of relative mean longitude are so large that the sensor cone avoidance constraints are violated.

Table 5.7 summarizes the key results of the 50 simulations for a 3.5 day maneuver cycle. The results in terms of $\Delta V$ are comparable to the numbers we have observed before, for satellites with a chemical propulsion system in the REF configuration flying a SPP strategy. In terms of thruster firings we would expect roughly 4 firings per cycle (two NS and two EW) coming to a total of 416 firings. The achieved results are indeed very similar. The achieved minimum distance of 7.97 km is much larger than the requirement (C2) of 5 km. The achieved minimum off-boresight angles for the Earth sensor (C3) and star sensor (C4) easily meet the required off-boresight angles of 9° and 26°.

Figure 5.13 shows simultaneously the relative eccentricity and relative inclination, together with the tolerance windows for one particular Monte-Carlo run. Only some minor constraint violations of the inclination vector tolerance window are observed. In terms of the rational constraint window (Figure 5.14) no constraint violations occurred This demonstrates that the design approach (which uses the minimum relative eccentricity magnitude to scale the tolerance windows) is conservative.

Table 5.7: Results of the application with rectangular rational windows for a 3.5 day maneuver cycle duration, over 50 Monte-Carlo cases.

| **Parameter** | **Unit** | **Value** | |
|---|---|---|---|
| Satellite | | L | F1 |
| Mean $\Delta V$ | m/s | 50.67 | 50.47 |
| Max $\Delta V$ | m/s | 50.85 | 50.80 |
| Mean firings | | 411 | 392 |
| Max. firings | | 416 | 399 |
| Min. Distance | km | - | 7.97 |
| Min. angle C3 | deg | - | 13.47 |
| Min. angle C4 | deg | - | 45.03 |

Figure 5.15 is included to show that the assumption that $\varphi_a$ (which is not constrained) stays in a window of ±0.1 is valid, under the settings in these simulations. Figure 5.16 shows the rational relative mean longitude variations. The figure shows that the constraint is met over the duration of the simulations. All the constraints in terms of rational orbital elements are satisfied over the simulation duration. From Table 5.7 we observe that the underlying constraints (minimum distance, sensor cone avoidance) were also met for all 50 Monte-Carlo cases. We show the distance in the RN-plane in Figure 5.17. Compared to, e.g., Figure 5.9 we observe that the relative motion in the RN-plane is no longer approximately circular, instead it is an approximate ellipse. The underlying reason is that the nominal relative $e/i$-configuration no longer has parallel $e/i$-vectors. Figures 5.18 and 5.19 show the off-boresight angles with respect to respectively Earth and star sensors over the simulation duration (for a particular MC run) and it is obvious from these figures that the constraints are met over the complete simulation. Figure 5.20 shows the relative motion in 3D. The figure also shows the two sensor-cones. We observe from the figure that both sensors “look” in the direction of the same open-end. The relative trajectory never crosses the sensor cones.

We also included Figures 5.21 and 5.22. These figures show that this design works only if the sensors are attached to the leader satellite. Figure 5.21 shows the off-boresight angle with respect to the Earth sensor and Figure 5.22 shows the relative motion of the leader satellite in the RTN frame attached to the follower satellite. In this case the constraint violations are evident. By comparing Figures 5.16 and 5.21 we clearly see the root cause of these constraint violations, namely, whenever the graph of $\varphi_L$ shows large violation of the constraint, the sensor cone avoidance constraint is violated as well. This is not unexpected; the design was only supposed to satisfy constraints on the leader satellite, and in Chapter 3 we saw that this could be achieved using only an upper bound on $\varphi_L$. If we would like to simultaneously satisfy constraints from sensors on leader and follower satellites, only a small change to the current guidance strategy would be required. For example, a symmetric control window on $\varphi_L$ (with upper and lower bounds of respectively 0.5 and -0.5) would do.

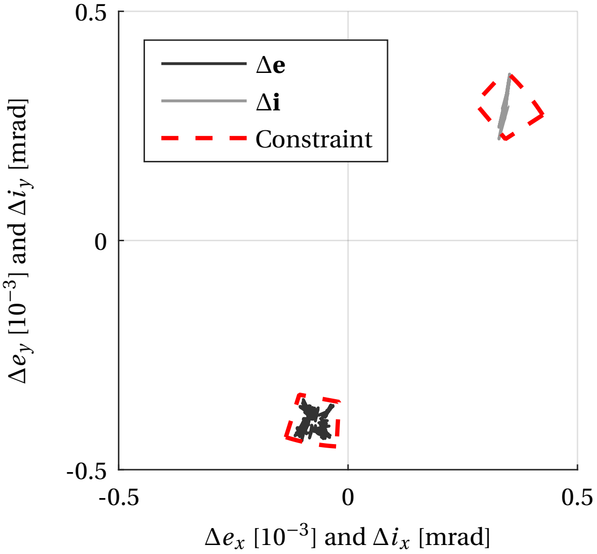

Figure 5.13: Relative eccentricity and inclination vector state trajectories, rectangular rational window, 3.5 day maneuver cycle.

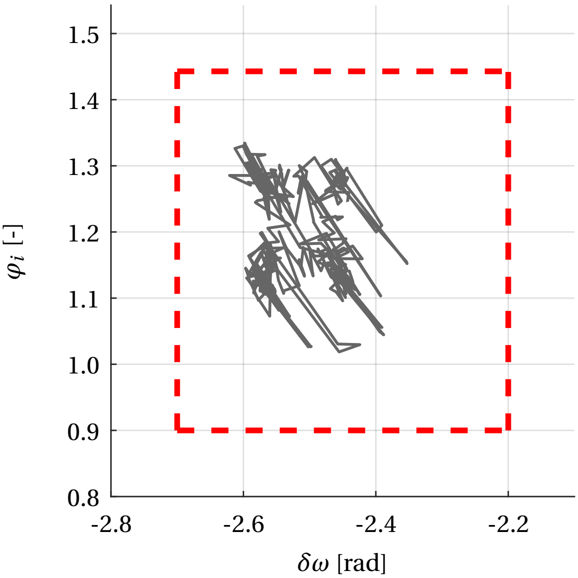

Figure 5.14: State trajectory in rational $\varphi_i$-$\delta\omega$ space, rectangular rational window, 3.5 day maneuver cycle.

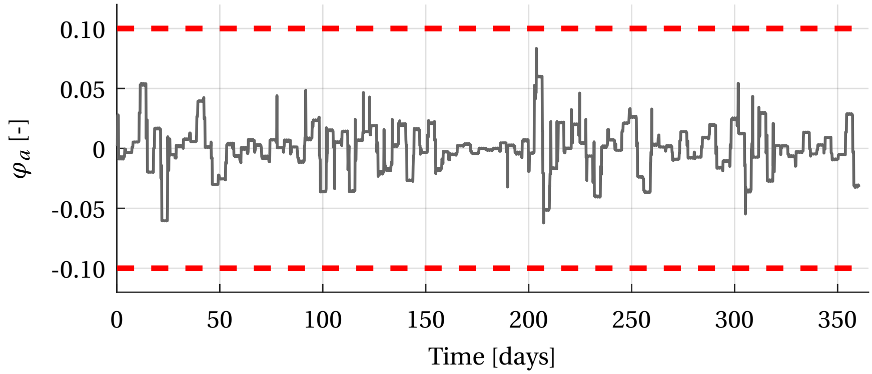

Figure 5.15: Rational relative semi-major axis, rectangular rational window, 3.5 day maneuver cycle.

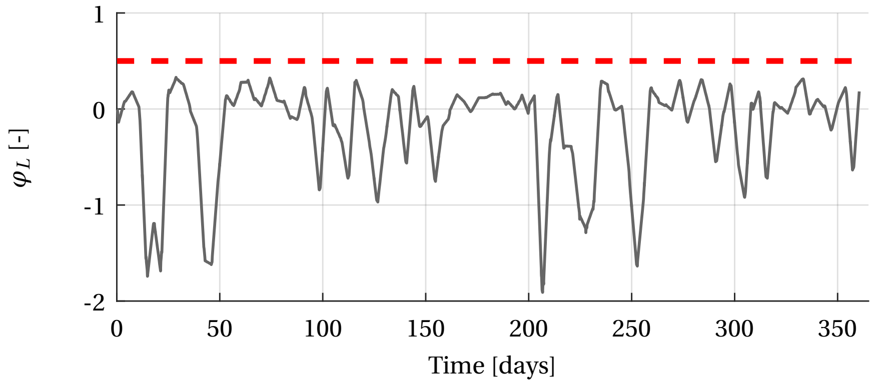

Figure 5.16: Rational relative mean longitude, rectangular rational window, 3.5 day maneuver cycle.

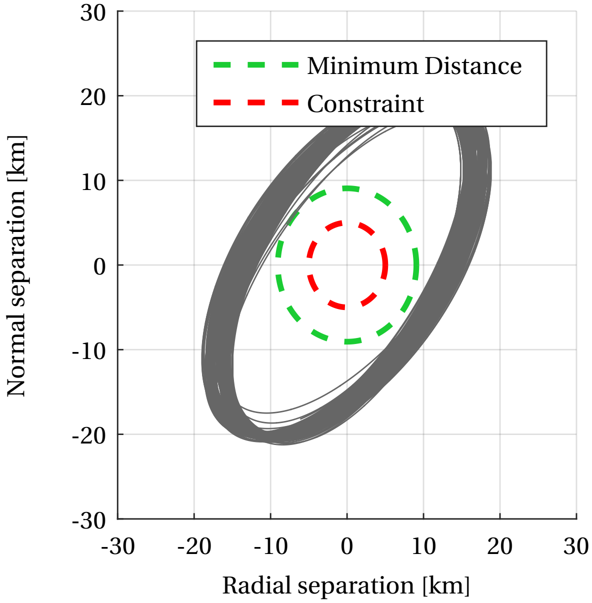

Figure 5.17: Minimum separation distance in the RN plance, rectangular rational window, 3.5 day maneuver cycle.

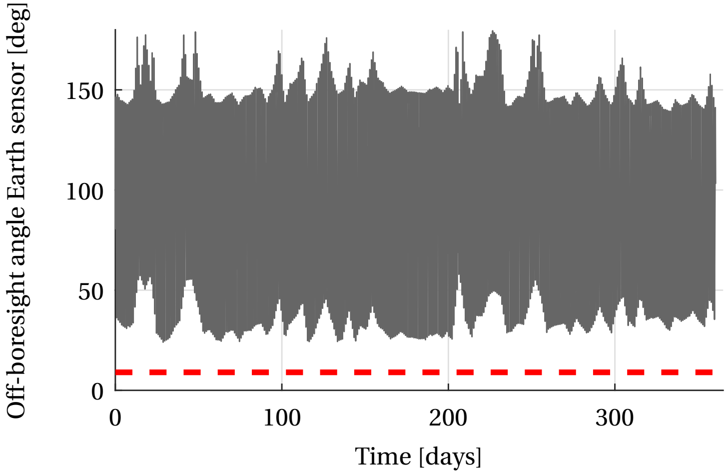

Figure 5.18: Off-boresight angle of satellite F1 with respect to an Earth-pointing sensor attached to the leader, rectangular rational window, 3.5 day maneuver cycle.

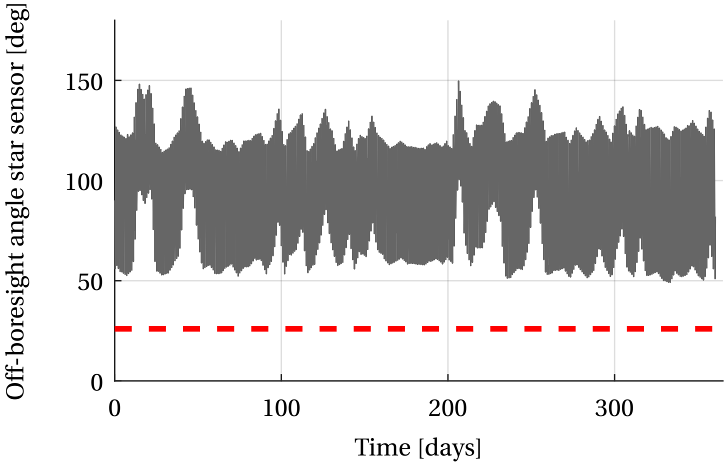

Figure 5.19: Off-boresight angle of satellite F1 with respect to a star sensor attached to the leader, rectangular rational window, 3.5 day maneuver cycle.

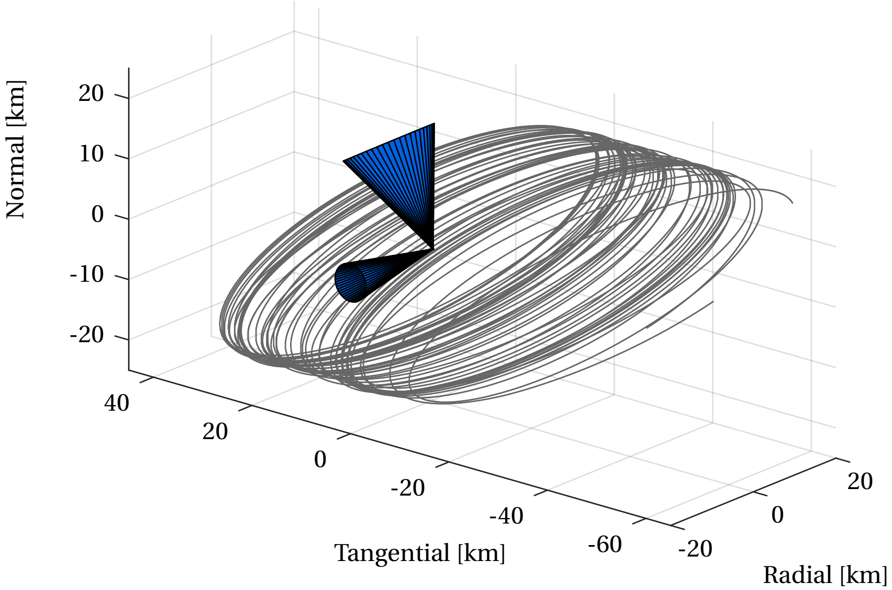

Figure 5.20: Sample relative motion (period of 4 weeks) of the follower satellite with respect to the leader satellite, rectangular rational window, 3.5 day maneuver cycle.

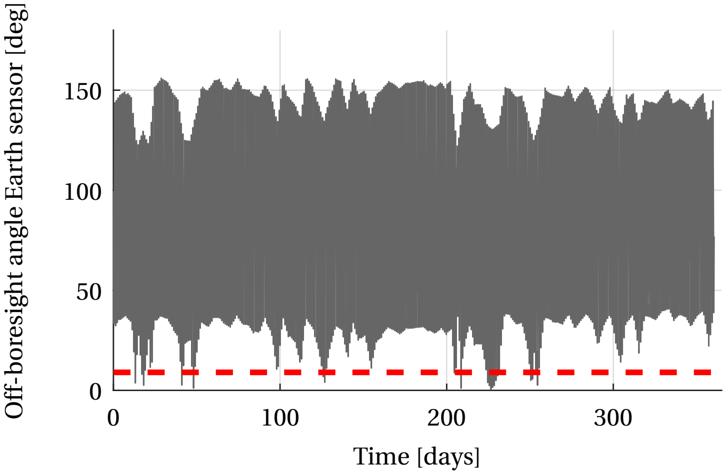

Figure 5.21: Off-boresight angle of the leader satellite with respect to an Earth-pointing sensor attached to the follower F1, rectangular rational window, 3.5 day maneuver cycle. Because only an upper bound on the relative mean longitude was defined we observe constraint violations for an Earth-pointing sensor on the follower satellite.

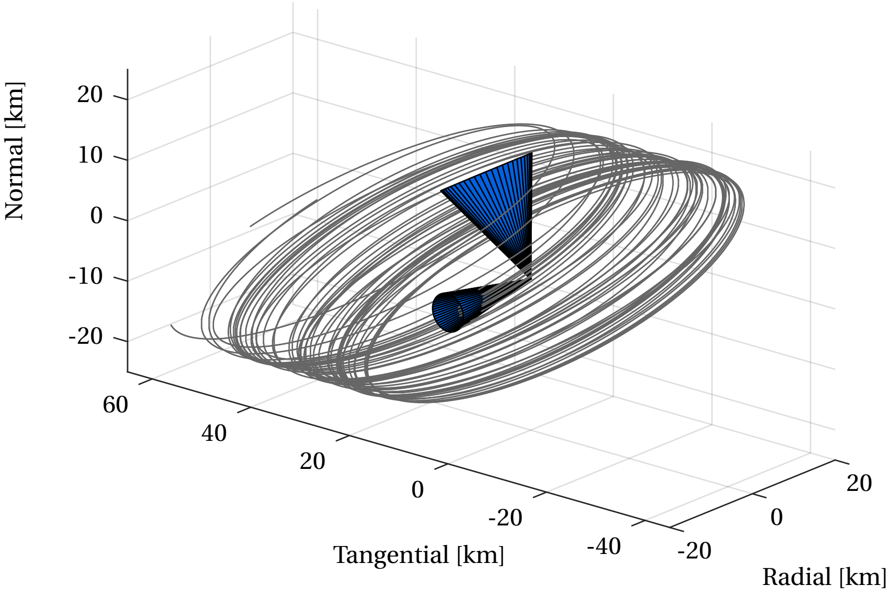

Figure 5.22: Sample relative motion (period of 4 weeks) of the leader satellite with respect to the follower satellite, rectangular rational window, 3.5 day maneuver cycle. The figure clearly shows constraint violations.

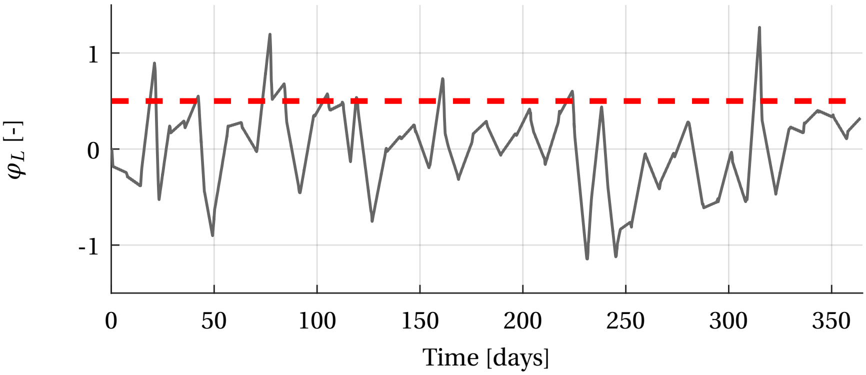

Figure 5.23: Rational relative mean longitude, rectangular rational window, 7 day maneuver cycle. The orbit prediction errors in mean longitude cause violations of the constraint.

Figures 5.23 and 5.24 show respectively $\varphi_L$ and the off-boresight angle of the follower satellite with respect to the Earth sensor on the leader satellite. These figures correspond to a maneuver cycle duration of 7 days. From Figure 5.23 we observe that the 7-day maneuver cycle is too long to achieve the constraints on $\varphi_L$ (i.e. the orbit prediction errors simply grow too large). From Figure 5.24 we see that large violations of the window on $\varphi_L$ correspond to constraint violations of the Earth sensor cone avoidance constraint.

### CIRCULAR $e/i$-WINDOWS

In this section we take the other guidance design from Chapter 3 with circular $e/i$-windows. These simulations intend to demonstrate that, although the design in Chapter 3 was derived for a two satellite fleet with a leader satellite carrying two sensors, we can actually satisfy the constraints simultaneously when all of the satellites carry (the same) Earth-pointing- and star sensors. We extend the configuration to four satellites, each equipped with an electric propulsion system in configuration B. A summary of the most important settings for this simulation is given in Table 5.8. A key difference with the simulations based on the rectangular rational window is that we now have a symmetric design in terms of constraining the relative mean longitude, i.e. we employed both an upper bound and a lower bound.

Table 5.9 shows a summary of the key results. In terms of propellant consumption and number of thruster firings, the results are very much in line with expectations. The minimum distance for each satellite is evaluated with respect to every other satellite and the overall minimum distance (in the RN-plane) occured between the leader satellite and follower satellite 3. The minimum angles between the boresight of the two sensors and another satellite in the fleet have also been investigated for all possible combinations of satellites. The results in the table show that the constraints have been met for all possible combinations.

The relative eccentricity and inclination vector state trajectories are depicted in Fig-

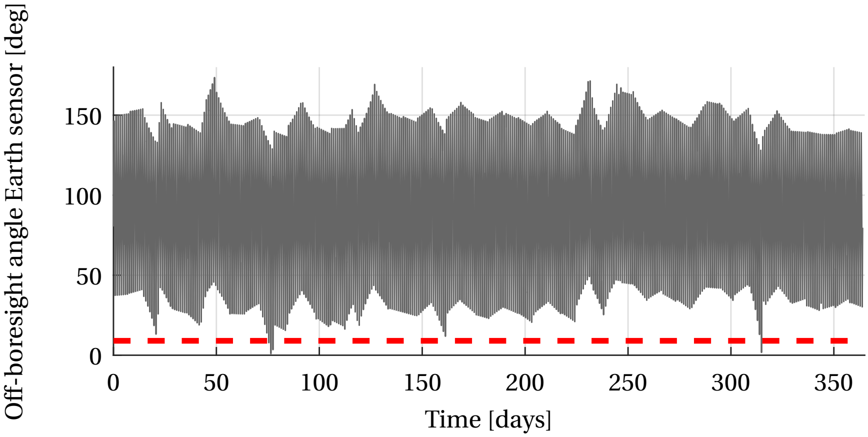

Figure 5.24: Off-boresight angle of satellite F1 with respect to an Earth-pointing sensor attached to the leader, rectangular rational window, 7 day maneuver cycle. The constraint violations correspond to violation in $\varphi_L$ in Figure 5.23.

Table 5.8: Key simulation settings for simulations with geometric constraints and circular $e/i$-windows

| **Parameter** | **Unit** | **Value** | | | |
|---:|:---:|:---:|:---:|:---:|:---:|
| Satellite | | L | F1 | F2 | F3 |
| Thruster configuration | | B | B | B | B |
| Thrust force | N | 0.08 | 0.08 | 0.08 | 0.08 |
| $A_s$ | m$^2$ | 120 | 120 | 120 | 120 |
| SPP | | No | - | - | - |
| Tolerance on **e** | $10^{-3}$ | - | 0.05 | 0.05 | 0.05 |
| Tolerance on **i** | mrad | - | 0.05 | 0.05 | 0.05 |
| Tolerance on abs $\Delta L$ | mrad | $[-0.175, 0.35]$ | $[-0.5, 0.5]$ | $[-0.5, 0.5]$ | $[-0.5, 0.5]$ |
| Tolerance on rel $\lvert\Delta L\rvert$ | mrad | - | 0.175 | 0.175 | 0.175 |
| Tolerance on final **e** | $10^{-3}$ | fixed final **e** | 0.025 | 0.025 | 0.025 |
| Tolerance on final **i** | mrad | fixed final **i** | 0.025 | 0.025 | 0.025 |
| Tolerance on final $\lvert\Delta L\rvert$ | mrad | fixed final $\Delta L$ | 0.044 (rel) | 0.044 (rel) | 0.044 (rel) |
| Elements constrained | | Mean | Mean/Rel. | Mean/Rel. | Mean/Rel. |
| Maneuver cycle | days | 7 | 7 | 7 | 7 |
| Schedule | | No | No | No | No |
| Use $\mathbf{W}_\tau$ | | No | No | No | No |

ures 5.25 and 5.26. We see that the constraints on relative eccentricity and inclination are met almost all the time (we can see some tiny violations of the relative eccentricity windows). The combination of having a tight control window on final state, having an electric propulsion system and considering satellites with identical characteristics greatly helps to satisfy these constraints. The rational control window (Figure 5.27) shows that the constraint is satisfied over the complete simulation (as before we have obtained a conservative design). The rational relative mean longitude in Figure 5.28 show some minor violations of the constraint, but these violations are so small that the design still meets the sensor cone avoidance and minimum distance constraints.

Figure 5.29 shows the trajectory of follower 2 relative to the leader satellite. In contrast to Figure 5.20, the sensors "look" through opposite sides of the tube. This was already theorized in Chapter 3 since the design point for the circular $e/i$-windows has opposite signs of the $\varphi_L$ that violates the constraints (Figures 3.18 and 3.19) for the two sensors.

Table 5.9: Key results for simulations with geometric constraints and circular $e/i$-windows. Target values for $\Delta V$ and # of firings are just an indication, taken from the leader satellite values in Table 5.4.

| **Parameter** | **Unit** | **Value** | | | | |
|---|---|---|---|---|---|---|
| Satellite | | L | F1 | F2 | F3 | Target |
| $\Delta V$ | m/s | 67.86 | 67.98 | 68.01 | 67.78 | 67.88 |
| # of Firings | | 1298 | 1318 | 1320 | 1316 | 1248 |
| Min. distance | km | 9.51 | 9.63 | 9.52 | 9.51 | $> 5$ |
| Min. angle C3 | deg | 18.11 | 20.82 | 23.17 | 21.41 | $> 9$ |
| Min. angle C4 | deg | 49.430 | 50.920 | 51.170 | 47.84 | $> 26$ |

The results in this section have shown that geometric constraints can be dealt with through relative orbit control. The key difference that these constraints impose on the control strategy is that (accurate) control of the relative mean longitude becomes mandatory to satisfy these constraints. Another impact is a different design in terms of nominal relative eccentricity and inclination vectors, where the usual (anti-)parallel $e/i$-vectors no longer lead to a satisfactory result and an adaption to the conventional eccentricity/inclination vector separation strategy was introduced in order to satisfy all geometric constraints simultaneously.

### 5.3.4. ROBUSTIFIED IMPLEMENTATION

This section analyzes the robustified implementation of the method for calculating the station-keeping maneuvers of the follower satellites. The theory from Section 5.2.3 was used to formulate constraints on relative inclination and eccentricity vectors. The solution of the robustified problem formulation then guarantees that the constraints are met over the duration of the maneuver cycle. We first perform an analysis using a worst-case (ROBWC) and a quadratic (ROBQ) implementation of the maneuver errors. Both methods are implemented with a CER of one (i.e. the constraints are enforced at every discrete node). The problem formulation no longer includes a tighter constraint on the final state, as was required in the simulations before. We also show the results of a sim-

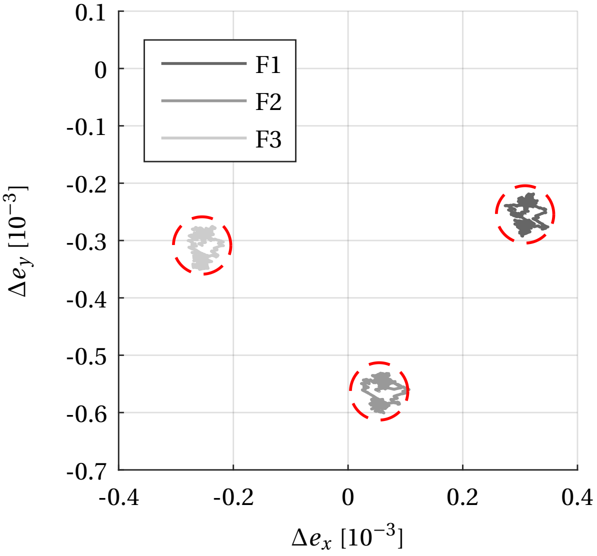

Figure 5.25: Relative eccentricity vectors for simulations with geometric constraints and circular $e/i$-windows

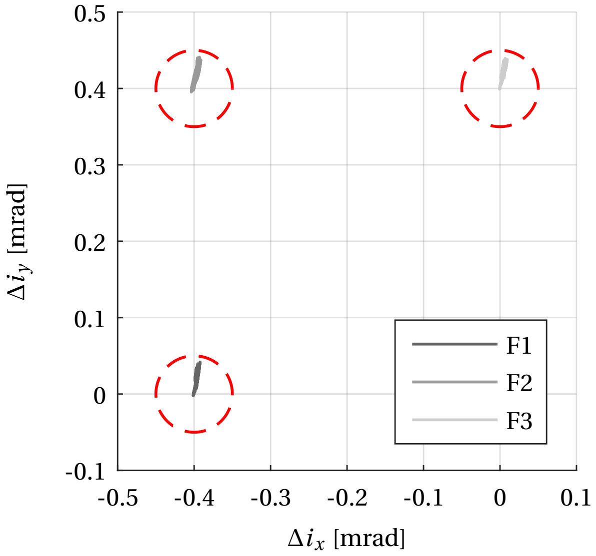

Figure 5.26: Relative inclination vectors for simulations with geometric constraints and circular $e/i$-windows

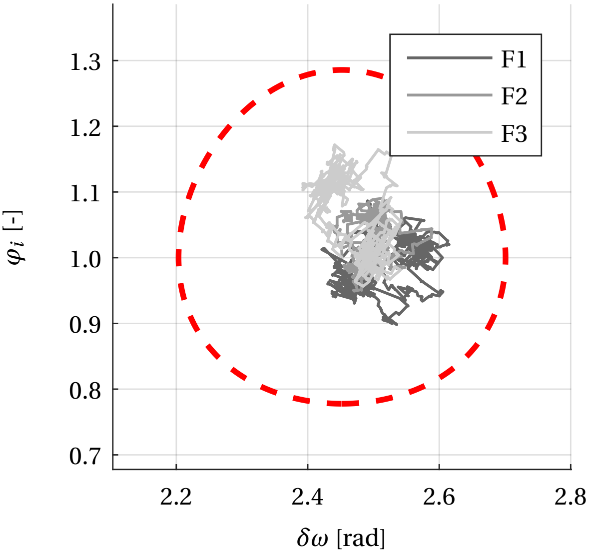

Figure 5.27: State trajectory in rational $\varphi_i$-$\delta\omega$ space for simulations with geometric constraints and circular $e/i$ windows

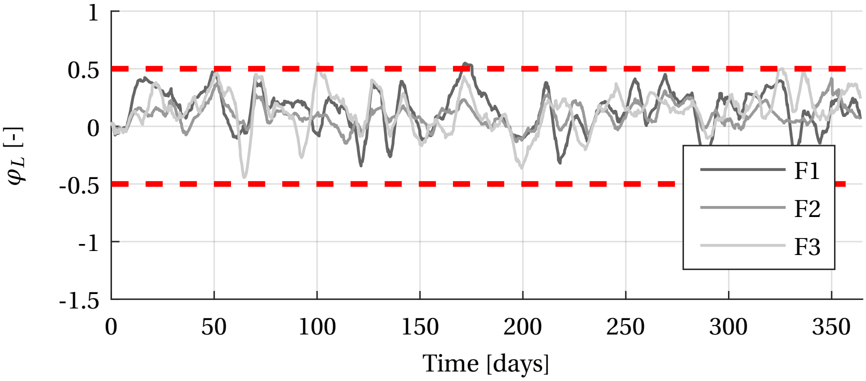

Figure 5.28: Rational relative mean longitude for simulations with geometric constraints and circular $e/i$-windows

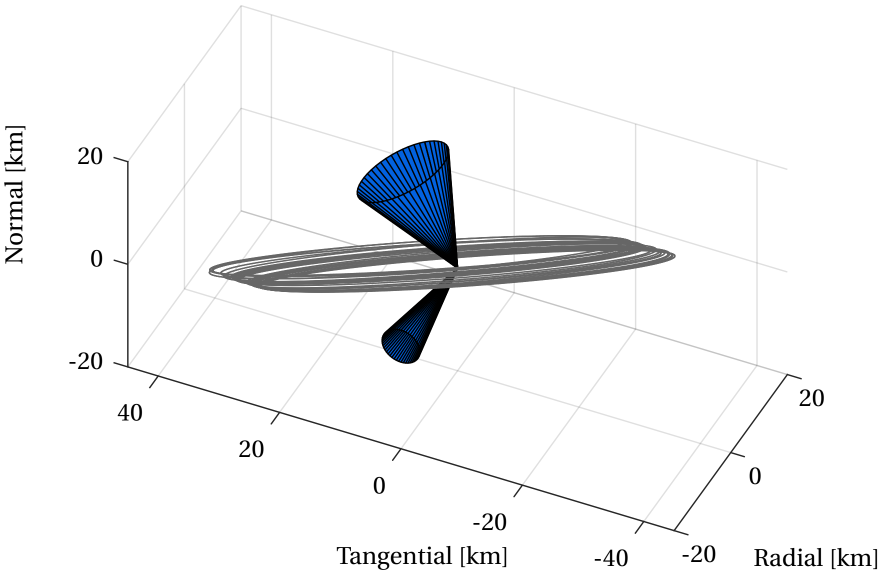

Figure 5.29: Sample relative motion (period of 4 weeks) of the leader satellite with respect to the follower satellite for simulations with geometric constraints and circular $e/i$-windows

ulation with a quadratic implementation of the maneuver errors, a CER of 10 and a final state constraint that is tighter than the other constraints (ROBQF). The merits of the different implementations are discussed.

We use the previously introduced case with the geometric constraints and the circular windows, albeit with a chemical propulsion system in the REF configuration, for a two-satellite fleet. We have chosen a chemical propulsion system for the demonstration of the robustified method because of the larger maneuver errors, therefore providing the most challenging case. We robustify only the constraints on relative eccentricity and inclination because the uncertainty in mean longitude is generally so large that the robustified method would only make sense either for very large mean longitude windows or for very short maneuver cycle durations (otherwise the algorithm would in essence control the relative mean longitude to the center of the control window for the last part of the maneuver cycle). We limit the maneuver cycle duration to 3.5 days because, as we have seen before, control of the mean longitude would be too inaccurate to guarantee satisfaction of the geometric constraints for longer maneuver cycle durations.

The key simulation settings are given in Table 5.10. The leader satellite is in every simulation aspect identical to the leader in Table 5.8, with the exception of the thruster configuration (REF) and the thrust force (10 N). The ROBWC case implements constraints using a linear addition of the standard deviations of the individual errors, Eq. (5.31), while the ROBQ case uses a quadratic addition of the standard deviations of errors, Eq. (5.32). The ROBQF case also uses the same quadratic addition, but enforces a tighter constraint on the final states, which is, on purpose, not formulated in a robustified manner. The leader's uncertainty is added as well, with thruster uncertainty added quadratically in ROBQ and ROBQF and linearly in ROBWC. No schedules or weight matrices were used in these simulations.

All three simulations were successful in achieving the key constraints: the geostationary slot boundaries were not violated, the minimum distance was always well above 5 km and the sensor cones constraints were met as well. Table 5.11 shows the performance in terms of propellant consumption and number of thruster firings. We first note that if we implement the constraints in a worst-case manner, the performance is good, both in terms of propellant consumption and number of thruster firings. From Figure 5.30 one observes that the constraints are met for the complete simulation duration. One might argue that the implementation using a linear addition is too conservative since the state trajectory is relatively far from the boundary. As long as the control window is large enough, this conservatism is not considered problematic.

Table 5.10: Key simulation settings of application cases with robustified constraint implementation

| **Parameter** | **Unit** | **Value** | | |
|---|---|---|---|---|
| Case | | ROBWC | ROBQ | ROBQF |
| Robustified method | | worst-case | quadratic | quadratic |
| Robustified final | | worst-case | quadratic | - |
| Thruster configuration | | REF | REF | REF |
| Thrust force | N | 10 | 10 | 10 |
| A | $m^2$ | 120 | 120 | 120 |
| CER | | 1 | 1 | 10 |
| Tolerance on **e** | $10^{-3}$ | 0.05 | 0.05 | 0.05 |
| Tolerance on **i** | mrad | 0.05 | 0.05 | 0.05 |
| Tolerance on abs. $\Delta L$ | mrad | $[-0.5, 0.5]$ | $[-0.5, 0.5]$ | $[-0.5, 0.5]$ |
| Tolerance on rel. $\lvert\Delta L\rvert$ | mrad | $[-0.175, 0.175]$ | $[-0.175, 0.175]$ | $[-0.175, 0.175]$ |
| Tolerance on final **e** | $10^{-3}$ | 0.05 | 0.05 | 0.0125 |
| Tolerance on final **i** | mrad | 0.05 | 0.05 | 0.0125 |
| Tolerance on final $\lvert\Delta L\rvert$ | mrad | 0.044 | 0.044 | 0.044 |
| Maneuver cycle | days | 3.5 | 3.5 | 3.5 |
| Schedule | | No | No | No |
| Use $\mathbf{W}_\tau$ | | No | No | No |

Figure 5.31 shows the relative eccentricity and inclination state trajectories for the

Table 5.11: Results of the robustified simulation cases.

| **Parameter** | **Unit** | **Value** | | |
|---|---|---|---|---|
| Case | | ROBWC | ROBQ | ROBQF |
| $\Delta V$ | m/s | 50.93 | 50.90 | 51.02 |
| # of Firings | | 610 | 2103 | 1027 |

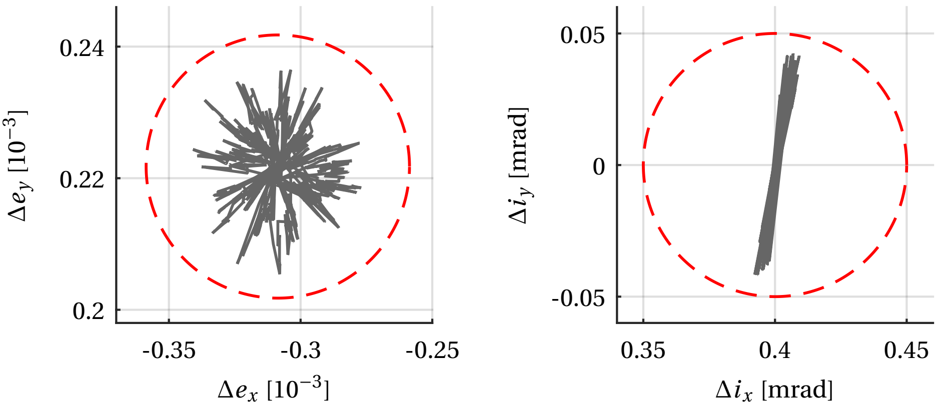

Figure 5.30: Relative eccentricity and inclination vectors for case ROBWC

ROBQ case. We clearly see that the eccentricity state trajectory remains much closer to the boundary than for the ROBWC case. The results of the ROBQ case in Table 5.11, however, reveals a very distinctive and undesired behavior: the number of thruster firings have increased to an undesired extent. The robustified implementation essentially shrinks the tolerance windows by the size of the uncertainty (3-sigma value). Now if the uncertainty due to thruster errors is measured using the $\ell_2$-norm, the magnitude of the uncertainty decreases if the same amount of change to an orbital element is spread over multiple firings. Figure 5.32 shows the thruster firings over the course of one day. From this figure we observe that the firings are clearly spread over several smaller burns. With a smaller magnitude of the uncertainty, the optimizer can keep the state trajectory closer to the boundary. If this happens to be the most propellant-efficient strategy, then the optimizer might choose to use several smaller burns instead of one large burn such that the uncertainty is reduced and the overall propellant consumption for that maneuver cycle is smaller. This explains also the relative inclination plot in Figure 5.31, namely, many maneuvers have not been executed at the optimal location for inclination maneuvers, instead, they have been spread over several smaller maneuvers. As a consequence we see more variations in the direction perpendicular to that of the natural secular variations of the mean inclination vector.

Figures 5.33 and 5.34 show the algorithm at work for one maneuver cycle of the ROBQ case. The light (red) dashdotted line shows the normal tolerance window boundary. The solid lines show the boundaries of the tolerance window on respectively leader, follower and combined leader and follower. The boundary is reduced by the $3\sigma$ errors arising from orbit determination errors, thruster errors and modeling errors. The orbit determination error is visible at the start of the maneuver cycle (most pronounced in Figure 5.34). The modeling errors were approximated as a linear function of time, hence the slope of the lines (the slope changes steepness, since the errors are added quadratically). The thruster errors depend on the optimization problem solution and are determined as

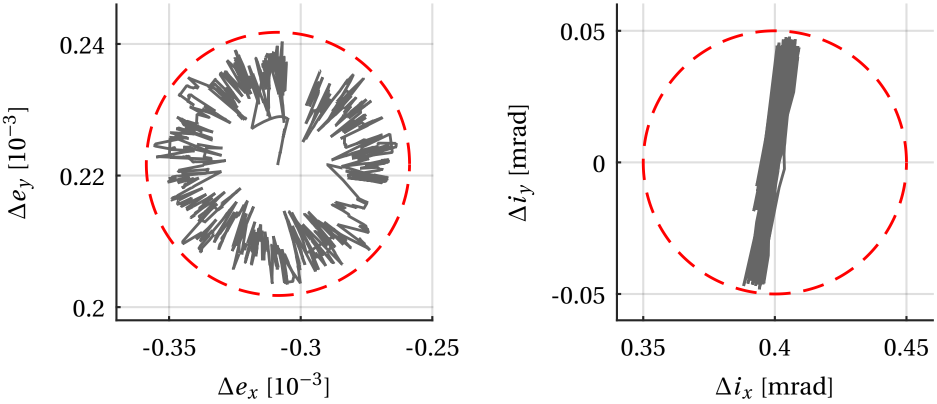

Figure 5.31: Relative eccentricity and inclination vectors for case ROBQ

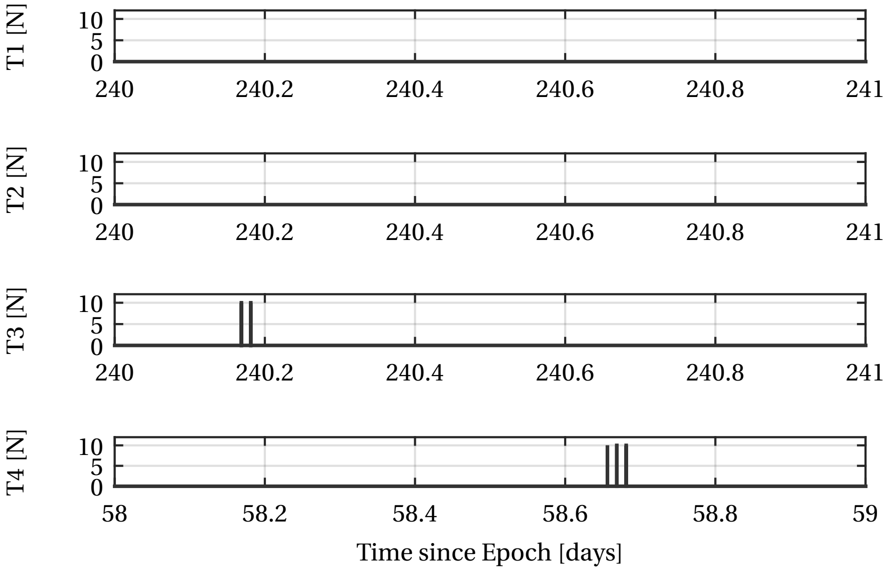

Figure 5.32: Thruster firing during the 240th day for case ROBQ

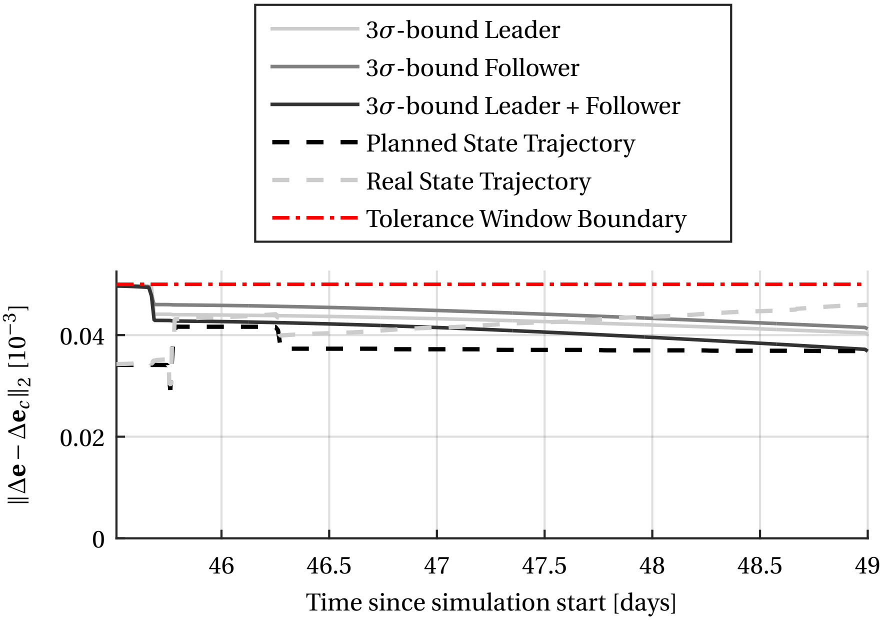

Figure 5.33: The tolerance window boundary on relative eccentricity is shrunk with the size of the 3$\sigma$ errors of leader and follower satellites, case ROBQ.

part of the problem solution. They appear in the figures at the locations where we observe sharp corners in the 3$\sigma$-bounds. The dashed lines show respectively the planned and the actual trajectory. As seen from the figures, the planned trajectory stays below the 3$\sigma$ error bounds, whereas the actual trajectory may cross these boundaries due to the impact of the various errors. The actual trajectories do stay below the tolerance window boundaries, demonstrating that the algorithm works as intended.

In order to counter the undesired behavior observed in the ROBQ case (i.e. the steep increase in thruster firings) we have added a tighter constraint on the final state (i.e. one that is relatively far away from the boundary). This additional constraint requires the optimizer to provide the $\Delta V$ to end up far away from the boundary anyhow. Therefore it cannot "save" propellant by reducing the uncertainty (and thereby the required change to the orbital elements) by making several smaller maneuvers. This is exactly what we observe from the results of the ROBQF case in Table 5.11. We see a major reduction in number of thruster firings. Figure 5.35 shows that the state trajectory for the eccentricity vector is much closer to the center and the inclination state trajectory looks again similar to that of Figure 5.30. Furthermore noteworthy is that this has been achieved with a CER of 10, hence a significant reduction in the number of constraints in the optimization problem.

The robustified implementation has shown that we can, with very high probability, maintain the relative state trajectories inside convex tolerance windows and the key advantage is the elimination of the tolerance window violations. However, it is possible

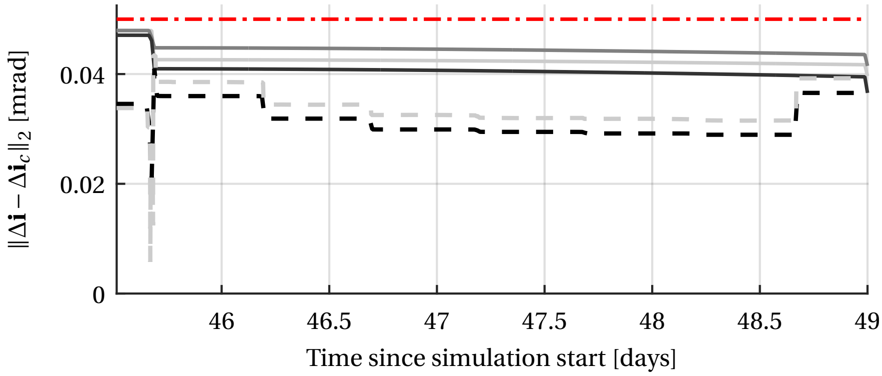

Figure 5.34: The tolerance window boundary on relative inclination is shrunk with the size of the 3$\sigma$ errors of leader and follower satellites, case ROBQ.

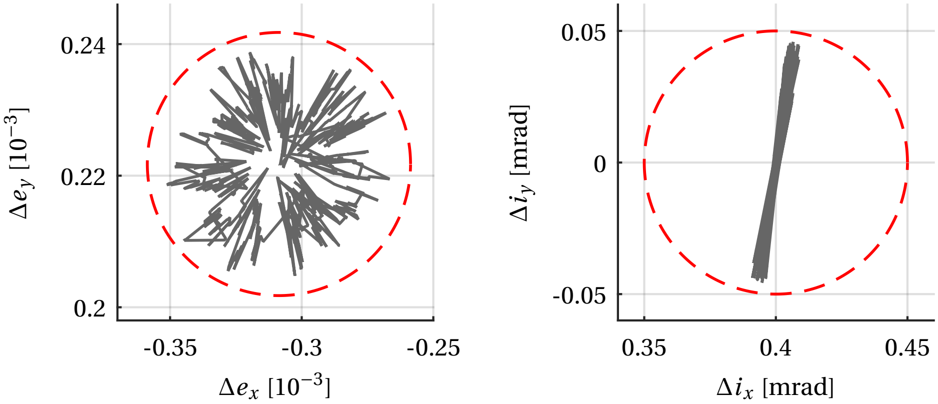

Figure 5.35: Relative eccentricity and inclination vectors for case ROBQF

only at the cost of a much more complex problem formulation and a higher computational load. Whether or not the elimination of the control window violations is worth the increased complexity is a question that can only be answered on a case-by-case basis. As observed in the other simulation cases in this chapter, even with the observed control window violations, no situations occurred that endangered the underlying constraints (most importantly the minimum distance constraint). The design approach generally led to a rather conservative design and minimum distances were far away form the specified thresholds. A use-case for a robustified implementation could arise when it is desired to significantly reduce the threshold on minimum distance. If the margin for error is much smaller, it can become of crucial importance to completely avoid control window violations.

Instead of formulating a robustified problem, the increased robustness may also be obtained by simpler means: one could formulate the problem without the robust additions, while reducing the tolerance windows by a margin. We could then, after solving the non-robust problem, use the problem solution and the equations in Section 5.2.3 to verify that the sum of the $3\sigma$ errors is smaller than the margin we introduced. If this is the case, the problem solution is also guaranteed to stay inside the tolerance windows (now including the margin) and there is no need to solve the more complex robustified problem. This will also avoid some undesired characteristics of the robustified problem, such as the steep increase in number of thruster firings observed in the ROBQ case. The disadvantage of this approach is that it is reactive: only after solving the optimization problem we can determine whether a solution robustly satisfies the constraints, whereas the robustified method proactively guarantees that the constraints are met.

## 5.4. CONCLUDING REMARKS

In this chapter we discussed the definition and solution of the station-keeping problem of a fleet of collocated satellites. The development of the method for calculating the station-keeping maneuvers of collocated satellites built strongly on the single-satellite station-keeping method. A leader-follower hierarchy was used and constraints on the relative states were defined between a follower satellite and the fleet leader. The key goals of the method were to minimize propellant consumption, while maintaining absolute and relative orbital elements inside predefined tolerance windows. A robustified problem formulation was introduced by explicitly accounting for the various errors affecting the (relative) motion in the formulation of the optimization problem.

The collocation control method was tested using a variety of simulation cases, each highlighting different aspects. Each of the simulations that were performed included errors in modeling, thrust errors and orbit determination errors as per Section 2.8. The first simulation case demonstrated that the collocation control method could be used successfully for an inhomogeneous fleet of four satellites. The satellites varied in propulsion system configuration and area-to-mass ratio. The results showed no (significant) increase in propellant consumption compared to single-satellite station-keeping. The observed minimum distance (8.61 km) was well above the threshold (a minimum distance of 6.74 km was theoretically possible without violating the control windows). In terms of the number of thruster firings a significant increase was observed only for the satellite carrying a chemical propulsion system. This increase resulted mainly from following a leader satellite with a low thrust propulsion system.

Another simulation case showed that with the collocation control method it is possible to control a fleet of sixteen identical satellites in a geostationary slot with a longitude and latitude window of ±0.05°. In terms of performance, we observed a small increase in propellant consumption (< 1%) and number of thruster firings (10-20%) compared to single-satellite station-keeping. To achieve the simultaneous control of sixteen satellites, the maneuver cycle duration was reduced to one day, necessitating the frequent availability of orbit determination solutions (possibly obtained through maneuver arcs), of each satellite in the fleet. This short maneuver cycle was also the reason for the increase in propellant and thruster firings.

Two sets of simulations were performed to demonstrate that the guidance method from Chapter 3, paired with the collocation control method, successfully dealt with the sensor cone avoidance constraints. The key difference with previous simulations was the necessity to actively control the relative mean longitude, in order to satisfy the sensor cone avoidance constraints. The first set of simulations showed that for satellites equipped with typical chemical propulsion systems, the impact of maneuver uncertainty on the control of the mean longitude is typically too large for a 7-day maneuver cycle. The reduction to a maneuver cycle duration of 3.5 days was necessary to simultaneously satisfy all geometric constraints (another possibility would be to try to reduce errors in orbit determination and maneuver execution). We then showed that with a symmetric relative mean longitude window, for circular eccentricity and inclination windows, satisfaction of the constraints does not only guarantee that a follower satellite does not enter the field of view of a sensor on the leader satellite, but also that none of the satellites enter the field of view of a sensor on another satellite, given that the satellites are equipped with sensors pointing in the same direction. We showed this for a fleet of four satellites equipped with electric propulsion systems. In this case we achieved satisfactory results also with a 7-day maneuver cycle.

The last set of simulations investigated the robustified problem formulation. Using the robustified formulation allowed to eliminate the small tolerance window violations that were observed in the preceding simulations. We observed a significant increase in thruster firings when the maneuver errors were treated as statistically independent events. This behavior was reduced by adding a tighter final state constraint and a successful implementation was shown. The real advantages of the robustified formulation may only arise when the margin for error is small. A trade-off is required to determine whether the increased complexity and computational power are worth the elimination of the tolerance window violations, especially when the same robust behavior could be achieved without solving a robustified optimization problem.

## REFERENCES

[1] E. M. Soop, *Handbook of Geostationary Orbits* (Microcosm and Kluwer, Dordrecht, 1994).

[2] M. Eckstein, C. Rajasingh, and P. Blumer, *Colocation strategy and collision avoidance for the geostationary satellites at 19 degrees west,* in *International Symposium on Space Flight Dynamics* (1989).

[3] P. Wauthier and P. Francken, *The ASTRA co-location strategy for three to six satellites,* Revista Brasileira de Ciencias Mecanicas (ISSN 0100-7386), vol. 16, p. 163-171 **16**, 163 (1994).

# 6

# CONCLUSION AND OUTLOOK

*My entire life consisted of musings, calculations, practical works, and trials.*
*Many questions remain unanswered; many works are incomplete or unpublished.*
*The most important things still lie ahead.*

Konstantin Tsiolkovsky

*I am, and ever will be, a white socks, pocket protector, nerdy engineer.*

Neil Armstrong

***Abstract***
*A novel method was developed to deal with the problems of single-satellite station-keeping and collocation of a fleet of satellites under geometric constraints. This method was enabled by the formulation of the equations of motion in the form of a linear, time-varying system. It is discussed how the development of this method and subsequent analysis relate to the research questions of this work. The limitations of the method are presented as well as a number of recommendations for further research.*

This work has treated the advanced guidance, control and dynamics of geostationary satellites. Both single-satellite station-keeping and collocation of a fleet of satellites were investigated. The primary motivation for studying the station-keeping of geostationary satellites was the need to mitigate sensor interference originating from a satellite passing through the field-of-view of a sensor on another satellite. Secondary motivations arose from the increased use of solar electric propulsion systems and the availability of an autonomous (on-board) orbit determination capability.

## 6.1. CONCLUSIONS

In this section we present the research questions, along with answers to these questions. In addition, we present conclusions from work that was not directly linked to the research questions. For convenience, each research question is repeated before it is answered.

**1. How to do safe and economic guidance and control of geostationary satellites based on convex optimization?**

(a) Can the perturbed equations of motion be described using convex functions only?

(b) Can station-keeping maneuver plans be determined using numerical optimization methods for convex problems?

(c) How are station-keeping strategies resulting from numeric optimization methods related to the current state-of-art?

(d) What are benefits and disadvantages compared to conventional methods in terms of propellant consumption, maneuver frequency, control accuracy, flexibility and robustness?

The dynamics of a satellite in a geostationary orbit were modeled using nonlinear and non-convex functions. A convexification of these nonlinear dynamics was achieved using two simplifying assumptions: both the input matrix and the perturbing accelerations of a satellite that is controlled to stay inside a geostationary slot can be approximated by the input matrix and the perturbing accelerations at the center of the geostationary slot. Using these assumptions the dynamics were formulated as a linear, time-varying system of first order differential equations, driven by time-dependent but known perturbing accelerations. An analytic investigation was performed to characterize the maximum errors introduced through these simplifying assumptions.

The LTV model was discretized using a Runge-Kutta fourth order method and a zero order hold on the controlled accelerations. The resulting system of equations formulates any future state as an affine combination of the initial state and controlled acceleration profile. This discretized model is directly suitable for use in numerical optimization problems. A numerical analysis was performed to investigate the propagation errors using the discretized LTV system.

A series of increasingly complex convex optimization problems were formulated that can be solved to obtain a maneuver plan for station-keeping of a geostationary satellite. The final optimization problem formulation has a number of desired characteristics: the problem is convex, the solution of the problem provides directly the thrust forces that are delivered by each thruster, the problem was scaled to improve the numerical solution and the problem was reformulated to guarantee that a solution exists that meets the constraints.

A comparative analysis of a conventional station-keeping algorithm and the convex optimization-based algorithm for calculating station-keeping maneuver was presented. With a conventional method, an analytic calculation of the station-keeping maneuvers under the assumption of impulsive $\Delta V$'s is meant. The algorithms were configured to follow the same strategy in terms of eccentricity control, inclination control and mean longitude difference control. The results showed that the convex optimization-based algorithm provided almost identical solutions to the conventional scheme, providing an important validation of the novel method. Both algorithms required exactly the same number of maneuvers over the course of a one-year simulation. The propellant consumption and state trajectories were also nearly identical.

To study the characteristics of solutions obtained using the novel algorithm, an optimization problem was formulated with a horizon of one year. The optimization problem formulation allows to include bounds on the state and control variables at any desired discrete node. Such investigations were not possible using conventional methods for calculating station-keeping maneuvers. The solutions to several formulations of the one year horizon problem further validated the methodology as classic guidance strategies were retrieved: the algorithm came up with a sun-pointing perigee strategy for eccentricity control and all inclination maneuver were made in the direction parallel to the long-term secular variation of the inclination vector. The problem formulation further allowed to investigate the influence of certain parameters or design choices on the station-keeping performance. It was shown that the SPP strategy has no benefits for typical electric propulsion configurations. Another important conclusion was that the structure of the solution of the station-keeping problem can be manipulated by choosing suitable weighting factors in the cost function, allowing indirect control over the number of thruster firings. Furthermore, the relation between the constraint enforcement ratio and tolerance window violations was investigated.

A key benefit of the novel method compared to the conventional station-keeping method is that the novel method can be used to calculate the station-keeping maneuvers for a large variety of propulsion systems. The magnitude of the thrust force is explicitly constrained in the formulation of the problem, allowing to use the method from high thrust chemical propulsion systems to very low thrust electric propulsion systems. The conventional method can be used as long as the error made by approximating a maneuver by an impulsive $\Delta V$ is small enough, hence, the conventional method fails for very low thrust-to-mass ratios. Another benefit of the novel method is that the satellite state can be constrained at arbitrary points in time in the station-keeping cycle, whereas conventional methods can generally deal only with a single constraint per synchronous element (usually an input to the algorithm is the orbital element differences to be achieved during the station-keeping cycle, with no explicit constraints on the orbital elements themselves). In the novel method it is straightforward to prevent thruster firings during certain (parts of) orbits, for example, to avoid thruster firings in eclipses. With a conventional scheme such constraints need to be dealt with on a case-by-case basis. If a maneuver is calculated to take place in a prohibited zone an operator intervention is usually required to relocate the maneuver. Such a situation is avoided altogether using the novel method.

To achieve a high control accuracy, a formulation of the problem in the form of a receding horizon controller was introduced. The method was shown to be compatible also with such an implementation scheme. In order for such an implementation to be successful in reality, frequent orbit determination solutions are required, possibly through maneuver arcs. The introduction of GNSS receivers on geostationary satellite can enable a receding horizon controller implementation. Using conventional methods it is difficult to achieve accurate control of the state variables, mostly because the state cannot be constrained at different locations in the maneuver cycle.

The key disadvantage of the novel method is that no explicit control can be exercised over the number of maneuvers that are executed within a station-keeping cycle. With the conventional scheme the number of maneuvers is explicitly defined, as well as the days on which these maneuvers are executed. These characteristics allow routine operations according to fixed schedules, accounting for the usual five-day work weeks. Although the novel method lacks this explicit control, some form of control can still be exercised by making a smart choice of weighting functions, and possibly by enforcing a schedule upon the algorithm, such as excluding maneuvers on certain days in the cycle. This applies dominantly to satellites with a chemical propulsion system, since for typical electric propulsion configurations, the thrust force is so low that maneuvers are required (almost) every day of the week.

**2. How to extend the proposed optimization methods to collocate several satellites under geometric constraints?**

(a) Can the geometric constraints be formulated as a convex constraint?

(b) What is the impact of the geometric constraints on the conventional coordination and station-keeping strategies?

(c) How to incorporate the geometric constraints and to solve the resulting constrained optimization problem?

(d) Can the conventional $e/i$-vector separation strategy be adapted to account for geometric constraints?

Three types of geometric constraints were analyzed in this research. The first constraint is to stay within the geostationary slot boundaries, which applies both to single-satellite station-keeping as well as to collocated satellites. This constraint is already convex. The second constraint was the minimum distance constraint. This constraint applies to collocated satellites and is non-convex. The third constraint is to avoid the field of view of a conic sensor attached to another satellite in the fleet. Also this constraint is non-convex.

The latter two constraints were not directly formulated as convex constraints. Instead, an analysis was made to identify the regions in terms of relative orbital elements that satisfy these constraints. A linear transformation between a state representation in terms of Cartesian position and velocity vectors and relative orbital elements was introduced to connect the analysis in Cartesian space to the relative orbital elements. For a fixed set of relative orbital elements, the relative orbit can be found by tracing out the Cartesian position for a mean longitude $L$ between 0 and $2\pi$ using the transformation mentioned before. We analyzed the satisfaction of the constraints for any position of the satellite inside this relative orbit. To deal with the geometric constraints we were essentially looking for a set of relative orbits that satisfied the constraints for any satellite position inside the relative orbit. A key ingredient of this analysis was the introduction of rational relative orbital elements. These rational relative orbital elements were helpful in reducing the dimensionality of the design space and visualize the constraint satisfaction for the relevant part of the design space in a single figure.

To satisfy the minimum distance constraint, only the radial-normal plane was used. The reason is that the orbit prediction accuracy in the tangential plane is much lower than in radial and normal directions, mostly because errors in the knowledge of the semi-major axis leads to errors in the prediction of the drift in the tangential direction. These tangential errors are usually an order of magnitude larger than errors in radial and normal direction. The satisfaction of the minimum distance constraint essentially becomes a function of the configuration of relative eccentricity and inclination vectors (with a small contribution from a difference in semi-major axis). Using the rational orbital elements, a map was created showing the achievable minimum distance for combinations of relative eccentricity and inclination vectors (parametrized using rational elements). This map was used to select windows on relative eccentricity and inclination vectors that satisfy the minimum distance constraint. The minimum distance constraint is taken into account in the conventional coordination strategy, the eccentricity/inclination vector separation strategy, and hence this constraint alone did not impact the conventional strategy.

The sensor cone avoidance constraints on the other hand had an important impact on the conventional strategy: they necessitated active control of the relative mean longitude difference between the satellites in the fleet. Since we investigated those combinations of relative orbital elements that satisfied the constraint for any satellite position inside the relative orbit, there is always a relative mean longitude difference for which the constraint is violated. Hence, in addition to tolerance windows on the relative eccentricity and inclination vectors, a tolerance window on relative mean longitude difference was required to satisfy the constraints. When including the sensor cone avoidance constraints, a combination of relative eccentricity and inclination vectors was deemed better than another combination if it allowed larger variations of the relative mean longitude difference. Again, a map was created in terms of rational relative orbital elements, showing the smallest relative mean longitude difference that would result in a violation of the constraint. Each sensor, specified by a pointing direction and half-cone angle, required its own map.

A design process, with an elaborate example, was introduced to select a region in rational space that simultaneously satisfies multiple geometric constraints. For two specific examples, a method was introduced to realize a region in rational space using tolerance windows on relative eccentricity and inclination vectors. Two types of convex tolerance windows on relative eccentricity and inclination vectors and a convex window on relative mean longitude difference were chosen that could be included directly in the optimization problem formulation.

The optimization problem formulation developed for single-satellite station-keeping was extended towards a fleet of collocated satellites. A leader/follower hierarchy was used and the follower satellites were assigned to relative orbital element tolerance windows with respect to the leader satellite. Tolerance windows were designed that account for the geometric constraints as introduced before. By maintaining the follower satellites inside these tolerance windows, satisfaction of the geometric constraints was guaranteed.

The geometric constraints required changes to the conventional eccentricity/inclination vector separation strategy. Two key changes were identified. The first change was already discussed: the sensor cone avoidance constraints necessitate control of the relative mean longitude difference. From the analysis of the minimum distance constraint it was observed that perpendicular relative eccentricity and inclination vectors are prohibited if a separation distance is to be guaranteed in the radial-normal plane. The typical configuration with parallel relative eccentricity and inclination vectors was not suitable for satisfying some sensor cone avoidance constraints, such as an Earth-pointing sensor. A suitable geometry depends on the involved sensors, their pointing direction and their field of view. The complexity of the strategy to satisfy all constraints simultaneously therefore depends on the satellite design. Although it was not investigated what the most optimal pointing directions are, it can be stated that having identical sensor pointing directions on different satellites in the fleet can make dealing with these constraints significantly easier.

Several simulation studies have confirmed that the method to design tolerance windows on relative orbital elements and the implementation of these tolerance windows in the optimization-based collocation control method led to the satisfaction of the geometric constraints. The simulation studies included the minimum distance constraint and two sensor cone avoidance constraints arising from respectively and Earth sensor and a star sensor. The various constraints had no (significant) impact on the propellant consumption, confirming the suitability of the approach to deal with the geometric constraints using relative orbital elements.

**3. Can station-keeping and collocation guidance and control of satellites in GEO be improved with on-board orbit determination and electric propulsion capabilities?**

(a) What are suitable sensors and actuators and what are their performance?

(b) Is it realistic to perform autonomous on-board station-keeping using numeric optimization based methods?

(c) What are potential concepts for collocation with increased on-board autonomy?

(d) How to transition towards on-board autonomous control within realistic operations constraints and requirements?

In terms of sensors for autonomous on-board orbit determination only a GNSS receiver was discussed briefly. Such receivers are being implemented already on current and next generation geostationary satellites and the latest results on performance testing of these receivers has shown their potential. The application of GNSS receivers on geostationary satellites is expected to make a continuous on-board orbit determination solution available, possibly with significant improvements in performance compared to current ground-station tracking.

A thorough review of existing and upcoming electric propulsion systems was omitted. Instead, a highly simplified electric propulsion system model was used in this work, with characteristics derived from two existing electric propulsion systems with ample flight heritage. The thrust level of such electric propulsion systems is significantly lower than for chemical propulsion systems. This low thrust-level invalidates the assumption that a maneuver can be approximated with an impulsive $\Delta V$ and hence required a maneuver planning algorithm that appropriately deals with the low thrust . The low thrust-level further impacted the frequency at which maneuvers were executed. The maneuver frequency was increased from once every week or fortnight, to several thruster firings per day.

Another important impact of an electric propulsion system is that the thrusters are required to point away from the solar panels to avoid contamination. Solar panels are typically mounted on the North and South facing panels of a geostationary satellite. Since a geostationary satellite usually requires more than 90% of $\Delta V$ in North and/or South directions a significant increase in required $\Delta V$ was observed in comparison to results with a chemical propulsion system. An investigation was performed to study the effect of the thrust direction (for a fixed 45° off-pointing with respect to the north or south direction). The investigation revealed that a small component of thrust is required in the tangential direction, but other than that, the pointing direction had only a minor influence on the number of thruster firings and required propellant. We did observe an influence of the pointing direction on the orbit prediction accuracy. Thrusters having a large component in radial direction showed smaller orbit prediction errors than thrusters with a large component in tangential direction, for the thruster errors implemented in this work. This behavior was most apparent for the prediction of the mean longitude difference and the orbital motion difference.

It was shown that a much higher accuracy of control could be achieved using the proposed station-keeping method in a receding horizon controller setting. Such implementation is only possible if frequent orbit determination solutions are available, as is the case with an on-board GNSS receiver. The maneuver plans resulting from the receding horizon controller implementation showed an increase in the number of required maneuvers. An electric propulsion system can usually sustain a much higher number of maneuvers than a typical chemical propulsion system. Hence, the combination of a GNSS receiver and an electric propulsion system enables an implementation relying on receding horizon control. Such an implementation would be most beneficial in a completely automated manner, to avoid the need for manual inspection of maneuver plans by an operator. Whether this automation is best achieved on-board or on-ground has not been investigated.

The remaining research sub-questions have have not been answered in this work and provide directions for further research. A discussion is presented in Section 6.3. In the sequel, several conclusions are presented that were not treated in response to the research questions.

A method was developed for transforming between mean and osculating orbital elements. This method relied on a similar assumption as the linear time-varying dynamics: the (periodic) variations induced by the perturbing accelerations at the slot center provide a good enough approximation of the periodic variations anywhere else in the slot. Only a subset of the perturbations were included, namely, the perturbations resulting in periodic variations of the orbital elements that were small enough to leave uncontrolled. The orbital element variations were averaged over a one year period, with the exception of the mean longitude difference. This last element was averaged over a one month period, because the yearly variations were too large to tolerate.

The robustified formulation of the collocation problem was introduced to guarantee satisfaction of the constraints on relative orbital elements. Robustly satisfying such constraints allows to reduce the minimum separation distance between the satellites, which in turn could increase the number of satellites that are collocated in a single slot. The robustified formulation was achieved by accounting for the various errors affecting the orbit prediction accuracy in the formulation of the optimization problem. The simulations showed both positive and negative aspects of the robustified implementation: the tolerance windows were kept for the duration of the simulation, however, for one of the implementations a significant increase in number of thruster firings was observed as a result of the robustified implementation.

## 6.2. CRITICAL REFLECTION

Several new methods were developed for the modeling as well as guidance and control of geostationary satellites. This section provides a critical reflection upon the developed methods.

The LTV model developed in this work was successful in covexifying the dynamics, albeit at the cost of a reduction in orbit prediction accuracy. Under the assumptions used for other modeling errors, orbit determination errors and actuator errors, the model was adequate and the contribution of the LTV dynamics to the orbit prediction errors was only minor. If, however, the other errors are reduced in magnitude, the contribution due the LTV model becomes more prominent and the LTV model may need to be replaced by a more accurate model.

In the analysis of the sensor cone avoidance constraints, maps were provided showing what bound on the mean longitude difference was required for combinations of relative $e/i$-vectors. These maps might be slightly misleading, which we motivate with an example. Figure 3.11 presents such a map for an Earth pointing sensor. This map shows clearly that the typical $e/i$-configuration with parallel relative eccentricity and inclination vectors is not ideal for this particular sensor cone avoidance constraint. What it does not show is that also for parallel relative eccentricity and inclination vectors it is possible to satisfy the sensor cone avoidance constraint, namely, by separating the satellite by a large enough distance in mean longitude difference. This design option is certainly viable, however, we focused on other options, because such a design quickly exhausts the configuration space.

When transforming from relative to rational orbital elements, information on the actual size of the minimum distance, or of the relative mean longitude difference is lost, but only available in units of $a\delta e$. In the design stage, the possible values of $\delta e$ are unknown. We therefore specified a minimum value $\delta e_{\text{min}}$ and used this minimum value to ensure satisfaction of the constraints. Although this works well, it leads to a conservative design since the worst-case combination of relative eccentricity and inclination vectors with respect to a certain constraint is determined by a combination of $\delta e$, $\delta i$ and $\delta \omega$ and the worst-case value of $\delta e$ may well be larger than $\delta e_{\text{min}}$. This was clearly observed from the results in Chapter 5: even in the presence of errors, the bounds on the rational elements were satisfied at all times with ample margin, whereas the tolerance windows on the relative orbital elements were violated at some points in time.

In the formulation of the optimization problem we allowed the thrust level to vary between zero and $T_{\text{max}}$. A maneuver calculated by the optimization problem is realized by making a burn with $T_{\text{max}}$ for a duration that achieves the same impulse as the maneuver resulting from the optimization problem. This realization introduces an error that we can control by choosing the length of the discretization interval. However, when a maneuver is calculated that has a duration smaller than the minimum on-time of the thruster, we discard the maneuver altogether. If a maneuver plan includes many small maneuvers, discarding all small maneuvers can lead to significant errors. Ideally these minimum on-times are included in the optimization problem formulation. However, this leads to a non-convex domain for the thrust force vector, which is something the method developed in this work cannot deal with.

A limitation of the developed method for station-keeping and collocation is that it provides no explicit control over the number of thruster firings. With conventional methods, or some other optimization-based methods, the number of thruster firings is defined explicitly and it is known before calculating a maneuver plan how many maneuvers will be executed during a maneuver cycle. Knowing a-priori the number of thruster firings makes it straightforward to control the number of on/off-cycles of a thruster over its lifetime. On the other hand, the advantage of a variable number of thruster firings is that state constraints can be enforced at many more points in time during a maneuver cycle. In case of conventional method with a fixed number of firings, we can only implement two constraints per firing (one firing has two unknowns; location in the orbit and duration/magnitude).

Collocating a fleet of satellites using the method developed in this work keeps the relative orbital elements of a follower satellite inside a tolerance window with respect to the leader satellite. The tolerance windows are defined as an offset from the leader state trajectory. The result of this formulation is that if a leader satellite makes a (large) maneuver, the follower satellite is required to make a similar maneuver to ensure that it maintains its relative state inside the predefined tolerance window. This leads to a natural synchronization of the maneuvers of the satellites in the fleet. From an operational point-of-view it may not be ideal to have each satellite in the fleet making a maneuver simultaneously, especially when taking into account that a maneuver on one of the satellites in the fleet may fail. Conventionally, the large inclination maneuvers are executed either individually or in pairs, with an orbit determination in between the maneuvers to ensure that the maneuver was executed successfully before commanding a similar maneuver to another satellite in the fleet. In terms of the control windows on relative eccentricity and inclination vectors defined in this work, such a maneuver strategy will temporarily violate the tolerance windows, without leading to a potentially dangerous situation. Thus, the specified tolerance windows over-constrain the problem, excluding some interesting strategies for spreading the maneuvers over the maneuver cycle. Note that this is true mostly for satellites with a chemical propulsion system. Satellites with an electric propulsion system make maneuvers on a daily basis, and since each orbit has only two locations where the NS maneuvers are most efficient, the maneuvers will be executed at those locations. This synchronization of maneuvers is not so problematic for electrically propelled satellites as the maneuvers are generally much smaller in terms of $\Delta V$.

The robustified problem formulation introduced additional conceptual and computational complexity. Using a quadratic addition of the maneuver errors led to a significant increase in thruster firings, whereas a linear addition may be deemed too conservative. Adding a tighter final state constraint, while using a quadratic addition of maneuver errors provided a compromise between the two options. Nevertheless one should analyze whether the increased complexity is worth the elimination of small control window violations.

## 6.3. RECOMMENDATIONS FOR FURTHER RESEARCH

In the sequel, several recommendations for further research are identified in the fields of guidance, control and dynamics of geostationary satellites.

The LTV dynamics relies on the assumption that the perturbing accelerations can be approximated by those accelerations affecting the geostationary slot center. This assumption becomes increasingly erroneous for larger distances from the slot center. In most realistic scenarios the state of a geostationary satellite is controlled towards some reference position. A good example is the eccentricity vector, which, in the case of a SPP-strategy, is controlled to lie on a circle with the perigee pointing towards the Sun. Instead of determining the perturbing accelerations with respect to the geostationary slot center, these accelerations can also be determined with respect to the reference state towards which the satellite is controlled. The deviations of the satellite state with respect to this reference state are usually smaller than the deviations with respect to the geostationary slot center and hence, by determining the perturbing accelerations with respect to this reference position, the accuracy of the LTV dynamics can be improved. If even higher accuracy is required, a sequential convex programming technique could be used by approximating the perturbing accelerations using the state trajectory obtained during the previous iterate of the maneuver planning algorithm to determine the perturbing accelerations, as well as the input matrix, and iterate until convergence is reached. This approach will significantly increase computation time since in general more than one convex programming problem needs to be solved and the perturbing accelerations need to be evaluated after each successive iteration. The method implemented in this work has the advantage that the perturbing accelerations can be determined off-line.

The thruster model that was used in this work was over-simplified. We identify several possible improvements to the model:

- If the thruster is switched on for short durations, the relative error in thrust force is usually larger than for long, stable burns. This characteristic should be reflected in the error model.

- The thrust direction errors can be separated into errors resulting from attitude control errors, errors resulting from the thruster plume direction variations, uncalibrated misalignment errors and errors resulting from plume impingement on other satellite surface areas (usually containing a deterministic and a stochastic part). Separating the thrust direction error into different components allows for a better characterization of these errors.
- The thruster minimum on-time can be taken into account in the formulation of the maneuver planning problem. Although this leads to a non-convex domain for the thrust force, other convex optimization techniques may be able to deal with this, such as mixed integer linear programming techniques.

Conventional methods for satellites with a typical chemical propulsion system usually place EW maneuvers shortly after NS maneuvers, with an orbit determination in between. This approach allows to correct for the cross-coupling errors introduced by the large NS maneuver. A similar idea could be implemented using the method developed in this work: in a typical scenario with a 7-day maneuver cycle, the NS maneuver can be forced to be executed on the 6th day of the maneuver cycle with the 7th day reserved for orbit determination. This approach is worth investigating as it could significantly reduce the orbit prediction errors (mostly in the tangential direction).

The initial state for solving the maneuver planning problem was obtained from the real satellite state (which originated from a propagation of the nonlinear dynamics). A random error was added to the real state from a distribution specified by an orbit determination error covariance matrix. A more consistent approach would be to model an orbit determination and, in this orbit determination, use the same dynamics model as used to propagate the state inside the maneuver planning algorithm: the LTV model. This more consistent approach could reduce the orbit prediction errors of the LTV model. In addition, to study the impact of orbit determination in a more realistic fashion it is recommended to simulate an orbit determination using a particular geometry with a realistic choice of ground stations, measurement types and measurement errors.

In the current work it was assumed that every maneuver is executed as it was planned (albeit with errors in magnitude and directions). In real operations it can happen that some maneuvers fail to execute altogether. Every strategy that is applied in a real operational scenario shall be able to deal with such thruster failures without putting the satellites at risk, i.e. a (reduced) minimum distance shall be guaranteed even in the case of thruster failures. Such thruster failures are one of the key reasons why, for typical satellites with chemical propulsion systems, the large NS maneuvers are scheduled on subsequent days, so that a thruster failure can be detected and corrective action can be applied without endangering the fleet. A study of the impact of maneuver failures is recommended to be performed for the maneuver strategies developed in this work.

As was discussed in Section 6.2, one result of the current formulation of the collocation control problem is that maneuvers are naturally synchronized between the different satellites in the fleet. For satellites with typical electrical propulsion systems this cannot be avoided, but for chemical propulsion satellites it is generally possible to avoid such synchronization. This is usually applied to avoid potentially dangerous situations when the execution of a NS maneuver fails. The constraints used in this work are too restrictive to allow for such subsequent scheduling of (large) inclination maneuvers. It is recommended to study whether the problem can be reformulated to avoid synchronized inclination maneuvers.

Instead of solving the collocation control problem using (convex) optimization techniques it would be interesting to study whether conventional methods with analytic maneuver calculations are suitable as well to simultaneously deal with the various geometric constraints discussed in this work. This is especially worthwhile for typical chemical propulsion satellites. Since the sensor cone avoidance constraints require active control of the relative mean longitude difference one idea is to synchronize EW maneuvers between the different satellites in the fleet so that similar mean longitude difference trajectories are obtained between the different satellites in the fleet, thereby (passively) minimizing the variations of the relative mean longitude difference. The same could be done for NS maneuvers. However, if operational constraints exist that prohibit synchronized NS maneuvers, solutions may still exist. Figure 3.21 in Chapter 3 shows that large inclination maneuvers are possible as long as they are in the direction of increasing $\varphi_i$ without significantly affecting $\delta\omega$. Such maneuvers are usually possible: making a maneuver parallel to the relative inclination vector such that the magnitude of the relative inclination vector is increased achieves such a desired effect. To guarantee that these maneuvers also effectively reduce the absolute inclination vector, the relative inclination vector should point in the direction of the secular variations of the absolute inclination vector. For a small fleet a possible $e/i$-configuration can have all satellites on a line. The maneuver can then be scheduled on different days for the different satellites in the fleet, as long as they are executed in a specific order. Larger fleets may need maneuvers executed in pairs.

The third research question focused on implementing a station-keeping algorithm in an on-board autonomous fashion. Before studying in detail an on-board autonomous implementation, the question whether an on-board autonomous maneuver planning algorithm has any significant benefits over an autonomous implementation with ground-in-the-loop autonomy needs to be answered. The key argument for increasing on-board autonomy is an improvement in response time. For a geostationary orbit however, a single ground station is visible 24/7. Since orbital dynamics are very slow, on time scales of 24 hours, situations where a response time resulting from on-board autonomy has any significant benefit over a response time achievable with ground-in-the-loop (in an autonomous setting) are rare. Thus before studying on-board autonomous concepts it is recommended to study what potential benefits can be obtained from on-board autonomy and characterize these benefits.

To apply the algorithm in a fully autonomous implementation several recommendations are in order. The processing of a maneuver plan leads to small changes of such a plan. Several maneuvers are grouped together into a single maneuver and small maneuvers (smaller than the minimum specified on-time) are discarded. A simple check can be performed to determine whether the state trajectories obtained from a processed maneuver plan are close enough to those resulting from the unprocessed plan. Another possibility for undesired behavior of the algorithm occurs when, at some point in time, the state trajectory is outside of the specified bounds. The slack variables ensure that the optimization problem is still feasible. However, since a high weight is generally placed on the slack variables (i.e. violations of the boundary are heavily penalized), some radical control action can result to bring the state back to within the boundaries. This behavior is especially obvious when the constraints are enforced at many discrete nodes. If such behavior is deemed undesired, it should be detected and avoided. An analysis of the slack variables resulting from the solution of the optimization problem can support the detection: if these variables are nonzero at some point along the trajectory resulting from solving the optimization problem, it signifies a control window violation. In practice (at least in our simulations) such a situation occurred only at the start of a maneuver cycle. The errors in the previous maneuver cycle were so large that the state trajectory was pushed over the boundary. To avoid such behavior a tighter constraint on the final state was implemented. Even though a tight final state constraint reduces the probability of such an event from occurring, such behavior should be detected and dealt with appropriately in any autonomous implementation, and is therefore recommended for further study.

The current work has omitted detailed quantitative statements on the computational time required to solve the maneuver planning problems. For an on-ground implementation, sufficient computational power is available and an optimization-based approach provides no computational difficulties. If an on-board autonomous implementation is targeted it is advised to design the algorithm such that it can be tested on flight-representative hardware and make appropriate tests to quantify the run-time and other characteristics of the algorithm.

# ACKNOWLEDGEMENTS

Overall, I have really enjoyed the years I have been working as a doctoral candidate. Some moments were tough with little progress. Other times turbulent but creative, with many ideas which were either crucial for this thesis, or unrelated to the thesis, but incredibly interesting and therefore distracting. However, most of all, the time has been absolutely wonderful. I had a chance to learn, to develop my own ideas, to fail and to succeed. I had a rather unusual setting in doing a PhD in Bremen, in a cooperation between the Delft University of Technology (TU Delft) and the German Aerospace Center (DLR), while at the same time working for a commercial company, OHB. I am grateful to all three organizations involved for supporting this scheme. DLR for employing me as a doctoral researcher and supporting the PhD work with guidance, but also with facilities. TU Delft for the academic, and to some extent also financial and facilitating support and OHB for giving me a chance to work on the development of real satellites, the first of which has arrived in a geostationary orbit.

First and foremost I would like to thank Eberhard Gill, my promotor, for his confidence, his support, his guidance, his feedback and his encouragement. Although a five-hour train ride was required to have a meeting, we managed to meet on a regular basis and I always left Delft energized and highly motivated and sometimes full of new ideas. Eberhard, you have been a wonderful promotor. I wish to thank my supervisor at DLR, Stephan Theil for his support, his guidance and his motivating words. I would also like to thank him for the many meetings, the feedback, the reviews and for giving me a place in the GNC department at DLR. I would like to thank Daniel Choukroun, my other supervisor and co-promotor for the (sometimes very long) discussions we had over Skype. Although we did not manage to speak regularly after you moved back to Israel, I do thank you for the discussions we still had and the feedback you were able to provide. Especially your never-ending questions and discussions on the introductions of my papers made the papers a lot better.

At DLR I would also like to thank David Seelbinder, my office mate and one of my fellow doctoral students. We had many technical discussions in our office from which I learned a lot and which were often inspirational. I had a lot of fun working on the application of a model predictive controller on TEAMS with you. I would also like to thank Michael Dumke not only for being one of the most practical guys that I know, being able to solve virtually every problem, but also for the good times during the many coffees and beers. I would further like to acknowledge Federico and Markus for the many discussion in our little formation flying group, for the reviews of some of my papers and Markus also for the support on the work that I did on TEAMS.

From all the people I have worked with at OHB I would like to thank especially Bernard Luebke-Ossenbeck and Nils Neumann, for the years of collaboration, the support for doing some research at OHB and for authoring and co-authoring some of the papers we have written together. I would also like to thank Juan Carlos Bastante, my current team leader, for his support and confidence, as well as my colleague Christopher Palm, for proof-reading this work.

I also express my gratitude towards Muriel Hooghe and Pascal Wauthier from SES. They came up with the motivation for this research and have supported the work in the early phases. Unfortunately, the cooperation had to come to an early close. I am still grateful for the hours of discussion and the technical guidance I received from both of you.

I would like to thank Suzanne Vromen, who was the first student I supervised on her Master thesis. Also from supervising you I have learned and it was fun to see you grow, culminating in the presentation of our paper at the international workshop on satellite constellations and formation flying.

I wish to thank Fabian Fleig. The many surf trips that we have made over the last years were not only great fun and a much needed mental relaxation, they also contributed significantly to the progress of my research. I spent many silent hours sitting next to you in the car to Denmark, or in an apartment on Fuerteventura working on my dissertation.

I am indebted to Teun Hoevenaars for providing me with a place to stay during many of my visits to Delft. We spent many nice evenings discussing, sometimes about our research, but usually completely unrelated subjects.

I am also grateful to Heinz Stoewer. Besides inspiring me to work in the space industry he supported creating the setting in which I did my research. We also spent several great evenings discussing about my work, space or life in general on his visits to Bremen.

Last but certainly not least I would like to thank Kim Mueller, my wonderful girlfriend for the love and support you have given me over the last four years. Your confidence in me, your endless optimism and your amazing smile have kept me happy and I hope will remain to keep me happy for many years to come.

# CURRICULUM VITÆ

Frederik Johannes (Ferdi) de Bruijn was born on March 11th 1985 in Sleeuwijk, the Netherlands. Between 1997 and 2003 he attended the gymnasium Camphusianum in Gorinchem. In 2003 he enrolled as an aerospace engineering student at the Delft university of technology (TU Delft). During his studies he was an active member of several student organisations, and served a year on the board of the study association for aerospace engineering students VSV 'Leonardo da Vinci'. During his studies, Ferdi worked three years for the international postgraduate program in systems and business engineering "SpaceTech", where he coordinated the organization of the program over five locations in Europe. Together with a team of three other students, Ferdi won the regional prize for South-Holland in the European Satellite Navigation Competition, resulting in a start-up company focusing on cellphone applications for festivals. Ferdi did his Master thesis on the topic of formation flying of satellites, in a cooperation with the Massachusetts Institute of Technology, where he spent two months as a guest researcher. Ferdi graduated (cum laude) in 2011. In 2012 Ferdi started his professional career working half-time as a development engineer at OHB-System, and half-time as a PhD researcher at the German Aerospace Center (DLR). His PhD research was performed in a cooperation between DLR and TU Delft. Currently Ferdi works full-time at OHB-System as systems engineer for mission analysis and flight dynamics.

# LIST OF PUBLICATIONS

## This thesis

4. **F.J. de Bruijn**, S. Theil, D. Choukroun, E. Gill, *Collocation of Geostationary Satellites Using Convex Optimization*, Journal of Guidance, Control, and Dynamics **39**, No. 6, pp. 1303-1313 (2016).

3. **F.J. de Bruijn**, S. Theil, D. Choukroun, E. Gill, *Geostationary Satellite Station-Keeping Using Convex Optimization*, Journal of Guidance, Control, and Dynamics **39**, No. 3, pp. 605-616 (2016).

2. **F.J. de Bruijn**, S. Theil, D. Choukroun, E. Gill, *Collocation of Geostationary Satellites Using Convex Optimization*, presented at: 8th International Workshop on Satellite Constellations and Formation Flying (2015).

1. **F.J. de Bruijn**, E. Gill, *Analysis of Relative Motion of Collocated Geostationary Satellites with Geometric Constraints*, presented at: 5th International Conference on Spacecraft Formation Flying and Mission Technologies (2013).

## Other publications

12. S. Vromen, **F.J. de Bruijn**, E. Mooij, *Guidance for Autonomous Rendezvous and Docking with Envisat using Hardware-in-the-Loop Simulations*, presented at: 8th International Workshop on Satellite Constellations and Formation Flying (2015).

11. **F.J. de Bruijn**, E. Gill, *Delayed Target Tracking for Along-Track Formations*, Journal of Guidance, Control, and Dynamics **38**, No. 7, pp. 1318-1324 (2015).

10. **F.J. de Bruijn**, E. Gill, *Influence of Sensor and Actuator Errors on Impulsive Satellite Formation Control Methods*, Acta Astronautica **94**, issue 2, pp. 608-618 (2014).

9. N. Neumann, **F.J. de Bruijn**, B. Lubke-Ossenbeck, R. Larsson, S. Zehetmayer, S. Sassen, P.A. Krauss, *Use of GNSS Receivers within the SmallGEO Product Line*, presented at: 65th International Astronautical Congress (2014).

8. **F.J. de Bruijn**, C. Bewick, B. Luebke-Ossenbeck, R. Janovsky, *Propellant-Efficient Method for Controlled Deorbit of LEO Satellites*, presented at: 64th International Astronautical Congress (2013).

7. **F.J. de Bruijn**, E. Gill, *Influence of Sensor and Actuator Errors on Impulsive Satellite Formation Control Methods*, presented at: 63rd International Astronautical Congress (2012).

6. **F. de Bruijn**, E. Gill, J. How, *Comparative Analysis of Cartesian and Curvilinear Clohessy-Wiltshire Equations*, Journal of Aerospace Engineering, Sciences and Applications **3**, issue 2, pp. 1-15 (2011).

5. **F. de Bruijn**, E. Gill, J. How, *Comparative Analysis of Cartesian and Curvilinear Clohessy-Wiltshire Equations*, presented at: 22 th International Symposium of Spaceflight Dynamics (2011).

4. E. Gill, G. Chiocchia, B. Escudier, M. Lisi, H. Stoewer, **F. de Bruijn**, *Integrated Post-graduate Space Education and Training*, presented at: 22nd International Conference of Education, Research and Innovation (2008).

3. **F.J. de Bruijn**, E. Gill, E.W. Ashford, *SpaceTech - International Postgraduate Education in Space Systems and Business Engineering*, presented at: 22nd International Conference of Education, Research and Innovation (2008).

2. **F.J. de Bruijn**, E.W. Ashford, W.J. Larson, *SpaceTech - Postgraduate Space Education*, Acta Astronautica **63**, issue 1-4, pp. 486-492 (2008).

1. **F.J. de Bruijn**, E.W. Ashford, W.J. Larson, *SpaceTech - Postgraduate Space Education*, presented at: 58th International Astronautical Congress (2007).